

DOCTORAL THESIS

STUDY OF AZIMUTHAL ASYMMETRIES IN
EXCLUSIVE LEPTOPRODUCTION OF VECTOR
MESONS ON TRANSVERSELY POLARISED
PROTONS AND DEUTERONS

by
Paweł Sznajder

supervised by
professor Andrzej Sandacz



National Centre For Nuclear Research, Otwock - Świerk

March 2015

Abstract

STUDY OF AZIMUTHAL ASYMMETRIES IN EXCLUSIVE LEPTOPRODUCTION OF VECTOR MESONS ON TRANSVERSELY POLARISED PROTONS AND DEUTERONS

Hard exclusive leptonproduction of mesons on nucleons has played an important role in studies of the hadron structure and recently gained a renewed interest as it allows access to the generalised parton distributions (GPDs). The GPDs provide a novel and comprehensive description of the nucleon partonic structure and contain a wealth of new information. In particular, the GPDs give a description of the nucleon as an extended object, referred to as the three-dimensional nucleon tomography, and give access to the orbital angular momentum of quarks. Hard exclusive meson production is sensitive to various types of the GPDs depending on a quark content and quantum numbers of the meson (ρ^0 , ω , π^0 , ...).

In this thesis recent results obtained by the author on hard exclusive vector meson production using data taken by the COMPASS experiment at CERN are presented. The measured observables are the azimuthal asymmetries in hard exclusive ρ^0 and ω meson productions on the transversely polarised protons and deuterons. Some of these asymmetries are sensitive to the GPDs E , which are related to the orbital angular momentum of quarks. Other asymmetries are sensitive to the parton helicity flip GPDs H_T , which are related to the transversity PDFs. In addition, the results for the ω meson are sensitive to the pion pole exchange contribution to the production mechanism. The measured $A_{UT}^{\sin(\phi-\phi_S)}$ asymmetry values are used in order to investigate sensitivity of the experimental results in constraining the GPDs E for the valence up and down quarks.

In addition to physics results, in this thesis two algorithms designed to improve the quality of data reconstruction in the COMPASS experiment are presented. These are the algorithms developed in order to make the beam momentum reconstruction and to improve the calibration of electromagnetic calorimeters. Both of them improve the precision of measurements presented in the thesis.

Author: mgr inż. Paweł Sznajder

Supervisor: prof. dr hab. Andrzej Sandacz

Streszczenie

BADANIE AZYMUTALNYCH ASYMETRII DLA EKSKLUZYWNEJ LEPTOPRODUKCJI MEZONÓW WEKTOROWYCH NA POPRZECZNIE SPOLARYZOWANYCH PROTONACH I DEUTERONACH

Twarda ekskluzywna produkcja mezonów w rozpraszaniu leptonów na nukleonach odgrywa ważną rolę w studiach struktury hadronów i obecnie jest jednym z głównych narzędzi badania uogólnionych rozkładów partonów (ang. Generalised Parton Distributions, GPDs). Rozkłady te umożliwiają wyjście poza jednowymiarowy opis nukleonu i pozwalają na wgląd w jego niezbadane dotąd własności. W szczególności, rozkłady GPD służą badaniu przestrzennego rozkładu partonów w nukleonie (tzw. tomografia nukleonu) oraz pomiarowi całkowitego momentu pędu partonów, który jest kluczowy dla dekompozycji spinu protonu i dla rozwiązania tzw. zagadki spinowej. Ekskluzywna produkcja mezonów jest czuła na różne rozkłady GPD w zależności od składu kwarkowego i liczb kwantowych wyprodukowanego mezonu (ρ^0 , ω , π^0 , ...).

W pracy zaprezentowane są ostatnie pomiary twardej ekskluzywnej produkcji mezonów wektorowych wykonane przez autora z użyciem danych zebranych przez eksperyment COMPASS w CERN-ie. Zmierzone są azymutalne asymetrie przekroju czynnego dla ekskluzywnej produkcji mezonów ρ^0 i ω na poprzecznie spolaryzowanych protonach i deuteronach. Niektóre z tych asymetrii są czułe na rozkłady GPD E , które są związane z całkowitym momentem pędu kwarków. Inne asymetrie są czułe na rozkłady GPD H_T , które są związane z rozkładami poprzeczności partonów (tzw. *transversity PDFs*). Co więcej, niektóre z asymetrii dla mezonu ω są czułe na proces wymiany pionu w mechanizmie produkcji (tzw. *pion pole exchange*). Rezultaty dla asymetrii $A_{UT}^{\sin(\phi-\phi_S)}$ zostały użyte w próbie nałożenia ograniczeń na rozkłady GPD E dla kwarków walencyjnych.

Poza wynikami fizycznymi, w pracy omówiono dwa algorytmy opracowane z myślą o udoskonaleniu rekonstrukcji danych w eksperymencie COMPASS. Algorytmy te służą do rekonstrukcji pędu wiązki mionowej oraz do poprawienia kalibracji kalorymetrów elektromagnetycznych. Oba algorytmy poprawiają precyzję pomiarów przedstawionych w tej pracy.

Autor: mgr inż. Paweł Sznajder

Promotor: prof. dr hab. Andrzej Sandacz

Contents

1	Introduction	1
2	Theoretical framework	5
2.1	GPD formalism	5
2.2	Hard exclusive meson production and transverse target spin asymmetries	10
3	The COMPASS experiment at CERN	15
3.1	Introduction	15
3.2	Beam line	16
3.3	Polarised target	18
3.4	Tracking spectrometers	20
3.5	Trigger system	21
3.6	Particle identification	22
4	Reconstruction of beam momentum	25
4.1	Introduction	25
4.2	Clusterisation of DAQ hits in BM01-BM04 detectors	26
4.3	Reconstruction of BMS tracks	26
4.4	Reconstruction of beam momentum	32
4.5	Alignment of BMS planes	33
4.6	Old BMS reconstruction algorithm	38
5	Calibration of ECALs based on π^0 signal and genetic algorithm	39
5.1	Introduction	39
5.2	Function of χ^2	39
5.3	Selection of π^0 sample	41
5.4	Genetic algorithm	42
5.5	Performance and results	44
6	Transverse target spin asymmetries in exclusive ρ^0 meson production	49
6.1	Event selection	50
6.2	Estimators of asymmetries	61
6.3	Semi-inclusive background subtraction	66
6.4	Studies of systematic uncertainties	73
6.5	Results	80
7	Transverse target spin asymmetries in exclusive ω meson production	85
7.1	Event selection	86
7.2	Studies of systematic uncertainties	98

7.3 Results	110
8 Analysis of measured asymmetries in the framework of the Goloskokov-Kroll model	117
8.1 Introduction to the Goloskokov-Kroll model	118
8.2 Analysis and results	122
8.3 Conclusions	126
8.4 Parameters of the model	127
9 Summary and outlook	129
Acknowledgement	133
Appendices	135
Bibliography	151

Introduction

One of the most fundamental questions in Science is that concerning the structure of matter. The idea that the matter is build of unbreakable pieces have appeared already in scriptures of ancient philosophers from India and Greece. The Greeks were referring such pieces to as atoms, which means "the uncuttables". In ancient times the idea of atoms was not founded on any observation or an experimental evidence. The first experimental evidences confirming the idea of atoms appeared in the 19th century together with a rapid progress in the chemistry science. The concept of atoms was successfully used in order to classify and explain properties of chemical compounds known at that time.

The atoms were believed to be the smallest pieces of the matter until 1897, when Thomson proved an existence of electrons. This discovery was also used to propose a first model of the atom, describing negatively charged electrons drown in a positively charged medium. This model was believed to be correct until 1909, when Rutherford performed his famous experiment by scattering alpha particles on the atoms of gold. The result of this experiment allowed Rutherford to propose a new model of the atom, where a heavy and compact nucleus is surrounded by a much more extended electron cloud. In the next years a major steps towards understanding the structure of the nucleus were the discoveries of the proton in 1920 by Rutherford and the neutron in 1932 by Chadwick.

In late 50s a new era has begun in the exploration of matter. At that time new accelerators and bubble chambers allowed to reveal a great number of new particles. In order to classify these particles, Gell-Mann and Zweig proposed independently an idea of quarks: objects that explain the most fundamental properties of hadrons, like for instance their charge. An existence of quarks has been confirmed in 1968 at SLAC, where deep inelastic scattering (DIS) of point-like electrons on the nucleons was used to probe the nucleon structure. Few years after the discovery of quarks at SLAC, Gross, Politzer and Wilczek predicted an existence of gluons caring the strong force. The concept of gluons was confirmed in 1979 at DESY. To this day, quarks and gluons are collectively referred to as partons. The term was used for the first time in 1969 by Feynman in his model to explain results of the SLAC DIS experiment.

Since the discoveries of partons a spectacular step forward has been made in order to understand how a longitudinal momentum of the nucleon is shared between individual quarks of different flavours and gluons. This information is contained in unpolarised parton density functions (PDF), which nowadays are well constrained by inclusive and semi-inclusive DIS measurements. While the "inclusive" term refers here to any particle in the final state, the semi-inclusive measurements require a production of specific hadrons, which may be used to probe individual quark flavours. Additional

constraints on the PDF functions come from cross section measurements for other processes, like for instance the production of jets or W and Z bosons. The PDF functions demonstrate a crucial role of gluons that carry about 50% of the nucleon longitudinal momentum.

The spin structure of the nucleon has become a subject of interest after the EMC experiment at CERN had published a surprising result that the total contribution of quark helicities to the nucleon spin, $1/2$, is unexpectedly small [1, 2]. In this pioneering experiment a polarised muon beam was used to probe a structure of polarised nucleons. Data taken in succeeding polarised DIS experiments carried out at CERN, SLAC, DESY and JLAB, but also in polarised proton-proton experiments at BNL, have confirmed the EMC observation that the quark helicities contribute only to about 30% of the nucleon spin. The contribution is significantly smaller than 100% expected in the static valence quark picture, or about 60% when a relativistic motion of quarks is taken into account. This puzzle, named "the nucleon spin crisis", is still an intriguing issue and naturally leads to a question about the contribution of gluon helicities and the role of orbital angular momentum of partons.

Another step forward has been made since the EMC experiment in order to measure the quark helicity distributions, $\Delta q(x)$, where x is the fraction of the nucleon longitudinal momentum carried by the quarks q . In particular, aforementioned polarised DIS and proton-proton measurements were used in global pQCD fits in order to extract the helicity distributions for individual quark flavours, see for instance Ref. [3, 4]. Nowadays, the $\Delta u(x)$ and $\Delta d(x)$ distributions are determined with a relatively good accuracy, while the precision of $\Delta \bar{u}(x)$, $\Delta \bar{d}(x)$, $\Delta s(x)$ and $\Delta \bar{s}(x)$ is still limited. Not much is known about the helicity distributions for heavier quarks, although their helicities can not contribute significantly to the nucleon spin, as densities of those quarks inside the nucleon are small.

In addition to quarks, from the pQCD fits there were also extracted the gluon helicity distribution, $\Delta g(x_g)$, where x_g is the fraction of the nucleon longitudinal momentum carried by the gluons, and its integral representing a total contribution of gluon helicities to the nucleon spin, $\Delta G = \int \Delta g(x_g) dx_g$. Uncertainties on these quantities are much larger than those for light quarks, as available data constrain the pQCD evolution only in a limited range of the scale parameter. Although a large ΔG contribution to the nucleon spin is disfavoured, the range of presently allowed values, $-0.3 < \Delta G < 0.3$, is rather wide. A significant improvement may be expected after data from a future polarised electron-proton collider become available. In addition to the results obtained from the pQCD fits, there exist also direct measurements probing the $\Delta g(x_g)$ distribution. They use the process of photon-gluon fusion that provides the most straightforward access to gluon distributions. The signature of the photon-gluon fusion is either production of hadrons with high transverse momenta (high- p_T process) or production of charm quarks bound in the D or D^* mesons (open-charm process). The present direct measurements allow to probe single values of $\Delta g(x_g)$, although in a limited range of x_g and with large uncertainties. The results of such measurements of $\Delta g(x_g)$ from the SMC [5], HERMES [6] and COMPASS [7, 8, 9] experiments are consistent with those obtained from the pQCD fits.

Not much is known about the orbital angular momentum of partons. Our present knowledge is based almost exclusively on lattice QCD calculations, see for instance Ref. [10]. These calculations indicate sizable values of the orbital angular momentum for the valence up and down quarks, but with opposite signs, $L_u \approx -L_d$. This leads to an almost complete cancellation of their contributions to the nucleon spin.

Another subject that recently attracts a big interest is a three-dimensional structure of the nucleon, which is described either by the generalised parton distributions (GPDs) or the transverse momentum distributions (TMDs). These two complementary approaches provide a comprehensive description of the nucleon and offer a deeper insight than the one-dimensional description used so far.

In the most simple terms, the GPDs correlate one-dimensional PDFs with form factors for each quark flavour and for gluons. The two most important features that can be investigated with the GPD formalism are the nucleon tomography and the total angular momentum of partons. The

nucleon tomography [11, 12, 13] refers to a correlation between spacial (transverse) and momentum (longitudinal) partonic degrees of freedom. The evaluation of this correlation relies only on the GPDs H . The total angular momentum can be calculated using the so-called Ji's sum rule [14], which combines second moments of the GPDs H and E . The Ji's sum rule provides an insight into orbital angular momentum of partons and it may help to resolve the nucleon spin crisis.

A reconstruction of the GPDs requires a comprehensive experimental programme for measurements of broad spectrum of observables probed in various processes and in wide kinematic ranges. The two most important reactions used in order to study the GPDs are deeply virtual Compton scattering (DVCS, $\gamma^*p \rightarrow \gamma p$) and hard exclusive meson production (HEMP, $\gamma^*p \rightarrow Vp$, where $V = \pi, \rho, \omega, \dots$). Nowadays, the GPDs H are constrained comparatively well by the unpolarised PDFs and cross section measurements for the DVCS and HEMP processes [15, 16, 17, 18]. However, more precise data covering a wide kinematic range are still needed. Measurements that will be able to provide such data are planned in the near future at JLAB and COMPASS. The reconstruction of the GPDs E is more difficult, as these GPDs are probed only by a limited number of observables. These are in particular the Pauli form factors for the proton and the neutron, azimuthal asymmetries for the DVCS and HEMP processes measured on transversely polarised targets and the DVCS cross section measured on unpolarised neutrons. The first measurements used to constrain the GPDs E were performed at JLAB, HERMES and COMPASS, see for instance Refs. [19, 20, 21, 22, 23, 24].

The TMDs correlate longitudinal and transverse momenta of partons inside the nucleon, also including dependences on the polarisation of these partons and the polarisation of the nucleon. Similarly to the GPDs, some of the TMDs are related to the orbital angular momentum of partons, however at present time an exact form of this relation is not known. The TMDs are studied in semi-inclusive DIS and Drell-Yan processes on both unpolarised and polarised targets. Much interest in the recent years has been devoted to the Sivers functions, which are the TMDs describing unpolarised partons inside transversely polarised nucleons. In an intuitive and qualitative way, the Sivers functions are related to the orbital angular motion of partons inside the nucleon. The so-called Sivers asymmetries were measured in the semi-inclusive DIS reaction by HERMES on transversely polarised protons [25, 26] and by COMPASS on transversely polarised protons [27, 28] and deuterons [29, 30, 31]. These results were used in order to extract the Sivers functions [32], which turned out to be different from zero and of opposite signs for the up and down quarks. This result is in a qualitative agreement with the aforementioned predictions of the lattice QCD calculations for the orbital angular momentum of quarks. Another key issue in the study of the TMDs is their universality. For certain of them, including the Sivers functions, the theory predicts a change of sign for those measured in the semi-inclusive DIS and Drell-Yan processes. The effect has been not confirmed yet experimentally and it became a subject of interest for future Drell-Yan programmes at several experiments, in particular at COMPASS and RHIC.

The main subject of this thesis is the measurement of azimuthal asymmetries for exclusive muon-production of ρ^0 and ω mesons on transversely polarised protons and deuterons. These asymmetries are important observables as they can be used to constrain specific types of the GPDs. In particular, they are sensitive to the GPDs E appearing in the Ji's sum rule and therefore to the orbital angular momentum of quarks. In addition, the asymmetries are sensitive to the GPDs H_T , which in the forward limit are equivalent to the poorly known transversity distributions. Because of the sensitivity of the meson wave function to specific types of the GPDs, a combination of the results for the ρ^0 and ω mesons may be used to disentangle contributions of the GPDs for the up and down quarks. The asymmetries for exclusive ω meson production are also sensitive to the pion pole exchange contribution to the production mechanism. Modelling of this contribution is not fully constrained by existing data. The measured spin asymmetries are expected to allow a determination of the sign of $\pi\omega$ form factor appearing in the production amplitudes.

The contents of this thesis are as follows. An introduction to the GPD formalism and the definition of the azimuthal asymmetries are given in Chapter 2. The data used in the analyses described in this thesis were taken by the COMPASS experiment at CERN, which is briefly introduced in Chapter 3. An algorithm designed to make a reconstruction of the beam momentum, which have been provided by the author, is described in Chapter 4. This algorithm is particularly important for the measurement of observables for hard exclusive meson production process that proceeds with relatively small cross sections. The new algorithm of the beam reconstruction allowed to increase an available statistics in one of the analyses presented in this thesis by about 25%. It is worth to mention, that this algorithm became the official one in the COMPASS reconstruction software and it is used in all recent COMPASS analyses. Another algorithm provided by the author, which is designed to improve the calibration of electromagnetic calorimeters, is described in Chapter 5. These calorimeters are key detectors for the reconstruction of the ω mesons and for the measurement of corresponding azimuthal asymmetries. The algorithm is based on the π^0 signal reconstructed from the data and on the genetic algorithm. The measurements of the azimuthal asymmetries for exclusive ρ^0 and ω meson productions are presented in Chapters 6 and 7, respectively. The measured asymmetries for two processes are used to set constraints on the total angular momenta of quarks. This is done within the GPD-based model of the HEMP reaction proposed by Goloskokov and Kroll [33, 34, 35, 36, 37, 38] and it is presented in Chapter 8. The summary of the thesis is given in Chapter 9.

The author is a member of the COMPASS collaboration and he took an active part in the work of the GPD analysis subgroup. He played a leading role in the analyses of exclusive ρ^0 and ω meson production processes that are presented in this thesis (Chapters 6 and 7). The ρ^0 analysis has been summarised in two publications [23, 24], while a publication of the ω results is in preparation [39]. The obtained results for both processes were analysed in the framework of the Goloskokov-Kroll model, which implementation has been provided by the author (Chapter 8). In addition to physics analyses, the author contributed to the common work of the COMPASS collaboration. The most important were the developments of algorithms designed to perform the beam momentum reconstruction and to improve the calibration of electromagnetic calorimeters. Both algorithms are described in this thesis (Chapters 4 and 5). In addition, the author participated in developments of the Monte Carlo software. For instance, he implemented Monte Carlo descriptions of the liquid hydrogen target, the small recoil proton detector (RPD) and the large RPD (called CAMERA) for simulations of COMPASS spectrometer response. He also helped to develop the HEPGEN generator [40]. The author participated actively in the data taking and he helped to solve several problems related to the data reconstruction, for instance problems of veto hermeticity and flatness of the random trigger time distribution in 2012 GPD pilot data.

Theoretical framework

A brief introduction to the generalised parton distribution formalism (GPD) is given in Sec. 2.1. In this section main properties of the nucleon GPDs are emphasised and selected reactions are used to illustrate the principles of this formalism. Note, that similarly to the one-dimensional PDFs, the GPDs can be defined for other particles as well, like for instance for the spin-1 deuteron. In addition, they can be studied in a very broad spectrum of reactions. Aside from the original papers where the GPD formalism has been introduced [14, 41, 42, 43], comprehensive overviews can be found in Refs. [44, 45, 46, 47].

Definitions of azimuthal asymmetries in hard exclusive meson production on transversely polarised targets, together with their relation to the GPDs, are given in Sec. 2.2. The measurement of these asymmetries is presented in Chapters 6 and 7, for exclusive ρ^0 and ω meson productions, respectively.

2.1 GPD formalism

Two processes play a special role in the GPD formalism: deeply virtual Compton scattering (DVCS),

$$\gamma^* p \rightarrow \gamma p, \quad (2.1)$$

and hard exclusive meson production (HEMP),

$$\gamma^* p \rightarrow V p, \quad \text{where } V = \rho, \omega, \pi, \dots \quad (2.2)$$

The handbag-like diagrams for these processes are shown in Fig. 2.1.

Under specific kinematic conditions and in the collinear approximation the factorisation theorem allows us to express amplitudes for these processes as a convolution of two terms. The first one, referred to as the hard scattering kernel, describes a perturbative part of the interaction. In the case of DVCS the second term represents an amplitude of emission of a parton from the nucleon and its subsequent absorption by that nucleon. It is a non-perturbative amplitude represented by one of the GPDs. For the HEMP process the second term contains in addition to the GPDs also another non-perturbative part that is specific to the produced meson. It describes a coupling of the partons to the meson that is represented by the distribution amplitudes (DA) [43].

The factorisation is applicable when the virtuality of the virtual photon, Q^2 , and the invariant mass of the $\gamma^* p$ system, W , are large, and if the four-momentum transfer to the target nucleon, t ,

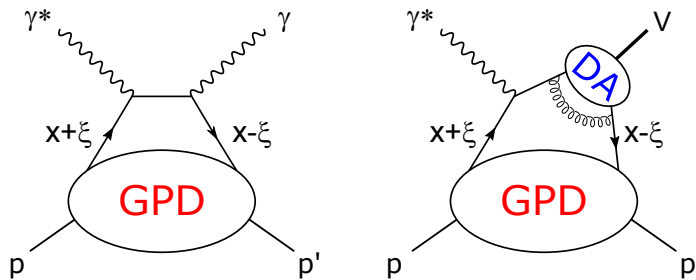


Figure 2.1: Exemplary handbag diagrams for the DVCS (left) and HEMP (right) processes.

is much smaller than Q^2 , $|t|/Q^2 \ll 1$. While the factorisation holds for the DVCS, for the HEMP process it has been proven strictly only for the longitudinal virtual photons, while for the transverse ones the collinear factorisation leads to infrared singularities [48, 49]. They may be overcome in phenomenological approaches, although in a model-dependent way. One of such models has been proposed by Goloskokov and Kroll in Refs. [33, 34, 35, 36, 37, 38] (see also Chapter 8), where the intrinsic transverse momenta of partons forming the meson and the so-called Sudakov term have been used to regularise the singularities.

In order to describe a complex structure of the nucleon the theory provides several types of the GPDs. Each of them is defined for a specific quark flavour or for gluons, $a = q, g$. The GPDs H^a , \tilde{H}^a , E^a and \tilde{E}^a , are defined for the case when parton helicities do not change in the reaction. In the leading twist approximation these GPDs are sufficient to describe both the DVCS and HEMP processes. The GPDs H^a and \tilde{H}^a correspond to no change of the nucleon helicity, while the GPDs E^a and \tilde{E}^a correspond to the nucleon helicity flip. Moreover, the GPDs H^a and E^a correspond to the sum over parton helicities, while the GPDs \tilde{H}^a and \tilde{E}^a to the difference. There exist also GPDs H_T^a , \tilde{H}_T^a , E_T^a and \tilde{E}_T^a , which describe processes when parton helicities change in the reaction. They appear in the description of higher-order effects.

The GPDs are scale dependent functions of three variables: the average longitudinal momentum of the emitted and reabsorbed parton, x , the skewness that describes the difference between the longitudinal momenta of these partons, ξ , and the four-momentum transfer to the target nucleon, t . While the one-dimensional PDFs describe the probability, $|\psi(x)|^2$, that a given parton carries a specific fraction of the nucleon longitudinal momentum, the GPDs describe a correlation between two partons inside the nucleon, $\psi^*(x-\xi)\psi(x+\xi)$. In addition, under specific conditions this correlation is related to a position in the plane transverse to the nucleon motion, as this position is related to the t variable by the Fourier transformation, see Eq. (2.13).

The longitudinal momentum of parton is defined in the GPD formalism in the $-1 < x < 1$ range, where a negative value of x denotes an antiparticle. Therefore, one can distinguish three ranges of x that are shown in Fig. 2.2. In the $-1 < x < -\xi$ and $\xi < x < 1$ ranges antiquarks and quarks are probed, respectively. In these ranges the scale dependence of the GPDs is described by the DGLAP evolution [50, 51, 52, 53]. In the $-\xi < x < \xi$ range quark-antiquark pairs are probed. It gives a unique possibility to study a mesonic structure of the nucleon, which is not possible in the case of one-dimensional PDFs. In this region the scale dependence is described by the ERBL evolution [54, 55]. Since gluons are their own antiparticles, their GPDs are symmetric functions of x .

Because of the convolution with the hard scattering kernel (and the meson wave function for the HEMP process) the GPDs can not be measured directly. Their reconstruction rely on phenomenological parameterisations that obey basic properties of the GPDs, see the following, and that free parameters are constrained by the experimental data. At the present time, there are several available parameterisations that differ by the construction and used parameters. The most

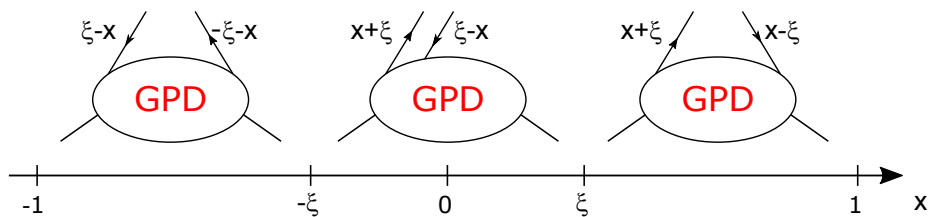


Figure 2.2: Three ranges of the $x \pm \xi$ momentum.

popular are the Vanderhaeghen-Guichon-Guidal (VGG) [56, 57, 15, 44] and Goloskokov-Kroll (GK) [33, 34, 35, 36, 37, 38] (see also Sec. 8.1.2) models based on the double distributions [43, 58] and Kumerički-Mueller (KM) model [16] based on the Mellin-Barnes parameterisations [16, 59]. The models reproduce reasonably well the available DVCS data collected by the JLAB, HERMES and HERA experiments. More precise DVCS data covering a wide region of x_{Bj} will be provided in the near future by the JLAB and COMPASS experiments. In addition to DVCS, the GK model reproduces also the HEMP data taken by the HERMES, HERA and COMPASS experiments. In particular, this model is able to overcome singularities appearing in the description for the transverse virtual photons, however in a model dependent way.

A given process probe different types of the GPDs. In particular, for the HEMP process described in the leading twist approximation the production of vector mesons ($\rho, \omega, \phi, \dots$) involves the GPDs H^a and E^a , while the production of pseudoscalar mesons (π, η, K, \dots) involves the GPDs \tilde{H}^a and \tilde{E}^a . There exists also a sensitivity on the quarks flavours related to the meson wave function. For instance, the overall contribution of GPD $F^a = H^a, E^a, \dots$ to the production of selected vector mesons reads

$$\begin{aligned}
 F_{\rho^0} &= \frac{1}{\sqrt{2}} \left(\frac{2}{3} F^u + \frac{1}{3} F^d + \frac{3}{8} F^g \right), \\
 F_{\omega} &= \frac{1}{\sqrt{2}} \left(\frac{2}{3} F^u - \frac{1}{3} F^d + \frac{1}{8} F^g \right), \\
 F_{\phi} &= -\frac{1}{3} F^s - \frac{1}{8} F^g.
 \end{aligned} \tag{2.3}$$

Note, that the ρ^0 and ω mesons probe the GPDs for up and down quarks in orthogonal combinations that can be used to disentangle their contributions. In addition, the HEMP process probe the gluons at the same order of pQCD as quarks, while in the DVCS process gluons appear only in the next-to-leading and higher orders of pQCD calculations.

The exact definition of the GPDs may be given through nucleon matrix elements of quark and gluon operators, see for instance Ref. [45]. To avoid a repetition of lengthy expressions here, the formulae are not given in this chapter. Note however, that the GPDs are known and distinguished mainly by their relations with physics observables. These relations are given in the following. The two first ones relate the GPDs to the one-dimensional PDFs and the form factors. The polynomiality and positivity bound properties are important as they are crucial to constrain parameterisations of the GPDs. The nucleon tomography and the Ji's sum rule are two intriguing features that attract nowadays much attention of theoreticians and experimentalists.

Forward limit In the forward limit, $t = 0$, and at $\xi = 0$, when the nucleon is untouched and thus its helicity is preserved, certain GPDs are equivalent to the one-dimensional PDFs,

$$\begin{aligned} H^q(x, 0, 0) &\equiv q(x), & H^g(x, 0, 0) &\equiv xg(x), \\ \tilde{H}^q(x, 0, 0) &\equiv \Delta q(x), & \tilde{H}^g(x, 0, 0) &\equiv x\Delta g(x), \\ H_T^q(x, 0, 0) &\equiv h_1^q(x), & H_T^g(x, 0, 0) &\equiv xh_1^g(x). \end{aligned} \quad (2.4)$$

Here, $q(x)$, $\Delta q(x)$ and $h_1^q(x)$ are the unpolarised, helicity and transversity PDF distributions for quarks, respectively, while $g(x)$, $\Delta g(x)$ and $h_1^g(x)$ are the corresponding distributions for gluons. No similar relations exist for other GPDs as at the $\xi = t = 0$ limit they decouple from physics observables. Note however, that in the forward limit the values of the GPDs E^a may not vanish as they carry an information about the total angular momentum of partons, see Eq. (2.10).

Form factors After integration over x the parton helicity-conserving GPDs for quarks are equivalent to the following form factors,

$$\begin{aligned} \int_{-1}^1 dx H^q(x, \xi, t) &\equiv F_1^q(t), & \int_{-1}^1 dx E^q(x, \xi, t) &\equiv F_2^q(t), \\ \int_{-1}^1 dx \tilde{H}^q(x, \xi, t) &\equiv g_A^q(t), & \int_{-1}^1 dx \tilde{E}^q(x, \xi, t) &\equiv g_P^q(t). \end{aligned} \quad (2.5)$$

Here, $F_1^q(t)$, $F_2^q(t)$, $g_A^q(t)$ and $g_P^q(t)$ are Dirac, Pauli, axial and pseudoscalar electromagnetic form factors, respectively. The corresponding relations exist also between the parton helicity-flip GPDs H_T^q , \tilde{H}_T^q , E_T^q and the tensor form factors. For the GPDs \tilde{E}_T^q one has explicitly

$$\int_{-1}^1 dx \tilde{E}_T^q(x, \xi, t) = 0. \quad (2.6)$$

The integrals shown in Eqs. (2.5) and (2.6) do not depend on ξ as a consequence of the Lorentz invariance of the GPDs.

Polynomiality The polynomiality is a non-trivial property of the GPDs. The term means that the Mellin moments of the GPDs are polynomial functions of ξ . For instance, for the GPDs H^q and E^q one has

$$\begin{aligned} \int_{-1}^1 dx x^n H^q(x, \xi, t) &= h_0^{q,n}(t) + \xi^2 h_2^{q,n}(t) + \dots + \xi^{n+1} h_{n+1}^{q,n}(t), \\ \int_{-1}^1 dx x^n E^q(x, \xi, t) &= e_0^{q,n}(t) + \xi^2 e_2^{q,n}(t) + \dots + \xi^{n+1} e_{n+1}^{q,n}(t). \end{aligned} \quad (2.7)$$

Here, only the terms with even powers of ξ are allowed. The polynomiality property is a consequence of the Lorentz invariance of the GPDs.

Note, that the polynomiality property allows to decompose a given Mellin moment of the specific GPD into a set of form factors. In particular, for the zero Mellin moment one has the relations given by Eqs. (2.5) and (2.6).

Positivity bounds The positivity bounds are a set of inequalities that restrict possible values of the GPDs in order to obey the unitarity. They were studied in several papers, for instance in Refs.

[60, 61, 62, 63, 64, 65, 66, 67], by analysing the unpolarised, helicity and transversity one-dimensional PDFs. An exemplary bound, which has been given in Ref. [61], reads

$$\left| H^q(x, \xi, t) - \frac{\xi^2}{1 - \xi^2} E^q(x, \xi, t) \right| \leq \sqrt{\frac{q(x_1)q(x_2)}{1 - \xi^2}}. \quad (2.8)$$

Here,

$$x_1 = \frac{x + \xi}{1 + \xi} \quad \text{and} \quad x_2 = \frac{x - \xi}{1 - \xi}, \quad (2.9)$$

while $q(x_1)$ and $q(x_2)$ are the values of the unpolarised one-dimensional PDF.

Ji's sum rule In the forward limit, $t = 0$, the sum of second Mellin moments of the GPDs H^a and E^a gives the fraction of the nucleon total angular momentum carried by partons a ,

$$\int_{-1}^1 dx x(H^a(x, \xi, 0) + E^a(x, \xi, 0)) = 2J_a. \quad (2.10)$$

The relation holds for any value of ξ as a consequence of the Lorentz invariance of the GPDs. It is known as the Ji's sum rule [14] and it may be used to solve the nucleon spin crisis,

$$1/2 = \sum_q J_q + J_g. \quad (2.11)$$

Note, that by combining the Ji's sum rule with the forward limit of the GPDs \tilde{H}^q , Eq. (2.4), one can extract the value of the orbital angular momentum of quarks,

$$L_q = J_q - \int_{-1}^1 dx \Delta q(x) = \frac{1}{2} \int_{-1}^1 dx x(H^q(x, \xi, 0) + E^q(x, \xi, 0)) - \int_{-1}^1 dx \tilde{H}^q(x, 0, 0). \quad (2.12)$$

A similar separation for gluons is also possible, however not in a gauge-invariant way. The problem was discussed in numerous papers, while the comprehensive summaries of this discussion can be found in Refs. [68, 69].

Nucleon tomography By performing the Fourier transformation of the GPDs H^a at $\xi = 0$, one can obtain the densities of partons carrying a given fraction of the nucleon longitudinal momentum, x , correlated to the position, \mathbf{b}_\perp^2 , in the plane transverse to the nucleon motion with respect to the nucleon center,

$$q(x, \mathbf{b}_\perp^2) = \int \frac{d^2\Delta}{4\pi^2} e^{-i\mathbf{b}_\perp \cdot \Delta} H^a(x, 0, t = -\Delta^2). \quad (2.13)$$

The \mathbf{b}_\perp position is often referred to as the impact space parameter, while the relation given by Eq. (2.13) is known as the nucleon tomography [11, 12, 13]. It allows to make a two-dimensional spacial scan of the nucleon inner structure as a function of x . This unique feature allows in particular to localise particular flavours of quarks and gluons inside the nucleon.

2.2 Hard exclusive meson production and transverse target spin asymmetries

In the kinematics covered by the COMPASS experiment a single photon exchange dominates and the cross section for exclusive meson production may be written as

$$\begin{aligned}
& \left[\frac{\alpha_{em}}{8\pi^3} \frac{y^2}{1-\epsilon} \frac{1-x_{Bj}}{x_{Bj}} \frac{1}{Q^2} \right]^{-1} \frac{d\sigma}{dx_{Bj} dQ^2 dt d\phi d\phi_S} = \\
& \frac{1}{2} (\sigma_{++}^{++} + \sigma_{++}^{--}) + \epsilon \sigma_{00}^{++} - \epsilon \cos(2\phi) \operatorname{Re} \sigma_{+-}^{++} \\
& - \sqrt{\epsilon(1+\epsilon)} \cos \phi \operatorname{Re} (\sigma_{+0}^{++} + \sigma_{+0}^{--}) \\
& - P_l \sqrt{\epsilon(1-\epsilon)} \sin \phi \operatorname{Im} (\sigma_{+0}^{++} + \sigma_{+0}^{--}) \\
& - S_T \left[\sin(\phi - \phi_S) \operatorname{Im} (\sigma_{++}^{+-} + \epsilon \sigma_{00}^{+-}) + \frac{\epsilon}{2} \sin(\phi + \phi_S) \operatorname{Im} \sigma_{+-}^{+-} \right. \\
& \quad + \frac{\epsilon}{2} \sin(3\phi + \phi_S) \operatorname{Im} \sigma_{+-}^{-+} + \sqrt{\epsilon(1+\epsilon)} \sin \phi_S \operatorname{Im} \sigma_{+0}^{+-} \\
& \quad \left. + \sqrt{\epsilon(1+\epsilon)} \sin(2\phi - \phi_S) \operatorname{Im} \sigma_{+0}^{-+} \right] \\
& + S_T P_l \left[\sqrt{1+\epsilon^2} \cos(\phi - \phi_S) \operatorname{Re} \sigma_{++}^{+-} - \sqrt{\epsilon(1-\epsilon)} \cos \phi_S \operatorname{Re} \sigma_{+0}^{+-} \right. \\
& \quad \left. - \sqrt{\epsilon(1-\epsilon)} \cos(2\phi - \phi_S) \operatorname{Re} \sigma_{+0}^{-+} \right]. \tag{2.14}
\end{aligned}$$

Here, only the terms relevant for measurements on transversely polarised targets are shown explicitly. The general cross section formula that includes also terms related to longitudinally polarised targets can be found in Ref. [70].

In Eq. (2.14), x_{Bj} is the Bjorken scaling variable, Q^2 is the negative squared four-momentum of the virtual photon and y is the fractional energy of the virtual photon. The azimuthal angles, ϕ and ϕ_S , are defined in the target rest frame. The angle ϕ is the azimuthal angle between the lepton plane, defined by the momenta of the incoming and scattered leptons, and the hadron plane, defined by the momenta of the virtual photon and the meson, see Fig. 2.3. The angle ϕ_S is the azimuthal angle between the lepton plane and the spin direction of the target nucleon.

The polarisation of the lepton beam is denoted by P_l . A component of the target spin that is perpendicular to the virtual photon direction, S_T , is in the COMPASS kinematics well approximated by the corresponding component perpendicular to the direction of the incoming muon, P_T . According to Ref. [70], the transition between S_T and P_T introduces in Eq. (2.14) a new dependence on the θ angle that is given by the beam and virtual photon directions. This new dependence makes the cross section sensitive to the asymmetries related to longitudinally polarised targets (A_{UL} , A_{LL}). However, those asymmetries are suppressed by the factor $\sin \theta$, which is small at COMPASS kinematics, and therefore their contribution to the cross section formula may be neglected.

The virtual photon polarisation parameter, ϵ , may be approximated by

$$\epsilon = \frac{1 - y - \frac{1}{4}y^2\gamma^2}{1 - y + \frac{1}{2}y^2 + \frac{1}{4}y^2\gamma^2}, \tag{2.15}$$

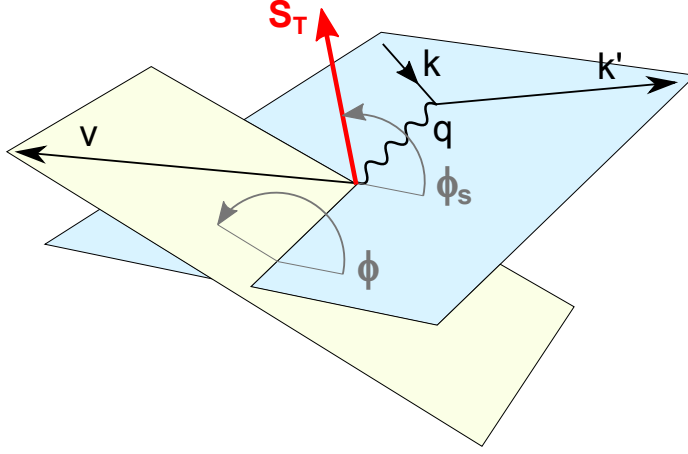


Figure 2.3: The kinematics of hard exclusive meson production in the target rest frame. Here, \mathbf{k} , \mathbf{k}' , \mathbf{q} and \mathbf{v} represent three-momentum vectors of the incident and scattered muons, the virtual photon and the meson, respectively, while S_T is the component of the target spin vector S (not shown) perpendicular to the virtual photon direction.

as in the considered kinematics the mass of an incoming lepton can be neglected. Here, $\gamma = 2x_{Bj}M_p/Q$ and M_p is the proton mass.

The photoabsorption cross sections and interference terms, σ_{mn}^{ij} , are proportional to bilinear combinations of the helicity-dependent amplitudes \mathcal{M} ,

$$\sigma_{mn}^{ij} \propto \sum \mathcal{M}_{i'm',im}^* \mathcal{M}_{i'm',jn}. \quad (2.16)$$

Here, the helicity of the virtual photon is denoted by $i, j = -1, 0, +1$ and the helicity of the initial-state proton is denoted by $m, n = -1/2, +1/2$. The sum runs over all possible combinations of the meson, $i' = -1, 0, +1$, and final-state proton, $m' = -1/2, +1/2$, helicities. For brevity a dependence on the kinematic variables is omitted here. In addition, in the following the helicities $-1, -1/2, 0, 1/2, 1$ will be labelled only by their signs or zero, omitting $1/2$ or 1 .

For transversely polarised targets five single (UT) and three double (LT) spin asymmetries can be defined. These are

$$\begin{aligned} A_{UT}^{\sin(\phi-\phi_S)} &= -\frac{\text{Im}(\sigma_{++}^{+-} + \epsilon\sigma_{00}^{+-})}{\sigma_0}, & A_{LT}^{\cos(\phi-\phi_S)} &= \frac{\text{Re}\sigma_{++}^{+-}}{\sigma_0}, \\ A_{UT}^{\sin(\phi+\phi_S)} &= -\frac{\text{Im}\sigma_{+-}^{+-}}{\sigma_0}, & A_{LT}^{\cos(2\phi-\phi_S)} &= -\frac{\text{Re}\sigma_{+0}^{-+}}{\sigma_0}, \\ A_{UT}^{\sin(2\phi-\phi_S)} &= -\frac{\text{Im}\sigma_{+0}^{-+}}{\sigma_0}, & A_{LT}^{\cos\phi_S} &= -\frac{\text{Re}\sigma_{+0}^{+-}}{\sigma_0}, \\ A_{UT}^{\sin(3\phi-\phi_S)} &= -\frac{\text{Im}\sigma_{+-}^{-+}}{\sigma_0}, & & \\ A_{UT}^{\sin\phi_S} &= -\frac{\text{Im}\sigma_{+0}^{+-}}{\sigma_0}. & & \end{aligned} \quad (2.17)$$

Here, σ_0 is the unpolarised cross section that it is given by the sum of cross sections for the longi-

tudinal, σ_L , and transverse, σ_T , virtual photons,

$$\sigma_0 = \frac{1}{2} (\sigma_{++}^{++} + \sigma_{++}^{--}) + \epsilon \sigma_{00}^{++} = \sigma_L + \epsilon \sigma_T. \quad (2.18)$$

Each asymmetry in Eq. (2.17) is related to a specific angular modulation of the cross section that is a function of the ϕ and ϕ_S angles, cf. Eq. (2.14). The relation between a given asymmetry and the modulation is indicated by the superscript of the asymmetry label. The modulations are orthogonal and they are used to extract the asymmetries from the cross section formula, see Sec. 6.2.

To demonstrate a connection between the GPDs and the azimuthal asymmetries, one could first express the latter ones by the helicity-dependent amplitudes. When using Eqs. (2.16) and (2.17), as well as the following relations being a consequence of the hermiticity and parity invariance of the helicity-dependent amplitudes,

$$\begin{aligned} \sigma_{nm}^{ji} &= (\sigma_{mn}^{ij})^*, \\ \sigma_{-m-n}^{-i-j} &= (-1)^{m-n-i+j} \sigma_{mn}^{ij}, \end{aligned} \quad (2.19)$$

one finds

$$\begin{aligned} \sigma_0 A_{UT}^{\sin(\phi-\phi_S)} &= -2\text{Im} [\epsilon \mathcal{M}_{0-,0+}^* \mathcal{M}_{0+,0+} + \mathcal{M}_{+-,++}^* \mathcal{M}_{++,++} + 1/2 \mathcal{M}_{0-,++}^* \mathcal{M}_{0+,++}] , \\ \sigma_0 A_{UT}^{\sin(\phi+\phi_S)} &= \text{Im} [\mathcal{M}_{0-,++}^* \mathcal{M}_{0+,++}] , \\ \sigma_0 A_{UT}^{\sin(2\phi-\phi_S)} &= -\text{Im} [\mathcal{M}_{0+,++}^* \mathcal{M}_{0-,0+}] , \\ \sigma_0 A_{UT}^{\sin(3\phi-\phi_S)} &= 0 , \\ \sigma_0 A_{UT}^{\sin\phi_S} &= -\text{Im} [\mathcal{M}_{0-,++}^* \mathcal{M}_{0+,0+} - \mathcal{M}_{0+,++}^* \mathcal{M}_{0-,0+}] , \\ \sigma_0 A_{LT}^{\cos(\phi-\phi_S)} &= -\text{Re} [2\mathcal{M}_{+-,++}^* \mathcal{M}_{++,++} - \mathcal{M}_{0-,++}^* \mathcal{M}_{0+,++}] , \\ \sigma_0 A_{LT}^{\cos(2\phi-\phi_S)} &= -\text{Re} [\mathcal{M}_{0+,++}^* \mathcal{M}_{0-,0+}] , \\ \sigma_0 A_{LT}^{\cos\phi_S} &= -\text{Re} [\mathcal{M}_{0-,++}^* \mathcal{M}_{0+,0+} - \mathcal{M}_{0+,++}^* \mathcal{M}_{0-,0+}] , \end{aligned} \quad (2.20)$$

where

$$\begin{aligned} \sigma_0 &= |\mathcal{M}_{++,++}|^2 + |\mathcal{M}_{+-,++}|^2 + |\mathcal{M}_{0+,++}|^2 + 1/2 |\mathcal{M}_{0-,++}|^2 \\ &\quad + \epsilon (|\mathcal{M}_{0+,0+}|^2 + |\mathcal{M}_{0-,0+}|^2). \end{aligned} \quad (2.21)$$

In Eqs. (2.20) and (2.21) only the helicity-dependent amplitudes that are the most sensitive to the GPDs are shown. They are related to the dominant $\gamma_L^* \rightarrow V_L$, $\gamma_T^* \rightarrow V_T$ and $\gamma_T^* \rightarrow V_L$ helicity transitions between the virtual photon and the produced meson. The terms related to the $\gamma_L^* \rightarrow V_T$ and $\gamma_T^* \rightarrow V_{-T}$ transitions are known to be suppressed to a large extent in the HEMP processes [37], and therefore they are neglected in this discussion. In particular, this approximation results in vanishing values of the $A_{UT}^{\sin(3\phi-\phi_S)}$ asymmetry.

The helicity-dependent amplitudes are related to specific types of the GPDs. For instance, the $\mathcal{M}_{0-,0+}$ amplitude is sensitive to the GPDs E^a , as only the proton helicity is changed. The relations between all amplitudes from Eqs. (2.20) and (2.21) and the GPD types are indicated in Table 2.1. A summary of the kinematic variables used for this thesis is given in Table 2.2.

Table 2.1: The sensitivity of the helicity-dependent amplitudes used in Eqs. (2.20) and (2.21) to the GPDs.

helicity transition	amplitude	GPD sensitivity
$\gamma_L^* \rightarrow V_L$	$\mathcal{M}_{0+,0+}$ $\mathcal{M}_{0-,0+}$	H^a E^a
$\gamma_T^* \rightarrow V_T$	$\mathcal{M}_{++,++}$ $\mathcal{M}_{+-,++}$	H^a E^a
$\gamma_T^* \rightarrow V_L$	$\mathcal{M}_{0-,++}$ $\mathcal{M}_{0+,++}$	$\overline{E}_T^a = 2\widetilde{H}_T^a - E_T^a$
$\gamma_L^* \rightarrow V_T$	neglected	
$\gamma_T^* \rightarrow V_{-T}$	neglected	

Table 2.2: The most important kinematic variables used in this thesis.

k	four-momentum of incident muon
k'	four-momentum of scattered muon
p	four-momentum of target nucleon
v	four-momentum of meson
$q = k - k'$	four-momentum of virtual photon
$Q^2 = -q^2$	invariant negative mass squared of virtual photon
$W = \sqrt{(p+q)^2}$	invariant mass of the $\gamma^* - N$ system
M_p	proton mass
$\nu = (p \cdot q)/M_p$	energy of virtual photon in the laboratory system
$x_{Bj} = Q^2/(2M_p\nu)$	Bjorken scaling variable
$y = (p \cdot q)/(p \cdot k)$	fraction of lepton energy lost in the laboratory system
M_v	invariant mass of meson
$M_X^2 = (p+q-v)^2$	missing mass squared of the undetected system
$E_{\text{miss}} = ((p+q-v)^2 - p^2)/(2M_p)$ $= (M_X^2 - M_p^2)/(2M_p)$ $= \nu - E_v + t/(2M_p)$	missing energy of the undetected system
$t = (q-v)^2$	square of the four-momentum transfer to the target nucleon
p_T^2	transverse momentum squared of meson with respect to the virtual photon direction
E_v	energy of meson in the laboratory system

The COMPASS experiment at CERN

3.1 Introduction

The COMPASS (Common Muon and Proton Apparatus for Structure and Spectroscopy) is a fixed target experiment at the CERN Super Proton Synchrotron (SPS). The main aim of this experiment is a study of the hadron structure and the hadron spectroscopy, which includes a very broad spectrum of considered reactions and measured observables.

The hadron structure study includes in particular an exploration of the spin structure of the nucleon. The main source of the new information come from semi-inclusive DIS measurements performed with polarised muon beams and polarised proton and deuteron targets. The most important results obtained so far are precise measurements of the helicity distributions for quarks [71] and one of the first direct measurements of the helicity distribution for gluons in the open charm [8] and high- p_T [9] reactions. The semi-inclusive DIS measurements were also used to explore the fragmentation functions [72] and the transverse momentum distributions (TMDs). The latter observables were studied for instance through the Collins [73] and Sivers [28] asymmetries. In order to examine the universality of TMDs, they will be also probed in the Drell-Yan process by scattering pions on a polarised proton target. Exclusive DIS measurements, like deeply virtual Compton scattering (DVCS) and hard exclusive meson production (HEMP), are used to explore the general parton distributions (GPDs).

The hadron spectroscopy study has been performed with high-intensity hadron beams of both charges and unpolarised liquid hydrogen or nuclear targets. The hadron beams consist of charged pions, kaons and protons (or antiprotons). The type of each beam particle can be distinguished by the Cerenkov counters (CEDARs), which are installed along the beam line. A very large statistics taken in those interactions is being used in the partial wave analysis (PWA). The most important results obtained so far are the measurements of the radiative width for the $a_2(1320)$ and $\pi_2(1670)$ resonances [74] and the discovery of the $a_1(1420)$ resonance [75]. The pion electric and magnetic polarisabilities were measured as well in the Primakov reaction [76].

The proposal of the COMPASS experiment [77] has been submitted in 1996. The first data were taken in 2002 for the polarised DIS programme and this programme was continued until 2004. In 2005 the data were not taken due to modifications in the beam optics related to the installation of the Large Hadron Collider (LHC). The data taking was resumed in 2006 and 2007 for a purpose of the polarised DIS programme. In 2008 and 2009 the programme was changed to study the hadron spectroscopy. The polarised DIS programme was continued in 2010 and 2011.

In addition, between 2002 and 2011 the collaboration performed several important test runs. Their main purpose was to check a feasibility of new measurements, but often they were also used to extract a physics content. These were in particular the measurements performed in 2004 to study the hadron spectroscopy and the measurements performed in 2009 to check a feasibility of the DVCS and Drell-Yan programmes.

In 2010 the new proposal of the experiment [78] has been approved by the CERN Research Board, opening a second phase of the COMPASS experiment. The programme described in this proposal includes measurements of pion and kaon polarisabilities *via* the Primakov reactions (data have been taken in 2012), Drell-Yan measurements with the negative hadron beam and a transversely polarised proton target (data were taken in 2014 and they will be taken in 2015) and measurements of the exclusive reactions performed in order to study the GPDs (data have been taken in a three week pilot in 2012 and they will be taken in 2016 and 2017). The key equipments of the new GPD programme are a 2.5 m long liquid hydrogen target surrounded by a 4 m long recoil proton detector (both ready in 2012) and a new large angle electromagnetic calorimeter (1/3 ready in 2012) that increases a coverage of the x_{Bj} region for the DVCS measurement. An extension of the new proposal by an addendum is foreseen in the near future. In this addendum the COMPASS collaboration will propose an extension of the Drel-Yann and GPD programmes. The latter will be performed with a transversely polarised target and a recoil proton detector.

The broad physics programme of the COMPASS experiment is possible due to an unique beam line and a multi-purpose, easily-configurable spectrometer. These features allow to take data with different experimental setups as required by the polarised DIS, hadron spectroscopy, Primakov, Drell-Yan and GPD programmes. Since the analyses presented in this thesis are based on the data taken for the polarised DIS programme, only the experimental setup for this programme will be discussed in the following. The most complete description of the spectrometer, which includes in particular details on detectors and used electronics, can be found in Refs. [79, 80].

3.2 Beam line

The COMPASS experiment is situated at the M2 beam line of the CERN Super Proton Synchrotron (SPS). Depending on physics programme, the M2 beam line can deliver either polarised muon or unpolarised hadron beams of both charges in the wide energy range between 50 GeV and 280 GeV. The polarised muon beams are used in the DIS-like measurements, while the hadron beams are used to explore the hadron spectroscopy and to study the Drell-Yan and Primakov processes. Unpolarised low-energy and low-intensity electron beams of both charges are also possible, however they are used only for the purpose of calibration, see for instance Sec. 3.6.

The muon beam is produced in tertiary interactions originated by 400 GeV/ c protons extracted from the SPS, see Fig. 3.1. After the extraction, the proton beam is split into three separate beam lines, where the share of the M2 beam line is about 70% of the extracted beam. In the next step, the proton beam scatters on a 500 mm beryllium target called T6 in order to produce secondary particles. The produced particles (mainly pions) are selected by a set of dipole and quadrupole magnets and the nominal momentum of these selected particles is 172 GeV/ c for a 160 GeV/ c muon beam. The beam is then delivered along a 600 m long channel composed of focusing and defocusing quadruples that prevent the beam to diverge. In this channel a fraction of pions decay into muons and neutrinos. Remaining hadrons in the beam are stopped by an absorber composed of nine 1.1 m long pieces of beryllium. This absorber is followed by another set of dipole and quadruple magnets that are used to clean and form the muon beam. Finally, the beam is delivered through a 250 m long channel to the experimental hall. The momentum spread of the final beam is typically 5% with respect to the nominal momentum. The direction and momentum of each beam particle are reconstructed as described in Chapter 4.

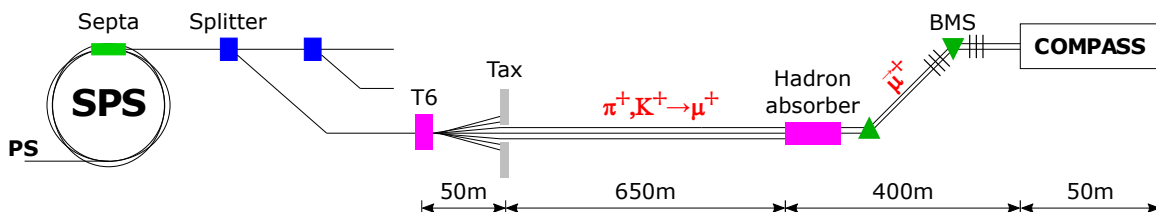
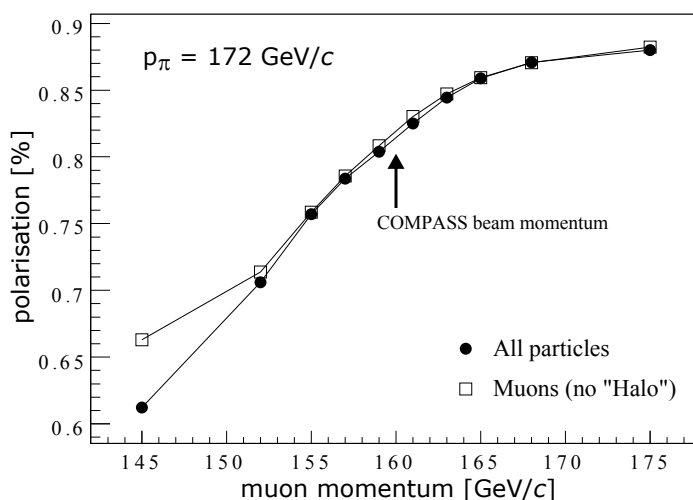


Figure 3.1: The M2 beam line scheme.

The nominal flux of the protons that are extracted from the SPS and that are available for the M2 beam line is $1.2 \cdot 10^{13}$ p during a 4.8 s long spill within a 16.8 s long SPS cycle. The flux of the final muon beam depends on its charge and the nominal momentum. For the 160 GeV/ c μ^+ beam the flux is $2 \cdot 10^8$ μ per the SPS cycle. The flux of the μ^- beam is typically three times smaller than that for the μ^+ beam.

The muon beam is naturally polarised due to the violation of the parity symmetry in the pion decay. For a given momentum of the initial pion beam, the polarisation value depends on the muon momentum, see Fig. 3.2. For the 160 GeV/ c μ^+ beam the polarisation is about -80% .

Figure 3.2: The absolute value of the muon beam polarisation as a function of the muon momentum. The dependence is shown for the initial 172 GeV/ c pion beam.

The muon beam that is passing the experimental hall is surrounded by a muon halo that could not be sufficiently absorbed or deflected in the beam line. The fraction of that halo with respect to the useful muon beam is about 35% for the μ^+ beam. To avoid an unnecessary triggering, a veto system that works with an anti-coincidence with the trigger logic, see Sec. 3.5, is used. The veto system is located upstream the experimental target and it consists of two detection planes. The larger (outer) one has a surface of 2.5 m \times 3.2 m with a hole of 30 cm \times 30 cm. The smaller (inner) plane covers this hole and has its own hole of 4 cm diameter. The size of planes is sufficient to discriminate the halo and those beam particles that do not illuminate the target.

3.3 Polarised target

The physics programme of the COMPASS experiment requires longitudinally and transversely polarised proton and deuteron targets. In order to polarise these particles, the so-called dynamic nuclear polarisation [81] is used. The principle of this effect is the transfer of the polarisation of atomic electrons to a nuclear material by using the microwaves. The required conditions to achieve this effect and to keep the polarisation for a long time are: a nuclear material containing paramagnetic centres, a strong and homogeneous magnetic field, a temperature below 1 K and a source of stable microwave field with a tunable frequency.

The dynamic nuclear polarisation may be explained by considering a simplified example of the electron-proton system in a homogeneous magnetic field, see Fig. 3.3. For such system only four spin states are possible, which are distinguished by the splitting energies given by the electron, ν_e , and proton, ν_p , Larmor frequencies. For a 2.5 T magnetic field these frequencies are $\nu_e = 70$ GHz and $\nu_p = 106$ MHz. In the conditions shown in Fig. 3.3, the $|\downarrow\uparrow\rangle \rightarrow |\uparrow\downarrow\rangle$ and $|\downarrow\downarrow\rangle \rightarrow |\uparrow\uparrow\rangle$ spin flips of the electron-proton system may be induced by microwaves of $\nu_e + \nu_p$ and $\nu_e - \nu_p$ frequencies, respectively, where \uparrow, \downarrow denote the electron spin and \uparrow, \downarrow denote the proton spin. A given flip is accompanied with an immediate relaxation of the electron spin, while the relaxation of the proton spin is much slower. The effect leads to a build-up of negative or positive proton polarisation for $\nu_e + \nu_p$ or $\nu_e - \nu_p$ frequencies, respectively.

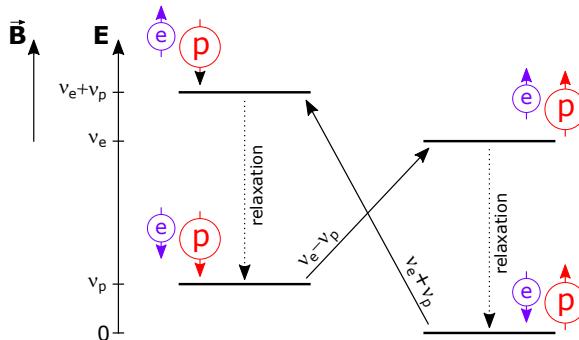


Figure 3.3: The dynamic nuclear polarisation for the proton-electron system.

In the muon programme of the COMPASS experiment two setups of the polarised target were used so far. In 2002-2004 the target build of two cells containing a polarisable material was used, while in 2005 it has been replaced by a new three-cell target that provides a better polar angle acceptance for the produced particles. The setups of both targets are very similar and only that for the three-cell target will be described in the following.

A sketch of the three-cell COMPASS target is shown in Fig. 3.4. The main elements of this target are: the dilution refrigerator, three target cells, the microwave cavity and the superconducting solenoid and dipole magnets. The dilution refrigerator is used to cool down a large amount of $^3\text{He}/^4\text{He}$ cooling mixture that is used in order to keep the target material at a low temperature of about 50 mK. The target material is lithium deuteride (^6LiD) for polarised deuterons or ammonia (NH_3) for polarised protons. The both cooling mixture and the polarisable material are stored inside the target cells made of a polyamide mesh. The central cell is 60 cm long and the outer cells are 30 cm long each (in the two-cell target the cells were 60 cm long each).

The polarisation is build-up by irradiating the target material by microwaves at resonant frequencies in a homogeneous field of 2.5 T solenoid magnet and the temperature of about 200 mK. The polarisation in the consecutive target cells is opposite, which is achieved by irradiating each target cell by microwaves of $\nu_e + \nu_{p/d}$ or $\nu_e - \nu_{p/d}$ frequencies that are produced by separate microwave

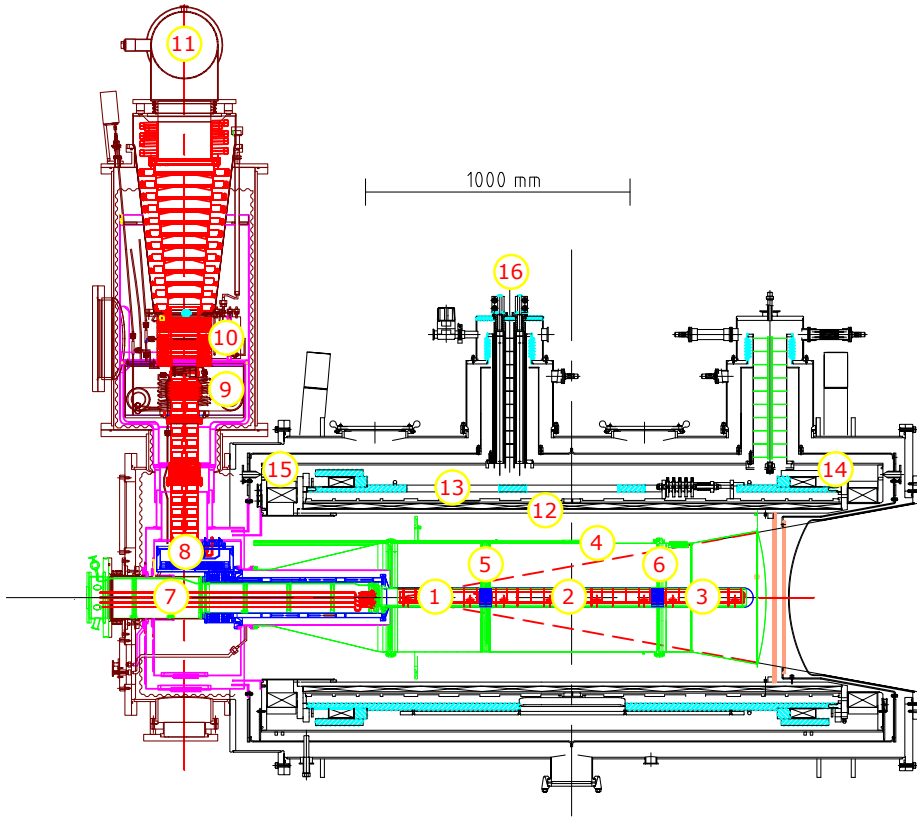


Figure 3.4: The sketch of the three-cell polarised COMPASS target according to Ref. [82]. The marked elements are: (1) upstream target cell, (2) middle target cell, (3) downstream target cell, (4) microwave cavity, (5) upstream microwave stopper, (6) downstream microwave stopper, (7) target holder, (8) still or ^3He evaporator, (9) ^4He evaporator, (10) ^4He liquid/gas separator, (11) ^3He pumping port, (12) solenoid magnet, (13) correction coils, (14) dipole coil, (15) solenoid end compensation coil and (16) magnet current leads.

sources. To avoid a leakage of the microwaves, the cells are separated by microwave stoppers. The solenoid magnet is used to build up the polarisation and to keep it in the longitudinal mode. A 0.63 T dipole magnet is used to keep the polarisation in the transverse mode. The both dipole and solenoid magnets are used to rotate adiabatically the spin orientation of polarised protons or deuterons.

In the longitudinal mode the polarisation is measured at short time intervals by ten NMR coils, which are evenly distributed along the target cells. In the transverse mode the polarisation is estimated from the measurements performed before and after the polarisation reversal. The achieved absolute value of the polarisation is about 80% for protons and about 45% for deuterons. The polarisation relaxation time is $< 0.1\%$ per day for the longitudinal mode and $< 1\%$ per day for the transverse mode.

The fraction of interactions of a given type that occurred on polarised protons or deuterons is given by the so-called dilution factor. The calculation of this factor takes into account the target composition, but also eventual nuclear effects that modify the considered cross section on a single proton or deuteron depending on a nuclei in which the interaction occurred. For incoherent exclusive ρ^0 meson production the dilution factor is about 45% for the ^6LiD target and about 25% for the

NH_3 target, see Ref. [23].

3.4 Tracking spectrometers

Momenta and charges of particles are reconstructed by analysing tracks left in two magnetic spectrometers, see Fig. 3.5. The upstream spectrometer, often referred to as the large angle spectrometer, uses a vertical dipole magnet called SM1. The $229 \text{ cm} \times 152 \text{ cm}$ aperture of this magnet and its $1 \text{ T} \cdot \text{m}$ field integral are sufficient to cover the polar angle acceptance of $\pm 180 \text{ mrad}$. The downstream spectrometer, often referred to as the small angle spectrometer, covers the polar angle acceptance of $\pm 30 \text{ mrad}$. It uses a second vertical dipole magnet called SM2, with the $2 \text{ m} \times 1 \text{ m}$ aperture and the $4.4 \text{ T} \cdot \text{m}$ field integral.

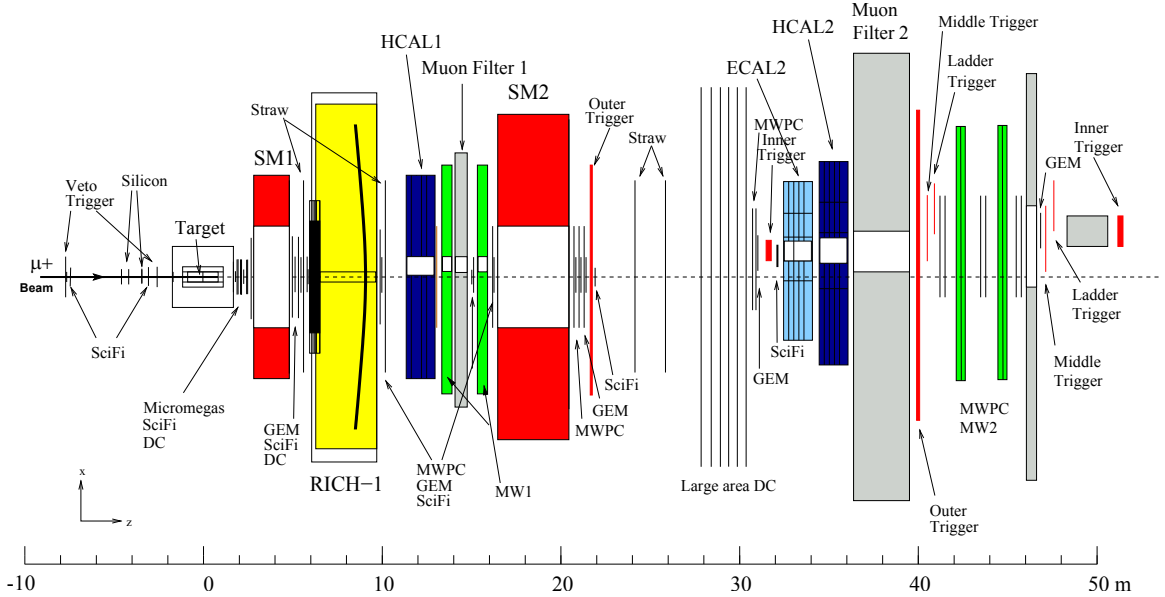


Figure 3.5: The top view of COMPASS 2004 muon setup.

Both spectrometer magnets are surrounded by tracking detectors of various types. These types may be categorised according to sizes and rate capabilities of the detection planes. Small area trackers are designed to operate in high particle flux regions near the beam axis. They stand up with a very good spacial resolution of the order of $100 \mu\text{m}$. These are silicon, scintillating fibers (SciFi), micromesh gaseous structure (Micromegas) and gas electron multiplier (GEM) detectors. Large area trackers cover areas defined by the acceptances of spectrometer magnets. They do not operate in high particle flux regions, however they have to keep a good spacial resolution of the order of $200 \mu\text{m}$. These are straw, drift chambers (DC) and multi-wire proportional chamber (MWPC) detectors.

In addition to the two spectrometers, the momentum and direction of each beam particle are reconstructed by detectors located upstream the target. The reconstruction involves two subsets of detectors: the beam telescope, which is located just in front of the target, and the beam momentum station, which is located about 100 m upstream the target. These elements of the setup are described in Chapter 4.

3.5 Trigger system

In the COMPASS experiment the trigger system is used to start a readout of the front-end electronics and to assign a reference time to a given event. It is designed to keep a minimum dead time and to cover the full range of the fractional energy of the virtual photon, $0 < y < 1$, and a large range of Q^2 , from a quasi-photoproduction at $Q^2 \approx 0$ to a maximum value allowed by the kinematics. The trigger system consists mainly of the fast hodoscopes that are used in order to detect the scattered muons. The veto system described in Sec. 3.2 and the calorimetry described in Sec. 3.6 are used as well. A detailed description of the trigger system can be found in Ref. [83].

The sketch of the most important elements of the trigger system is shown in Fig. 3.6. The system consists of several subsystems. Each of them is based on two hodoscope stations separated by one of the hadron absorbers, see Sec. 3.6, which are used in order to suppress an occupancy caused by hadrons and electrons. These are the inner subsystem with the H4I and H5I hodoscope stations, the ladder subsystem with the H4L and H5L stations, the middle subsystem with the H4M and H5M stations and the outer subsystem with the H3O and H4O stations. The planes of the inner and ladder subsystems have vertical strips of 6-12 mm and 62-77 mm, respectively, while those of the outer subsystem have horizontal strips of 70-150 mm. In the middle subsystem each hodoscope station consists of planes that measure positions of the crossing particles in the horizontal and vertical directions. The widths of strips used in these hodoscopes are 21.5-77 mm.

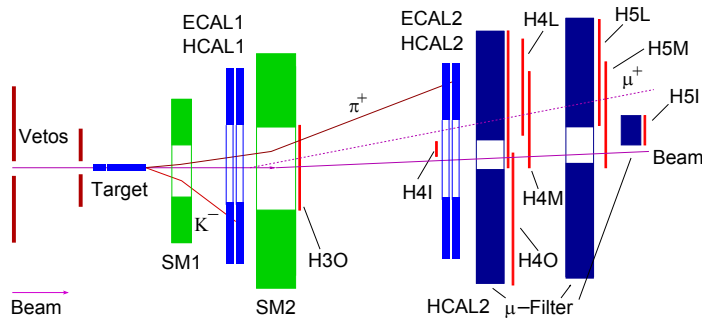


Figure 3.6: The sketch of the most relevant elements for the trigger system.

For a given subsystem, the trigger logic requires a coincidence in two hodoscopes and an anti-coincidence with the veto system. The ladder and outer triggers are semi-inclusive, which means that they require also an energy deposition in one of the calorimeters. The energy threshold is set to be larger than a typical energy deposited by a single muon and it is of the order of 5 GeV.

Not only the time coincidence between elements of the trigger system and the energy deposition in the calorimeters are examined. Because of a large distance between the hodoscopes and their good spacial resolution, the direction of each crossing muon can be estimated at the trigger system level. This information is used to distinguish between halo muons, which pass far away from the beam axis, and scattered muons, which are emitted from the target region. The discrimination is based on predefined coincidence matrices, which accept only those trigger attempts that are caused by the hits detected in certain combinations of the hodoscope strips.

In addition to the four trigger subsystems based on the hodoscopes, there exist also the so-called pure calorimetric trigger. It allows to trigger events even if the scattered muons are outside of the acceptance of trigger hodoscopes. This trigger requires only a large deposition of the energy, about 15 GeV, in one of the calorimeters.

A coverage of the y vs. Q^2 phase space by the inner, ladder, middle, outer and pure calorimetric triggers is shown in Fig. 3.7. Except those mentioned, there exist also several other types of triggers.

They are used mainly for monitoring and calibration purposes and they are taken with small rates. The most important ones are the pure random trigger, which is based on a radioactive source, the beam trigger, which requires only a signal in the beam telescope, and the veto trigger, which requires only a signal in the veto system.

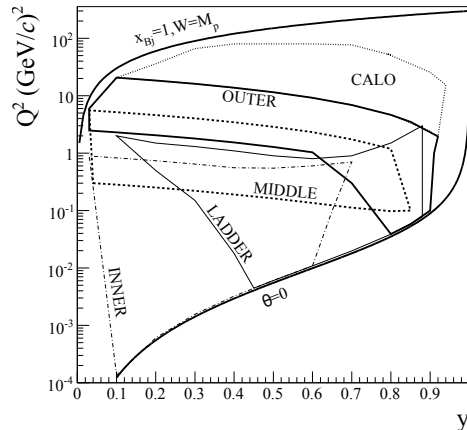


Figure 3.7: The coverage of the Q^2 vs. y phase space for the inner, ladder, middle, outer and pure calorimetric triggers.

3.6 Particle identification

There are several particle identification systems in the COMPASS experiment. Both stages of the spectrometer are equipped with the so-called muon walls for an identification of muons. These are the MW1 station in the large angle spectrometer and the MW2 station in the small angle spectrometer. Each station consists of a hadron absorber that is placed between two hodoscopes. A 60 cm thick absorber made of the iron is used for the MW1 station, while a 2.4 m thick absorber made of the concrete is used for the MW2 station. A coincidence in a given pair of the hodoscopes is used to assign a number of the radiation lengths to the crossing particle, which is related to the thickness of the corresponding absorber. This information is used in the event reconstruction to distinguish between hadrons and muons.

Each stage of the spectrometer is equipped with one pair of hadron and electromagnetic calorimeters. These are ECAL1 and HCAL1 in the large angle spectrometer and ECAL2 and HCAL2 in the small angle spectrometer. The hadron calorimeters serve mainly in the trigger system, see Sec. 3.5. The electromagnetic calorimeters serve in the trigger system as well, but their main purpose is the reconstruction of photons. These calorimeters are key detectors for the analysis of exclusive ω meson production that is presented in Chapter 7.

A sketch of the ECAL1 calorimeter is shown in Fig. 3.8 (left). This calorimeter is a $3.97 \text{ m} \times 2.87 \text{ m}$ matrix of three types of blocks: 608 GAMS blocks of $38 \text{ mm} \times 38 \text{ mm}$ in the central region, 572 Maiz blocks of $75 \text{ mm} \times 75 \text{ mm}$ in the middle region and 320 Olga blocks of $143 \text{ mm} \times 143 \text{ mm}$ in the left and right outer regions. According to Ref. [84], the measured energy resolutions are $\sigma/E = 6.2\% \cdot \sqrt{E} \oplus 1.4\%$ for the GAMS blocks, $\sigma/E = 7.0\% \cdot \sqrt{E} \oplus 1.8\%$ for the Maiz blocks and $\sigma/E = 4.3\% \cdot \sqrt{E} \oplus 3.2\%$ for the Olga blocks, where $a \oplus b = \sqrt{a^2 + b^2}$. The ECAL1 has the $38 \text{ mm} \times 38 \text{ mm}$ hole, which corresponds to the polar acceptance of the small angle spectrometer.

The ECAL2 calorimeter is shown in Fig. 3.8 (right). This calorimeter is a $2.45 \text{ m} \times 1.84 \text{ m}$ matrix of three types of blocks: 764 SHASHLIK blocks of $38 \text{ mm} \times 38 \text{ mm}$ in the inner region, 768

RHGAMS blocks of $38 \text{ mm} \times 38 \text{ mm}$ in the intermediate region and 1440 GAMS blocks in the outer region (the same type of blocks as used in ECAL1). According to Ref. [85], the measured energy resolutions are $\sigma/E = 6.5\% \cdot \sqrt{E} \oplus 1\%$ for the SHASHLIK blocks, $\sigma/E = 6\% \cdot \sqrt{E} \oplus 4\%$ for the RHGAMS blocks. The ECAL2 has the $38 \text{ mm} \times 38 \text{ mm}$ hole to avoid a hitting from non-interacting beam particles.

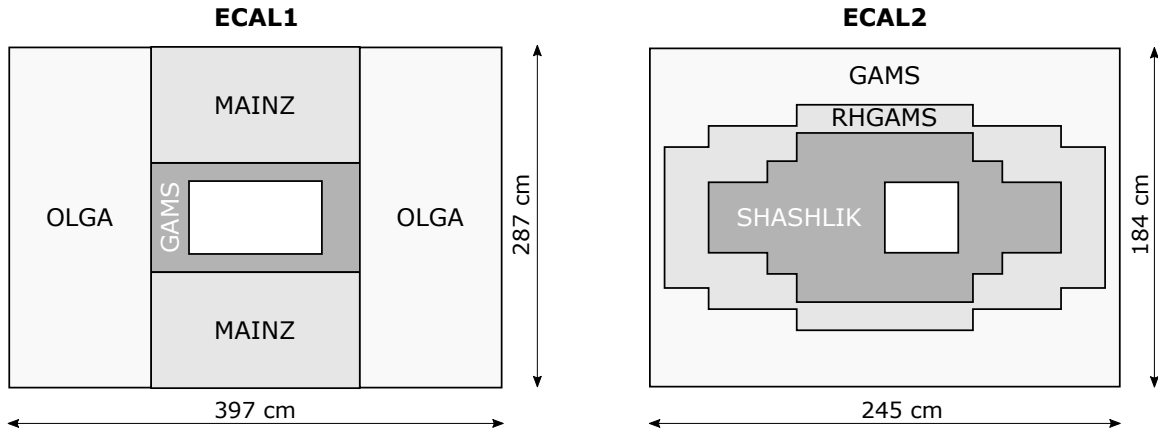


Figure 3.8: The sketch of the ECAL1 (left) and ECAL2 (right) calorimeters. The types of calorimeter cells are denoted by labelled area.

There are several steps to calibrate the ECALs. In the first step a given calorimeter is illuminated by a nearly mono-energetic 40 GeV electron beam. During this step the calorimeter is moved in both the horizontal and vertical directions in order to allow the beam to hit each cell. The calibration with the electron beam is used to tune high voltage amplifiers used in the electronic readout, which allows to keep an uniform response of the calorimeter. It is of special importance, as the calorimeters are included in the trigger system, which rely on the electronic readout. The calibration with the electron beam is done at the beginning of each year of the data taking. The stability of this calibration during the data taking is controlled by a monitoring system, in which the calorimeter blocks are illuminated between the beam spills by a light of known energy. The light it generated by LASER and LED diodes, for ECAL1 and ECAL2, respectively, and it is delivered to the cells by waveguides. Measured amplitudes are averaged for each run and compared with those measured just after the calibration with the electron beam. The correction factors found for each run are applied at the reconstruction level. Finally, the calibration of the cells may be tuned offline by analysing the position and width of the π^0 peak that is seen in the reconstructed data. A procedure of such calibration, which is used in the present analysis, is discussed in Chapter 5.

In the COMPASS experiment hadrons can be identified as well. The identification of hadrons is provided by a large Ring Imaging Cherenkov detector (RICH) installed in the large angle spectrometer. It allows to identify pions, kaons and protons in the momentum range between 5 GeV/ c and 43 GeV/ c . The detector vessel of $6.6 \text{ m} \times 5.3 \text{ m} \times 3.3 \text{ m}$ is filled with the pure C_4H_{10} gas radiator of the 1.0015 refractive index. The Cherenkov light produced by the crossing particles is reflected by two spherical mirror surfaces that allowed to install the readout electronics outside the acceptance of the spectrometer. The readout is provided by multi-wire proportional chambers (MWPC) detecting photoelectrons induced in the CsI converters and by multi-anode photo-multiplier tubes (MAPMTs).

Reconstruction of beam momentum

4.1 Introduction

In order to reach a large intensity of the muon beam, the beam optics keeps a large spread of the beam momentum, typically about 5% with respect to the nominal value. In addition, a spot of the beam at the COMPASS target is about $\sigma_x \times \sigma_y = 3 \text{ mm} \times 3 \text{ mm}$, which is comparatively large to a precision required by the primary vertex reconstruction. With such conditions, the DIS-like programmes of the COMPASS experiment require a reconstruction of the both momentum and direction of each beam particle.

The momentum and direction of each beam particle are reconstructed separately in two subsets of detectors. The direction is reconstructed in the beam telescope station (BT), which is located just in front of the target, while the momentum is reconstructed in the beam momentum station (BMS), which is located about 100 m upstream the target. Setups of the BT and the BMS have been only slightly modified in the last ten years of the COMPASS experiment. Exemplary setup that was used in 2010 is shown in Fig. 4.1.

In 2010 the BT was composed of three silicon and three scintillating fiber detectors. Each silicon detector consists of four detection planes that measure positions of the crossing beam particles in the horizontal (X), vertical (Y) and two inclined, -45° (U) and $+45^\circ$ (V), directions. These planes have a very good spacial resolution, $\sigma_{xyuv}^{\text{SI}} = 8 - 11 \text{ } \mu\text{m}$, but their time resolution is relatively poor, $\sigma_t^{\text{SI}} = 2.5 \text{ ns}$. Each scintillating fiber detector consists of two detection planes: X and Y . Their spacial resolution is worse than that for the silicon planes, $\sigma_{xy}^{\text{FI0102}} = 0.12 \text{ mm}$ for FI01-FI02 and $\sigma_{xy}^{\text{FI15}} = 0.20 \text{ mm}$ for FI15, but they are characterised by a much better time resolution, $\sigma_t^{\text{FI}} = 0.4 \text{ ns}$.

The BMS is a magnetic spectrometer composed of three dipole magnets that deflect the beam in the vertical direction. The dipole magnets are surrounded by two pairs of quadrupoles that are used in order to avoid the beam to diverge. The magnetic fields in the dipole and quadrupole magnets are optimised for the nominal momentum and charge of the beam. For the nominal momentum each dipole deflects the beam by 0.01 rad. The beam particles are reconstructed by using six detectors located upstream and downstream the magnets. These are four hodoscopes, BM01-BM04, and two scintillating fiber detectors, BM05 and BM06. The hodoscopes serve in the BMS since several decades, keeping their good time resolution undegraded, $\sigma_t^{\text{BM01:04}} = 0.3 \text{ ns}$. The width of a single slab in these detectors is 5 mm, which gives the spacial resolution of $\sigma_y^{\text{BM01:04}} = 5/\sqrt{12} \text{ mm} = 1.4 \text{ mm}$. The scintillating fiber detectors have been added to the BMS at the beginning of the

COMPASS experiment. Their time resolution is $\sigma_t^{\text{BM05:06}} = 0.5$ ns, while the spacial resolution is $\sigma_y^{\text{BM05}} = 0.72$ mm and $\sigma_y^{\text{BM06}} = 0.36$ mm, for BM05 and BM06, respectively.

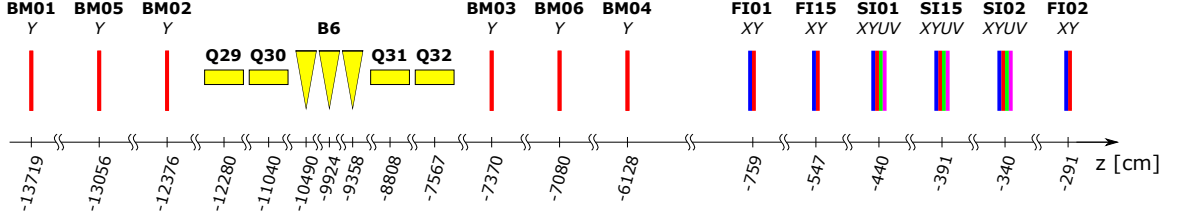


Figure 4.1: The scheme of the beam momentum station and the beam telescope.

Each beam particle leaves a track in the both BMS and the BT. The tracks left in the BT (referred in the following as the BT tracks) are reconstructed by the TRAFDIC algorithm [86], which is also used for the reconstruction of tracks left by other particles downstream the target. The tracks left in the BMS (referred in the following as the BMS tracks) are reconstructed by a dedicated algorithm that is described in this chapter. This algorithm is also used to match the BMS and BT tracks and to estimate momenta of the beam particles from the reconstructed bends in the BMS dipole magnets.

The reconstruction of the BMS data consists of three steps. These are: the clusterisation of DAQ (detector) hits for the BM01-BM04 detectors (Sec. 4.2), the reconstruction of the BMS tracks (Sec. 4.3) and the momentum estimation for each reconstructed BMS track (Sec. 4.4). In addition, the procedure used to align the BMS detectors is described in Sec. 4.5. Some remarks about the reconstruction used before that described in this chapter are given in Sec. 4.6.

4.2 Clusterisation of DAQ hits in BM01-BM04 detectors

The clusterisation is done only for the hodoscope detectors, *i.e.* BM01 - BM04. The slabs in these detectors overlap by tens of millimeter [79], which is possible because the slabs are distributed along the beam direction, see Fig. 4.2. A need for the clusterisation may be demonstrated by analysing the correlation between the differences of time, $\Delta t = t_i - t_j$, and position, $\Delta y = y_i - y_j$, for any two DAQ hits, i and j , collected in a single event. Such correlation is shown in Fig. 4.3 for the BM03 detector. In this figure, the correlation peak at $\Delta t = 0$ is clearly visible for the same, $|\Delta y| < 5$ mm, and adjacent, $5 \text{ mm} < |\Delta y| < 10$ mm, rows of slabs.

Two DAQ hits are considered as a cluster if: they are reconstructed in the same or adjacent rows of slabs and if the absolute time difference between these hits is not larger than $3 \times \sigma_t^{\text{BM01:04}} = 0.9$ ns. The mean time and mean position of DAQ hits determine the time and position of the corresponding cluster.

The fibers in the BM05 and BM06 detectors overlap as well, however the clusterisation is much more difficult in this case. It is mainly because of a round shape of the fibers that induce different amount of light depending on a position of the crossing particle. The effect has an impact on the hardware time calibration and it makes difficult the time alignment of two DAQ hits. The clusterisation for the scintillating fiber detectors is foreseen in the future.

4.3 Reconstruction of BMS tracks

In the COMPASS reconstruction software the tracks of particles left in the BT are reconstructed before those left in the BMS. Therefore, one can propose two possible scenarios to make the reconstruction of the BMS tracks. In the first one, which was used in the old BMS reconstruction code

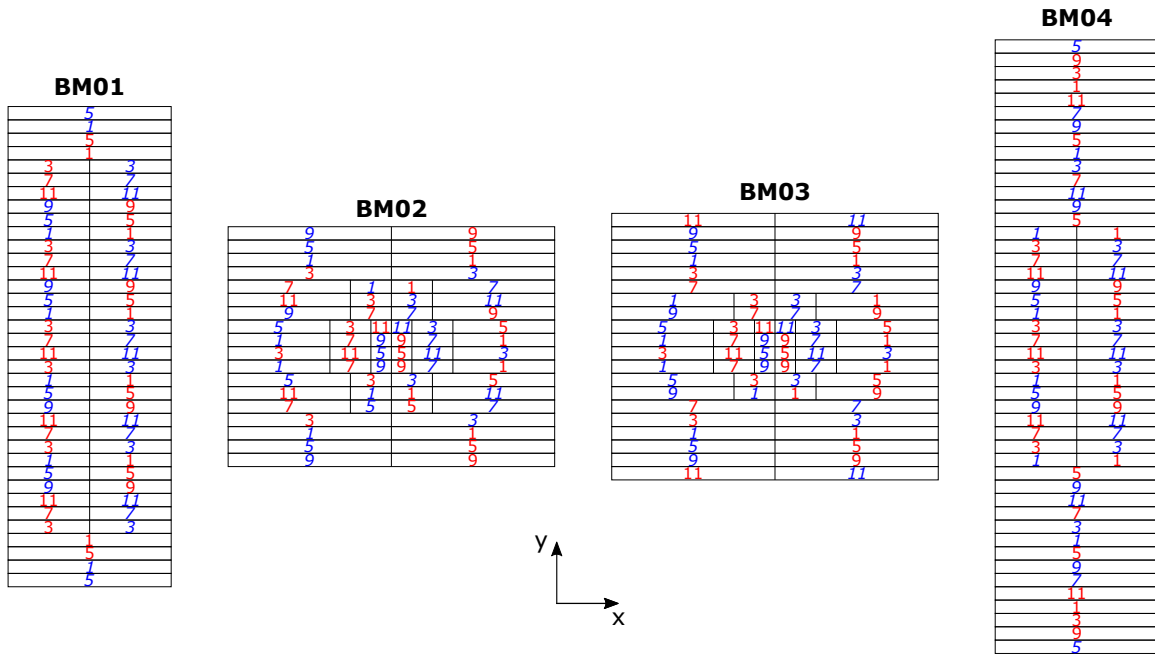


Figure 4.2: The internal structure of the BM01-BM04 detectors. The z position (along the beam) of each slab is denoted by a number, where italic blue (regular red) numbers indicate negative (positive) values. The units are centimeters.

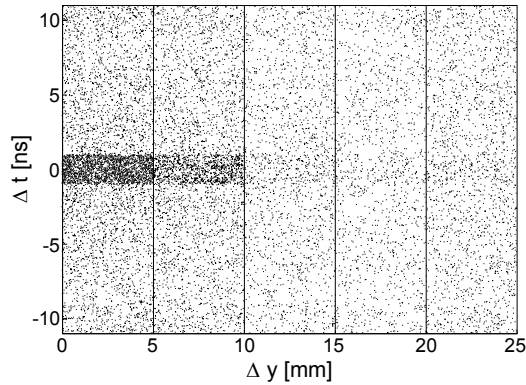


Figure 4.3: The position *vs.* time difference for any two DAQ hits in the BM03 detector. The Δy bins, which width corresponds to a width of a single slab in the BM03 detector, are separated by the vertical lines.

(Sec. 4.6), the BMS and BT tracks are reconstructed separately and they are matched afterwards. In the second scenario, which is used presently, the reconstruction of the BMS tracks takes advantage of some data already reconstructed in the BT. The second scenario is more beneficial, as the BT data provide additional constraints for the reconstruction of the BMS tracks. In addition, such way of the reconstruction ensures that the BT and BMS tracks were caused by the same beam particle. It allows to skip the step where the BMS and BT tracks were matched afterwards.

Each BT track is considered separately in order to find its counterpart in the BMS. For a given BT track all possible combinations of the BMS hits are examined. To select only one, the combinations are distinguished by values of the χ_{s+t}^2 function, which is defined as

$$\chi_{s+t}^2 = \sum_i \left(\frac{t_i - t_{\text{BT}} - \Delta_t^i}{\sigma_t^i} \right)^2 + \sum_i \left(\frac{y_i - y_i^{\text{BP}} - \Delta_y^i}{\sigma_y^i} \right)^2. \quad (4.1)$$

Here, the sums run over the BMS planes in which the hits were observed. The time and vertical position of a hit seen in the plane i are given by t_i and y_i , respectively. The time of an input BT track is given by t_{BT} , while its vertical position after an extrapolation to the plane i is given by y_i^{BP} . This extrapolation (referred to in the following as the back propagation) and the choice of the normalisation, σ_t^i and σ_y^i , and offset, Δ_t^i and Δ_y^i , parameters are discussed in the separate paragraphs at the end of this section.

In the procedure only combinations composed of three or more hits are allowed. In addition, a given combination has to have at least one hit in the upstream or downstream arm of the BMS. These requirements ensure a feasibility of the momentum reconstruction.

The decision on which combination of the BMS hits matches an input BT track is done according to the following criteria. To separate good combinations left by a single beam particle from those being a combinatorial background, only those combinations are accepted that satisfy the requirement $P(\chi_{s+t}^2, \text{ndf}) > P_R$, where $P(\chi_{s+t}^2, \text{ndf})$ is the probability of χ_{s+t}^2 at the number of degrees of freedom equal ndf and $P_R = 0.01$. From the combinations that pass this requirement, the one is selected that is composed of the highest number of the BMS hits. In a case of the ambiguity, the $P(\chi_{s+t}^2, \text{ndf})$ probability is decisive again.

The P_R probability can be set to such a small value, as the combinatorial background is suppressed by the both time and spacial constraints, cf. Eq. (4.1). The combinations composed of the highest number of BMS hits are of special interest, as they provide the most accurate reconstruction of the momentum. The procedure has been confirmed by analysing four distributions of the missing energy, E_{miss} , for exclusive ρ^0 meson production, see Fig. 4.4. The missing energy corresponds to the energy of undetected particles, see Eq. (6.15), and for exclusive processes its value vanishes. Each distribution shown in Fig. 4.4 has been obtained for events where only three, four, five or six BMS hits were used to calculate the beam momentum. In the case of six hits the resolution of the exclusive peak is the best one. A tail in the large negative E_{miss} region, which indicates wrongly reconstructed momenta of either BMS or COMPASS spectrometer tracks, is small and similar in each case.

The distribution of the $P(\chi_{s+t}^2, \text{ndf})$ probability for the reconstructed beam tracks and the distribution of the number of BMS hits per beam track are shown in Fig. 4.5. The discontinuity at $P(\chi_{s+t}^2, \text{ndf}) = P_R = 0.01$ is related to giving the priority to the most numerous combinations. The tracks with $P(\chi_{s+t}^2, \text{ndf}) < 0.01$ are not recommended to be used in physics analyses.

Back propagation The back propagation of a given BT track to the BMS is done with the transport matrix, $M_{\text{BT:BMS}}$, which describes a beam line section between the BT and the upstream edge of the BMS. The matrix has been provided by the beam experts [87] and it is used in order to find expected positions of the BMS hits, $y_{\text{BM}01}^{\text{BP}}, \dots, y_{\text{BM}06}^{\text{BP}}$, by starting from measured parameters of a single BT track,

$$\begin{pmatrix} y_{\text{BM}01}^{\text{BP}} \\ \vdots \\ y_{\text{BM}06}^{\text{BP}} \end{pmatrix} = M_{\text{BT:BMS}} \cdot \begin{pmatrix} y_{\text{BT}} \\ y'_{\text{BT}} \\ \Delta p \end{pmatrix}. \quad (4.2)$$

Here, the vertical position, y_{BT} , and vertical slope, $y'_{\text{BT}} = dy_{\text{BT}}/dz$, of the input BT track are measured in a certain point of the BT. The momentum of a mother particle expressed with respect to

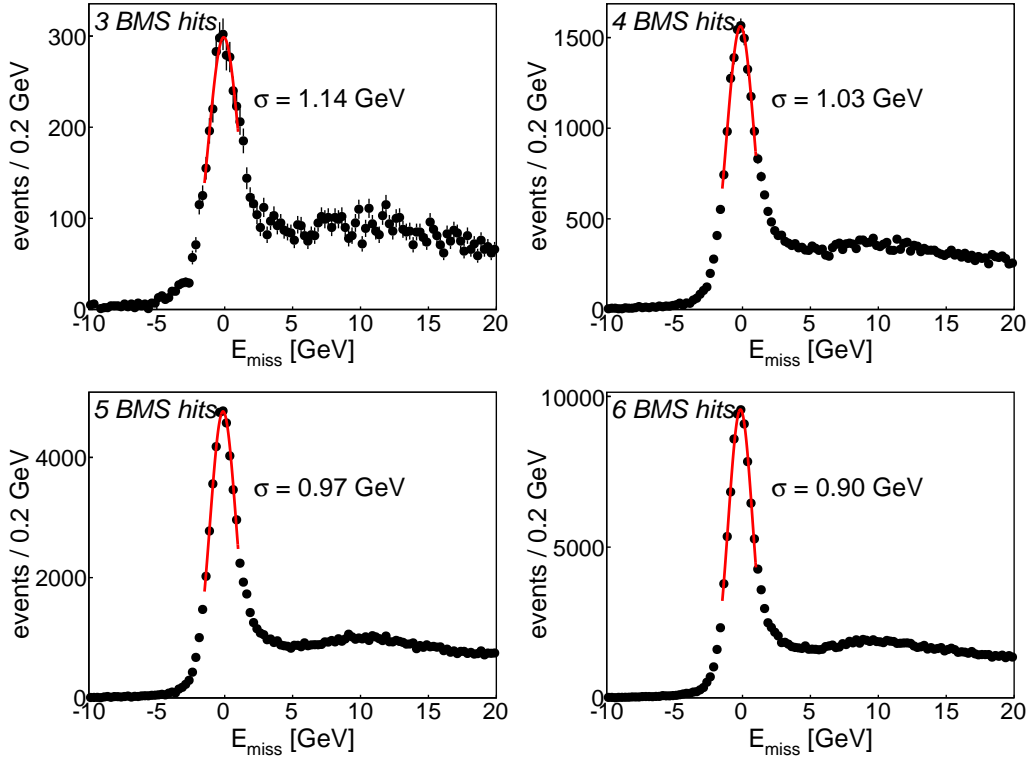


Figure 4.4: The missing energy distributions for exclusive ρ^0 meson production for events where three, four, five, or six BMS hits were used to calculate the beam momentum. The tentative values of the exclusive peak width are found from a Gaussian fit in the $-1.5 \text{ GeV} < E_{\text{miss}} < 1.0 \text{ GeV}$ range.

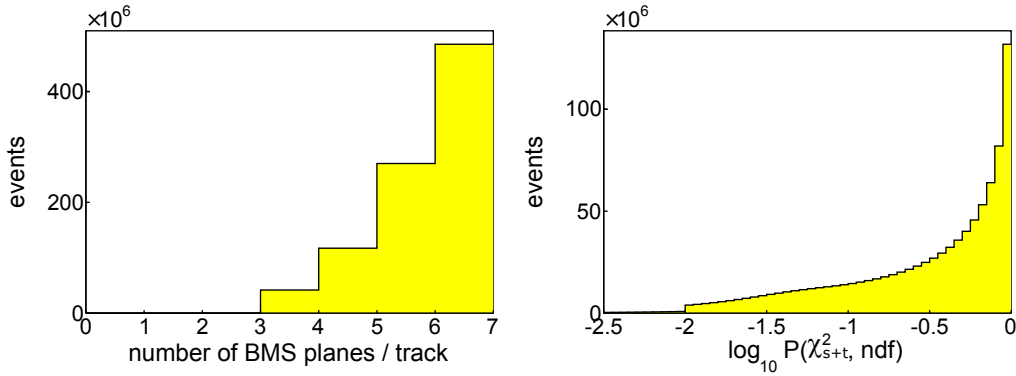


Figure 4.5: The distribution of number of BMS hits per beam track and the distribution of probability returned by the beam reconstruction.

the nominal beam momentum, $\Delta p = (p - p_0)/p_0$, is important as the back propagation is performed through the magnet elements.

When the beam reconstruction procedure starts, the value of Δp is unknown and it has to be assumed in Eq. (4.2). Note, that in Eq. (4.1) the expected positions of the BMS hits, y_i^{BP} , are

calculated in order to be compared with a specific combination of the observed positions of hits, y_i . Thus, the momentum calculated from the y_i positions, Sec. 4.4, is used to fix Δp in Eq. (4.2). It allows to check, if a given BT track is compatible with a specific combination of the BMS hits, when the momentum calculated from this combination is used to perform the back propagation.

Calibration coefficients The reconstruction of the BMS tracks involves two groups of coefficients, see Eq. (4.1), whose values can be only extracted from the data. The first group represents the time resolution and the time offset between an input BT track and the corresponding BMS hits. These parameters are

$$\sigma_t^i, \Delta_t^i, \quad \text{where } i = \text{BM01}, \dots, \text{BM06} . \quad (4.3)$$

They are extracted from the data by analysing $t_i - t_{\text{BT}}$ distributions, which are obtained for a dedicated reconstruction of the BMS tracks. This special reconstruction makes use of a modified definition of the χ_{s+t}^2 function,

$$\chi_s^2 = \sum_i \left(\frac{y_i - y_i^{\text{BP}} - \Delta_y^i}{\sigma_y^i} \right)^2 . \quad (4.4)$$

Here, only the spacial constraints are taken into account, so the coefficients related to the time constraints can be extracted from the data without any bias. Exemplary $t_i - t_{\text{BT}}$ distributions are shown in Fig. 4.6, together with fits used to extract values of the σ_t^i and Δ_t^i coefficients. A non-symmetric shape of those distributions for BM05 and BM06 is caused by a missing clusterisation for these detectors, see Sec. 4.2.

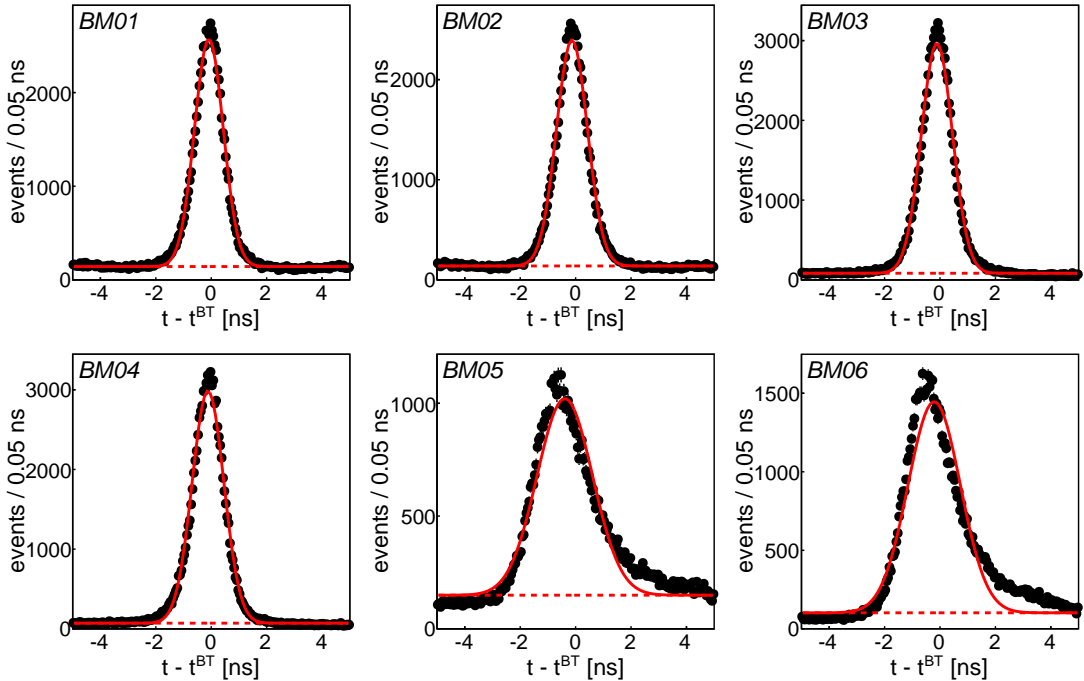


Figure 4.6: The extraction of the σ_t^i and Δ_t^i coefficients.

The second group of the coefficients are those related to the spacial resolution and the spacial offset between an input BT track and the corresponding BMS hits,

$$\sigma_y^i, \Delta_y^i, \quad \text{where } i = \text{BM01}, \dots, \text{BM06} . \quad (4.5)$$

Similarly to the previous case, these parameters are extracted from the data by analysing $y_i - y_i^{\text{BP}}$ distributions. These distributions are obtained for another dedicated reconstruction of the BMS tracks that makes use of a modified definition of the χ_{s+t}^2 function,

$$\chi_t^2 = \sum_i \left(\frac{t_i - t_{\text{BT}} - \Delta_t^i}{\sigma_t^i} \right)^2 . \quad (4.6)$$

Here, only the time constraints are taken into account, so the coefficients related to the spacial constraints can be extracted without any bias. Exemplary $y_i - y_i^{\text{BP}}$ distributions are shown in Fig. 4.7, together with fits used to extract values of the σ_y^i and Δ_y^i coefficients.

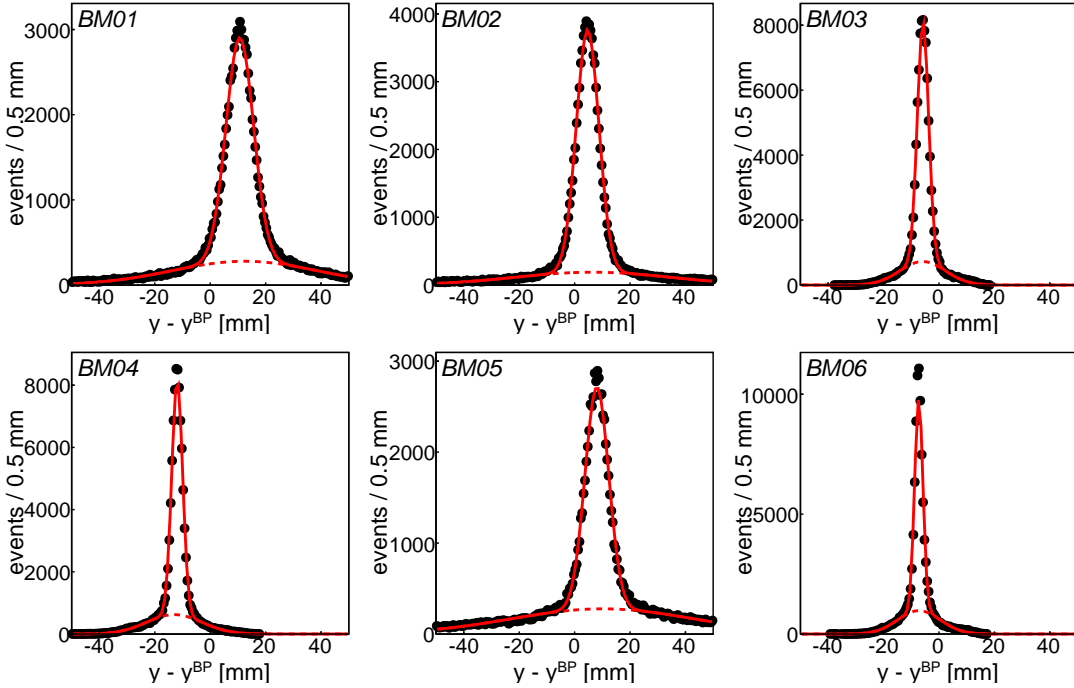


Figure 4.7: The extraction of the σ_y^i and Δ_y^i coefficients.

The σ_t^i and Δ_t^i coefficients are sensitive to the hardware time calibration of involved detectors and they are extracted separately for each year of the data taking. The σ_y^i and Δ_y^i coefficients are sensitive to the alignment of involved detectors. Because of the back propagation, they are also sensitive to the tuning of the beam line elements between the BT and the upstream edge of the BMS. As a consequence, the σ_y^i and Δ_y^i coefficients have to be extracted for each period of the data taking, in parallel to the COMPASS spectrometer alignment procedure.

4.4 Reconstruction of beam momentum

There are seven parameterisations that translate the bend of a given BMS track into the momentum. These are functions of three or four variables,

$$\begin{aligned}
 p &= f(y_U, y'_U, y_D, y'_D) , \\
 p &= f(y_i, y_D, y'_D), & i = \text{BM01, BM05, BM02} , \\
 p &= f(y_i, y_U, y'_U), & i = \text{BM03, BM06, BM04} .
 \end{aligned} \tag{4.7}$$

The first parameterisation is used only when an input BMS track is reconstructed from two or three hits in each arm of the BMS. In such case, input parameters are the vertical positions, y_U and y_D , and the vertical slopes, y'_U and y'_D , reconstructed at specific points of the upstream (U) and downstream (D) arms of the BMS. If only two hits are found in a given arm of the BMS, the computation of position and slope is straightforward. In a case of three hits, the least square method is used, where a spacial resolution of each plane is taken into account. The remaining six parameterisations are used when only one hit is found in a given arm of the BMS. The vertical position of such hit is denoted by y_i , where $i = \text{BM01, } \dots, \text{BM06}$.

The parameterisations shown in Eq. (4.7) have been obtained by using Monte Carlo (MC) simulation of the BMS response. The code of this simulation was provided by the beam experts [88]. In order to obtain the parameterisations, the MC setup was illuminated by almost six millions MC tracks of the beam particles. A given MC track was generated with specific values of y_U , y'_U and p , while after the BMS propagation y_D and y'_D were determined. The input parameters were chosen in order to map the following ranges,

$$\begin{aligned}
 -90 \text{ mm} &< y_U < 90 \text{ mm}, \\
 -4 \text{ mrad} &< y'_U < 4 \text{ mrad}, \\
 140 \text{ GeV} &< p < 180 \text{ GeV}.
 \end{aligned} \tag{4.8}$$

These ranges are sufficiently wide to cover the corresponding ones observed in the real data. The horizontal position and the horizontal slope were ignored in the simulation, as those variables are not used in the reconstruction and their impact on the momentum reconstruction is negligible.

After the simulation, the MC data were analysed by the principle component analysis [89]. This method allows to redefine input variables in order to simplify the considered problem. The principle component analysis was used separately for each set of the input variables that are used in the parameterisations shown in Eq. (4.7),

$$\begin{aligned}
 y_U, y'_U, y_D, y'_D &\xrightarrow{\text{pca}} y_A^0, y_B^0, y_C^0, y_D^0 , \\
 y_i, y_D, y'_D &\xrightarrow{\text{pca}} y_A^i, y_B^i, y_C^i , & i = \text{BM01, BM05, BM02} , \\
 y_i, y_U, y'_U &\xrightarrow{\text{pca}} y_A^i, y_B^i, y_C^i , & i = \text{BM03, BM06, BM04} .
 \end{aligned} \tag{4.9}$$

In each case, the transformation from one set of variables to another is possible by using coefficients found by the principle component analysis. The redefined variables describe the momentum in an ordered way, *i.e.* the sensitivity of the momentum reconstruction to variables from the *A*-group is stronger than that to variables from the *B*-group, *etc.* Since only three variables are mandatory to describe the momentum, the sensitivity to the y_D^0 variable is negligible.

The MC data in the new basis were used to parameterise the momentum dependence. Similarly as for Eq. (4.9), the parameterisations were obtained separately for each set of the input variables,

$$p = c_0^i + c_1^i y_A^i + c_2^i y_B^i + c_3^i y_C^i + c_4^i y_A^i y_B^i + c_5^i y_A^i y_C^i + c_6^i y_B^i y_C^i + \dots , \tag{4.10}$$

where

$$i = 0 \text{ or } \text{BM01, BM02, BM03, BM04, BM05, BM06} .$$

The c_j^i coefficients, where $j = 0, \dots, 14$, multiply certain combinations of the redefined variables. The values of these coefficients were found in a multidimensional fit to the MC data in the new basis.

The way how the parameterisations have been obtained determines their usage in the reconstruction. In order to estimate the beam momentum for a given BMS track, one should start from a calculation of the input variables, see Eq. (4.7). After the transformation of these variables to the new basis, see Eq. (4.9), the momentum value can be calculated from the corresponding parameterisation, see Eq. (4.10). An exemplary distribution of the reconstructed beam momentum is shown in Fig. 4.8 for the 2010 data. The spikes in this distribution are caused by the finite resolution of the BMS planes that is often referred to as the granularisation effect.

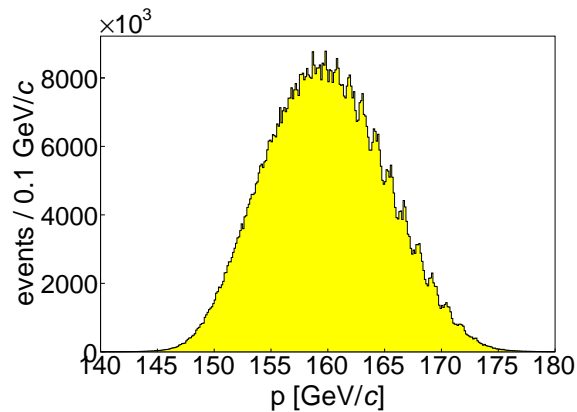


Figure 4.8: The distribution of reconstructed beam momentum for 2010 data.

With the MC description of the BMS one can study several important sources of the reconstruction uncertainty, in particular the one related to the granularisation effect. The effect is different for various combinations of the reconstructed BMS hits, as one can see in Table 4.1. The average uncertainty, taking into account a frequency of how often a given combination is reconstructed in the data, is $\sigma_p/p = 0.38\%$. The uncertainty related to the parameterisations defined in Eq. (4.7) has been estimated to be $\sigma_p/p = 0.05\%$. There are also several other important uncertainties that are related to approximations in the MC description and to uncertainties of such parameters as positions of the BMS elements and values of the magnetic fields. These uncertainties are unknown, however from the analysis of physics observables, in particular by analysing the position of the exclusive ρ^0 peak, one can conclude that these uncertainties are small and the upper limit of a conservative estimate of σ_p/p is 0.5%.

4.5 Alignment of BMS planes

The standard alignment procedure of the COMPASS spectrometer does not include the planes installed in the BMS. However, by having three planes in each arm of the BMS, which are not separated by any magnet, one can easily check if the vertical alignment of these planes is correct. For instance, for the upstream arm of the BMS one can analyse the tracks reconstructed from all three planes (BM01, BM05, BM02). For these tracks, any two planes can be used as a reference for the third one, *e.g.* hits in BM01 and BM05 planes can be used to predict a position of the hit

Table 4.1: The uncertainty of the beam momentum reconstruction related to the granularisation effect. The values are given for all combinations of the BMS hits that are possible in the reconstruction. The "x" symbol indicates the planes used in a given combination.

<i>BM01</i>	<i>BM05</i>	<i>BM02</i>	<i>BM03</i>	<i>BM06</i>	<i>BM04</i>	$\sigma_{p/p}$ [%]	<i>BM01</i>	<i>BM05</i>	<i>BM02</i>	<i>BM03</i>	<i>BM06</i>	<i>BM04</i>	$\sigma_{p/p}$ [%]
x	—	x	x	—	—	0.62	x	—	x	—	x	—	0.50
x	—	x	—	—	x	0.38	x	—	—	x	x	—	1.13
x	—	—	x	—	x	0.40	—	—	x	x	x	—	1.74
—	—	x	x	—	x	0.67	x	—	—	—	x	x	0.36
x	x	—	x	—	—	0.96	—	—	x	—	x	x	0.59
—	x	x	x	—	—	0.91	x	x	—	—	x	—	0.80
x	x	—	—	—	x	0.59	—	x	x	—	x	—	0.76
—	x	x	—	—	x	0.58	—	x	—	x	x	—	1.31
—	x	—	x	—	x	0.47	—	x	—	—	x	x	0.42
x	—	x	x	—	x	0.31	—	—	x	x	x	x	0.56
x	x	x	x	—	—	0.62	x	x	x	—	x	—	0.49
x	x	x	—	—	x	0.38	x	x	—	x	x	—	0.77
x	x	—	x	—	x	0.42	—	x	x	x	x	—	0.77
—	x	x	x	—	x	0.43	x	x	—	—	x	x	0.42
x	—	x	x	x	—	0.71	—	x	x	—	x	x	0.43
x	—	x	—	x	x	0.31	—	x	—	x	x	x	0.40
x	—	—	x	x	x	0.34							
x	x	x	x	—	x	0.31	x	x	x	—	x	x	0.31
x	—	x	x	x	x	0.31	x	x	—	x	x	x	0.42
x	x	x	x	x	—	0.71	—	x	x	x	x	x	0.43
x	x	x	x	x	x	0.31							

in BM02. Distributions showing the differences between the expected and observed positions of the hits, referred to as the residual distributions, should be centred at zero. These distributions are shown in Fig. 4.9 for the 2010 data. They are not smooth as a consequence of the granularisation effect. However, the shift is clearly visible that demonstrates the need of alignment.

Any direct survey of the vertical positions would be difficult because of a compact construction of the BMS. In addition, an uncertainty of such measurement would be relatively large. There are few scenarios how to perform the alignment by using the data, however in each scenario positions of some planes have to be fixed, *i.e.* they have to be assumed to be known. According to the detector experts [90], the most safe to fix are positions of the BM01-BM04 planes as their frames are fixed to the ground and the crates containing the detectors are heavy that ensures a good stability.

The first scenario for performing the alignment of BMS detectors by using physics data is shown in Fig. 4.10 (a). It is the simplest scenario when positions of four planes are fixed and two remaining planes are aligned with respect to these fixed ones. This scenario does not require any propagation of tracks through the magnet elements as the alignment is independent in each arm of the BMS. However, this scenario suffers because of a large number of the fixed planes. In the second scenario, which is shown in Fig. 4.10 (b), the positions of three planes are fixed, with one of them in the upstream or downstream arm of the BMS. In this scenario the influence of the magnets have to be simulated, although the number of fixed planes is reduced by one with respect to the first scenario.

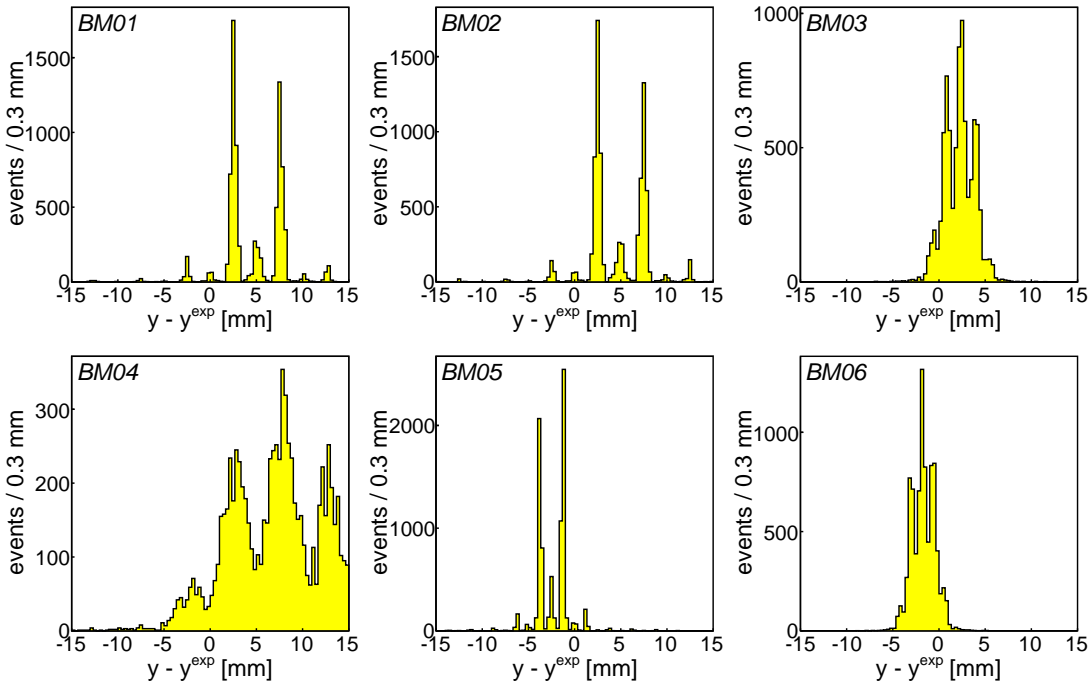


Figure 4.9: The residual distributions before the alignment procedure.

In the third scenario, which is shown in Fig. 4.10 (c), only two planes are fixed. However, it is assumed that momenta assigned to the tracks used in the alignment procedure are known, which is needed to determine the bends of tracks in the BMS. These momenta are referred in the following as the reference ones and they are denoted by p^{ref} . As in the previous case, the simulation of magnet elements is required. The third scenario is the default one.

To fix momenta of tracks used in the alignment procedure one can use a non-interacting beam particles collected with the random trigger events. The momenta of such non-interacting beam particles can be measured by the COMPASS spectrometer. However, such a measurement is not precise enough, as the non-interacting beam is little deflected by the COMPASS spectrometer magnets and the beam particles hit only a limited number of the detection planes. In addition, the alignment of the BMS could be influenced by an eventual misalignment of the COMPASS spectrometer.

For consistency with the reconstruction used previously by COMPASS, see Sec. 4.6, it was decided to use momenta calculated from the BM01-BM04 planes as the reference in the alignment procedure. Therefore, after the alignment procedure there should be no systematic difference between the momenta reconstructed by the present and previously used algorithms.

In the alignment procedure only tracks reconstructed using hits in all six BMS planes are used. The positions of the BM01 and BM04 planes are fixed in the procedure. It is the most safe choice, as these planes are far away from the dipole magnets and their eventual misalignment does not change the reconstructed bends so strongly as a misalignment of other planes.

Because the momenta calculated from the BM01-BM04 planes are used as the reference and the positions of the BM01 and BM04 planes are fixed, the sensitivity to correct a misalignment of the BM02 and BM03 planes is limited. However, these planes can be still aligned, as only three planes are required in order to perform the momentum reconstruction. For instance, a systematic difference between momenta reconstructed from the BM01-BM04 planes and the BM01-BM03 planes would

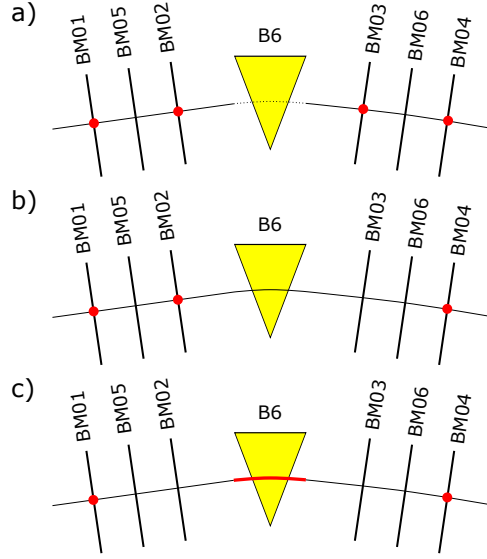


Figure 4.10: Three scenarios for performing the alignment of the BMS planes. The planes whose positions are fixed in the procedure are marked by the red dots. In the last scenario, it is assumed that the momenta of particles are known, which fixes bends of tracks in the dipoles magnets.

indicate a misalignment of BM04.

As one may argue, the most straightforward way to do the alignment would be to minimise

$$\chi^2 = \sum_i \sum_j \left(\frac{y_i^j - y_i^{j,\text{exp}}(p_i^{\text{ref}}, y_i^{\text{BM01}}, y_i^{\text{BM04}}) - c_j}{\sigma_j^{\text{y-res}}} \right)^2, \quad (4.11)$$

where

$$j = \text{BM02, BM03, BM05, BM06} .$$

Here, the first sum runs over all tracks used in the alignment procedure, while the second one runs over the planes to be aligned. For a given track and plane, the observed position of the hit, y_i^j , is compared with the expected position, $y_i^{j,\text{exp}}$. The latter is calculated from the reference momentum, p_i^{ref} , and from the measured hits in the BM01 and BM04 planes, y_i^{BM01} and y_i^{BM04} , respectively. The difference is normalised by a corresponding resolution of the residual distribution, $\sigma_j^{\text{y-res}}$. The χ^2 function is minimised as a function of the alignment correction parameters, c_j . Note however, that the calculation of such χ^2 is difficult because of the granularisation effect. As one can see from Fig. 4.9, the residual distributions are not Gaussian-like, therefore the $\sigma_j^{\text{y-res}}$ coefficients are ill-defined.

One could also define the χ^2 function in a similar way,

$$\chi^2 = \sum_i \sum_j \left(\frac{p(y_i^j - c_j, y_i^{\text{BM01}}, y_i^{\text{BM04}}) / p_i^{\text{ref}}}{\sigma_j^{\text{p-res}}} \right)^2, \quad (4.12)$$

where

$$j = \text{BM02, BM03, BM05, BM06} .$$

This definition is similar to that in Eq. (4.11). However, here for a given beam track and a detection plane, the reference momentum is compared directly with the one calculated from the j -th and fixed

planes. This definition is much more convenient, as the momentum parameterisations, Eq. (4.7), contain the whole information about the BMS, thus the explicit propagation through the magnet elements is not necessary here. In addition, the resolutions of the residual distributions, $\sigma_j^{\text{p-res}}$, are now well defined, as one can see in Fig. 4.11. After the minimisation of the χ^2 function, the residual distributions shown in Figs. 4.9 and 4.11 move to their expected positions, *i.e.* zero and one, respectively. Exemplary values of the alignment correction parameters are given in Table 4.2 for a selected period of the 2010 data.

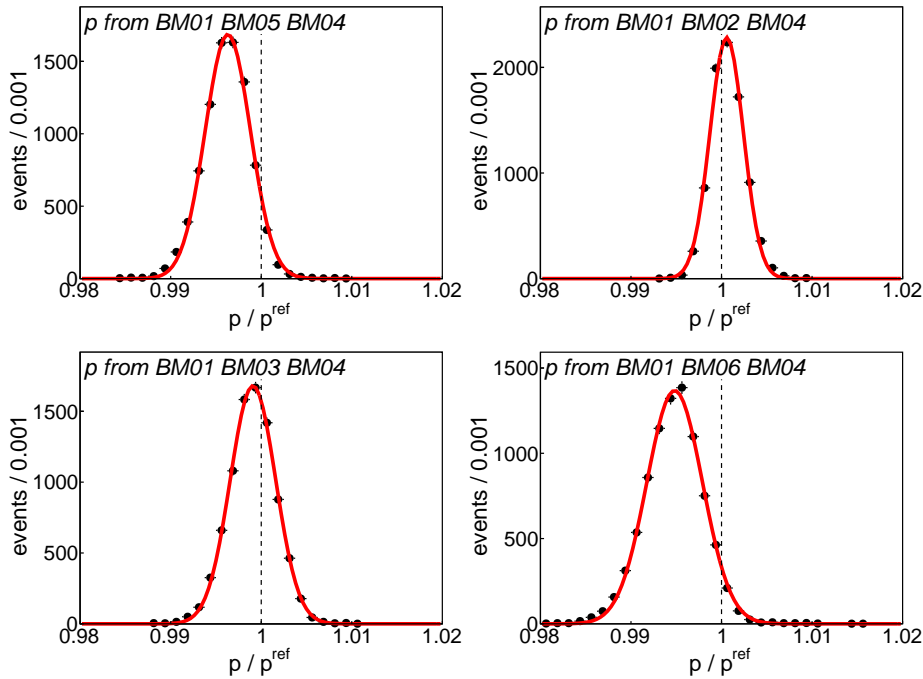


Figure 4.11: The comparison between the momenta reconstructed from the BM01-BM05-BM04, BM01-BM02-BM04, BM01-BM03-BM04 and BM01-BM06-BM04 combinations of the planes and reference momentum before the alignment procedure. The Gaussian fits are used to find $\sigma_j^{\text{p-res}}$ coefficients.

The presented procedure of the alignment examines only the vertical direction. Because of the large distance between the planes the sensitivity to other degrees of freedom is limited and usually smaller than that provided by direct surveys. By analysing the residual distribution as a function of the vertical position, Δy *vs.* y , it was only qualitatively checked that the positions of the planes along the beam direction agree with values used in the reconstruction. There is no sensitivity either to check the pitch of the planes or to make the alignment in the horizontal direction.

Table 4.2: The corrections to the vertical alignment of the BMS planes found for the W33 period of the 2010 data. The values for other periods of this year are similar. In the procedure the positions of the BM01 and BM04 planes were fixed.

BM01	BM02	BM03	BM04	BM05	BM06
fixed	0.34 mm	-0.39 mm	-1.99 mm	-2.04 mm	fixed

4.6 Old BMS reconstruction algorithm

In 2011 the BMS reconstruction algorithm described in this chapter has replaced that used previously. The decision was motivated by a problem spotted by analysing muon data taken after 2006, but only if these data were reconstructed with the old BMS reconstruction code. In these data, a significant fraction of events populates kinematically forbidden regions, like for instance large negative y and E_{miss} ranges. It was a clear indication of a problem in either the BMS or COMPASS reconstruction. After an investigation the BMS reconstruction appeared to be responsible. The explanation is still not known, but it seems that an increase of the beam intensity achieved after 2006 has saturated the old algorithm capability of the clean reconstruction.

The old algorithm is described in Ref. [91]. In this algorithm the reconstructions of the BT and BMS tracks were fully separated (in particular the BT data were not used as an input to the BMS reconstruction). The BMS tracks were reconstructed mainly by examining the time correlation between the BMS hits. The reconstruction was based on the BM01 - BM04 detectors, with BM05 and BM06 used when the number of hits in old planes was not sufficient. The BMS and BT tracks were matched, if the time difference between both tracks was within the $-1.6 \text{ ns} < t_{\text{BMS}} - t_{\text{BT}} < 1.4 \text{ ns}$ range. A spacial correlation between both tracks was used only in the case of ambiguity, *i.e.* when two or more BMS tracks were matched to the same BT track. It was recently discovered, that the purity of the BMS reconstruction is sensitive to the spacial correlation, which can be used to suppress wrongly reconstructed BMS tracks. This information is used for instance in the ρ^0 analysis, see Eq. (6.3).

Calibration of ECALs based on π^0 signal and genetic algorithm

5.1 Introduction

The algorithm designed to perform a calibration of electromagnetic calorimeters is described in this chapter. The algorithm finds calibration coefficients for each cell of a given electromagnetic calorimeter by looking at the π^0 peak reconstructed in the data. A deviation of peak position from the π^0 mass and the width of this peak are used in the χ^2 function that is sensitive to the goodness of the calorimeter calibration.

The π^0 peak must be seen in the data, as the algorithm analyses its properties. Therefore, an initial calibration should be available before an attempt to use this algorithm. In the COMPASS experiment, such initial calibration is obtained with the electron beam and the LED/LASER monitoring, see Sec. 3.6.

The calibration coefficients are found by the algorithm by minimising the χ^2 function. Typical minimisation algorithms, like for instance Minuit from the ROOT package [92], are not suitable to perform this minimisation, as the number of parameters to be found is too large. For instance, at least three calibration coefficients per cell have to be used in order to take into account nonlinearities observed in the calibration of the COMPASS calorimeters. Thus, for the ECAL1 calorimeter, which consists of 1500 cells, there are $3 \times 1500 = 4500$ calibration coefficients to be found. Here, the genetic algorithm is used to perform the minimisation of the χ^2 function.

5.2 Function of χ^2

The calibration function corrects an initially reconstructed energy, E , in a given calorimeter cell,

$$E'(E) = c_0^i + c_1^i \cdot E + c_2^i \cdot E^2 . \quad (5.1)$$

Here, c_0^i , c_1^i and c_2^i are the calibration coefficients defined for the cell i . The form of calibration function is arbitrary. If a given cell provides a linear energy-to-amplitude response, only the c_1^i coefficient is required. The additional coefficients, c_0^i and c_2^i , have been introduced in Eq. (5.1) to correct for nonlinearities observed in the calibration of COMPASS calorimeters.

For a calorimeter build of N_{cell} cells and for three calibration coefficients per cell, a set of the calibration coefficients to be found, C , reads

$$C = \begin{pmatrix} c_0^1 & c_1^1 & c_2^1 \\ \vdots & \vdots & \vdots \\ c_0^i & c_1^i & c_2^i \\ \vdots & \vdots & \vdots \\ c_0^{N_{\text{cell}}} & c_1^{N_{\text{cell}}} & c_2^{N_{\text{cell}}} \end{pmatrix}. \quad (5.2)$$

For N_{event} events containing π^0 mesons, one can define a χ^2 -like function, whose values are sensitive to the goodness of the calorimeter calibration,

$$\chi^2(C) = \sum_{i=1}^{N_{\text{event}}} \left(\frac{m_{\pi^0}^{\text{PDG}} - m_{\gamma\gamma,i}(C)}{\sigma_{\pi^0}(0)} \right)^2. \quad (5.3)$$

Here, $m_{\pi^0}^{\text{PDG}} \approx 0.135 \text{ GeV}/c^2$ is the π^0 mass. Each reconstructed π^0 candidate returns an invariant mass of two decay photons, $m_{\gamma\gamma,i}(C)$, where

$$m_{\gamma\gamma,i}(C) = \sqrt{2 \cdot E_{1,i}(C) \cdot E_{2,i}(C) \cdot (1 - \cos \theta_i)}. \quad (5.4)$$

Here, $E_{1,i}(C)$ and $E_{2,i}(C)$ are the calibration-dependent reconstructed energies of the decay photons and θ_i is the opening angle between these photons. The energies $E_{1,i}(C)$ and $E_{2,i}(C)$ are reconstructed by the so-called clusterisation algorithm, which is specific for a given calorimeter. The main purpose of this algorithm is the energy reconstruction of electromagnetic showers from the energies deposited in single calorimeter cells. Since one electromagnetic shower can deposit its energy in few calorimeter cells, the energy of a single decay photon, $E_{k,i}$, where $k = 1, 2$, is given by

$$E_{k,i}(C) = E_{\text{dark},k,i}(C) + \sum_j E_{k,i,j}(C). \quad (5.5)$$

Here, $E_{k,i,j}$ is the energy deposited in the cell $j = 1, \dots, N_{\text{cell}}$. This energy depends directly on the calibration coefficients, as it is shown in Eq. (5.1). The so-called dark energy, $E_{\text{dark},1,i}$, takes into account not measured energy losses, which are related for instance with electronic thresholds, not-active areas of the calorimeter or leakages of the shower particles. Since for example the length of a given electromagnetic shower depends on the energy, a reconstruction of the dark energy may also depend on the energy deposited in the cells and therefore on the calibration coefficients.

The decomposition shown in Eq. (5.5) must be known to the user in order to apply the algorithm. The energy $E_{k,i,j}(C)$ can be recalculated for any set of the calibration coefficients by using Eq. (5.1). However, the energy $E_{\text{dark},k,i}(C)$ can be recalculated only by the clusterisation algorithm. To avoid such a time-consuming step of the calibration procedure, it is assumed that for a given shower the ratio of the dark energies obtained before (0) and after (C) the calibration is the same as the corresponding ratio of the energies measured in the cells,

$$\frac{E_{\text{dark},k,i}(C)}{E_{\text{dark},k,i}(0)} = \frac{\sum_j E_{k,i,j}(C)}{\sum_j E_{k,i,j}(0)}. \quad (5.6)$$

This assumption allows to recalculate the dark energy for any set of the calibration coefficients.

A value in the denominator of Eq. (5.3) has to be fixed during the minimisation of the χ^2 function. If it were a calibration-dependent width of the π^0 peak, $\sigma_{\pi^0}(C)$, the χ^2 function would be minimised only by changing the peak position. The fixed value is arbitrary and it can be for instance a width of the π^0 peak found before the minimisation, $\sigma_{\pi^0}(0)$.

The definition of the χ^2 function given in Eq. (5.3) has to be modified, if the used data are contaminated by a combinatorial background. In addition, one may want to take into account that the available π^0 statistics falls rapidly with the π^0 energy, so the calibration coefficients are not equally constrained by the statistics at different energies. The modified definition of the χ^2 function reads

$$\chi^2(C) = \sum_{i=1}^{N_{\text{Ebin}}} w_i^e(C) \sum_{j=1}^{N_{\text{event},i}(C)} w_{i,j}^{\text{sig}}(C) \left(\frac{m_{\pi^0}^{\text{PDG}} - m_{\gamma\gamma,i,j}(C)}{\sigma_{\pi^0,i}(0)} \right)^2. \quad (5.7)$$

Here, the first sum runs over N_{Ebin} bins of the π^0 energy, while $w_i^e(C)$ are the weights introduced in order to ensure that an impact of each energy bin on the χ^2 function is the same. A given weight is inversely proportional to the number of the π^0 events, $N_{\text{event},i}(C)$, observed in the corresponding bin of the energy,

$$w_i^e(C) = \frac{1}{N_{\text{event},i}(C)}. \quad (5.8)$$

The weights depend on the calibration coefficients, as for various sets of these coefficients the events can migrate between the energy bins.

The combinatorial background is taken into account for each energy bin by filling a histogram of the $m_{\gamma\gamma}$ invariant mass. A given histogram is fitted in order to distinguish between resonant-like and combinatorial contributions. The fits are used to calculate the weights, $0 \leq w_{i,j}^{\text{sig}}(C) \leq 1$, where a single weight describes a probability that a given event contributes to the π^0 peak. The weights depend on the calibration coefficients, as for various sets of these coefficients a given $m_{\gamma\gamma}$ distribution may look different. Exemplary $m_{\gamma\gamma}$ distribution is shown in Fig. 5.1 together with the fits.

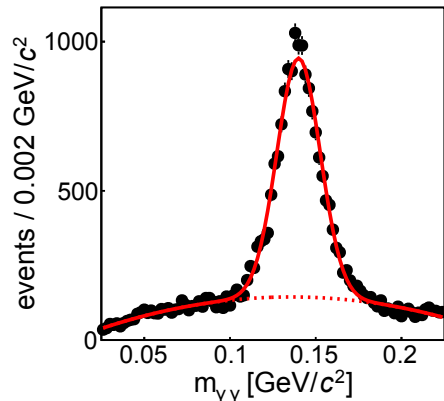


Figure 5.1: Exemplary $m_{\gamma\gamma}$ distribution together with the fit distinguishing signal and background contributions.

5.3 Selection of π^0 sample

The π^0 sample used in the calibration procedure should be large enough to constrain the calibration of all calorimeter cells in a wide range of the energy. The selection of the π^0 sample should suppress

the combinatorial background. In addition, an information about the decomposition of each shower energy into energies deposited in the calorimeter cells, see Eq. (5.5), must be known.

In the COMPASS experiment and for the muon data the algorithm can be used only for the ECAL1 calorimeter. The algorithm can not be applied for the ECAL2 calorimeter, as the π^0 statistics reconstructed in this calorimeter is not sufficient to constrain the calibration of all cells.

For ECAL1 one needs at least 100k π^0 events to constrain all calorimeter cells (for the explanation see Sec. 5.5). For the 2010 data such number of the π^0 events corresponds to about 1200 spills taken by the experiment in this year. Therefore, it makes possible to obtain about 10 independent sets of the calibration coefficients for each week of the 2010 data taking. It allows to track a time dependence of the calibration.

5.4 Genetic algorithm

The genetic algorithm [93] is a computation technique designed to make an optimisation of objects and processes and to find useful solutions of complex problems. It is particularly useful if standard computation techniques fail because of an unacceptably long computation time. In addition, it has an ability to avoid local minima and it can be used to fit not-continuous distributions, where the derivative methods can not be applied. The genetic algorithm finds an application in many fields, like physics, mathematics, engineering and manufacturing.

The algorithm mimics the process of natural selection known from Nature. It defines a set of candidates, known as a population, where each candidate represents a single solution of a considered problem. Therefore, the candidate is a set of properties, known as a genotype, that describes the problem. For instance, it can be a vector of numbers that represents a single solution of a fitted function. The candidates are judged by the so-called fitness function, which describes how well a given candidate solves the problem. In the case of fits it can be for instance the χ^2 function. The algorithm is iterative and it is based on three processes inspired by Nature. These are: selection, crossover and mutation processes.

Each single iteration proceeds as follows. The iteration starts with the selection process, where each candidate is judged by the fitness function. A predefined fraction of the best candidates is kept, while all other candidates are erased. The empty space in the population is filled by the crossover process, where new candidates are created. To create a new candidate, the best candidates exchange parts of their genotypes. It is assumed that two good candidates should yield a better one. The last step of the iteration is the mutation process, where single genes (parts of the genotype) are randomly changed. The mutation process keeps a diversity of genes and it is useful in particular to avoid local minima. The probability of mutation has to be low. In other case the good candidates are spoiled and the search of the solution is purely random.

A next iteration contains better candidates than the previous one. The algorithm stops after a predefined number of the iterations or if one of the candidates has reached a predefined value of the fitness function. The genotype, the fitness function and the selection, crossover and mutation processes depend on a considered problem and their implementation can be very different.

An implementation scheme of the genetic algorithm used to find the calibration coefficients of an electromagnetic calorimeter is shown in Fig. 5.2. The candidate is defined by its genotype. Here, the genotype is a matrix of real numbers that represents the C matrix from Eq. (5.2). The fitness function is equivalent to the χ^2 function defined in Eq. (5.7). The population consists of 3000 candidates. Such size of population allows us to keep a reasonable diversity of the genes and an acceptable computation time.

The algorithm starts with the generation of an initial population. For each candidate the genes

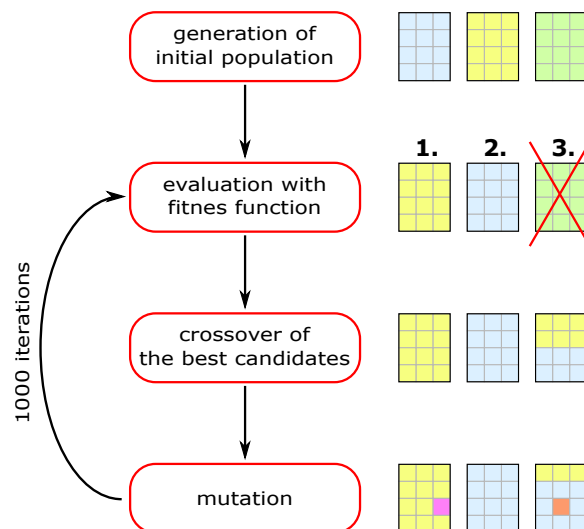


Figure 5.2: The genetic algorithm scheme. An exemplary population of three candidates represented by matrices of numbers is shown on the right side of the plot.

from the genotype are generated randomly from the following ranges

$$\begin{aligned}
 -0.25 < c_0^i < 0.25 , \\
 0.96 < c_1^i < 1.04 , \\
 -0.05 < c_2^i < 0.05 .
 \end{aligned} \tag{5.9}$$

The ranges reflect a miscalibration of the cells and they have to be wide enough to accommodate searched values of the coefficients. However, the convergence of the algorithm would be slow if the ranges were too wide.

A single iteration starts with the selection process, where each candidate is judged by the fitness function. The 30% fraction of the best candidates is kept, while all other candidates are erased. This fraction has been chosen in order to keep a reasonable diversity of the genes, which can be achieved only if a large fraction of the best candidates survives. However, the algorithm would converge slowly, if this fraction were too large. It is because an empty space left for the new candidates would be limited in that case.

To calculate the fitness function the w_i^e and $w_{i,j}^{\text{sig}}$ weights must be known, see Eq. (5.7). Since both types of weights depend on the calibration coefficients, they have to be calculated separately for each candidate. In particular, to find $w_{i,j}^{\text{sig}}$ weights the $m_{\gamma\gamma}$ distributions have to be filled and fitted separately for each candidate, cf. Fig. 5.1. The calculation of the weights is the most time-consuming part of the algorithm.

The second step of a single iteration is the crossover process. Two randomly chosen candidates, which have survived the selection process, exchange their genes in order to create a new candidate. During the exchange the genotypes of the candidates are randomly split and merged. The process is being repeated until the whole population is rebuild.

In the third step, called the mutation, a small number of genes is changed randomly. There are two types of the mutation. The first one occurs with the probability of 0.8% per gene. This type of the mutation changes only slightly values of the genes and it has been introduced to the algorithm in order to make a final tuning of the correction coefficients. The new value of a given gene is randomly generated from the Gaussian distribution. The mean of this distribution is given by the

old value of the gene, while its width is taken as 5% of the corresponding range from Eq. (5.9). The new value must belong to that range. The second type of the mutation occurs with the probability of 0.2% per gene and it generates new values of the selected genes from a corresponding range from Eq. (5.9). It has been introduced to the algorithm in order to extend the pool of the available genes. The mutation does not include the best ten candidates, as one does not want to spoil them.

The iteration is repeated 1000 times. The best candidate in the last iteration is considered as the solution, *i.e.* it is taken as the final set of the calibration coefficients.

5.5 Performance and results

A single iteration of the algorithm takes about two minutes at a typical computing centre like Lyon [94] or CERN [95], which requires more than one day in order to finish the calibration for a single part of the data. The algorithm writes down the population to a file every 25 iterations. It allows to restart the algorithm if it crashed or has been terminated by a computing centre fair share algorithm.

The value of χ^2 function for the best candidate in a given iteration is shown in Fig. 5.3. This value decreases as a function of the iteration number that indicates that the algorithm is converging. The distribution shown in Fig. 5.3 can be used to estimate how many iterations one needs in order to achieve a satisfactory result. As one can see, the χ^2 function starts to saturate after about 500 iterations.

The mean position and width of the π^0 peak obtained from the data after applying a set of calibration coefficients for the best candidate in a given iteration are shown in Figs. 5.4 and 5.5, respectively. These distributions are displayed separately for each energy bin used in the procedure. It is shown that the algorithm corrects the position of the peak in the first iterations. The width of the peak is being continuously reduced as the algorithm proceeds, until the full saturation of the χ^2 function.

The distributions of the correction coefficients for the best candidate after the last iteration are shown in Fig. 5.6. Note, that the algorithm starts with the random generation of the correction coefficients, so the corresponding distributions for any candidate in the first iteration are flat. The change of shapes of these distributions indicates that the algorithm is converging.

The distributions of the $m_{\gamma\gamma}$ invariant mass obtained from the data before and after the calibration procedure are shown in Fig. 5.7 and Fig. 5.8, respectively. These distributions are shown separately for each energy bin used in the procedure. By comparing both figures one can notice an improvement, *i.e.* a given π^0 peak returns to its nominal position, while its width is considerably reduced.

The position and width of π^0 peak parameterised as a function of the π^0 energy are shown in Fig. 5.9. The parameterisations are obtained from the data before and after the calibration. Also here, an improvement is visible. The nominal position of the peak is kept in a wide energy range. The width of the π^0 peak is reduced after the calibration and it is decreasing with the energy. It is expected, as the resolution of electromagnetic calorimeters is decreasing with the energy.

In order to constrain the calibration of all calorimeter cells in a wide energy range, a specific number of the π^0 events is required. If this number is too small, the cells are populated by a limited statistics and the search of the calibration coefficients is not well constrained. However, if this number is too large, the computation is slow. Moreover, in that case the calibration coefficients are calculated for a large part of data, which makes difficult to track the time evolution of calibration.

To check how many events are needed to constrain the calibration, the width of the π^0 peak measured after the calibration was studied as a function of the number of input π^0 events. The results are shown in Fig. 5.10. As one can see, the calibration is biased, if the number of input π^0 events is too low. The shown results indicate that at least 100k π^0 events are needed in order to avoid a bias of the procedure.

An important test is also to check if the algorithm gives similar results for the consecutive parts of the data. It is shown in Fig. 5.11, where the correction functions found for two randomly selected cells and for 10 independent parts of data are plotted. As one can see, the outcome of this test is satisfactory.

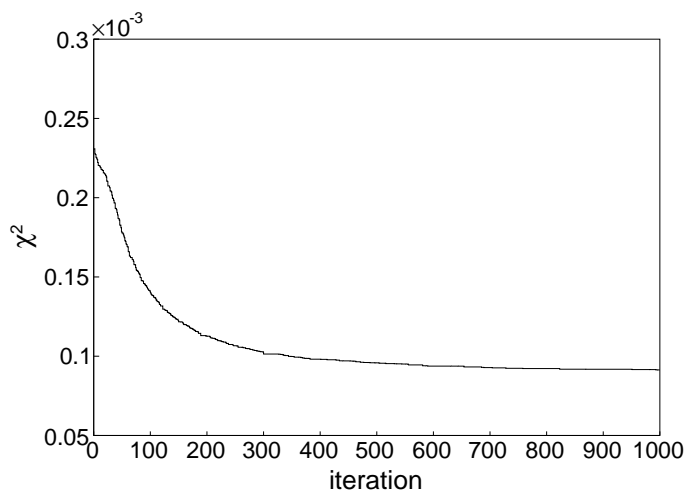


Figure 5.3: The χ^2 value for the best candidate in a given iteration.

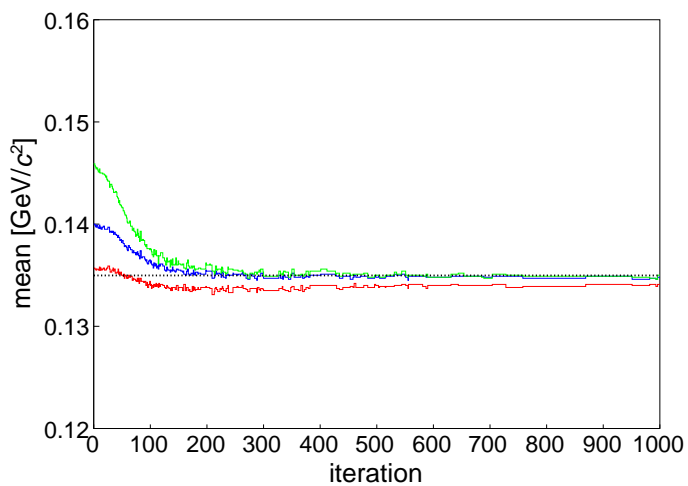


Figure 5.4: The position of the π^0 peak obtained from the data after applying a set of calibration coefficients for the best candidate in a given iteration. The curves correspond to three bins of the π^0 energy: $2 \text{ GeV} \leq E_{\pi^0} < 10 \text{ GeV}$ (red), $10 \text{ GeV} \leq E_{\pi^0} < 15 \text{ GeV}$ (blue) and $15 \text{ GeV} \leq E_{\pi^0} < 25 \text{ GeV}$ (green).

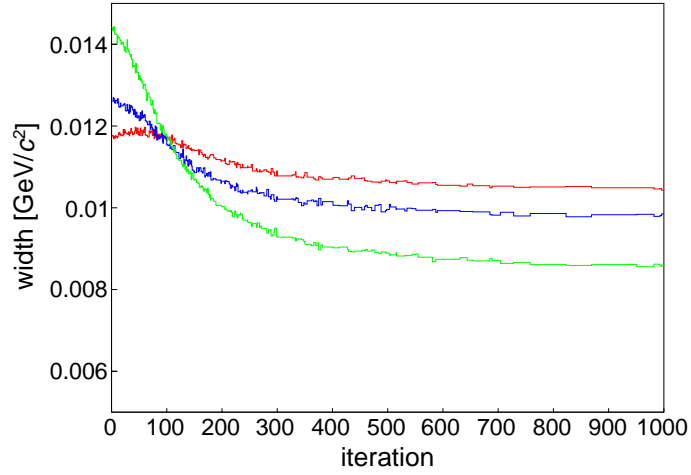


Figure 5.5: The width of the π^0 peak obtained from the data after applying a set of calibration coefficients for the best candidate in a given iteration. The curves correspond to three bins of the π^0 energy: $2 \text{ GeV} \leq E_{\pi^0} < 10 \text{ GeV}$ (red), $10 \text{ GeV} \leq E_{\pi^0} < 15 \text{ GeV}$ (blue) and $15 \text{ GeV} \leq E_{\pi^0} < 25 \text{ GeV}$ (green).

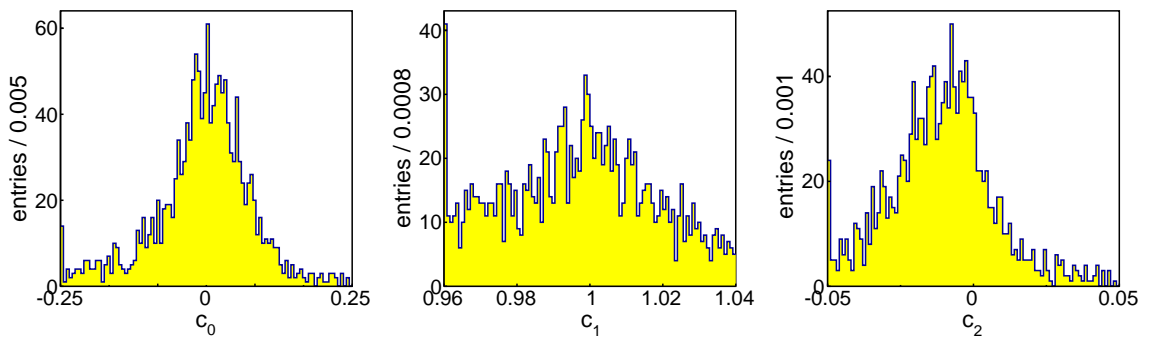


Figure 5.6: The distributions of the calibration coefficients obtained for the best candidate in the last iteration.

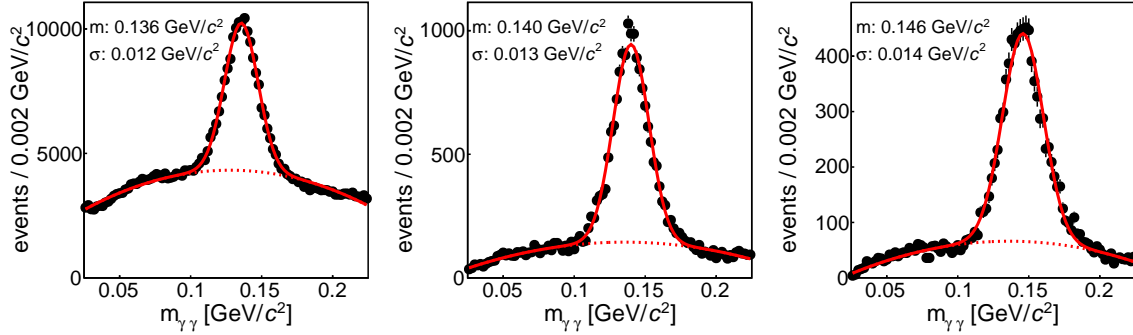


Figure 5.7: The distributions of the $m_{\gamma\gamma}$ invariant mass obtained from the data before the calibration together with the fits. The distributions are obtained in three bins of the π^0 energy: $2 \text{ GeV} \leq E_{\pi^0} < 10 \text{ GeV}$ (left), $10 \text{ GeV} \leq E_{\pi^0} < 15 \text{ GeV}$ (center) and $15 \text{ GeV} \leq E_{\pi^0} < 25 \text{ GeV}$ (right). The mean position and width of the π^0 peak found by the fits are indicated in the upper-left corner of each distribution.

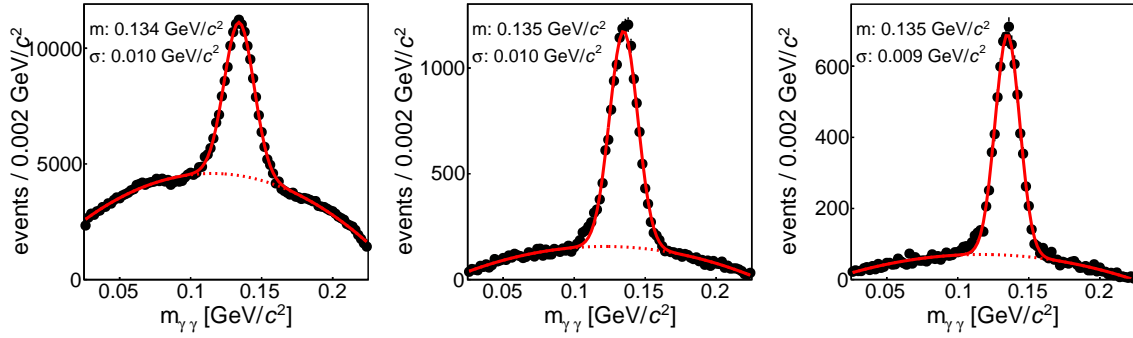


Figure 5.8: The distributions of the $m_{\gamma\gamma}$ invariant mass obtained from the data after the calibration together with the fits. The distributions are obtained in three bins of the π^0 energy: $2 \text{ GeV} \leq E_{\pi^0} < 10 \text{ GeV}$ (left), $10 \text{ GeV} \leq E_{\pi^0} < 15 \text{ GeV}$ (center) and $15 \text{ GeV} \leq E_{\pi^0} < 25 \text{ GeV}$ (right). The mean position and width of the π^0 peak found by the fits are indicated in the upper-left corner of each distribution.

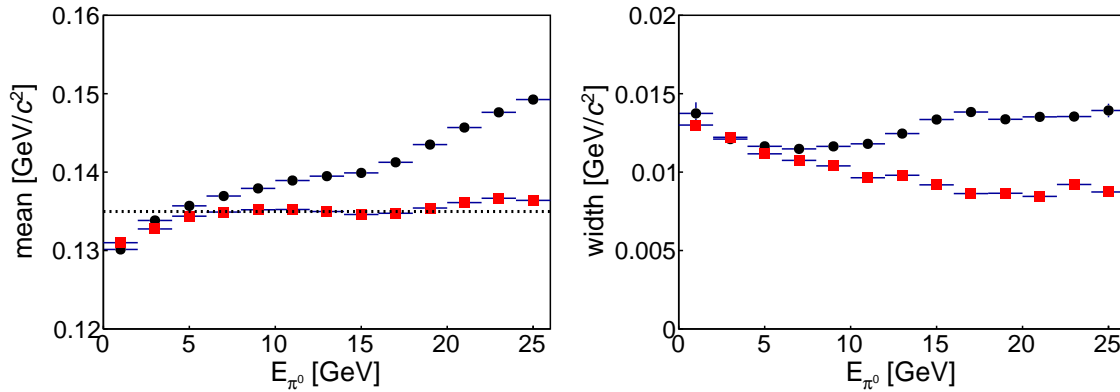


Figure 5.9: The position (left) and width (right) of the π^0 peak as a function of the π^0 energy obtained from the data before (black circles) and after (red squares) the calibration.

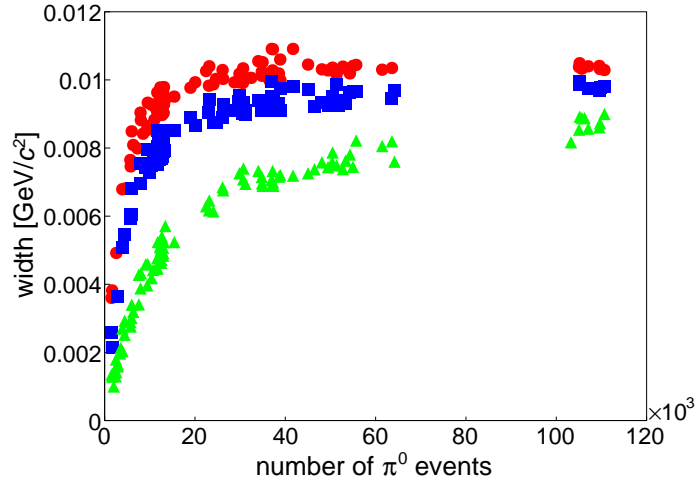


Figure 5.10: The width of the π^0 peak obtained from the data after the calibration as a function of the number of input π^0 events used in the procedure. The points correspond to three bins of the π^0 energy: $2 \text{ GeV} \leq E_{\pi^0} < 10 \text{ GeV}$ (red circles), $10 \text{ GeV} \leq E_{\pi^0} < 15 \text{ GeV}$ (blue squares) and $15 \text{ GeV} \leq E_{\pi^0} < 25 \text{ GeV}$ (green triangles).

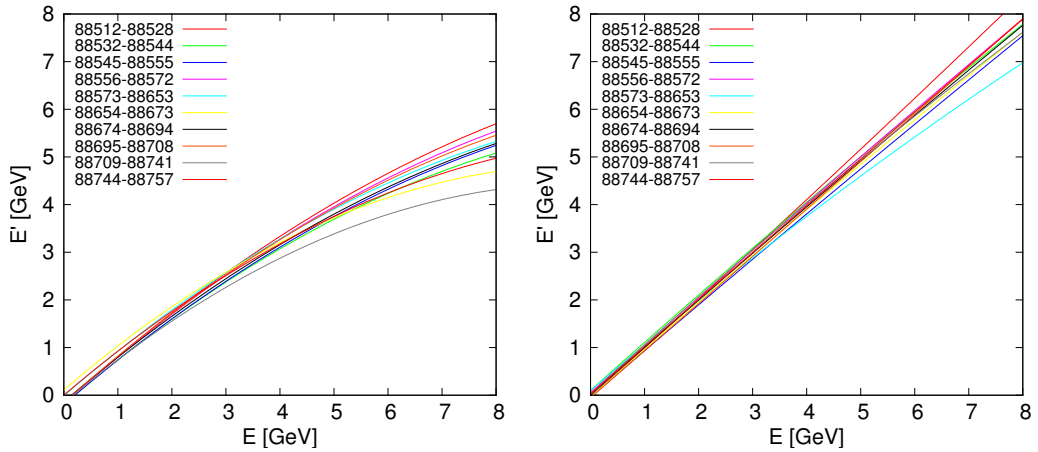


Figure 5.11: The correction functions, see Eq. (5.1), obtained for ten consecutive subsamples of data. Each sample contains data taken in the runs specified in the upper-left corners of the plots. The plots are made for the cell 58 (left) and 388 (right) of the ECAL1 calorimeter.

Transverse target spin asymmetries in exclusive ρ^0 meson production

The measurement of azimuthal asymmetries for exclusive ρ^0 meson production on transversely polarised protons and deuterons is described in this chapter. The observed process is

$$\mu N \rightarrow \mu N \rho^0 , \quad (6.1)$$

where

$$\rho^0 \rightarrow \pi^+ + \pi^- . \quad (6.2)$$

The samples of data used in this measurement are defined by cuts and selections described in Sec. 6.1. The extraction of azimuthal asymmetries is discussed in Sec. 6.2, while the subtraction of the remaining semi-inclusive background is described in Sec. 6.3. The estimation of systematic effects is discussed in Sec. 6.4. The final results are given in Sec. 6.5.

The first results on the azimuthal asymmetries have been published by the COMPASS collaboration in Ref. [23] for both protons and deuterons. In this measurement the 1D binned likelihood estimator, see Sec. 6.2.3, and the method A of the semi-inclusive background subtraction, see Sec. 6.3.2, were used. The measurement was performed only for the $A_{UT}^{\sin(\phi-\phi_S)}$ asymmetry that is the most sensitive one to the orbital angular momentum of partons.

The next measurement was performed for all eight azimuthal asymmetries defined in Eq. (2.17), however only for protons. In this analysis the 2D binned likelihood estimator, see Sec. 6.2.4, and the method B of the semi-inclusive background subtraction, see Sec. 6.3.3, were used. The analysis with the 2D estimator for deuterons was not possible due to the limited statistics of the data. The results have been published in Ref. [24]. Since the 2D estimator is sensitive to a correlation between the asymmetries, the new results on the $A_{UT}^{\sin(\phi-\phi_S)}$ asymmetry have superseded those published in Ref. [23] for protons. Note however, that both results have been found to be compatible.

The azimuthal asymmetries are measured in one-dimensional bins of Q^2 , x_{Bj} and p_T^2 . These bins are defined in Table 6.1. The results on the azimuthal asymmetries without the division in bins are also given.

Table 6.1: The kinematic bins used in the ρ^0 analysis. The first bin of p_T^2 is used only for the proton data.

Q^2 bin [[GeV/c] ²]	x_{Bj} bin	p_T^2 bin [[GeV/c] ²]	note
$1.0 \leq Q^2 < 1.2$	$0.003 \leq x_{Bj} < 0.02$	$0.05 \leq p_T^2 < 0.10$	proton data only
$1.2 \leq Q^2 < 1.6$	$0.02 \leq x_{Bj} < 0.03$	$0.10 \leq p_T^2 < 0.15$	
$1.6 \leq Q^2 < 2.4$	$0.03 \leq x_{Bj} < 0.05$	$0.15 \leq p_T^2 < 0.25$	
$2.4 \leq Q^2 < 10.0$	$0.05 \leq x_{Bj} < 0.35$	$0.25 \leq p_T^2 < 0.35$	
		$0.35 \leq p_T^2 < 0.50$	

6.1 Event selection

The deuteron data used in this measurement were taken in 2003-2004 with the 160 GeV μ^+ beam and with the transversely polarised target filled with the lithium deuteride, see Sec. 3.3. These data consist of six periods, where a given period corresponds to about one week of the data taking.

The proton data used in this measurement were taken in 2007 and 2010 with the 160 GeV μ^+ beam and with the transversely polarised target filled with the ammonia, see Sec. 3.3. These data consist of eleven periods taken in 2007 and twelve periods taken in 2010. In 2007 the W42 period consists of two subperiods taken with the opposite target polarisation, while in 2010 each period consists of two or three such subperiods.

The COMPASS names of the subperiods used in this analysis are listed in Table 6.2 together with the numbers of events left after all cuts and selections described in this chapter. The selections are the same for the proton and deuteron data unless it is noted otherwise.

6.1.1 Data quality

Only the data that pass the COMPASS quality checks are used in this measurement. These checks are done separately for each run or beam spill taken by the experiment, where a single run corresponds to up to 200 beam spills. In this paragraph only the most important quality checks are discussed, while a detailed description of the procedure used to examine the quality of data can be found in Ref. [96].

For a given run it is checked in the logbook of experiment if during the data taking there were no major problems with the apparatus. Additionally, distributions of fifteen inclusive and semi-inclusive variables obtained from the run are compared with those obtained for a whole period. A quality of the reconstruction is also examined by looking at the measured position of K^0 resonance.

For a given spill the average number of events and the average numbers of tracks and vertices per event are examined. It is checked if the numbers are compatible with the expectations obtained for a larger sample of data.

For each period of data the runs and beam spills marked as bad ones are listed in a file that is provided in order to be used by the COMPASS collaboration members. These official files are also used in this measurement.

6.1.2 Primary vertex

The primary vertex contains an incoming beam track and a number of outgoing tracks. Since the considered reaction occurs in a primary vertex and the ρ^0 meson decays too fast to distinguish a decay vertex only the primary vertices are considered in this analysis. It is possible that more than one primary vertex is reconstructed in a single event. In such case only the so-called best primary vertex is considered. The best primary vertex contains the largest number of outgoing tracks. In a

Table 6.2: The list of periods used in the ρ^0 analysis together with the corresponding numbers of selected events after all cuts, N_{select} . The entries are grouped according to the polarisation signs obtained in the target cells, where *e.g.* (+ - +) denotes the positive polarisation (spin up) in the both upstream and downstream cells and the negative polarisation (spin down) in the central cell. The N_{select} numbers correspond to $-2.5 \text{ GeV} < E_{\text{miss}} < 2.5 \text{ GeV}$ region, see Eq. (6.16), and account for both signal and semi-inclusive background events. The latter ones contribute in this region of E_{miss} with an estimated fraction of 18% for the deuteron data and 22% for the proton data.

year/target	period (+ -)	N_{select}	period (- +)	N_{select}
2003/d	P1H	15861	P1G	17725
2004/d	W33	14862	W34	12648
	W36	13461	W35	22089
SUM		44184		52462

year/target	period (+ - +)	N_{select}	period (- + -)	N_{select}	
2007/p	W26	20473	W25	17495	
	W28	21319	W27	11560	
	W30	22204	W31	29826	
	W39	33041	W40	19552	
	W42a	18788	W41	23113	
	W42b	9036	W43	11285	
2010/p	W23b	13293	W23a	14751	
	W24a	16853	W24b	8049	
	W26b	13702	W26a	13872	
	W27a	11809	W27b	14668	
	W29a	20151	W29b	18357	
	W31b	24554	W31a	24053	
	W33a	27374	W33b	22333	
	W35b	27683	W35a	32364	
	W37a	30034	W37b	28186	
	W39b	51212	W39a/c	35948	
	W42b	31881	W42a	26309	
	W44a	26122	W44b	25884	
	SUM		419529		377605

case of ambiguity the best primary vertex has the lowest value of χ^2 function returned by the vertex reconstruction software.

A given event is selected only if the best primary vertex contains an incoming beam track (μ^+ candidate), one outgoing muon track ($\mu^{+'}$ candidate), two outgoing hadrons tracks of opposite charges (π^+ and π^- candidates) and no other outgoing tracks. The vertex has to be reconstructed in a part of the target filled with the polarisable material. This is checked by selecting only those vertices that pass cuts on the position of vertex, both along the beam direction and in the perpendicular plane. The cuts depend on the alignment of target and on the filling of cells by the target material. They are given separately for each year of data taking and the polarisation mode by the `PaAlgo::InTarget()` function that is included in the COMPASS analysis software [97]. The distributions of primary vertex position along the beam direction, z_V , are shown in Fig. 6.1 for the

proton and deuteron data. In these distributions the separation between either three or two target cells is clearly visible.

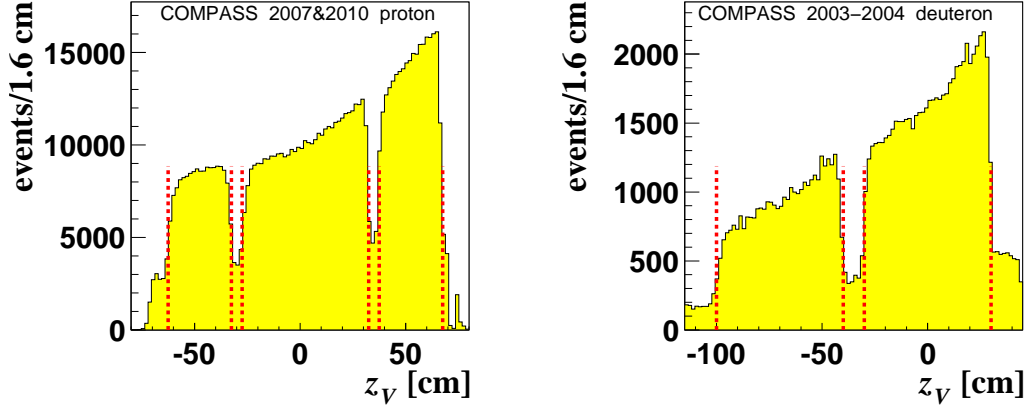


Figure 6.1: The reconstructed positions of the primary vertices along the beam direction, z_V , for the proton (left) and deuteron (right) data. The events accepted in this analysis are denoted by the red vertical lines. All cuts used in this analysis are applied here, except those related to the plotted variable.

The beam track must have at least three hits in the planes of the Beam Momentum Station (BMS). This requirement selects only those beam tracks that have a reconstructed momentum. In this analysis the data reconstructed with the old code of BMS reconstruction are used, see Chapter 4.

For the data taken after 2006 and reconstructed with the old code of BMS reconstruction a wrong value of momentum have been assigned to a fraction of beam tracks. The reason of this problem is still unknown, but possibly a growth of beam intensity achieved after 2006 has oversaturated the capability of clean reconstruction by the old algorithm. In analyses of exclusive reactions this problem is seen as an excess of events in the range of large negative values of E_{miss} (for the definition of this variable see Eq. (6.15)). This range is kinematically forbidden for all types of reactions, therefore it is populated only by events that are affected by a reconstruction problem of either BMS or COMPASS spectrometer data. To suppress such wrongly reconstructed events a cut on the probability of χ_s^2 defined in Eq. (4.4) is used,

$$\text{Prob}(\chi_s^2, \text{ndf}) > 0.005 . \quad (6.3)$$

In the proton data used in this measurement the fraction of wrongly reconstructed events is estimated to be $\approx 20\%$ before and $\approx 5\%$ after applying this cut. Since the deuteron data used in this measurement were produced with the old reconstruction software, which does not allow to access the value of $\text{Prob}(\chi_s^2, \text{ndf})$ probability, the cut defined in Eq. (6.3) can not be applied in this case. However, the deuteron data were taken before 2006 and here the fraction of wrongly reconstructed events is estimated to be $\approx 7\%$.

In order to cancel out the beam flux in the extraction of asymmetries, see Sec. 6.2, it is checked if the beam particles could pass through the all target cells. Here, the direction of a given beam particle is examined with respect to the alignment of target by the `PaAlgo::CrossCells()` function included in the COMPASS analysis software [97].

In order to distinguish between the muon and hadron tracks the number of normalised radiation lengths, X/X_0 , accumulated by a given track is examined,

$$\begin{aligned} X/X_0 > 30 & \quad (\text{to be muon}), \\ X/X_0 < 10 & \quad (\text{to be hadron}). \end{aligned} \quad (6.4)$$

The value of X/X_0 accounts for all media crossed by a given track,

$$X/X_0 = \sum_{\text{media}} X_i/X_{0,i} , \quad (6.5)$$

where X_i is the distance passed by the track in a given medium and $X_{0,i}$ is the radiation length of this medium.

In order to suppress the number of muons misidentified as hadron tracks it is checked if the π^+ candidate does not cross the hole of hadron absorbers. Moreover, the tracks of both hadron candidates should start before the SM1 magnet and they must stop before the last hadron absorber,

$$\begin{aligned} z_{\text{first}} &< 350 \text{ cm} , \\ 350 \text{ cm} &< z_{\text{last}} < 3300 \text{ cm} . \end{aligned} \quad (6.6)$$

For all types of tracks the quality of reconstruction is examined by the χ^2/ndf value returned by the track reconstruction software,

$$\chi^2/\text{ndf} < 10 . \quad (6.7)$$

Additionally, it is checked if the tracks do not cross the yoke of SM2 magnet where the magnetic field is known with a large uncertainty.

6.1.3 Inclusive variables

The following cuts on the inclusive variables are used in this measurement

$$\begin{aligned} 1 \text{ (GeV}/c)^2 &< Q^2 < 10 \text{ (GeV}/c)^2 , \\ 0.1 &< y < 0.9 , \\ W &> 5 \text{ GeV}/c^2 . \end{aligned} \quad (6.8)$$

The lower cut on Q^2 ensures that the perturbative region is probed, so the results of this measurement can be compared with the predictions of pQCD-based models. The cross section as a function of Q^2 falls much faster for exclusive events than that for semi-inclusive ones. Therefore, the upper cut on Q^2 has been introduced to suppress the semi-inclusive background.

The lower cut on y removes events where the smearing of reconstructed variables is large. In those events the scattered muons have large momenta and they are barely deflected by the magnets of COMPASS spectrometer. The upper cut on y removes events where the radiative corrections can be large. The cut on W has been introduced to avoid the so-called resonance region where the cross section for semi-inclusive reactions is large and it changes rapidly due to a production of resonances. Note however, that due to the correlation between y and W variables the cut on W removes only little remaining events.

The distributions of Q^2 , x_{Bj} , y and W for the proton and deuteron data are shown in Figs. 6.2 - 6.5.

6.1.4 Reconstruction of ρ^0

The ρ^0 resonance is selected by the cut on the invariant mass of two outgoing hadrons, $M_{\pi\pi}$. Since the particle identification given by the RICH detector is not used in this measurement, as its impact after presented selection is limited, it is assumed that the outgoing hadrons are pions. The cut on $M_{\pi\pi}$ is tuned by analysing the spectrum of this variable with the Ross-Stodolsky [98] and Söding [99] parametrisations. Both parametrisations account for the resonant ρ^0 and non-resonant $\pi^+\pi^-$ productions, where the latter is introduced as a modification to the relativistic Bright-Wigner distribution.

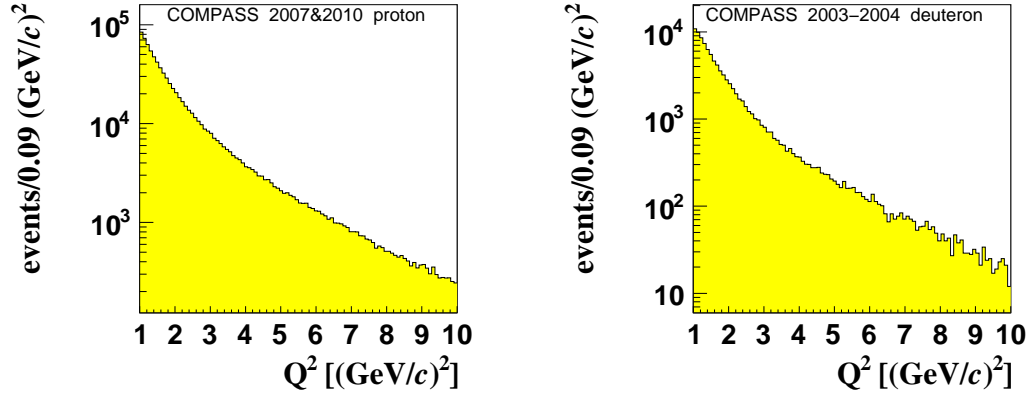


Figure 6.2: The distributions of Q^2 for the proton (left) and deuteron (right) data. All cuts used in this analysis are applied here.

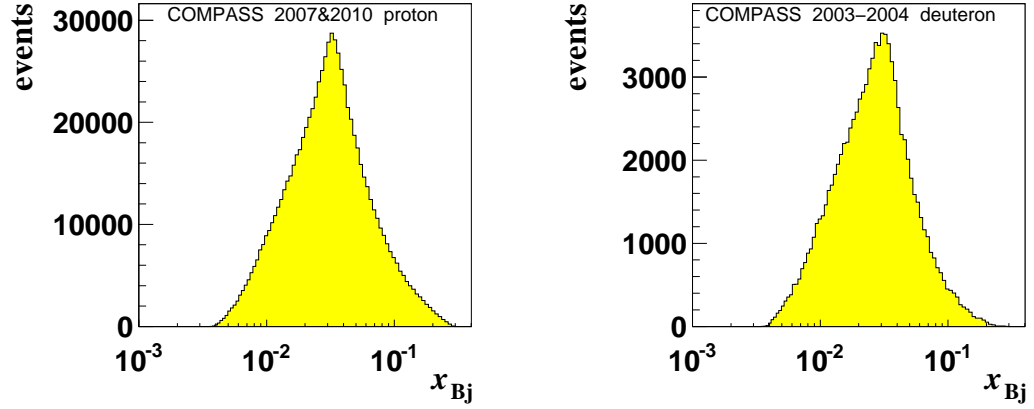


Figure 6.3: The distributions of x_{Bj} for the proton (left) and deuteron (right) data. All cuts used in this analysis are applied here.

In the Ross-Stodolsky parameterisation the non-resonant production "skews" the Breit-Wigner distribution,

$$\frac{dn}{dM_{\pi\pi}} \propto \left| \frac{\sqrt{M_\rho M_{\pi\pi} \Gamma(M_{\pi\pi})}}{M_\rho^2 - M_{\pi\pi}^2 + iM_\rho \Gamma(M_{\pi\pi})} \right|^2 \left(\frac{M_\rho}{M_{\pi\pi}} \right)^n, \quad (6.9)$$

where $M_\rho \simeq 0.775 \text{ GeV}/c^2$ is the nominal ρ^0 mass, n is the skewness parameter and

$$\Gamma(M_{\pi\pi}) = \Gamma_0 \left(\frac{p_\pi(M_{\pi\pi})}{p_\pi(M_\rho)} \right)^3 \frac{M_\rho}{M_{\pi\pi}} \quad (6.10)$$

is the resonance width. Here, Γ_0 is the nominal resonance width and $p_\pi(M)$ is the momentum of decay pions in the ρ^0 centre of mass system. In the Söding parameterisation the non-resonant production is introduced as an additional amplitude,

$$\frac{dn}{dM_{\pi\pi}} \propto \left| \frac{\sqrt{M_\rho M_{\pi\pi} \Gamma(M_{\pi\pi})}}{M_\rho^2 - M_{\pi\pi}^2 + iM_\rho \Gamma(M_{\pi\pi})} + \frac{f}{2} \right|^2. \quad (6.11)$$

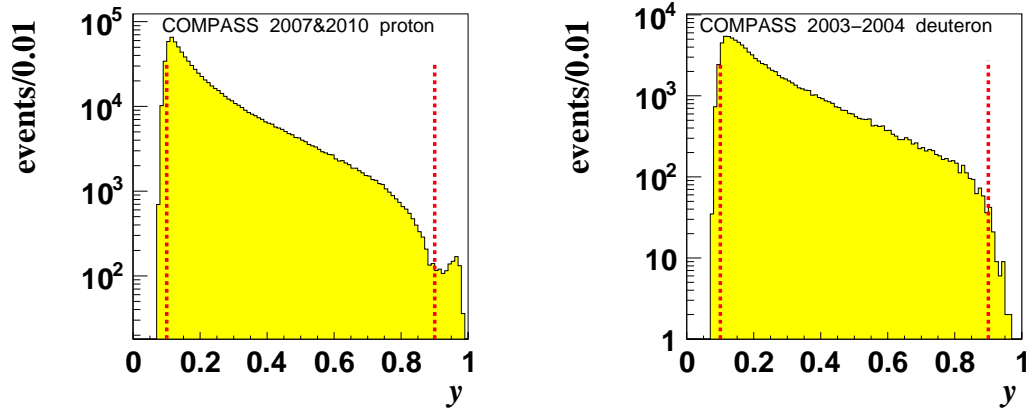


Figure 6.4: The distributions of y for the proton (left) and deuteron (right) data. All cuts used in this analysis are applied here except the cut on y . The events accepted in this analysis are denoted by the red vertical lines.

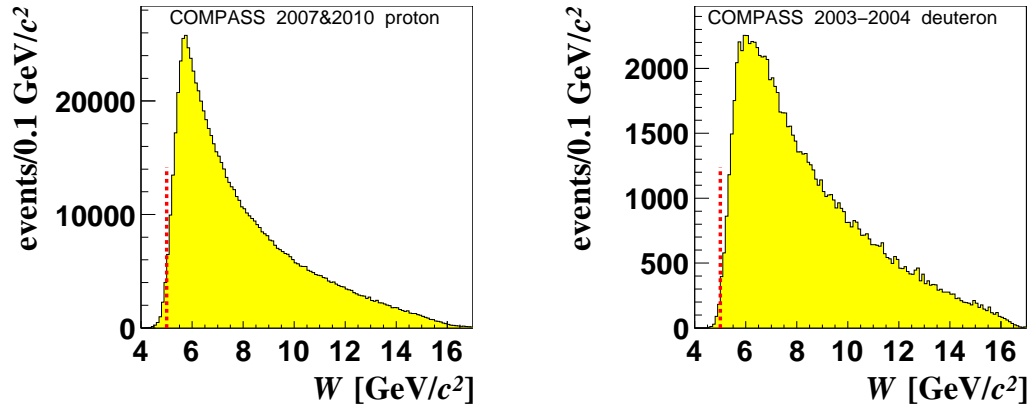


Figure 6.5: The distributions of W for the proton (left) and deuteron (right) data. All cuts used in this analysis are applied here except the cut on W . The events accepted in this analysis are distributed on the right side of the red vertical lines.

Here, f is the amplitude of non-resonant production. Although the f amplitude is small, its interference with the resonance amplitude is typically large. In addition, the interference changes its sign at $M_{\pi\pi} = M_\rho$.

An exemplary invariant mass distribution parametrised with either Ross-Stodolsky or Söding parameterisation is shown in Fig. 6.6. For the Söding parameterisation the separate contributions from the resonant ρ^0 and non-resonant $\pi^+\pi^-$ productions and the interference between both processes are also shown. The distribution was obtained with the modified cut on the missing energy, $-2.5 \text{ GeV} < E_{\text{miss}} < 0$, cf. Eq. (6.16), that suppresses the semi-inclusive background to a large extent but reduces the signal statistics by half.

The final cut on the invariant mass reads

$$0.5 \text{ GeV}/c^2 < M_{\pi\pi} < 1.1 \text{ GeV}/c^2 . \quad (6.12)$$

The cut is wide enough to cover $\approx 90\%$ of all observed ρ^0 events. A wider cut would result in an increased fraction of semi-inclusive background without a significant gain of the signal statistics. The

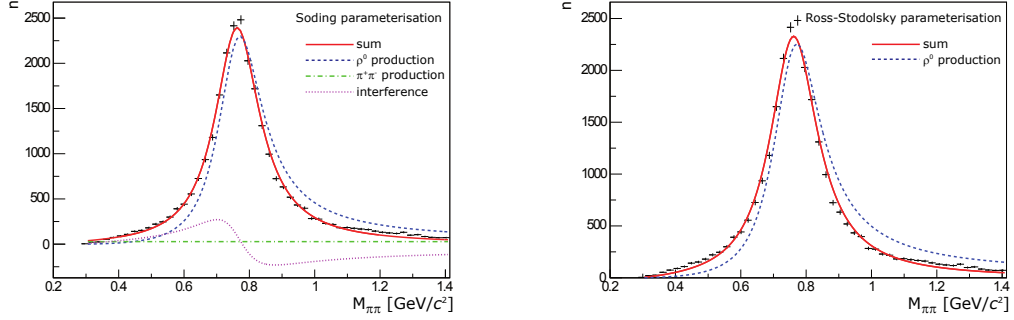


Figure 6.6: The distribution of $M_{\pi\pi}$ fitted with the Söding (left) and Ross-Stodolsky (right) parameterisations. The distribution is shown for the proton data in the range of $1 (\text{GeV}/c)^2 < Q^2 < 1.2 (\text{GeV}/c)^2$ using the restrictive cut on E_{miss} , $-2.5 \text{ GeV} < E_{\text{miss}} < 0$, to suppress the semi-inclusive background. The specific contributions are marked by the curves that are explained in the legend.

cut boundaries have been chosen also to ensure that the integrated contribution from the interference term in the Söding parameterisation, $\text{Int}(M_{\pi\pi})$, approximately vanishes,

$$\int_{0.5 \text{ GeV}/c^2}^{1.1 \text{ GeV}/c^2} \text{Int}(M_{\pi\pi}) dM_{\pi\pi} \approx 0. \quad (6.13)$$

Therefore, the selected number of ρ^0 events is approximately the same as it would be with no interference term.

The contribution from the $\phi \rightarrow K^+K^-$ decay is removed with the cut

$$M_{KK} > 1.04 \text{ GeV}/c^2. \quad (6.14)$$

Because an information from the RICH detector is not used in this analysis, the M_{KK} invariant mass is calculated assuming the kaon mass for the outgoing hadrons instead of the pion mass. The distributions of $M_{\pi\pi}$ variable for the proton and deuteron data are shown in Fig. 6.7.

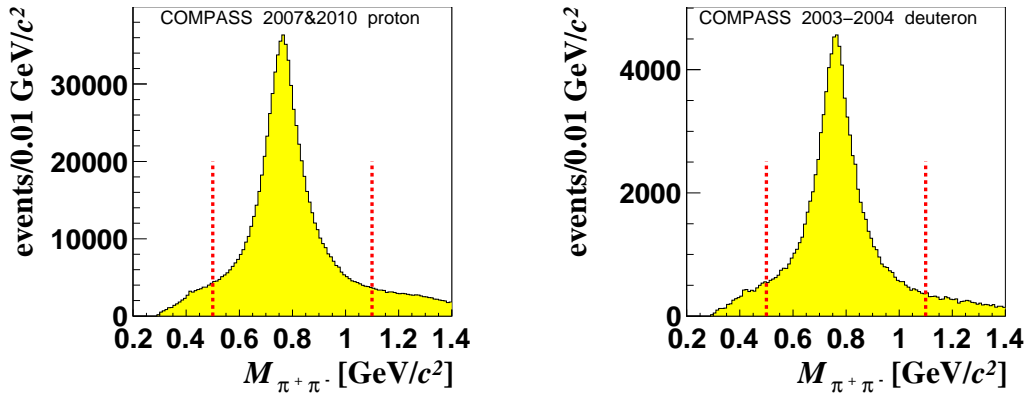


Figure 6.7: The distributions of the invariant mass of two pions, $M_{\pi\pi}$, for the proton (left) and deuteron (right) data. All cuts used in this analysis are applied here except the cut on $M_{\pi\pi}$. The events accepted in this analysis are denoted by the red vertical lines.

6.1.5 Exclusivity and incoherence

The exclusivity of each event is examined by the calculation of missing energy, E_{miss} , defined as

$$E_{\text{miss}} = \frac{(p + q - v)^2 - p^2}{2M_p} = \frac{M_x^2 - M_p^2}{2M_p} . \quad (6.15)$$

Here, M_p is the proton mass and M_x is the mass of undetected recoiled particles calculated from the four-momentum vectors p , q and v of the proton, the virtual photon and the ρ^0 meson, respectively. For the exclusive events one expects $E_{\text{miss}} = 0$, however the measured values are smeared due to the experimental resolution. Taking into account the measured resolution of exclusive peak (≈ 1.25 GeV) the cut on E_{miss} has been set to

$$-2.5 \text{ GeV} < E_{\text{miss}} - E_{\text{miss}}^{\text{corr}} < 2.5 \text{ GeV} . \quad (6.16)$$

Here, $E_{\text{miss}}^{\text{corr}}$ has been introduced to correct for a small shift of the exclusive peak position observed in the data. The shift is estimated separately for each period or subperiod of data from a fit to the E_{miss} distribution, see Sec. 6.3.1. The values of $E_{\text{miss}}^{\text{corr}}$ varies between -0.36 GeV and 0.12 GeV. The distributions of E_{miss} variable for the proton and deuteron data are shown in Fig. 6.8.

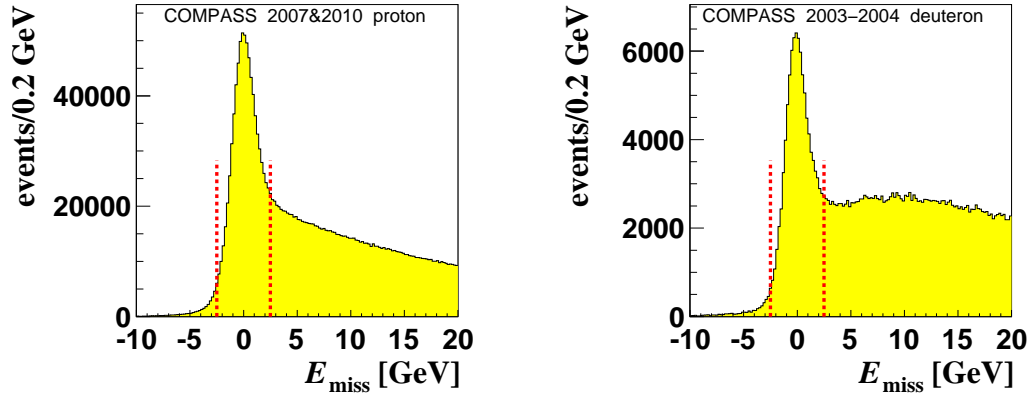


Figure 6.8: The distributions of the missing energy, E_{miss} , for the proton (left) and deuteron (right) data. All cuts used in this analysis are applied here except the cut on E_{miss} . The events accepted in this analysis are denoted by the red vertical lines.

The semi-inclusive background is further suppressed with the following cut on the energy of ρ^0 candidate,

$$E_{\pi\pi} > 14 \text{ GeV} . \quad (6.17)$$

This cut is related to the kinematic limit that is set for the exclusive reactions by the lower cut on y , $y_{\text{min}} = 0.1$, see Eq. (6.8), as $E_{\pi\pi} \approx \nu$ and $\nu = y \cdot E_\mu$, where E_μ is the beam energy. The distributions of E_{miss} vs. $E_{\pi\pi}$ for the proton and deuteron data are shown in Fig. 6.9.

In addition, the semi-inclusive background is suppressed by the cut on the squared transverse momentum of ρ^0 candidate with respect to the virtual photon direction,

$$p_T^2 < 0.5 \text{ (GeV}/c)^2 . \quad (6.18)$$

The cut is motivated by the observation that the cross section as a function of p_T^2 decreases faster for exclusive signal than that for semi-inclusive background.

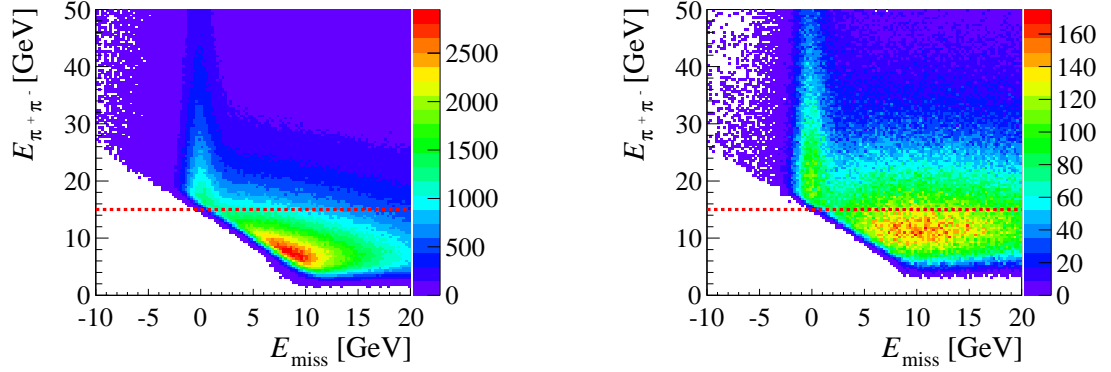


Figure 6.9: The correlation between the missing energy, E_{miss} , and the energy of exclusive ρ^0 candidate, $E_{\pi\pi}$, for the proton (left) and deuteron (right) data. All cuts used in this analysis are applied here except those on E_{miss} and $E_{\pi\pi}$. The red horizontal line denotes the cut on $E_{\pi\pi}$ used for this analysis.

The additional cut on the p_T^2 variable,

$$\begin{aligned} p_T^2 &> 0.1 \text{ (GeV}/c)^2 && \text{(for } ^6\text{LiD target) ,} \\ p_T^2 &> 0.05 \text{ (GeV}/c)^2 && \text{(for NH}_3 \text{ target) ,} \end{aligned} \quad (6.19)$$

is used to suppress the ρ^0 coherent production, which proceeds with small values of p_T^2 . This production occurs when the target nucleus remains intact after the interaction. The distributions of p_T^2 for the proton and deuteron data are shown in Fig. 6.10.

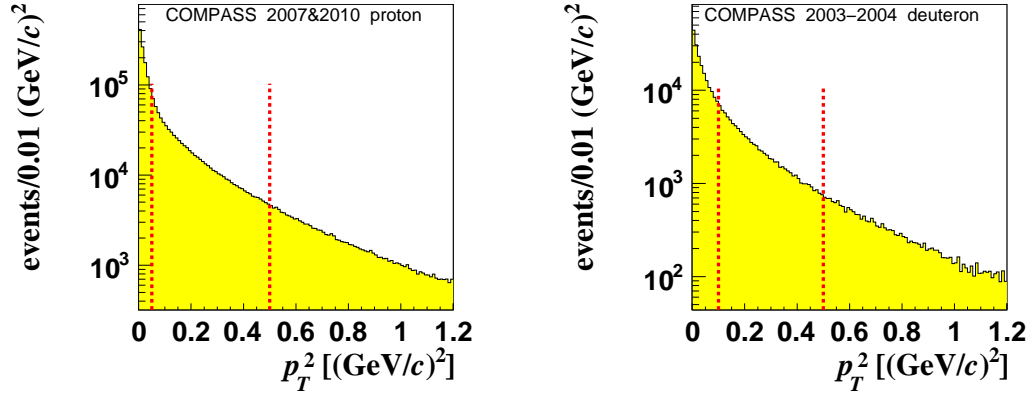


Figure 6.10: The distributions of p_T^2 for the proton (left) and deuteron (right) data. All cuts used in this analysis are applied here except the cut on p_T^2 . The events accepted in this analysis are denoted by the red vertical lines.

6.1.6 Background to exclusive production

The selected sample of data is contaminated by several types of background, which could not be separated entirely from the useful events by the cuts presented in this chapter. The main contribution

of background comes from semi-inclusive events and it varies between 5% and 40% depending on the kinematic bin and the target setup. On average, the semi-inclusive background contributes to the selected sample of data with the average fraction of 22% and 18%, for the proton and deuteron data, respectively. Such contamination is taken into account by a subtraction as described in Sec. 6.3.

Another type of background comes from diffractive dissociation events ($\mu N \rightarrow \mu N^* \rho^0$, $N^* \rightarrow N + n\pi$, where $n = 1, 2, \dots$). These events are reconstructed with small values of E_{miss} and only a fraction of them is removed by the cut defined in Eq. (6.16). The diffractive dissociation events that pass this cut contribute to the selected sample of data with the fraction of 14%. This fraction was found by analysing Monte Carlo data produced with the HEPGEN generator [40]. At present this type of background is not taken into account in the extraction of asymmetries. It is motivated by HERA results on ρ^0 meson production on unpolarised protons [100, 101, 102], where angular distributions of diffractive dissociation events were found consistent to those for exclusive production.

The background contribution due to non-resonant $\pi^+\pi^-$ pair production has been estimated from fits to $M_{\pi\pi}$ distributions with the Ross-Stodolsky and Söding parameterisations as described in Sec. 6.1.4. The contribution of non-resonant production was found to be less than 2% in any kinematic bin of Q^2 , x_{Bj} and p_T^2 . Because of such small contribution, this type of background is not taken into account in the extraction of asymmetries.

Coherent production of target nuclei has been estimated by analysis the shapes of p_T^2 distributions. The found contribution of incoherent events to the selected sample of the data was found to be 12% and 8%, for NH_3 and ${}^6\text{LiD}$ targets, respectively. The coherent background is not taken into account in the extraction of asymmetries. It is justified by the observation that the extracted asymmetries in the nominal range of p_T^2 are compatible within statistical uncertainties with those extracted in the modified range of p_T^2 . The latter is dominated by coherent production and it is defined by the cut $p_T^2 < 0.05 \text{ (GeV}/c)^2$ for NH_3 target and the cut $p_T^2 < 0.1 \text{ (GeV}/c)^2$ for the ${}^6\text{LiD}$ target.

6.1.7 Summary

All cuts that define the sample of events used for this analysis are summarised in Table 6.3. The numbers of accepted events after all cuts are given in Table 6.2.

Table 6.3: The summary of cuts and selections used in the ρ^0 analysis.

Purpose	Constraint
Topology	The best primary vertex made by an incoming beam track, one outgoing muon track and only two outgoing hadron tracks of opposite charges.
Vertex in target polarisable material	The function <code>PaAlgo::InTarget()</code> of COMPASS analysis software.
Track identification	$X/X_0 > 30$ to be identified as muon $X/X_0 < 10$ to be identified as hadron
Track reconstruction quality	$\chi_{\text{red}}^2 < 10$
Suppression of misidentified hadron tracks	$z_{\text{first}} < 350$ cm $350 \text{ cm} < z_{\text{last}} < 3300$ cm does not cross the yoke of SM2 magnet does not cross the hole of absorber system (only for the positive hadron track)
Same beam flux in all target cells	The function <code>PaAlgo::CrossTarget()</code> of COMPASS analysis software.
Reconstructed beam momentum	At least three hits in the BMS detectors
Suppression of beam tracks that have wrongly reconstructed momenta	$\text{Prob}(\chi_s^2, \text{ndf}) > 0.005$
Kinematic domain of analysis	$1 \text{ (GeV}/c)^2 < Q^2 < 10 \text{ (GeV}/c)^2$ $0.1 < y < 0.9$ $W > 5 \text{ GeV}/c^2$
ρ^0 resonance	$0.5 \text{ GeV}/c^2 < M_{\pi\pi} < 1.1 \text{ GeV}/c^2$ $M_{KK} > 1.04 \text{ GeV}/c^2$
Exclusivity and further suppression of semi-inclusive background	$-2.5 \text{ GeV} < E_{\text{miss}} - E_{\text{miss}}^{\text{corr}} < 2.5 \text{ GeV}$ $E_{\pi\pi} > 14 \text{ GeV}$ $p_T^2 < 0.5 \text{ (GeV}/c)^2$
Suppression of coherent events	$p_T^2 > 0.1 \text{ (GeV}/c)^2$ (for ${}^6\text{LiD}$ target) $p_T^2 > 0.05 \text{ (GeV}/c)^2$ (for NH_3 target)

6.2 Estimators of asymmetries

The overview of estimators of the asymmetries is given in this section. The overview starts in Sec. 6.2.1 with the introduction that contains the common definitions. In Sec. 6.2.2 the double ratio estimator is introduced. Although this estimator is used neither in the ρ^0 analysis nor in the ω one, it is the simplest estimator and it demonstrates intuitively how the acceptance and other factors cancel out in the calculations. In Secs. 6.2.3 and 6.2.4 the 1D and 2D binned likelihood estimators are introduced, respectively. These estimators are used in the ρ^0 analysis. In Sec. 6.2.5 the unbinned likelihood estimator is introduced that is used in the ω analysis.

6.2.1 Introduction

For a transversely polarised target the number of reconstructed events as a function of azimuthal angles ϕ and ϕ_S , $N(\phi, \phi_S)$, is given by

$$N(\phi, \phi_S) = F \cdot n \cdot \sigma_0 \cdot a(\phi, \phi_S) \times \\ \times \left(1 \pm A_{\text{raw}}^{\sin(\phi - \phi_S)} \sin(\phi - \phi_S) \pm A_{\text{raw}}^{\sin(\phi + \phi_S)} \sin(\phi + \phi_S) \pm \dots \right). \quad (6.20)$$

Here, F is the muon flux, n is the number of target nucleons, $a(\phi, \phi_S)$ is the angle-dependent acceptance and σ_0 is the unpolarised cross section defined in Eq. (2.18). The raw asymmetries, $A_{\text{raw}}^{\text{mod}}$, where $\text{mod} = \sin(\phi - \phi_S), \sin(\phi + \phi_S), \dots$, contain an information about the physics asymmetries and they contribute in Eq. (6.20) with the sign that corresponds to the target spin direction. For the up direction of spin the contribution is positive, while for the opposite direction the contribution is negative.

In order to calculate the physics asymmetries from the raw asymmetries, the latter ones have to be corrected for the dilution factor, f , defined in Sec. 3.3, the target polarisation, P_{target} , and the depolarisation factors, D^{mod} . In addition to these factors, the double spin asymmetries (LT) have to be corrected also for the beam polarisation, P_{beam} ,

$$A_{UT}^{\text{mod}} = \frac{A_{\text{raw}}^{\text{mod}}}{f \cdot |P_{\text{target}}| \cdot D^{\text{mod}}}, \\ A_{LT}^{\text{mod}} = \frac{A_{\text{raw}}^{\text{mod}}}{f \cdot |P_{\text{target}} \cdot P_{\text{beam}}| \cdot D^{\text{mod}}}. \quad (6.21)$$

The depolarisation factors appear in the cross section formula, see Eq. (2.14), and they depend on the virtual photon polarisation parameter, ϵ , that has been defined in Eq. (2.15). The depolarisation factors read

$$D^{\sin(\phi - \phi_S)} = 1, \\ D^{\sin(\phi + \phi_S)} = D^{\sin(3\phi - \phi_S)} = \frac{\epsilon}{2}, \\ D^{\sin(2\phi - \phi_S)} = D^{\sin \phi_S} = \sqrt{\epsilon(1 + \epsilon)}, \\ D^{\cos(\phi - \phi_S)} = \sqrt{1 - \epsilon^2}, \\ D^{\cos(2\phi - \phi_S)} = D^{\cos \phi_S} = \sqrt{\epsilon(1 - \epsilon)}. \quad (6.22)$$

Note, that each denominator in Eq. (6.21) gives the analysing power for the measurement of corresponding asymmetries. Together with the statistics of used data, the analysing power determines the statistical precision for the measurement of a given asymmetry. Since the depolarisation factors

are different for various asymmetries, the latter will be measured with different precisions. In particular, the statistical uncertainties for the double spin asymmetries will be larger than those for the single spin asymmetries.

The COMPASS polarised target is made of two or three cells, see Sec. 3.3. The polarisation in the consecutive cells is opposite and it is being reversed periodically. Therefore, one can define four independent subsamples of data. By combining these subsamples in the extraction of asymmetries one can cancel out the muon flux, the number of target nucleons and the acceptance, see the following.

For the three-cell target used after 2005 the subsamples used by the estimators are

$$\begin{aligned} N_{\text{U+D}}^{\uparrow}(\phi, \phi_S), \quad N_{\text{C}}^{\downarrow}(\phi, \phi_S), \\ N_{\text{U+D}}^{\downarrow}(\phi, \phi_S), \quad N_{\text{C}}^{\uparrow}(\phi, \phi_S). \end{aligned} \quad (6.23)$$

Here, $N_{\text{U+D}}^{\uparrow/\downarrow}(\phi, \phi_S)$ denote combined numbers of events reconstructed in the upstream and downstream target cells, while $N_{\text{C}}^{\uparrow/\downarrow}(\phi, \phi_S)$ denote the numbers of events reconstructed in the central target cell. The arrows in the superscripts denote the direction of target spin, where \uparrow denotes the up spin and \downarrow denotes the down spin.

For the two-cell target used before 2005 the subsamples used by the estimators are defined in a similar way as in Eq. (6.23),

$$\begin{aligned} N_{\text{U}}^{\uparrow}(\phi, \phi_S), \quad N_{\text{D}}^{\downarrow}(\phi, \phi_S), \\ N_{\text{U}}^{\downarrow}(\phi, \phi_S), \quad N_{\text{D}}^{\uparrow}(\phi, \phi_S). \end{aligned} \quad (6.24)$$

6.2.2 Double ratio estimator

In the double ratio estimator each asymmetry is extracted separately. Therefore, this estimator does not examine the correlation between the asymmetries and it relies on the assumption that the angular modulations related to the corresponding asymmetries can be probed independently.

For a given modulation, $\text{mod} = \sin(\phi - \phi_S), \sin(\phi + \phi_S), \dots$, the corresponding asymmetry is extracted from a fit to the double ratio distribution. This distribution is a product of four 1D distributions of events,

$$\text{DR}_i(\text{mod}) = \frac{N_{\text{U+D},i}^{\uparrow}(\text{mod})}{N_{\text{C},i}^{\downarrow}(\text{mod})} \cdot \frac{N_{\text{C},i}^{\uparrow}(\text{mod})}{N_{\text{U+D},i}^{\downarrow}(\text{mod})}. \quad (6.25)$$

Here, a given bin of distribution is denoted by $i = 1, \dots, N_{\text{bin}}$, where N_{bin} is the number of bins. The $N_{\text{U+D/C},i}^{\uparrow/\downarrow}(\text{mod})$ distributions correspond to the subsamples of data defined in Eq. (6.23). The definition of the double ratio distribution for the subsamples defined in Eq. (6.24) is similar.

To find the fit function the definition from Eq. (6.25) is expanded using Eq. (6.20),

$$\begin{aligned} \text{DR}(\text{mod}) &= \frac{F_{\text{U+D}}^{\uparrow} \cdot n_{\text{U+D}}^{\uparrow} \cdot \sigma_0}{F_{\text{C}}^{\downarrow} \cdot n_{\text{C}}^{\downarrow} \cdot \sigma_0} \cdot \frac{F_{\text{C}}^{\uparrow} \cdot n_{\text{C}}^{\uparrow} \cdot \sigma_0}{F_{\text{U+D}}^{\downarrow} \cdot n_{\text{U+D}}^{\downarrow} \cdot \sigma_0} \times \\ &\times \frac{a_{\text{U+D}}^{\uparrow}(\text{mod})}{a_{\text{C}}^{\downarrow}(\text{mod})} \cdot \frac{a_{\text{C}}^{\uparrow}(\text{mod})}{a_{\text{U+D}}^{\downarrow}(\text{mod})} \cdot \left(\frac{1 + A_{\text{raw}}^{\text{mod}} \cdot \text{mod}}{1 - A_{\text{raw}}^{\text{mod}} \cdot \text{mod}} \right)^2 = \\ &= C \cdot \left(\frac{1 + A_{\text{raw}}^{\text{mod}} \cdot \text{mod}}{1 - A_{\text{raw}}^{\text{mod}} \cdot \text{mod}} \right)^2. \end{aligned} \quad (6.26)$$

As by the definition, the unpolarised cross section does not depend on the polarisation of target, thus it cancels out. The beam flux also cancels out, if one accepts only those beam tracks that *a priori* could pass all target cells. With such requirement the beam flux in all target cells is the same, $F_{\text{U+D}}^\uparrow = F_{\text{C}}^\downarrow$ and $F_{\text{U+D}}^\downarrow = F_{\text{C}}^\uparrow$, and it cancels out in Eq. (6.26). The number of nucleons in a given cell is approximately the same before and after the target polarisation reversal, $n_{\text{U+D}}^\uparrow = n_{\text{U+D}}^\downarrow$ and $n_{\text{C}}^\uparrow = n_{\text{C}}^\downarrow$. Therefore, it also cancels out in Eq. (6.26).

The acceptance cancels out with the so-called reasonable assumption,

$$\frac{a_{\text{U+D}}^\uparrow(\text{mod})}{a_{\text{C}}^\downarrow(\text{mod})} = \frac{a_{\text{U+D}}^\downarrow(\text{mod})}{a_{\text{C}}^\uparrow(\text{mod})}. \quad (6.27)$$

The assumption is valid if for different cells the ratio of acceptances is the same before and after the target polarisation reversal. A new parameter, $C \neq 1$, can be introduced to the fit if the reasonable assumption does not hold, but only if the acceptance is changed by a constant factor. If the change of acceptance depends on the azimuthal angles, the extraction of asymmetries is biased. Such possibility is examined in the systematic studies, where the asymmetries are extracted from various combinations of target cells, see Secs. 6.4.1 and 7.2.1.

The function defined in Eq. (6.26) has two free parameter, C and $A_{\text{raw}}^{\text{mod}}$. By fitting this function to the double ratio distribution defined in Eq. (6.25) one can extract the raw asymmetry. The physics asymmetry can be calculated from the raw asymmetry according to Eq. (6.21).

6.2.3 1D binned maximum likelihood estimator

Similarly to the double ratio estimator the 1D binned maximum likelihood estimator allows to extract only one asymmetry at the time and it does not examine the correlation between the asymmetries.

Let ϕ' be a combination of ϕ and ϕ_S angles that corresponds to the asymmetry $A_{\text{raw}}^{\text{mod}}$. For example $\phi' = \phi - \phi_S$ for $\text{mod} = \sin(\phi - \phi_S)$. The number of events in a given bin of one of four 1D distributions of ϕ' angle is given by

$$N_{t,i}^p(\phi') = \frac{1}{\Delta_i} \int_{\bar{\phi}'_i - \frac{\Delta_i}{2}}^{\bar{\phi}'_i + \frac{\Delta_i}{2}} c_{t,i}^p(\phi') \cdot (1 \pm A_{\text{raw}}^{\text{mod}} \cdot \text{mod}) d\phi'. \quad (6.28)$$

Here, $p = \uparrow, \downarrow$ denotes the direction of target spin, while t denotes the target cell, where $t = \text{U+D}, \text{C}$ for the three-cell target and $t = \text{U}, \text{D}$ for the two-cell target. A bin that probes the ϕ' angle is denoted by $i = 1, \dots, N_{\text{bin}}$, where N_{bin} is the number of bins. A given bin probes $\bar{\phi}'_i - \Delta_i/2 < \phi' < \bar{\phi}'_i + \Delta_i/2$ range, where the central value and width of the bin are given by $\bar{\phi}'_i$ and Δ_i , respectively. A product of beam flux, number of target nucleons and angle-dependent acceptance, cf. Eq. (6.20), is denoted by $c_{t,i}^p(\phi')$.

Eq. (6.28) defines $2 \times 2 \times N_{\text{bin}}$ non-linear equations. The number of unknowns is $2 \times 2 \times N_{\text{bin}} + 1$ that accounts for $2 \times 2 \times N_{\text{bin}}$ values of $c_{t,i}^p$ and one $A_{\text{raw}}^{\text{mod}}$ asymmetry. The number of unknowns is reduced with the reasonable assumption,

$$\frac{c_{\text{U+D},i}^\uparrow(\phi')}{c_{\text{C},i}^\downarrow(\phi')} = \frac{c_{\text{U+D},i}^\downarrow(\phi')}{c_{\text{C},i}^\uparrow(\phi')}, \quad (6.29)$$

to $2 \times 2 \times N_{\text{bin}} + 1 - N_{\text{bin}}$, which allows to perform the extraction of asymmetry.

The extraction is performed using the maximum likelihood method that compares the set of equations defined in Eq. (6.28) with the data. For a given equation, which is denoted here by $a = 1, \dots, 2 \times 2 \times N_{\text{bin}}$, the probability is calculated, $P_a(\vec{b})$, that this equation describes the corresponding

bin of data. The probability depends on a vector \vec{b} that includes all $2 \times 2 \times N_{\text{bin}} + 1 - N_{\text{bin}}$ unknowns. For the whole system of equations one can define a product of probabilities,

$$\mathcal{L}(\vec{b}) = \prod_{a=1}^{2 \times 2 \times N_{\text{bin}}} P_a(\vec{b}), \quad (6.30)$$

or equivalently

$$\ln \mathcal{L}(\vec{b}) = \sum_{a=1}^{2 \times 2 \times N_{\text{bin}}} \ln P_a(\vec{b}). \quad (6.31)$$

The minimisation of $-\ln \mathcal{L}(\vec{b})$ allows to find the \vec{b} vector that in a most complete way describes the data. A description of technical implementation of such minimisation can be found in Ref. [96].

6.2.4 2D binned maximum likelihood estimator

The 2D binned maximum likelihood estimator allows to extract all asymmetries at the same time and it can be used to study correlations between the asymmetries. In this estimator the ϕ vs. ϕ_S phase space is probed in 2D bins. The number of events in a given bin is estimated by

$$N_{t,i}^p(\phi, \phi_S) = \frac{1}{\Delta^2} \int_{\bar{\phi}_i - \frac{\Delta}{2}}^{\bar{\phi}_i + \frac{\Delta}{2}} \int_{\bar{\phi}_{s,i} - \frac{\Delta}{2}}^{\bar{\phi}_{s,i} + \frac{\Delta}{2}} c_{t,i}^p(\phi, \phi_S) \cdot (1 \pm A_{\text{raw}}^{\sin(\phi - \phi_S)} \sin(\phi - \phi_S) \pm \dots) d\phi d\phi_S. \quad (6.32)$$

Here, the convention for symbols is similar to Eq. (6.28). A given 2D bin is denoted by $i = 1, \dots, N_{\text{bin}}^2$, where N_{bin}^2 is the number of bins. For the simplicity all bins in Eq. (6.32) are quadratic and they have the same area, Δ^2 .

Eq. (6.32) defines $2 \times 2 \times N_{\text{bin}}^2$ non-linear equations with $2 \times 2 \times N_{\text{bin}}^2 + N_a$ unknowns, where $N_a = 8$ is the number of asymmetries to be extracted. With the reasonable assumption,

$$\frac{c_{\text{U+D},i}^{\uparrow}(\phi, \phi_S)}{c_{\text{C},i}^{\downarrow}(\phi, \phi_S)} = \frac{c_{\text{U+D},i}^{\downarrow}(\phi, \phi_S)}{c_{\text{C},i}^{\uparrow}(\phi, \phi_S)}, \quad (6.33)$$

one can reduce the number of unknowns to $2 \times 2 \times N_{\text{bin}}^2 + N_a - N_{\text{bin}}^2$ that allows the extraction of asymmetries. The extraction is done with the maximum likelihood method as described in Sec. 6.2.3. The uncertainties of asymmetries found by a minimisation software include eventual correlations between the asymmetries. A description of technical implementation of such minimisation can be found in Ref. [96].

6.2.5 Unbinned maximum likelihood estimator

The unbinned maximum likelihood estimator allows to extract all asymmetries at the same time and it can be used to study correlations between the asymmetries. In this estimator it is assumed that each event follows one of four probability distribution functions, $P_t^p(\phi, \phi_S)$, where

$$P_t^p(\phi, \phi_S) = \frac{N_t^p(\phi, \phi_S)}{N_t^p}. \quad (6.34)$$

Here, the convention for symbols is similar to that in Eq. (6.28). The numerator of Eq. (6.34) corresponds to Eq. (6.20),

$$N_t^p(\phi, \phi_S) = c_t^p(\phi, \phi_S) \cdot (1 \pm A_{\text{raw}}^{\sin(\phi - \phi_S)} \sin(\phi - \phi_S) \pm \dots), \quad (6.35)$$

while the normalisation factor, N_t^p , is equivalent to the angle-integrated number of events measured in the corresponding subsample of data,

$$N_t^p = \int_{-\pi}^{\pi} \int_{-\pi}^{\pi} c_t^p(\phi, \phi_S) \cdot (1 \pm A_{\text{raw}}^{\sin(\phi - \phi_S)} \sin(\phi - \phi_S) \pm \dots) d\phi d\phi_S . \quad (6.36)$$

Since the probability is calculated for each event, the likelihood product, $\mathcal{L}(\vec{b})$, for N_{event} events reads

$$\mathcal{L}(\vec{b}) = \prod_{i=1}^{N_{\text{event}}} P_i(\vec{b}) . \quad (6.37)$$

Here, $P_i(\vec{b})$ is the probability given by Eq. (6.34) for the event $i = 1, \dots, N_{\text{event}}$, while \vec{b} is a vector that contains the unknowns. The number of unknowns is $4 + N_a$, which accounts for four $c_t^p(\phi, \phi_S)$ functions and N_a asymmetries. The number of unknowns can be reduced to $3 + N_a$ with the reasonable assumption,

$$\frac{c_{\text{U+D}}^{\uparrow}(\phi, \phi_S)}{c_{\text{C}}^{\downarrow}(\phi, \phi_S)} = \frac{c_{\text{U+D}}^{\downarrow}(\phi, \phi_S)}{c_{\text{C}}^{\uparrow}(\phi, \phi_S)} . \quad (6.38)$$

To perform the extraction of asymmetries a functional form of $c_t^p(\phi, \phi_S)$ must be known. Several forms of this function were examined in Monte Carlo studies [96]. The sensitivity of the extraction of asymmetries on the form of $c_t^p(\phi, \phi_S)$ function has been found negligible. Therefore, a constant value is being used here, $c_t^p(\phi, \phi_S) \equiv c_t^p$.

6.3 Semi-inclusive background subtraction

The overview of methods of the semi-inclusive background subtraction is given in this section. Each method of subtraction is related to a specific type of estimator of the asymmetries. The methods A and B, which are introduced in Secs. 6.3.2 and 6.3.3, are compatible with the binned estimators, *i.e.* the double ratio estimator given in Sec. 6.2.2 and the 1D and 2D binned likelihood estimators given in Secs. 6.2.3 and 6.2.4. The method C introduced in Sec. 6.3.4 is compatible with the unbinned likelihood estimator given in Sec. 6.2.5.

6.3.1 Introduction

The background subtraction in a given subsample of data always relies on the estimation of signal and semi-inclusive background contributions. These contributions are estimated from a fit to the corresponding E_{miss} distribution in the range $-10 \text{ GeV} < E_{\text{miss}} < 20 \text{ GeV}$. The fit function is

$$f_{\text{S+B}}(E_{\text{miss}}) = f_{\text{S}}(E_{\text{miss}}) + f_{\text{B}}(E_{\text{miss}}) , \quad (6.39)$$

where $f_{\text{S}}(E_{\text{miss}})$ and $f_{\text{B}}(E_{\text{miss}})$ describe the E_{miss} -dependent signal and semi-inclusive background contributions, respectively. They are given in the following by Eqs. (6.40) and (6.42).

The signal contribution is described by the Gaussian function,

$$f_{\text{S}}(E_{\text{miss}}) = p_{\text{S},0} \cdot \exp\left(-\frac{1}{2} \left(\frac{E_{\text{miss}} - p_{\text{S},1}}{p_{\text{S},2}}\right)^2\right) . \quad (6.40)$$

Here, $p_{\text{S},0}$ is the normalisation parameter, while $p_{\text{S},1}$ and $p_{\text{S},2}$ describe the position and width of the exclusive peak, respectively.

The shape of background contribution is obtained from a sample of Monte Carlo events produced with the LEPTO generator [103], followed by a full simulation of the COMPASS apparatus and the same reconstruction as for the real data. However, in the analysis presented in this thesis the shape of semi-inclusive background is usually not well reproduced by the Monte Carlo events. This can be noted in the large E_{miss} region that is dominated by the semi-inclusive background, see Fig. 6.11 (left). *A priori* the problem could be related to either a wrong simulation of the semi-inclusive reactions in the selected kinematics by the LEPTO generator or to a wrong description of the apparatus or to both of them.

A good agreement between the real and Monte Carlo data was proven in the COMPASS experiment for a minimum-bias semi-inclusive samples *e.g.* in the high- p_T measurement of the gluon helicity distribution [9]. However, in the present analysis the Monte Carlo events pass complex selection criteria designed to extract exclusive events, which reside only in a narrow corner of the phase space covered by LEPTO. There has been no attempt to make a tuning of the generator in this particular region of the phase space. Instead, to improve the agreement between the real and Monte Carlo data a given bin of the E_{miss} distribution for the Monte Carlo events is weighted by

$$w(E_{\text{miss}}) = \frac{N_{\text{rd}}^{\text{scc}}(E_{\text{miss}})}{N_{\text{MC}}^{\text{scc}}(E_{\text{miss}})} . \quad (6.41)$$

Here, $N_{\text{rd}}^{\text{scc}}(E_{\text{miss}})$ and $N_{\text{MC}}^{\text{scc}}(E_{\text{miss}})$ are the numbers of events measured in the corresponding bins of the E_{miss} distributions for the real and Monte Carlo data, respectively, when the same-sign charge sample is used. The same-sign charge sample is defined in the same way as the nominal sample, but instead of two hadrons with the opposite charges the selection requires two hadrons with the same charges, *i.e.* $\pi^+\pi^+$ and $\pi^-\pi^-$ in the ρ^0 analysis or $\pi^+\pi^+\gamma\gamma$ and $\pi^-\pi^-\gamma\gamma$ in the ω analysis. Additionally, a cut on the invariant mass of the produced meson is released here to increase the statistics. An example that demonstrates the calculation of weights is shown in Fig. 6.12.

Because of the charge conservation the same-sign charge sample excludes any exclusive production. Therefore, the weights can be calculated for any value of E_{miss} for the semi-inclusive events only. The procedure relies on the assumption that the disagreement between the real and Monte Carlo data is the same for the nominal and same-sign charge samples, which is well confirmed in the high E_{miss} region, *i.e.* outside of the exclusive signal peak.

To include the shape of the background contribution in the fit given by Eq. (6.39) the weighted E_{miss} distribution for the Monte Carlo events is parameterised with

$$\begin{aligned}
 f_{\text{B}}(E_{\text{miss}}) &= p_{\text{B},0} \times \\
 &\times \left(1 - \left(1 + \exp \frac{E_{\text{miss}} - p_{\text{B},1}}{p_{\text{B},2}} \right)^{p_{\text{B},3}} \right) \\
 &\times \left(1 + \exp \frac{E_{\text{miss}} - p_{\text{B},4}}{p_{\text{B},5}} \right)^{p_{\text{B},6}} .
 \end{aligned} \tag{6.42}$$

Here, $p_{\text{B},0}, \dots, p_{\text{B},6}$ are parameters fitted to the Monte Carlo distribution, for an example see Fig. 6.13. The values of $p_{\text{B},1}, \dots, p_{\text{B},6}$ parameters found in this fit are subsequently fixed in the fit to the experimental data that is given by Eq. (6.39). The normalisation parameter $p_{\text{B},0}$ is unconstrained in the latter fit together with the $p_{\text{S},0}, p_{\text{S},1}$ and $p_{\text{S},2}$ parameters, cf. Eq. (6.40). An example of the final fit to the real data is shown in Fig. 6.11 (right). The excess of events observed in this figure for the $2 \text{ GeV} < E_{\text{miss}} < 5 \text{ GeV}$ range is caused by the diffractive dissociation reaction, see Sec. 6.1.6, that is not taken into account in the fit. Note however, that an attempt to include this reaction in the fits changed only negligibly the estimated signal and semi-inclusive background contributions.

It is assumed that the azimuthal asymmetries of the semi-inclusive background do not depend on E_{miss} . This assumption allows us to probe these asymmetries in a range of E_{miss} dominated by the semi-inclusive background and to extrapolate them to the signal range where both signal and background events contribute. This assumption is examined by extracting the azimuthal asymmetries in bins of E_{miss} in the background-dominated range, $7 \text{ GeV} < E_{\text{miss}} < 20 \text{ GeV}$. An example of such investigation is shown in Fig. 6.14. As for all asymmetries measured on protons and deuteron no dependence of extracted values on E_{miss} is visible, one can conclude that the assumption is justified. A similar test was done also for the ω analysis, where a similar conclusion was found.

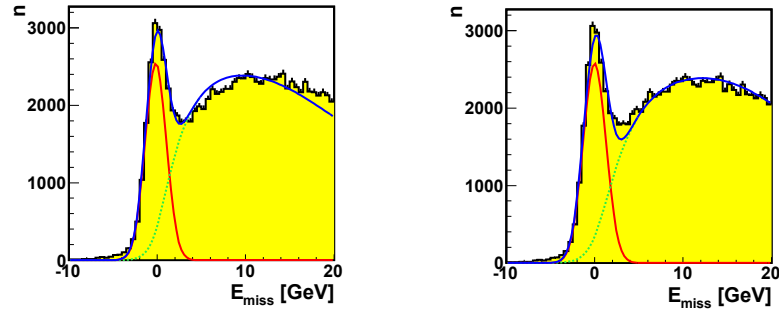


Figure 6.11: Distribution of E_{miss} fitted when the unweighted (left) or weighted (right) Monte Carlo events are used in the parametrisation of the semi-inclusive background. The signal and background contributions are denoted by the red and green lines, respectively, while the sum of both contributions is denoted by the blue line.

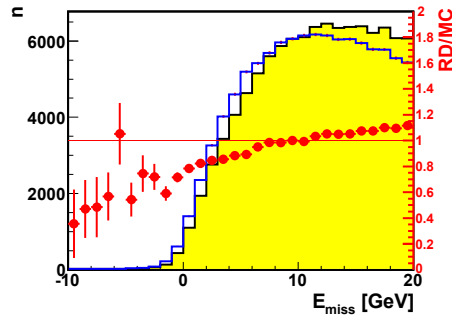


Figure 6.12: Distributions of E_{miss} for the same sign-combination sample for real data (yellow filled histogram) and unweighted Monte Carlo events (blue line histogram). The ratio between these two distributions (red points and right axis) is equivalent to the weights used in the re-weighting procedure.

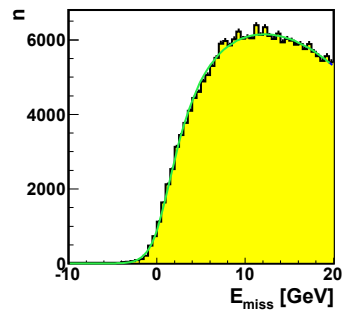


Figure 6.13: Distribution of E_{miss} for the weighted Monte Carlo events parameterised with the fit given by Eq. (6.42).

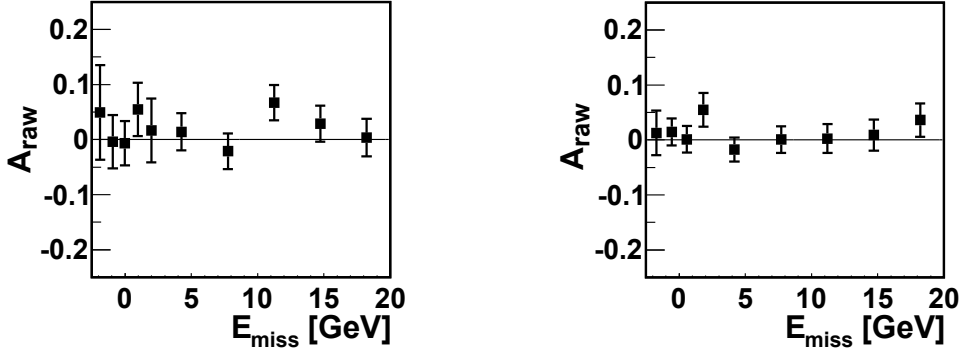


Figure 6.14: Raw $A_{UT}^{\sin(\phi-\phi_S)}$ asymmetry extracted in various ranges of E_{miss} for the deuteron data (left) and for the 2007 proton data (right).

6.3.2 Method A

The method A of background subtraction is compatible with the binned estimators of asymmetries, *i.e.* the double ratio estimator (Sec. 6.2.2) and the 1D and 2D binned maximum likelihood estimators (Secs. 6.2.3 and 6.2.4).

In this method the background subtraction is performed separately for each bin used by a given estimator. For example, for the 1D binned likelihood estimator the subtraction is done separately for each of $2 \times 2 \times N_{\text{bin}}$ bins of ϕ' used there. Let $N_{\text{S+B}} = N_{\text{S}} + N_{\text{B}}$ be a sum of signal, N_{S} , and background, N_{B} , events measured in a given bin. Therefore, $N_{\text{S}} = \alpha_{\text{S}} \cdot N_{\text{S+B}}$, where α_{S} is the signal fraction that corrects the measured number of events. This fraction is estimated from a fit to the E_{miss} distribution that corresponds to the considered bin. The fit is performed as described in Sec. 6.3.1. The signal and background contributions found by this fit allows us to estimate α_{S} ,

$$\alpha_{\text{S}} = \frac{\int_{E_{\text{miss}}^{\text{min}}}^{E_{\text{miss}}^{\text{max}}} f_{\text{S}}(E_{\text{miss}}) dE_{\text{miss}}}{\int_{E_{\text{miss}}^{\text{min}}}^{E_{\text{miss}}^{\text{max}}} f_{\text{S+B}}(E_{\text{miss}}) dE_{\text{miss}}} . \quad (6.43)$$

Here, $E_{\text{miss}}^{\text{min}}$ and $E_{\text{miss}}^{\text{max}}$ indicate the boundaries of the signal window in which the $N_{\text{S+B}}$ number was obtained. For instance, for the ρ^0 analysis these boundaries correspond to Eq. (6.16).

Note, that the assumption that the background asymmetries do not depend on E_{miss} is not used directly here. However, the target polarisation is not simulated in the Monte Carlo analysis, so the E_{miss} shape of background contribution fitted to the real data is the same for both states of the target polarisation. Thus, the background asymmetries are probed only by the change of E_{miss} -independent $p_{\text{B},0}$ parameter, see Eq. (6.42), whose values are obtained in the fits.

6.3.3 Method B

The method B of background subtraction is compatible with the binned estimators of asymmetries, *i.e.* the double ratio estimator (Sec. 6.2.2) and the 1D and 2D binned maximum likelihood estimators (Secs. 6.2.3 and 6.2.4).

Four distributions of events, which are related to the subsamples of data defined either in Eq. (6.23) or in Eq. (6.24), are used by the binned estimators. If the data are contaminated by the semi-inclusive background, a given distribution of events is a superposition of two distributions that account separately for the signal and semi-inclusive events.

In this method the background subtraction is performed separately for each of four measured angular distributions, each of them being decomposed into the distributions for the signal and background events. Here, the assumption that the background asymmetries do not depend on E_{miss} is used directly. The angular distribution for the background events, referred in the following to as the benchmark distribution, is obtained in the pure-background E_{miss} region, $7 \text{ GeV} < E_{\text{miss}} < 20 \text{ GeV}$. The benchmark distribution fixes the shape of a given angular distribution for the semi-inclusive events. To make the subtraction one has to scale this distribution to the number of semi-inclusive events measured in the nominal range of E_{miss} . The scaling factor, β_{B} , is calculated from a fit to the E_{miss} distribution that is obtained as described in Sec. 6.3.1. The signal and background contributions found by this fit are used to estimate β_{B} ,

$$\beta_{\text{B}} = \frac{\int_{E_{\text{miss}}^{\text{min}}}^{E_{\text{miss}}^{\text{max}}} f_{\text{B}}(E_{\text{miss}}) dE_{\text{miss}}}{\int_{7 \text{ GeV}}^{20 \text{ GeV}} f_{\text{B}}(E_{\text{miss}}) dE_{\text{miss}}} . \quad (6.44)$$

In order to correct for the background contribution the benchmark distribution is scaled by the β_{B} factor and then it is subtracted from the distribution measured in the signal range. An advantage of this method is a small number of fits to the E_{miss} distributions. Since the subtraction is obtained separately for each of four distributions, four fits are only needed here. Note, that in the method A of background subtraction, see Sec. 6.3.2, the subtraction is obtained separately for each bin of four distributions, therefore the number of bins determines the number of fits. If the number of bins is large, the fits are done to the not-well populated distributions and they can be unstable.

6.3.4 Method C

The method C of background subtraction is compatible with the unbinned likelihood estimator that is introduced in Sec. 6.2.5. Here, the probability density function defined in Eq. (6.34) is replaced by

$$P_t^p(\phi, \phi_s, E_{\text{miss}}) = \frac{N_{t,\text{S+B}}^p(\phi, \phi_s, E_{\text{miss}})}{N_{t,\text{S+B}}^p} , \quad (6.45)$$

where the angle-dependent number of reconstructed events accounts for both signal and background processes, $N_{t,\text{S}}^p(\phi, \phi_s, E_{\text{miss}})$ and $N_{t,\text{B}}^p(\phi, \phi_s, E_{\text{miss}})$, respectively. Two processes can be distinguished only by a new degree of freedom, which has been chosen to be the missing energy. By expanding

the numerator of Eq. (6.45) one may find that

$$\begin{aligned}
N_{t,S+B}^p(\phi, \phi_s, E_{\text{miss}}) &= N_{t,S}^p(\phi, \phi_s, E_{\text{miss}}) + N_{t,B}^p(\phi, \phi_s, E_{\text{miss}}) = \\
&= c_{t,S}^p(\phi, \phi_s, E_{\text{miss}}) \cdot \left(1 \pm A_{\text{raw},S}^{\sin(\phi-\phi_s)}(E_{\text{miss}}) \sin(\phi - \phi_s) \pm \dots \right) + \\
&+ c_{t,B}^p(\phi, \phi_s, E_{\text{miss}}) \cdot \left(1 \pm A_{\text{raw},B}^{\sin(\phi-\phi_s)}(E_{\text{miss}}) \sin(\phi - \phi_s) \pm \dots \right) = \\
&= c_{t,S+B}^p(\phi, \phi_s, E_{\text{miss}}) \cdot \left(1 \pm \right. \\
&\pm \gamma_{t,S}^p(\phi, \phi_s, E_{\text{miss}}) A_{\text{raw},S}^{\sin(\phi-\phi_s)}(E_{\text{miss}}) \sin(\phi - \phi_s) \pm \\
&\left. \pm \gamma_{t,B}^p(\phi, \phi_s, E_{\text{miss}}) A_{\text{raw},B}^{\sin(\phi-\phi_s)}(E_{\text{miss}}) \sin(\phi - \phi_s) \pm \dots \right). \quad (6.46)
\end{aligned}$$

The product of beam flux, number of target nucleons, acceptances and unpolarised cross sections for signal and background processes reads

$$\begin{aligned}
c_{t,S+B}^p(\phi, \phi_s, E_{\text{miss}}) &= c_{t,S}^p(\phi, \phi_s, E_{\text{miss}}) + c_{t,B}^p(\phi, \phi_s, E_{\text{miss}}) = \\
&= F \cdot n \cdot (\sigma_{0,S} \cdot a_S(\phi, \phi_s, E_{\text{miss}}) + \sigma_{0,B} \cdot a_B(\phi, \phi_s, E_{\text{miss}})). \quad (6.47)
\end{aligned}$$

Similarly to the estimator described in Sec. 6.2.5, it is assumed that $c_{t,S+B}^p(\phi, \phi_s)$ obeys the reasonable assumption,

$$\frac{c_{U+D,S+B}^\uparrow(\phi, \phi_s, E_{\text{miss}})}{c_{C,S+B}^\downarrow(\phi, \phi_s, E_{\text{miss}})} = \frac{c_{U+D,S+B}^\downarrow(\phi, \phi_s, E_{\text{miss}})}{c_{C,S+B}^\uparrow(\phi, \phi_s, E_{\text{miss}})}. \quad (6.48)$$

The weights,

$$\begin{aligned}
\gamma_{t,S}^p(\phi, \phi_s, E_{\text{miss}}) &= \frac{c_{t,S}^p(\phi, \phi_s, E_{\text{miss}})}{c_{t,S+B}^p(\phi, \phi_s, E_{\text{miss}})} = \\
&= \frac{\sigma_{0,S} \cdot a_S(\phi, \phi_s, E_{\text{miss}})}{\sigma_{0,S} \cdot a_S(\phi, \phi_s, E_{\text{miss}}) + \sigma_{0,B} \cdot a_B(\phi, \phi_s, E_{\text{miss}})} \quad (6.49)
\end{aligned}$$

and

$$\begin{aligned}
\gamma_{t,B}^p(\phi, \phi_s, E_{\text{miss}}) &= \frac{c_{t,B}^p(\phi, \phi_s, E_{\text{miss}})}{c_{t,S+B}^p(\phi, \phi_s, E_{\text{miss}})} = \\
&= \frac{\sigma_{0,B} \cdot a_B(\phi, \phi_s, E_{\text{miss}})}{\sigma_{0,S} \cdot a_S(\phi, \phi_s, E_{\text{miss}}) + \sigma_{0,B} \cdot a_B(\phi, \phi_s, E_{\text{miss}})}, \quad (6.50)
\end{aligned}$$

describe the probability that a given event is the signal or background event, respectively. The number of reconstructed events in a given subsample of data that is used in the denominator of Eq. (6.45) reads

$$N_{t,S+B}^p = \iiint N_{t,S+B}^p(\phi, \phi_s, E_{\text{miss}}) d\phi d\phi_s dE_{\text{miss}}. \quad (6.51)$$

To perform the extraction of asymmetries two simplifications of Eq. (6.46) are made. In the first simplification it is assumed that both signal and background asymmetries do not depend on E_{miss} , $A_{\text{raw},B}^{\sin(\phi-\phi_s)} \equiv A_{\text{raw},B}^{\sin(\phi-\phi_s)}(E_{\text{miss}})$ and $A_{\text{raw},B}^{\sin(\phi-\phi_s)} \equiv A_{\text{raw},B}^{\sin(\phi-\phi_s)}(E_{\text{miss}})$. This assumption is well justified for the signal asymmetries, however for the background asymmetries the assumption has to be examined, see Sec. 6.3.1.

In the second simplification it is assumed that the weights do not depend on azimuthal angles, $\gamma_{t,S}^p(\phi, \phi_s, E_{\text{miss}}) \equiv \gamma_{t,S}^p(E_{\text{miss}})$ and $\gamma_{t,B}^p(\phi, \phi_s, E_{\text{miss}}) \equiv \gamma_{t,B}^p(E_{\text{miss}})$. By examining Eq. (6.49) or Eq. (6.50) one may find the equivalent assumption: the ratio of acceptances for signal and background processes does not depend on azimuthal angles, $a_S(\phi, \phi_s, E_{\text{miss}})/a_B(\phi, \phi_s, E_{\text{miss}}) \equiv a_S(E_{\text{miss}})/a_B(E_{\text{miss}})$. This assumption has been confirmed in Monte Carlo studies where the acceptances for events produced with HEPGEN and LEPTO generators were compared in the signal range of E_{miss} , however with a limited statistics. In such the case, a violation of this assumption may lead only to a small systematic effect, as an eventual angular dependence of the acceptance ratio may not couple to the angular modulations and its magnitude has a limited impact on the extraction of the asymmetries.

To find the weights the E_{miss} distributions that correspond to four subsamples of data used by the estimator are fitted as described in Sec. 6.3.1. For a given subsample of data, which is defined for a specific cell (t) and spin direction of target (p), the signal and background contributions distinguished by the fit are used to estimate the weights,

$$\gamma_{t,S}^p(E_{\text{miss}}) = 1 - \gamma_{t,B}^p(E_{\text{miss}}) = \frac{f_{t,S}^p(E_{\text{miss}})}{f_{t,S+B}^p(E_{\text{miss}})}. \quad (6.52)$$

The extraction of asymmetries is done in a similar way as described in Sec. 6.2.5. However, the number of unknowns increases here to $4 + 2 \times N_a$ that accounts for four acceptance products $c_{t,S+B}^p(\phi, \phi_s, E_{\text{miss}})$ and $2 \times N_a$ asymmetries. With the reasonable assumption the number of unknowns is reduced to $3 + 2 \times N_a$.

6.4 Studies of systematic uncertainties

In order to estimate the systematic uncertainties of this measurement the following possible sources were examined:

- false asymmetries
- background subtraction
- estimator of the asymmetries
- compatibility with alternative estimator
- compatibility between subsamples of the data
- compatibility of mean asymmetries for Q^2 , x_{Bj} and p_T^2 bins
- dilution factor, beam and target polarisations

The investigation of each source is given in the following sections, while the summary of systematic studies is given in Sec. 6.4.6.

6.4.1 False asymmetries

As described in Chapter 6.2 the asymmetries are extracted from four independent subsamples of data, where a given subsample is defined for a specific target cell and target spin direction. In a combination with the reasonable assumption such division of data leads to a cancellation of the acceptance and other factors. Here, it is checked if the reasonable assumption holds, *i.e.* whether during the data taking the acceptance has been changed or not in a way that influences the extraction of the asymmetries.

The issue is investigated by comparing the asymmetries extracted from two independent configurations of target cells denoted by c_1^{false} and c_2^{false} . For this test a part of target cells is artificially divided as explained in Fig. 6.15.

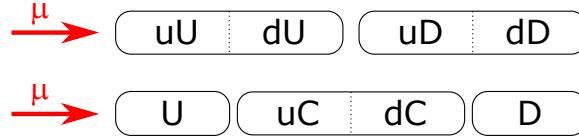


Figure 6.15: The naming of target cells for two-cell (up) and three-cell (bottom) target.

For the two-cell target the c_1^{false} configuration combines the upstream (uU) and downstream (dU) halves of the upstream cell, while for the three-cell target it combines the upstream (U) and downstream (D) cells. Similarly, for the two-cell target the c_2^{false} configuration combines the upstream (uD) and downstream (dD) halves of the downstream cell, while for the three-cell target it combines the upstream (uC) and downstream (dC) halves of the central cell.

Taking into account that the spin direction in all target cells was being reversed periodically each configuration defines four subsamples of data that are used for the extraction of the $A_{\text{raw}}^{\text{mod},c}$ asymmetries, cf. Eqs. (6.23) and (6.24). For the two-cell target these subsamples are

$$\begin{aligned} N_{\text{uU}}^{\uparrow}(\phi, \phi_S), N_{\text{dU}}^{\uparrow}(\phi, \phi_S), N_{\text{uU}}^{\downarrow}(\phi, \phi_S), N_{\text{dU}}^{\downarrow}(\phi, \phi_S) & \text{ for } c_1^{\text{false}}, \\ N_{\text{uD}}^{\uparrow}(\phi, \phi_S), N_{\text{dD}}^{\uparrow}(\phi, \phi_S), N_{\text{uC}}^{\downarrow}(\phi, \phi_S), N_{\text{dC}}^{\downarrow}(\phi, \phi_S) & \text{ for } c_2^{\text{false}}, \end{aligned}$$

while for the three-cell target these are

$$\begin{aligned} N_U^\uparrow(\phi, \phi_S), N_D^\uparrow(\phi, \phi_S), N_U^\downarrow(\phi, \phi_S), N_D^\downarrow(\phi, \phi_S) & \text{ for } c_1^{\text{false}}, \\ N_{uC}^\uparrow(\phi, \phi_S), N_{dC}^\uparrow(\phi, \phi_S), N_{uD}^\downarrow(\phi, \phi_S), N_{dC}^\downarrow(\phi, \phi_S) & \text{ for } c_2^{\text{false}}, \end{aligned}$$

where *e.g.* $N_{uU}^\uparrow(\phi, \phi_S)$ denotes the number of events reconstructed in the upstream half of the upstream target cell with the up direction of the target spin.

The c_1^{false} and c_2^{false} configurations combine the cells with the same sign of target polarisation. Therefore, the extraction does not depend on the target polarisation and all extracted values of asymmetries are expected to be compatible with zero. The asymmetries that do not vanish are considered as false ones.

To increase the statistical sensitivity of this test the $A_{\text{raw}}^{\text{mod},c}$ asymmetries are extracted from the data selected in the extended range of E_{miss} , $-2.5 \text{ GeV} < E_{\text{miss}} < 20 \text{ GeV}$. In order to avoid a bias related to the semi-inclusive background subtraction the asymmetries are extracted without this correction. Since the dilution factor is not well defined for a mixture of signal and background events this test is done for the raw asymmetries defined in Eq. (6.21).

For a given asymmetry the systematic uncertainty is estimated from the $\Delta_+/\sigma_{\text{stat}}$ and $\Delta_-/\sigma_{\text{stat}}$ quantities, which are defined as

$$\frac{\Delta_\pm}{\sigma_{\text{stat}}} = \frac{\sum_{i=1}^{N_{\text{bin}}} \left| A_{\text{raw},i}^{\text{mod},c_1^{\text{false}}} \pm A_{\text{raw},i}^{\text{mod},c_2^{\text{false}}} \right| \frac{1}{\sigma_i^2}}{\sum_{i=1}^{N_{\text{bin}}} \frac{1}{\sigma_i^2}}, \quad (6.53)$$

where

$$\sigma_i = \sqrt{\left(\sigma_{\text{raw},i}^{\text{mod},c_1^{\text{false}}} \right)^2 + \left(\sigma_{\text{raw},i}^{\text{mod},c_2^{\text{false}}} \right)^2}. \quad (6.54)$$

The sums in Eq. (6.53) run over all kinematic bins of Q^2 , x_{Bj} and p_T^2 that are used in the extraction, where $N_{\text{bin}} = 4 + 4 + 4 = 12$ for the deuteron data and $N_{\text{bin}} = 4 + 4 + 5 = 13$ for the proton data, see Table 6.1. For a given kinematic bin and the configuration $c = c_1^{\text{false}}, c_2^{\text{false}}$ the value of extracted asymmetry is denoted by $A_{\text{raw},i}^{\text{mod},c}$, while the corresponding statistical uncertainty is denoted by $\sigma_{\text{raw},i}^{\text{mod},c}$.

The $\Delta_\pm/\sigma_{\text{stat}}$ quantities denote the mean sum (+) and difference (−) of the asymmetries normalised by the mean statistical uncertainty of both extractions. In the absence of the systematic bias all $A_{\text{raw},i}^{\text{mod},c}$ values are expected to be compatible with zero and by following the Gaussian statistics both $\Delta_\pm/\sigma_{\text{stat}}$ quantities should be equal to 0.80. Any value greater than 0.80 would indicate the systematic bias that is estimated as

$$\frac{\sigma_{\text{sys}}}{\sigma_{\text{stat}}} = \sqrt{\left(\frac{\Delta_\pm}{\sigma_{\text{stat}}} \right)^2 - 0.80^2}. \quad (6.55)$$

The estimate returns the systematic uncertainty that is expressed with respect to the statistical uncertainty. This ratio allows us to estimate the systematic uncertainty of the final asymmetries extracted in the nominal range of E_{miss} and with the semi-inclusive background subtraction. For a given target and each asymmetry both $\Delta_+/\sigma_{\text{stat}}$ and $\Delta_-/\sigma_{\text{stat}}$ quantities are examined, while the greater value is used to assign the systematic uncertainty.

In the results on the azimuthal asymmetries published by the COMPASS collaboration in Refs. [23] and [24] the wrong expected value on the $\Delta_\pm/\sigma_{\text{stat}}$ quantities was used, 0.68 instead of 0.80.

Therefore, for the published results a part of systematic uncertainties is overestimated, up to 20% of the statistical uncertainty. The final results given in Sec. 6.5 are those published ones with the overestimated systematic uncertainties. These uncertainties for all asymmetries and for both proton and deuteron data are given in Table 6.4.

6.4.2 Estimator of the asymmetries

The systematic uncertainty related to the choice of estimator is examined by comparing the results of two extractions performed with the nominal and unbinned likelihood estimators. For the deuteron data the nominal estimator is the 1D binned likelihood estimator, while for the proton data it is the 2D binned likelihood estimator. The 1D, 2D and unbinned likelihood estimators are described in Sec. 6.2.

The subtraction of the semi-inclusive background differs significantly for the binned and unbinned estimators, see Sec. 6.3. Since this difference can introduce a bias this test is done by using the uncorrected data for the semi-inclusive background. Moreover, since the dilution factor is not well defined for a mixture of signal and background events this test is done for the raw asymmetries defined see Eq. (6.21).

For a given target and each asymmetry the systematic uncertainty is estimated from a pull-like distribution. A single entry to this distribution, p_i^{mod} , is the difference of asymmetries that is normalised by the mean statistical uncertainty,

$$p_i^{\text{mod}} = \frac{A_{\text{raw},i}^{\text{mod,nom}} - A_{\text{raw},i}^{\text{mod,UN}}}{\sigma_i}, \quad (6.56)$$

where

$$\sigma_i = \frac{\sigma_{\text{raw},i}^{\text{mod,nom}} + \sigma_{\text{raw},i}^{\text{mod,UN}}}{2}. \quad (6.57)$$

Here, $\text{mod} = \sin(\phi - \phi_S)$, $\sin(\phi + \phi_S)$, ... denotes the asymmetry modulation and i refers to a given bin of Q^2 , x_{Bj} or p_T^2 variable, see Table 6.1. The extraction of each asymmetry with the nominal and unbinned maximum likelihood estimators gives $A_{\text{raw},i}^{\text{mod,nom}}$ and $A_{\text{raw},i}^{\text{mod,UN}}$, respectively. The statistical uncertainties of both extractions are approximately the same, $\sigma_{\text{raw},i}^{\text{mod,nom}} \simeq \sigma_{\text{raw},i}^{\text{mod,UN}}$.

If both estimators would give exactly the same results, then $p_i^{\text{mod}} = 0$ for all kinematic bins. On the contrary, in a case of discrepancy $p_i^{\text{mod}} \neq 0$, which would indicate the systematic bias. Therefore the values of mean, m_p , or/and root mean square, rms_p , of the corresponding pull-like distribution would be also different from zero. Since a single entry to this distribution is expressed in terms of the statistical uncertainty, see Eq. (6.56), the estimation of systematic uncertainty reads

$$\frac{\sigma_{\text{sys}}}{\sigma_{\text{stat}}} = \sqrt{m_p^2 + \text{rms}_p^2}. \quad (6.58)$$

An example of pull-like distribution is shown in Fig. 6.16. The systematic uncertainties related to the choice of the estimator are given in Table 6.4 for all asymmetries and for both proton and deuteron data.

6.4.3 Background subtraction

The physics asymmetries are extracted from the data by applying a correction for the semi-inclusive background. To make this correction the method A of background subtraction is used for the deuteron data, while the method B is used for the proton data. Both methods of background subtraction are described in Sec. 6.3.

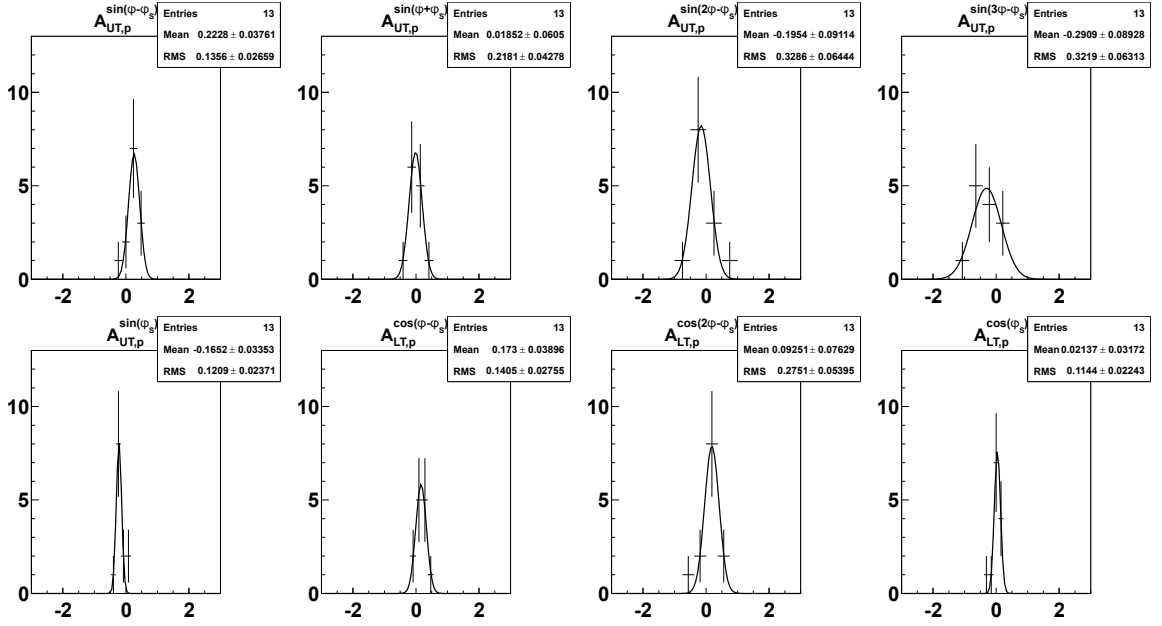


Figure 6.16: Pull distributions, see Eq. (6.56), used in order to check compatibility between the raw asymmetries extracted with 2D and unbinned estimators.

The estimate of systematic uncertainties related to the semi-inclusive background subtraction relies on three tests. In the first one the final asymmetries are compared with those extracted with the alternative method of the background subtraction, *i.e.* the method B for the deuteron data and the method A for the proton data. The test demonstrates a very good agreement between both methods of subtraction. The difference between extracted values does not exceed $0.1 \sigma_{stat}$ and therefore the systematic uncertainty is not assigned here.

Both methods of subtraction depend on the evaluation of the semi-inclusive background contribution, see Sec. 6.3.1. For a given subsample of data this contribution is estimated from a fit to the corresponding E_{miss} distribution. In this fit the shape of semi-inclusive background is fixed by the Monte Carlo sample produced with the LEPTO generator. In order to test the sensitivity on the choice of Monte Carlo generator in the second test the final asymmetries are compared with those extracted with the alternative Monte Carlo sample that was produced with the PYTHIA generator.

The comparison of asymmetries extracted with both the Monte Carlo samples demonstrates a low sensitivity on the chosen generator. It is not unexpected, since in this analysis the Monte Carlo sample is used only to estimate the fraction of semi-inclusive background and it does not introduce any azimuthal asymmetry that could influence the extraction of physics asymmetries. The systematic uncertainty related to the choice of Monte Carlo generator has been assigned only for the deuteron data in the first publication [23], where $\sigma_{sys} = 0.04 \sigma_{stat}$. For the proton data this uncertainty has been found to be negligible for all azimuthal asymmetries and it has been not assigned neither in Ref. [23] nor in Ref. [24].

The fraction of semi-inclusive background is different in each kinematic bin, *e.g.* it varies between $\approx 15\%$ and $\approx 33\%$ as a function of Q^2 . In the third test, for a given target and each azimuthal asymmetry the mean asymmetry for each kinematic variable is calculated. If the background subtraction had not introduced any bias, these mean asymmetries should be the same. In other case the half of maximal difference between mean asymmetries expressed in terms of statistical uncertainty

is taken as the estimation of systematic uncertainty.

The estimated values of systematic uncertainties related to the background subtraction are summarised in Table 6.4 for all asymmetries and for both proton and deuteron data.

6.4.4 Compatibility between subsamples of the data

In order to test the stability over the whole data taking period the asymmetries were extracted from the independent subsamples of data. A given subsample consists of two consecutive periods or subperiods of data taken with the opposite target polarisation, see Table 6.2. It gives three subsamples for the deuteron data and eighteen subsamples for the proton data. For the stable data taking the asymmetries extracted from the subsamples should be compatible with those extracted from the whole sample.

Since only the stability of data taking is examined in this test the subtraction of the semi-inclusive background is not used here. Moreover, since the dilution factor is not well defined for a mixture of signal and background events this test is done for the raw asymmetries defined in Eq. (6.21).

To test the compatibility between the subsamples of data for a given target and each asymmetry the corresponding pull distribution is examined. A single entry to this distribution, $p_{i,j}^{\text{mod}}$, reads

$$p_{i,j}^{\text{mod}} = \frac{A_{\text{raw},i}^{\text{mod}} - A_{\text{raw},i,j}^{\text{mod}}}{\sigma_{i,j}}, \quad (6.59)$$

where

$$\sigma_{i,j} = \sqrt{(\sigma_{\text{raw},i,j}^{\text{mod}})^2 - (\sigma_{\text{raw},i}^{\text{mod}})^2}. \quad (6.60)$$

Here, $\text{mod} = \sin(\phi - \phi_S)$, $\sin(\phi + \phi_S)$, ... denotes the asymmetry modulation, i refers to a given bin of Q^2 , x_{Bj} or p_T^2 , see Table 6.1, and j denotes a given subsample. The extraction of a single asymmetry in each subsample and kinematic bin gives $A_{\text{raw},i,j}^{\text{mod}}$ and $\sigma_{\text{raw},i,j}^{\text{mod}}$, while the extraction performed for all data in the same kinematic bin gives $A_{\text{raw},i}^{\text{mod}}$ and $\sigma_{\text{raw},i}^{\text{mod}}$.

To estimate the systematic uncertainty the mean and root mean square values of each pull distribution are examined. If the data taking were stable these values should be compatible with zero and one, respectively. Example pull distributions are shown in Fig. 6.17. For both targets and all asymmetries the pull distributions agree with the expectations for no systematic difference between the subsamples of data. Therefore, the systematic uncertainty is not assigned here.

6.4.5 Dilution factor, beam and target polarisations

The muon beam polarisation depends on the ratio between momenta of initial pions and decay muons, see Sec. 3.2. The relative uncertainty on the polarisation value for 160 GeV μ^+ beam that originates from 174 GeV π^+ beam is 5%. This uncertainty accounts mainly for the momentum spread of both muon and pion beams that is estimated by the Monte Carlo model of the beam line [104]. The estimate of the beam polarisation has been confirmed by direct measurements performed by the SMC collaboration [105].

The relative uncertainty of the target polarisation is 5% for the transversely polarised deuteron target and 3% for the transversely polarised proton target. The estimates take into account uncertainties of the measurements with the NMR coils done before and after the transverse polarisation mode but also the uncertainty of the extrapolation between the direct measurements, see Sec. 3.3.

The relative uncertainty of the dilution factor is 2%. The estimate takes into account the uncertainties related to the determination of the relative contribution of different elements to the target material, but also the uncertainties related to the parametrisation of the nuclear shadowing effect [23].

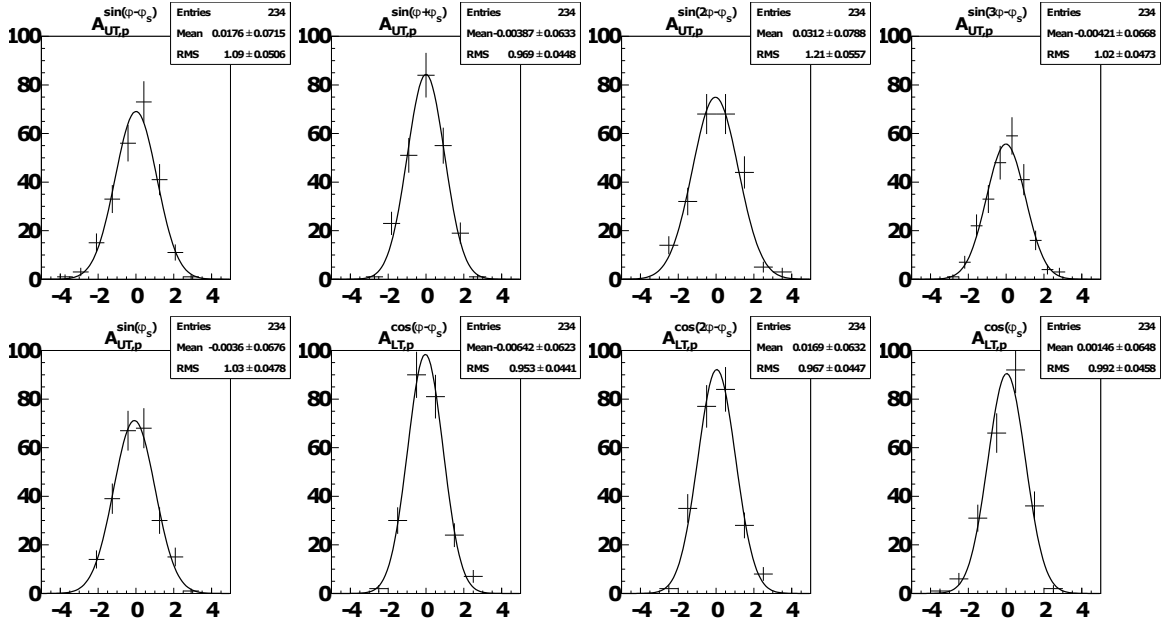


Figure 6.17: Pull distributions, see Eq. (6.59), used in order to check compatibility between the raw asymmetries extracted from different periods of 2010 data taking.

The asymmetries are proportional to the target polarisation and the dilution factor, see Eq. (6.21). The double spin asymmetries are also proportional to the beam polarisation. Therefore, the scale normalisation systematic uncertainty for the deuteron target is $0.054 \cdot A_{UT}^{\sin(\phi-\phi_S)}$. For the proton target it is $0.036 \cdot A_{UT}^{\text{mod}}$ for the single spin asymmetries and $0.062 \cdot A_{LT}^{\text{mod}}$ for the double spin asymmetries, where $\text{mod} = \sin(\phi - \phi_S), \sin(\phi + \phi_S), \dots$

6.4.6 Summary of systematic studies

The systematic uncertainties for all asymmetries are summarised in Table 6.4.

Table 6.4: Summary of systematic uncertainties for the measurement of azimuthal asymmetries in the ρ^0 analysis.

asymmetry target	$A_{UT}^{\sin(\phi-\phi_S)}$	$A_{UT}^{\sin(\phi-\phi_S)}$	$A_{UT}^{\sin(\phi+\phi_S)}$	$A_{UT}^{\sin(2\phi-\phi_S)}$	$A_{UT}^{\sin(3\phi-\phi_S)}$	$A_{UT}^{\sin\phi_S}$	$A_{LT}^{\cos(\phi-\phi_S)}$	$A_{LT}^{\cos(2\phi-\phi_S)}$	$A_{LT}^{\cos\phi_S}$
	d	p	p	p	p	p	p	p	p
false asymmetries Sec. 6.4.1	0.014	0.002	0.004	0.001	0.003	0.003	0.011	0.016	0.029
background subtraction Sec. 6.4.3	0.001	0.000	0.000	0.000	0.000	0.000	0.000	0.000	0.000
Estimator Sec. 6.4.2	0.003	0.002	0.004	0.002	0.006	0.001	0.005	0.016	0.006
compatibility between extractions from integrated sample and kinematic bins Sec. 6.4.3	0.002	0.001	0.004	0.002	0.003	0.000	0.023	0.018	0.023
$f, P_{\text{target}}, P_{\text{beam}}$ (together) Sec. 6.4.5	0.001	0.000	0.001	0.000	0.001	0.001	0.004	0.004	0.006
TOTAL σ_{sys} ($\sigma_{\text{sys}}/\sigma_{\text{stat}}$)	0.015 0.51	0.003 0.24	0.006 0.29	0.003 0.34	0.008 0.31	0.003 0.39	0.026 0.55	0.029 0.41	0.038 0.58

6.5 Results

The $A_{UT}^{\sin(\phi-\phi_S)}$ asymmetry measured for deuterons in the bins of Q^2 , x_{Bj} and p_T^2 is shown in Fig. 6.18. The numerical results of this measurement are given in Appendix A in Table A.1. In addition, the result of measurement obtained without the division of data into bins is given in Table 6.5.

The asymmetries measured on protons in the bins of Q^2 , x_{Bj} and p_T^2 variable are shown in Figs. 6.19 and 6.20, for the single spin and double spin asymmetries, respectively. The numerical results of this measurement are given in Appendix A in Table A.2. The results of measurement without the division of data into bins are shown in Fig. 6.21 and they are given in Table 6.5.

In Figs. 6.18, 6.19 and 6.20 the predictions of GPD-based model given by Goloskokov and Kroll [36, 37, 106] are compared with the experimental points. The predictions are calculated for the average W , Q^2 and p_T^2 of the COMPASS data. For the both protons and deuterons the predictions are given at $W=8.1$ GeV/ c^2 and $p_T^2=0.2$ (GeV/ c) 2 for the x_{Bj} and Q^2 dependences and at $W=8.1$ GeV/ c^2 and $Q^2=2.2$ (GeV/ c) 2 for the p_T^2 dependences.

For both targets and all asymmetries the experiment does not see any significant dependence of measured values on Q^2 , x_{Bj} and p_T^2 . All asymmetries are compatible with zero except $A_{UT}^{\sin\phi_S} = -0.019 \pm 0.008 \pm 0.003$ measured on protons.

The results for both targets are compatible with predictions of the GPD-based model proposed by Goloskokov and Kroll. The small values of the $A_{UT}^{\sin(\phi-\phi_S)}$ asymmetry for the ρ^0 meson are interpreted as an approximate cancellation of contributions from the GPDs $E^{u_{val}}$ and $E^{d_{val}}$ for valence quarks due to their different signs but similar magnitude. This observation agrees with lattice QCD calculations [10], which predict similar magnitude but opposite sign of the orbital angular momentum for valence up and down quarks. The gluon and sea quarks GPDs, E^g and $E^{g_{sea}}$, have a very small effect on the predicted values of the $A_{UT}^{\sin(\phi-\phi_S)}$ asymmetry. The comparison of measured values of $A_{UT}^{\sin\phi_S}$ (negative) and $A_{UT}^{\sin(2\phi-\phi_S)}$ (vanishing) asymmetries on protons implies a non-negligible contribution of the GPDs H_T that are related to the transversity distributions, cf. Eq. (2.20). It is the first experimental evidence from hard exclusive ρ^0 meson production for the observation of these parton helicity flip GPDs.

The $A_{UT}^{\sin(\phi-\phi_S)}$ asymmetry measured on protons by the HEREMS experiment [22] is compatible with this measurement, while the latter is more precise by a factor of about three and cover a wider kinematic range. The results for the deuteron target are obtained for the first time.

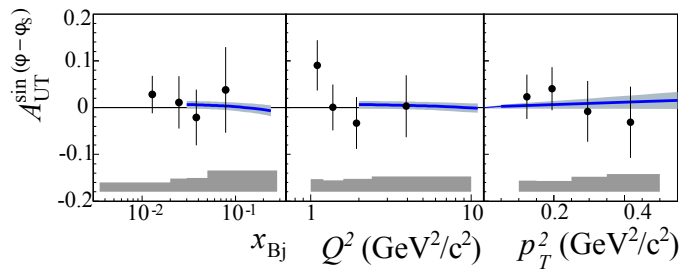


Figure 6.18: Single spin azimuthal asymmetry $A_{UT}^{\sin(\phi-\phi_S)}$ for exclusive ρ^0 meson production on transversely polarised deuterons. The error bars (bands) represent the statistical (systematic) uncertainties. The curves show the predictions of the GPD-based model [36] (see the text for more details).

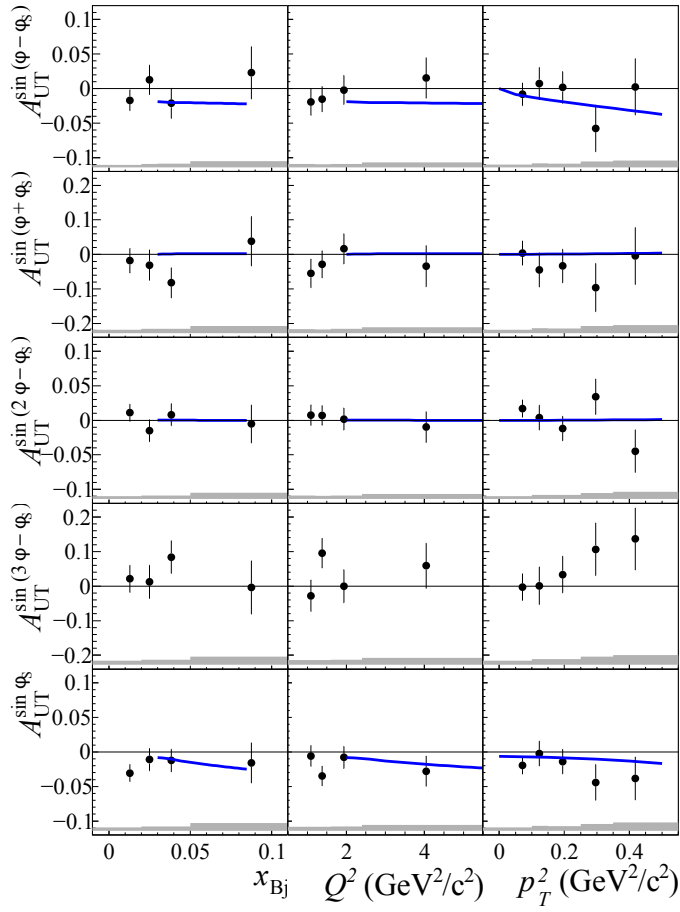


Figure 6.19: Single spin azimuthal asymmetries for exclusive ρ^0 meson production on transversely polarised protons. The error bars (bands) represent the statistical (systematic) uncertainties. The curves show the predictions of the GPD-based model [37, 106], where the $A_{UT}^{\sin(3\phi-\phi_S)}$ asymmetry is assumed to be zero in this model (see the text for more details).

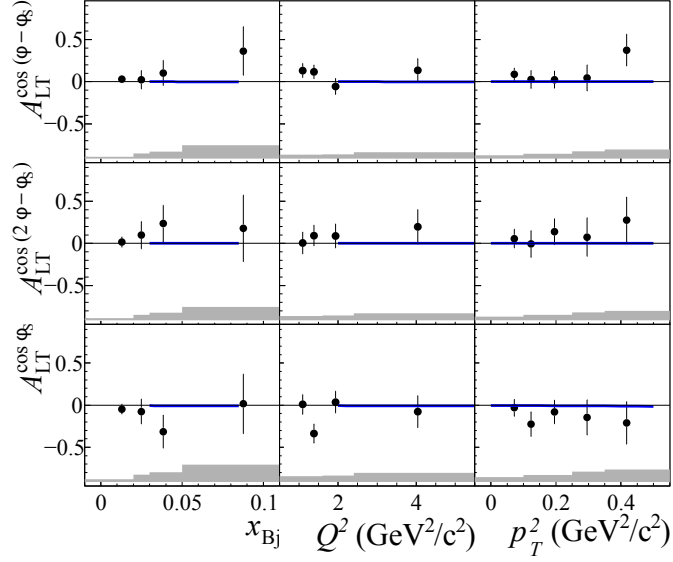


Figure 6.20: Double spin azimuthal asymmetries for exclusive ρ^0 meson production on transversely polarised protons. The error bars (bands) represent the statistical (systematic) uncertainties. The curves show the predictions of the GPD-based model [37, 106] (see the text for more details).

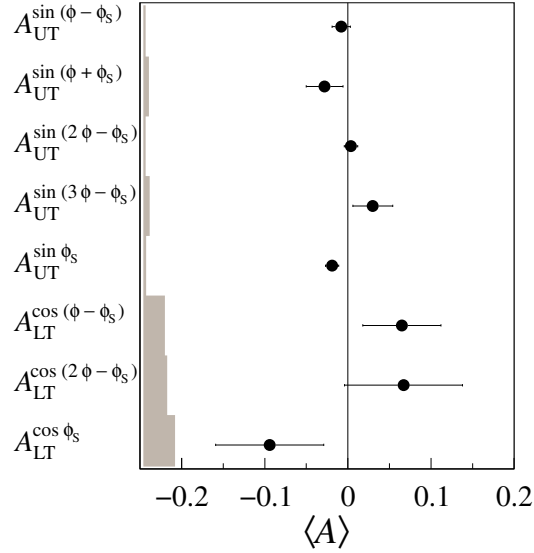


Figure 6.21: The azimuthal asymmetries for exclusive ρ^0 meson production on transversely polarised protons without division of data into bins. The error bars (left bands) represent the statistical (systematic) uncertainties. For the mean values of kinematic variables see Table 6.5.

Table 6.5: The azimuthal asymmetries for exclusive ρ^0 meson production on transversely polarised deuterons and protons without division of data into bins.

target	asymmetry	$\langle Q^2 \rangle$ [[GeV/c] ²]	$\langle x_{Bj} \rangle$	$\langle p_T^2 \rangle$ [[GeV/c] ²]	$A \pm \sigma_{stat} \pm \sigma_{sys}$
d	$A_{UT}^{\sin(\phi-\phi_S)}$	2.0	0.032	0.23	$0.015 \pm 0.028 \pm 0.015$
	$A_{UT}^{\sin(\phi-\phi_S)}$				$-0.008 \pm 0.011 \pm 0.003$
	$A_{UT}^{\sin(\phi+\phi_S)}$				$-0.028 \pm 0.022 \pm 0.006$
	$A_{UT}^{\sin(2\phi-\phi_S)}$				$0.004 \pm 0.008 \pm 0.003$
p	$A_{UT}^{\sin(3\phi-\phi_S)}$	2.2	0.039	0.18	$0.030 \pm 0.024 \pm 0.008$
	$A_{UT}^{\sin\phi_S}$				$-0.019 \pm 0.008 \pm 0.003$
	$A_{LT}^{\cos(\phi-\phi_S)}$				$0.065 \pm 0.047 \pm 0.026$
	$A_{LT}^{\cos(2\phi-\phi_S)}$				$0.067 \pm 0.071 \pm 0.029$
	$A_{LT}^{\cos\phi_S}$				$-0.094 \pm 0.065 \pm 0.038$

Transverse target spin asymmetries in exclusive ω meson production

The measurement of azimuthal asymmetries for exclusive ω meson production on the transversely polarised proton target is described in this chapter. The observed process is

$$\mu N \rightarrow \mu N \omega , \quad (7.1)$$

where

$$\omega \rightarrow \pi^+ + \pi^- + \pi^0 , \pi^0 \rightarrow \gamma\gamma . \quad (7.2)$$

The sample of data used in this measurement is defined by cuts and selections described in Sec. 7.1. Note, that the selection of events is mostly the same as described for the ρ^0 analysis in Sec. 6.1. The main difference is related to the electromagnetic calorimetry that has to be used for the reconstruction of decay photons. The estimation of systematic effects is discussed in Sec. 7.2, while the final results are given in Sec. 7.3.

The results of this measurement have been released by the COMPASS experiment at the beginning of 2015 and they are going to be published [39]. In this measurement the values of the azimuthal asymmetries are extracted from the data by using the unbinned maximum likelihood estimator, see Sec. 6.2.5, where the asymmetries for the signal and background processes are fitted simultaneously, see Sec. 6.3.4.

The azimuthal asymmetries are measured in one-dimensional bins of Q^2 , x_{Bj} and p_T^2 . These bins are defined in Table 7.1. The results on the azimuthal asymmetries without the division in bins are also given.

Table 7.1: The kinematic bins used in the ω analysis.

Q^2 bin [(GeV/c) ²]	x_{Bj} bin	p_T^2 bin [(GeV/c) ²]
$1.0 \leq Q^2 < 1.8$	$0.003 \leq x_{Bj} < 0.04$	$0.05 \leq p_T^2 < 0.15$
$1.8 \leq Q^2 < 10.0$	$0.04 \leq x_{Bj} < 0.30$	$0.15 \leq p_T^2 < 0.50$

7.1 Event selection

The data used for this measurement were taken in 2010 with the 160 GeV μ^+ beam and the transversely polarised ammonia target. These data are grouped into twelve periods, where each of them consists of two or three subperiods taken with the opposite target polarisation. The subperiods are listed in Table 7.2 together with the numbers of events left after all cuts and selections described in this chapter.

The deuteron data taken by the experiment in 2003-2004 are not used in this measurement. The statistics of the exclusive ω events is very limited in those data, mainly because only one electromagnetic calorimeter was available at that time. The proton data taken in 2007 are also not used in this measurement. In the reconstruction of 2007 data a preliminary calibration of the electromagnetic calorimeters has been used that may bias the extraction of the azimuthal asymmetries.

Table 7.2: The list of periods used in the ω analysis together with the corresponding numbers of selected events after all cuts, N_{select} . The entries are grouped according to the polarisation signs obtained in the target cells, where *e.g.* (+ - +) denotes the positive polarisation (spin up) in the both upstream and downstream cells and the negative polarisation (spin down) in the central cell. The N_{select} numbers correspond to $-3 \text{ GeV} < E_{\text{miss}} < 3 \text{ GeV}$ region, see Eq. (7.11), and account for both signal and semi-inclusive background events. The latter ones contribute in this region of E_{miss} with an estimated fraction of 34%.

year/target	period (+ - +)	N_{select}	period (- + -)	N_{select}	
2010/p	W23b	477	W23a	495	
	W24a	567	W24b	564	
	W26b	470	W26a	446	
	W27a	442	W27b	542	
	W29a	535	W29b	559	
	W31b	769	W31a	767	
	W33a	888	W33b	703	
	W35b	865	W35a	980	
	W37a	943	W37b	980	
	W39b	1621	W39a/c	1100	
	W42b	988	W42a	884	
	W44a	998	W44b	983	
	SUM		9563		9003

7.1.1 Data quality

In this measurement only events that pass COMPASS quality checks are used, see Sec. 6.1.1. However, these checks do not include the stability of the electromagnetic calorimeters, as they are not routinely used in the measurements performed by the collaboration from the data taken with the muon beam.

To examine the stability of a given electromagnetic calorimeter in a specific run, the average number of clusters per event is compared with the corresponding numbers measured in the preceding and following runs. A large deviation with respect to the neighboring runs is interpreted as the instability. The procedure is done separately for the clusters associated with the charged particles and for those that are not associated to any charged particle.

7.1.2 Primary vertex

The selection of primary vertices and charged particles, *i.e.* incoming and scattered muons and two pions of opposite charges, is the same as in the case of ρ^0 analysis, see Sec. 6.1.2. The only difference is related to a different reconstruction of the beam momentum, as in this analysis the so-called new beam reconstruction has been used, see Sec. 4. For this reconstruction the cut defined in Eq. (6.3) has been replaced with

$$\text{Prob}(\chi_{s+t}^2, \text{ndf}) > 0.01 . \quad (7.3)$$

The reconstructed positions of selected primary vertices are shown in Fig. 7.1. This figure clearly demonstrates the separation between three target cells. Note the difference between this figure and that for the ρ^0 case shown in Fig. 6.1. This difference is caused mainly by a different acceptance for the ω decay and by the absorption of photons that are coming from the π^0 decay.

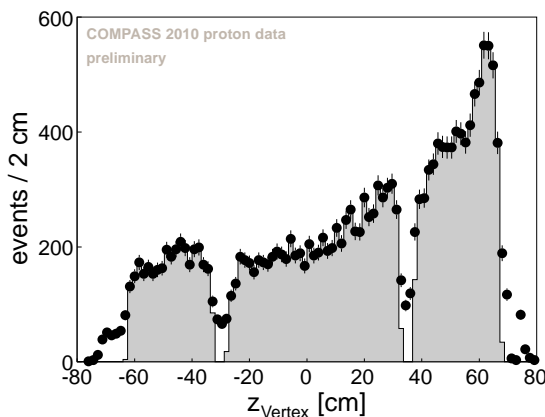


Figure 7.1: The reconstructed positions of the primary vertices along the beam direction, z_{Vertex} . The events accepted in this analysis are indicated in grey colour. All cuts used in this analysis are applied here, except those related to the plotted variable.

7.1.3 Inclusive variables

The cuts on inclusive variables are the same as in the ρ^0 analysis, see Sec. 6.1.3. The distributions of Q^2 , x_{Bj} , y and W are shown in Fig. 7.2.

7.1.4 Reconstruction of π^0 resonance

In addition to three tracks left in the spectrometer by the charged particles a single π^0 is required to make up the event topology of the observed process. The π^0 meson is reconstructed *via* two clusters in the electromagnetic calorimeters (ECALs), which pass selections described in the following and that are not associated to any charge particle. Events where the number of accepted clusters is different from two are removed from the analysis. The combinatorial method, where more than two clusters are accepted and the combinations of these clusters are considered, is not applied since it would lead to a large fraction of background.

In this analysis the calibration of ECAL1 was corrected with an offline method. This method uses the reconstructed width and position of π^0 peak in the distribution of the invariant mass of

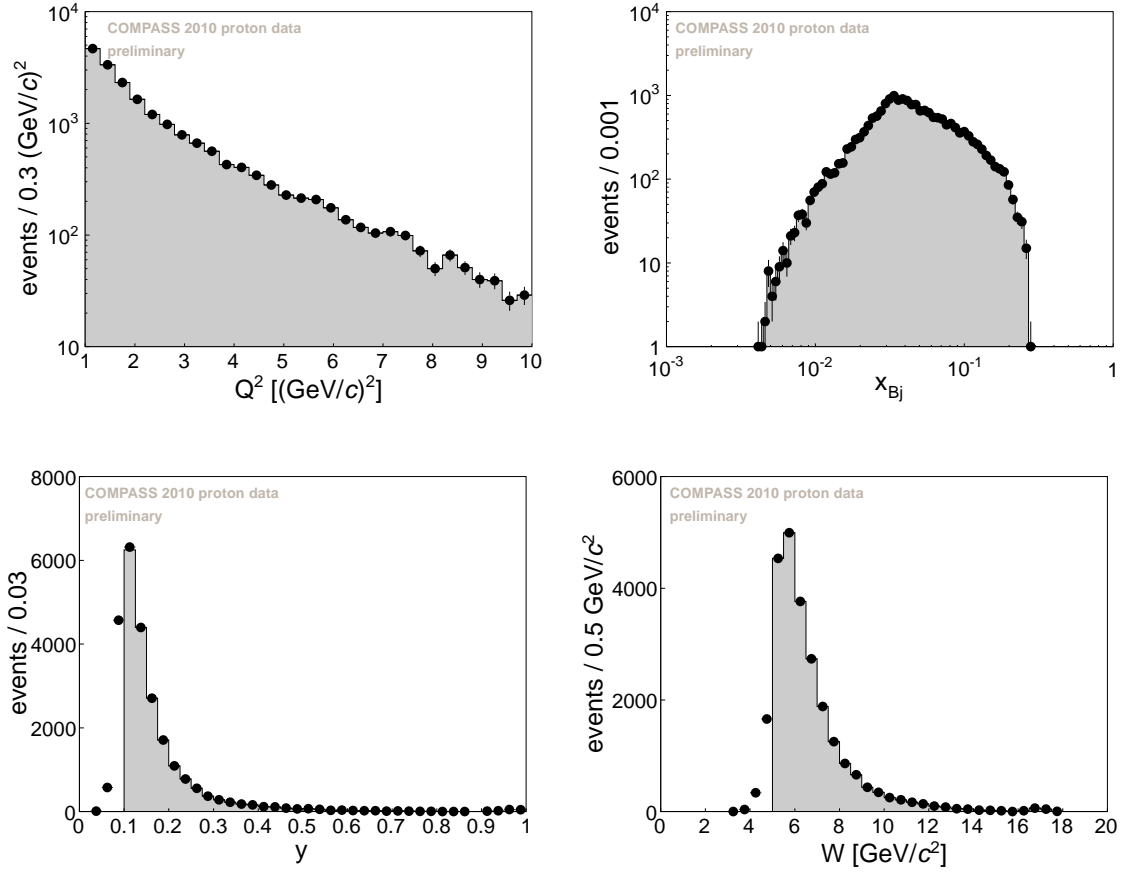


Figure 7.2: The distributions of Q^2 (upper-left), x_{Bj} (upper-right), y (bottom-left) and W (bottom-right). All cuts used in this analysis are applied here except those related to the plotted variables. The accepted events are indicated in grey colour.

two observed photons as sensitive observables to test the quality of the calibration. It finds energy correction parameters for all cells of ECAL1 that provide the best quality of π^0 reconstruction in this calorimeter. It is an iterative method based on the genetic algorithm, see Chapter 5.

A photon reconstructed in a given ECAL is accepted only if its energy, E_γ , is in the range

$$\begin{aligned} 0.6 \text{ GeV} < E_\gamma < 25 \text{ GeV} & \quad \text{for ECAL1,} \\ 1.0 \text{ GeV} < E_\gamma < 50 \text{ GeV} & \quad \text{for ECAL2.} \end{aligned} \quad (7.4)$$

The lower cuts on E_γ have been chosen by studying the yields of exclusive ω mesons as a function of the values of these cuts. For ECAL1 only the class of events where both decay photons were reconstructed in this calorimeter was analysed. For ECAL2 two other classes of events were taken into account, *i.e.* when both photons were reconstructed in ECAL2 or when one photon was reconstructed in ECAL1, while the second one was reconstructed in ECAL2. The result of this study for the both calorimeters is shown in Fig. 7.3. For ECAL1 the ω yield reaches its maximum at ≈ 0.6 GeV, where the cut on E_γ is set. For ECAL2 the ω yield summed up from two analysed

classes of events was analysed, where for the mixed class the cut $E_\gamma > 0.6$ GeV for the photons reconstructed in ECAL1 was used. In this case the yield reaches its maximum at ≈ 1.0 GeV.

In addition to the yields, the signal fraction (purity) as a function of the lower cut on E_γ was also studied. The outcome of this test is shown in Fig. 7.4. One can conclude a weak sensitivity of the purity to the lower value of the E_γ cut.

The upper cuts on E_γ restrict the selection of photons to the region where parameterisations of time correlations between incoming beam tracks and ECAL clusters were obtained, see Eq. (7.6).

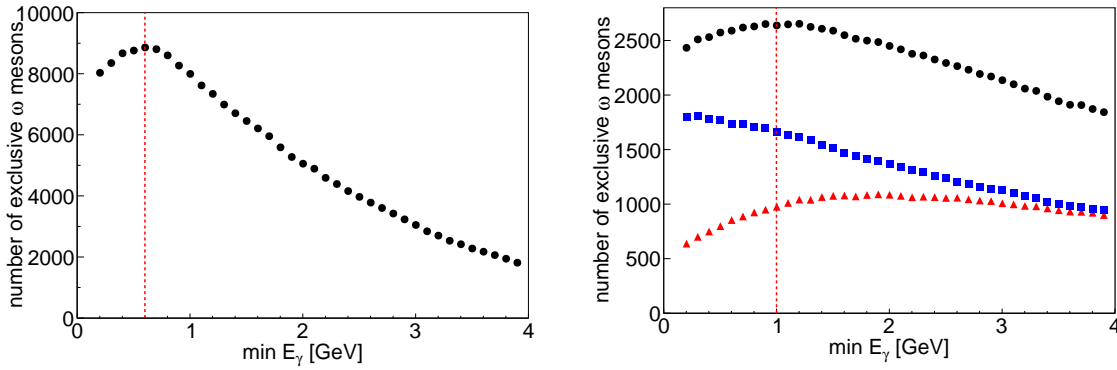


Figure 7.3: The number of reconstructed exclusive ω mesons in the selected data as a function of the lower cut on the photon energy, $\min E_\gamma$, for ECAL1 (left) and ECAL2 (right). For ECAL1 only the events when both photons were reconstructed in this calorimeter are shown. For ECAL2 the events are shown when both photons were reconstructed in ECAL2 (red triangles) or when each photon was reconstructed in a different calorimeter (blue squares) or when at least one photon was reconstructed in ECAL2 (black circles). The red vertical lines denote the values of cuts used for this analysis.

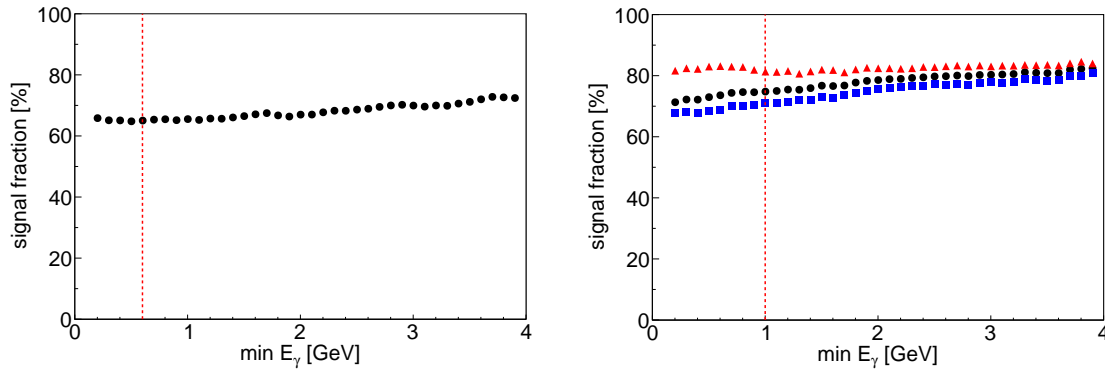


Figure 7.4: The fraction of exclusive ω mesons in the selected data as a function of the lower cut on the photon energy, $\min E_\gamma$, for ECAL1 (left) or ECAL2 (right). For the description of curves and lines see Fig. 7.3.

To ensure the time correlation between a given decay photon candidate and primary vertex, the time of ECAL cluster is examined with respect to the time of incoming beam track, $\Delta t = t_\gamma - t_\mu$. Since the time reconstruction in ECALs is energy-dependent, the boundaries of the Δt cut are set

as a function of the photon energy,

$$|\Delta t - \Delta t_{\text{par}}(E_\gamma)| < 3 \cdot \sigma_{\text{par}}(E_\gamma) . \quad (7.5)$$

The position, $\Delta t_{\text{par}}(E_\gamma)$, and width, $\sigma_{\text{par}}(E_\gamma)$, of the γ - μ correlation peak have been parameterised as a function of E_γ using the semi-inclusive π^0 data in the range

$$\begin{aligned} E_\gamma < 25 \text{ GeV} & \quad \text{for ECAL1,} \\ E_\gamma < 50 \text{ GeV} & \quad \text{for ECAL2.} \end{aligned} \quad (7.6)$$

The parameterisations have been obtained for each period of data taking and they are shown in Fig. 7.5.

The cut on Δt is omitted for ECAL2 in the period 10W27. Due to a wrong time calibration used for the production of this period, the corresponding Δt distribution shows three γ - μ correlation peaks. Since in this analysis the reconstruction of photons is dominated by ECAL1, this problem leads to a negligibly small increase of the semi-inclusive background contribution. The cut on Δt is omitted for both calorimeters in Monte Carlo data that are used for the background subtraction procedure, see Sec. 6.3, as the ECAL timing has not been introduced yet in the simulations.

Similarly to the Δt cut, the cut on the invariant mass of two photons, $M_{\gamma\gamma}$, depends on the energy of the π^0 candidate, $E_{\gamma\gamma}$,

$$|M_{\gamma\gamma} - M_{\pi^0, \text{par}}(E_{\gamma\gamma})| < 3 \cdot \sigma_{\text{par}}(E_{\gamma\gamma}) . \quad (7.7)$$

Here, the position, $M_{\pi^0, \text{par}}(E_{\gamma\gamma})$, and the width, $\sigma_{\text{par}}(E_{\gamma\gamma})$, of the π^0 peak have been parameterised as a function of the π^0 energy using the semi-inclusive data for three sets of periods and for each possible combination of ECALs. Similar parameterisations have been obtained also for Monte Carlo data that are used for the procedure of background subtraction, see Sec. 6.3. The parameterisations are valid in the following ranges of energy

$$\begin{aligned} 1.2 \text{ GeV} < E_{\gamma\gamma} < 25 \text{ GeV} & \quad \text{for ECAL1,} \\ 2.0 \text{ GeV} < E_{\gamma\gamma} < 50 \text{ GeV} & \quad \text{for ECAL2,} \\ 1.6 \text{ GeV} < E_{\gamma\gamma} < 35 \text{ GeV} & \quad \text{for ECAL1 + ECAL2,} \end{aligned} \quad (7.8)$$

and they are shown in Fig. 7.6. The selection of π^0 mesons is restricted to the ranges of energy indicated in Eq. (7.8).

The distributions of $M_{\gamma\gamma}$ are shown in Fig. 7.7 for various combinations of ECALs. In order to reduce the smearing related to the ECAL reconstruction, after the π^0 selection the energies of decay photons are scaled by the factor

$$\frac{M_{\pi^0}^{\text{PDG}}}{M_{\gamma\gamma}}, \quad (7.9)$$

where $M_{\pi^0}^{\text{PDG}} \approx 0.135 \text{ GeV}/c^2$ is the nominal π^0 mass. After the scaling $M_{\gamma\gamma} = M_{\pi^0}^{\text{PDG}}$ for each event and the width of the reconstructed ω resonance is reduced from $0.025 \text{ GeV}/c^2$ to $0.020 \text{ GeV}/c^2$.

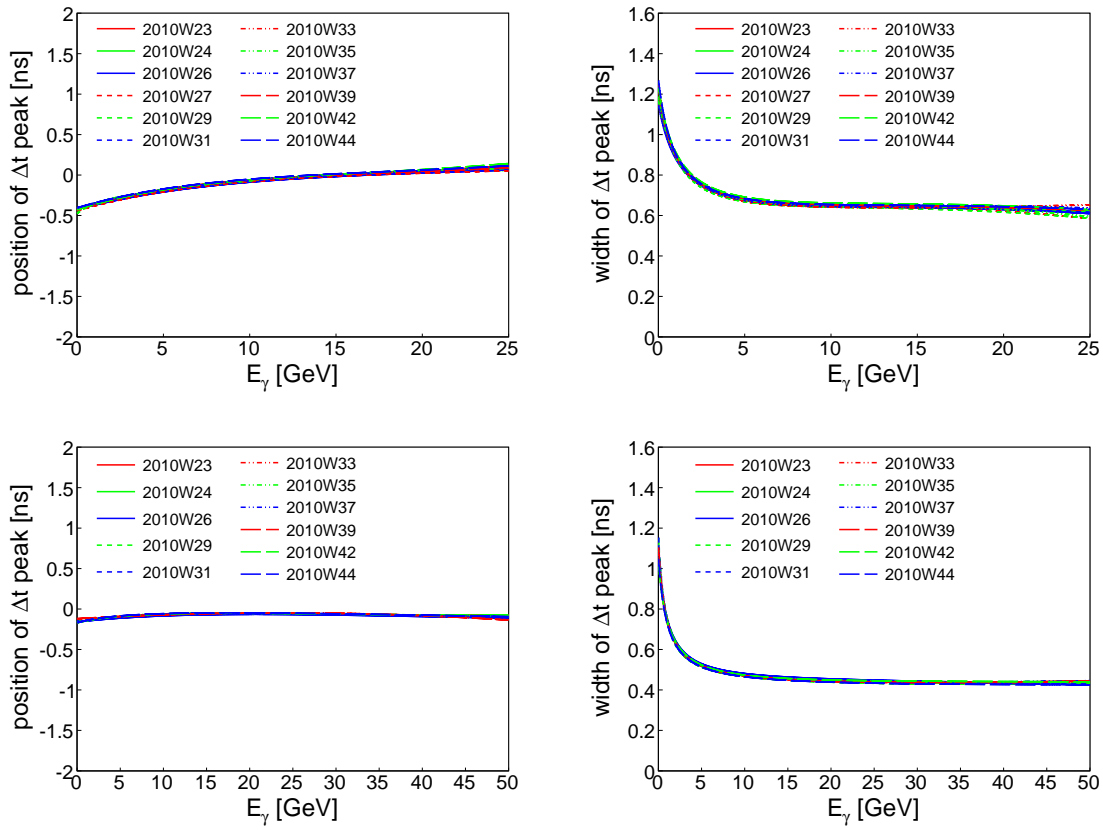


Figure 7.5: Parameterisation of the mean value and the width of $\Delta t = t_\gamma - t_\mu$ peak as a function of photon energy for ECAL1 (up) and ECAL2 (bottom) for the subsets of data indicated in the legend.

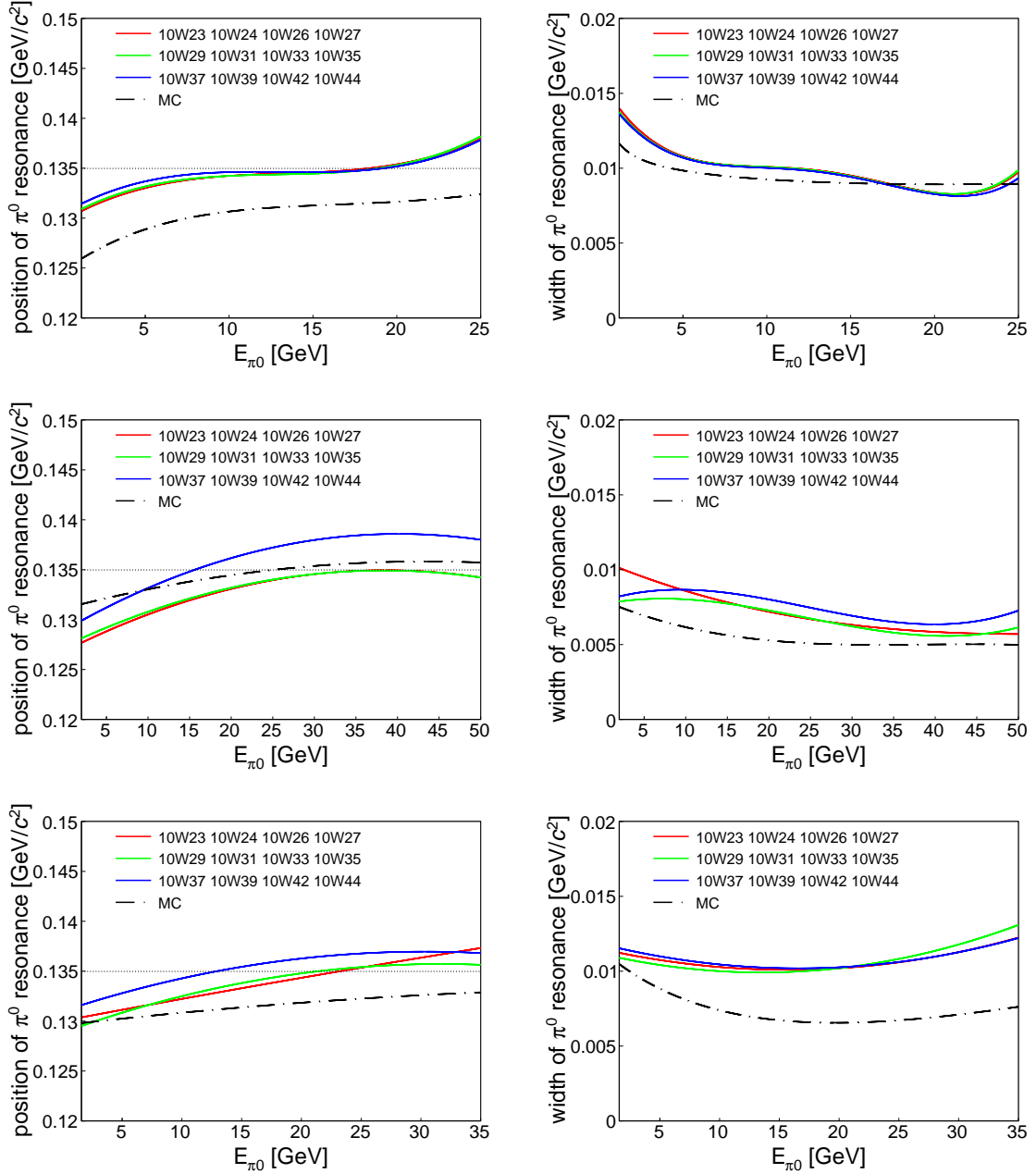


Figure 7.6: Parameterisation of the mean value and the width of the π^0 peak as a function of the π^0 energy for events where both photons are reconstructed either in ECAL1 (up) or ECAL2 (middle), or if photons are reconstructed in various calorimeters (bottom). The parameterisations were obtained for the subsets of data indicated in the legend.

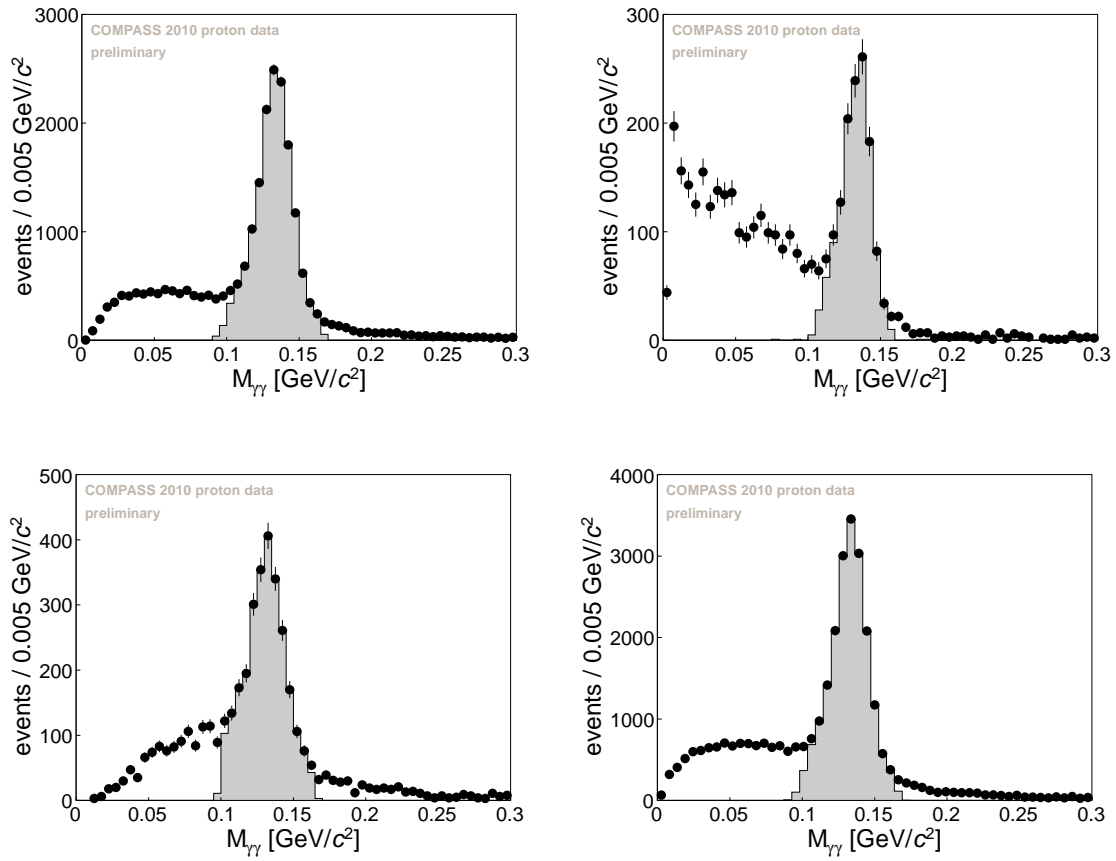


Figure 7.7: The distributions of the invariant mass of two photons, $M_{\gamma\gamma}$, when both photons are reconstructed in ECAL1 (upper-left) or in ECAL2 (upper-right), or when each photon is reconstructed in a different calorimeter (bottom-left). The distribution for all reconstructed events is shown in the bottom-right panel. The accepted events are indicated in grey colour.

7.1.5 Reconstruction of ω resonance

The ω meson is reconstructed *via* two charged hadrons and two photons. It is assumed that the hadrons are π^+ and π^- , while the photons come from the π^0 decay. The corresponding invariant mass spectrum is shown in Fig. 7.8, where the ω resonance is clearly visible at its nominal position, $M_\omega^{\text{PDG}} = 0.782 \text{ GeV}/c^2$. For the further analysis the following cut on the invariant mass is applied

$$|M_{\pi^+\pi^-\pi^0} - M_\omega^{\text{PDG}}| < 0.07 \text{ GeV}/c^2, \quad (7.10)$$

that corresponds to the 3σ region around M_ω^{PDG} .

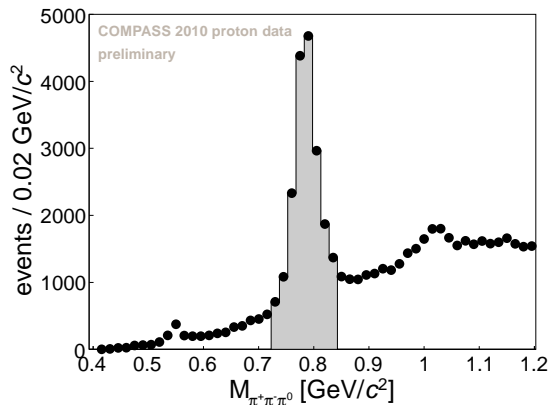


Figure 7.8: The distribution of the invariant mass of three pions, $M_{\pi^+\pi^-\pi^0}$. All cuts used in this analysis are applied here except the cut on $M_{\pi^+\pi^-\pi^0}$. The accepted events are indicated in grey colour.

7.1.6 Exclusivity and incoherence

The exclusivity and the incoherence selections are analogous to the ρ^0 analysis, see Sec. 6.1.3. However, here the boundaries of the E_{miss} region are changed to

$$-3 \text{ GeV} < E_{\text{miss}} < 3 \text{ GeV}. \quad (7.11)$$

The wider range is motivated by the worse resolution of the exclusive peak. In the case of this analysis, the resolution of the exclusive peak is 1.5 GeV, while for the ρ^0 analysis it was 1.25 GeV. In this analysis the boundaries of the E_{miss} cut are not corrected for an eventual shift of the exclusive peak observed in the data. Because of the limited statistics it is not possible to estimate the value of this shift for individual periods of data as it was done in the ρ^0 analysis. Note however, that the estimated position of the exclusive peak in the ω analysis was found to be compatible with zero within the statistical precision.

The distribution of E_{miss} is shown in Fig. 7.9. The correlation between the missing energy and the energy of ω meson, E_ω , is shown in Fig. 7.10, while the distribution of p_T^2 is shown in Fig. 7.11.

7.1.7 Background to exclusive production

The main contribution of background comes from semi-inclusive events. On average, the semi-inclusive background contributes to the selected sample of data with the average fraction of 34%.

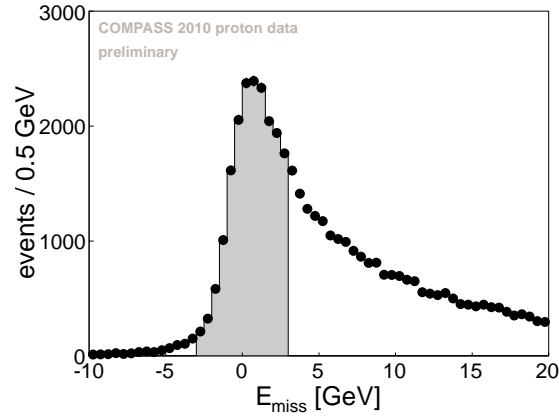


Figure 7.9: The distribution of the missing energy, E_{miss} . All cuts used in this analysis are applied here except the cut on E_{miss} . The accepted events are indicated in grey colour.

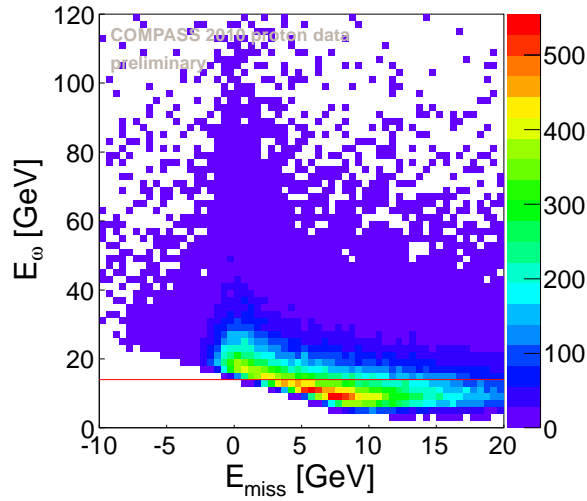


Figure 7.10: The correlation between the missing energy, E_{miss} , and the energy of the exclusive ω candidate, E_{ω} . All cuts used in this analysis are applied here except those on E_{miss} and E_{ω} . The red horizontal line denotes the cut on E_{ω} used for this analysis.

Such contamination is taken into account by a simultaneous extraction of signal and background asymmetries, see Sec. 6.3. The contributions of other sources to the background were studied analogously to the ρ^0 analysis, see Sec. 6.1.6, and they have been found to be at a similar order as in that analysis.

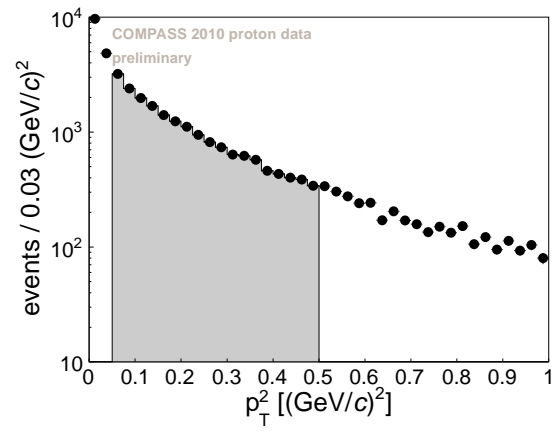


Figure 7.11: The distribution of p_T^2 . All cuts used in this analysis are applied here except the cut on p_T^2 . The accepted events are indicated in grey colour.

7.1.8 Summary

All cuts that define the final sample used for this analysis are summarised in Table 7.3. The numbers of accepted event after all cuts are given in Table 7.2.

Table 7.3: The summary of cuts and selections used in the ω analysis.

Purpose	Constraint
Topology	The best primary vertex made by an incoming beam track, only one outgoing muon track, only two outgoing hadron tracks of opposite charges and only two photons passing the ECAL selections.
Vertex in target polarisable material	The function <code>PaAlgo::InTarget()</code> of COMPASS analysis software.
Track identification	$X/X_0 > 30$ to be identified as muon $X/X_0 < 10$ to be identified as hadron
Track reconstruction quality	$\chi_{\text{red}}^2 < 10$
Suppression of misidentified hadron tracks	$z_{\text{first}} < 350$ cm $350 \text{ cm} < z_{\text{last}} < 3300$ cm does not cross the yoke of SM2 magnet does not cross the hole of absorber system (only for the positive hadron track)
Same beam flux in all target cells	The function <code>PaAlgo::CrossTarget()</code> of COMPASS analysis software.
Reconstructed beam momentum	At least three hits in the BMS detectors
Suppression of beam tracks that have wrongly reconstructed momenta	$\text{Prob}(\chi_{s+t}^2, \text{ndf}) > 0.01$
Kinematic domain of analysis	$1 \text{ (GeV}/c)^2 < Q^2 < 10 \text{ (GeV}/c)^2$ $0.1 < y < 0.9$ $W > 5 \text{ GeV}/c^2$
Decay photons	only two photons, where for each of them <ul style="list-style-type: none"> • $0.6 \text{ GeV} < E_\gamma < 25 \text{ GeV}$ (if γ in ECAL1) • $1.0 \text{ GeV} < E_\gamma < 50 \text{ GeV}$ (if γ in ECAL2) • 3σ cut on $\Delta t(E_\gamma)$ according to the parameterisations
π^0 resonance	3σ cut on $M_{\gamma\gamma}(E_{\gamma\gamma})$ according to the parameterisations $1.2 \text{ GeV} < E_{\gamma\gamma} < 25 \text{ GeV}$ (if both γ in ECAL1) $2.0 \text{ GeV} < E_{\gamma\gamma} < 50 \text{ GeV}$ (if both γ in ECAL2) $1.6 \text{ GeV} < E_{\gamma\gamma} < 35 \text{ GeV}$ (if each γ in different ECAL)
ω resonance	$ M_{\pi^+\pi^-\pi^0} - M_\omega^{\text{PDG}} < 0.07 \text{ GeV}/c^2$
Exclusivity and further suppression of semi-inclusive background	$-3 \text{ GeV} < E_{\text{miss}} < 3 \text{ GeV}$ $E_\omega > 14 \text{ GeV}$ $p_T^2 < 0.5 \text{ (GeV}/c)^2$
Suppression of coherent events	$p_T^2 > 0.05 \text{ (GeV}/c)^2$

7.2 Studies of systematic uncertainties

In order to estimate systematic uncertainties of this measurement the following possible sources were examined:

- false asymmetries
- background subtraction
- estimator of the asymmetries
- compatibility with alternative estimator
- compatibility between subsamples of the data
- compatibility of mean asymmetries for Q^2 , x_{Bj} and p_T^2 bins
- dilution factor, beam and target polarisations

The investigation of each source is given in the following sections, while the summary of systematic studies is given in Sec. 7.2.8.

7.2.1 False asymmetries

As described in Sec. 6.2.1, the asymmetries are extracted from four independent subsamples of the data, where a given subsample is defined for a specific target cell and target spin direction. In combination with the reasonable assumption such division of data leads to a cancellation of the acceptance and other factors. Here, it is checked if the reasonable assumption holds, *i.e.* whether during the data taking the acceptance has changed or not in a way that influences the extraction of the asymmetries.

The issue is investigated by comparing the asymmetries extracted from four configurations of target cells denoted by c_1^{true} , c_2^{true} , c_3^{false} and c_4^{false} . In this test the central cell is artificially divided into two halves, see Fig. 6.15.

The asymmetries are extracted either in the nominal, $-3 \text{ GeV} < E_{\text{miss}} < 3 \text{ GeV}$, or in the extended, $-3 \text{ GeV} < E_{\text{miss}} < 20 \text{ GeV}$, range of E_{miss} . The latter increases the statistical sensitivity of this test. In order to avoid a bias related to the semi-inclusive background subtraction the asymmetries are extracted without this correction. Since the dilution factor is not well defined for a mixture of signal and background events this test is done for the raw asymmetries, see Eq. (6.21).

The c_1^{true} configuration combines the upstream cell (U) and the downstream half of the central cell (dC), while the c_2^{true} configuration combines the upstream half of the central cell (uC) and the downstream cell (D). Both configurations combine the cells with the opposite directions of the target spin, thus the extraction of the azimuthal asymmetries from these configurations should give compatible results.

The raw asymmetries extracted from the c_1^{true} and c_2^{true} configurations are shown in Fig. 7.12, separately for the nominal and extended ranges of E_{miss} . As one can conclude, for both ranges of E_{miss} and for each asymmetry the values extracted from the c_1^{true} and c_2^{true} configurations are compatible within the statistical fluctuations. Therefore, the consistency check is passed successfully.

The c_3^{false} configuration combines the upstream (U) and downstream (D) cells, while the c_4^{false} configuration combines the upstream (uC) and downstream (dC) halves of the central cell. Both configurations combine the cells with the same directions of the target spin. Therefore, the extraction does not probe the target polarisation and all extracted values of asymmetries are expected to be compatible with zero. The asymmetries that do not vanish are considered as false ones.

The raw asymmetries measured from the c_3^{false} and c_4^{false} configurations are shown in Fig. 7.13, separately for the nominal and extended ranges of E_{miss} . All values of asymmetries extracted from the c_3^{false} and c_4^{false} configurations have been found to be compatible with zero within the statistical fluctuations. Therefore, one can conclude that this consistency check is passed successfully.

To assign a limit on the false asymmetries it is assumed that the reasonable assumption is broken in one of the subsamples of the data by a modulation-like deviation,

$$\frac{c_{\text{U+D}}^{\uparrow}(\phi, \phi_S)(1 + 0.01 \sin(\phi - \phi_S) + \dots)}{c_{\text{C}}^{\downarrow}(\phi, \phi_S)} \neq \frac{c_{\text{U+D}}^{\downarrow}(\phi, \phi_S)}{c_{\text{C}}^{\uparrow}(\phi, \phi_S)}. \quad (7.12)$$

The magnitude of this deviation is 1% that expresses the best knowledge on the limit of the detector stability.

To assign the values of systematic uncertainties the final asymmetries are compared with those obtained in the modified extraction, where the events reconstructed in the $N_{\text{U+D}}^{\uparrow}(\phi, \phi_S)$ subsample of data are weighted by $1 + 0.01 \sin(\phi - \phi_S) + \dots$. These weights come from the replacement

$$c_{\text{U+D}}^{\uparrow}(\phi, \phi_S) \longrightarrow c_{\text{U+D}}^{\uparrow}(\phi, \phi_S)(1 + 0.01 \sin(\phi - \phi_S) + \dots) \quad (7.13)$$

in Eq. (6.34). The found values of systematic uncertainties are summarised in Table 7.5.

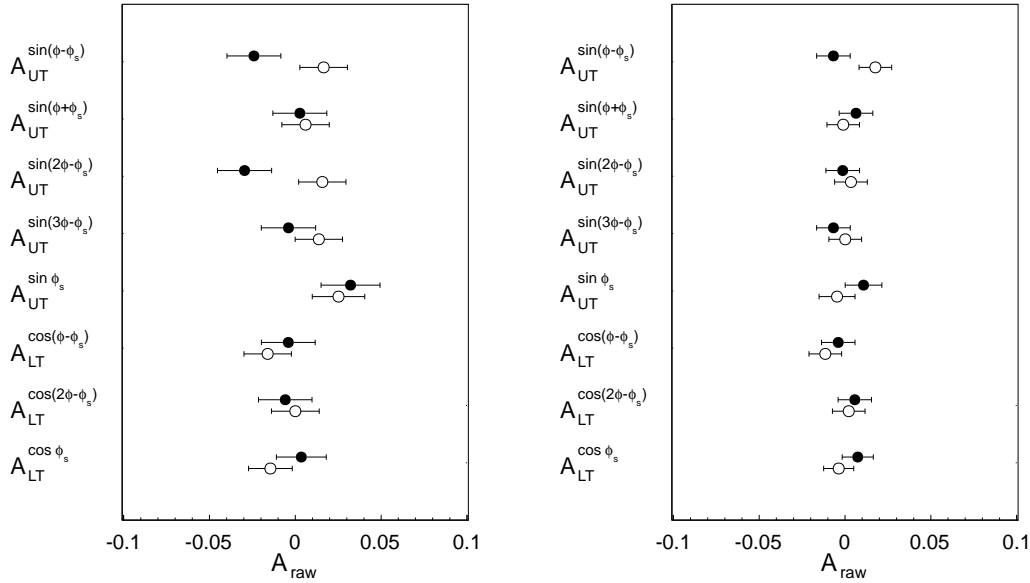


Figure 7.12: Comparison of the background-uncorrected raw asymmetries extracted from the c_1^{true} and c_2^{true} configurations of the target cells (filled and open circles, respectively). The extraction is performed in the nominal and extended ranges of E_{miss} (left and right, respectively).

7.2.2 Background subtraction

The background subtraction relies on the evaluation of the semi-inclusive background contribution as described in Sec. 6.3.1. For a given subsample of data this contribution is estimated from a fit

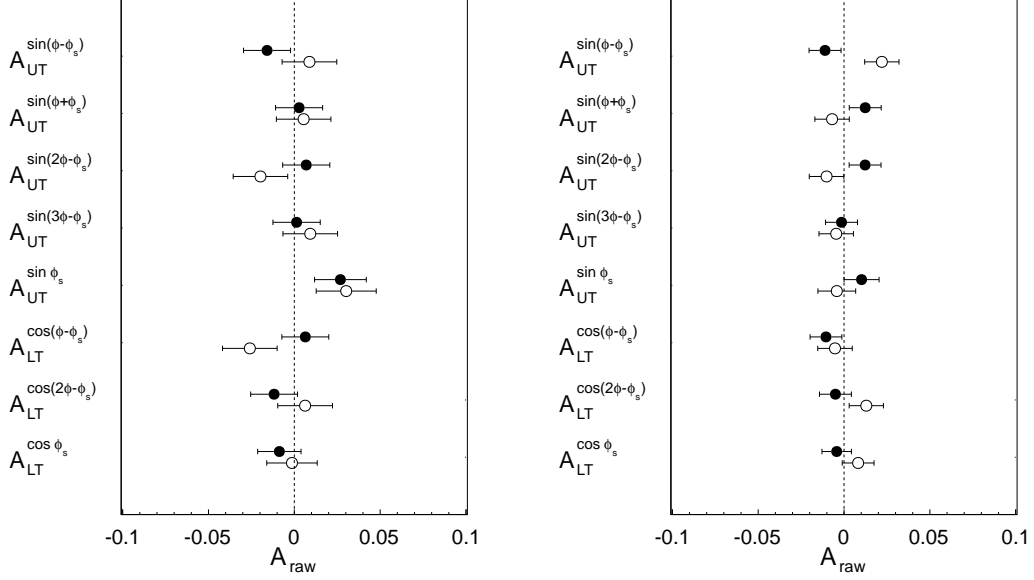


Figure 7.13: Comparison of the background-uncorrected raw asymmetries extracted from the c_3^{false} and c_4^{false} configurations of the target cells (filled and open circles, respectively). The extraction is performed in the nominal and extended ranges of E_{miss} (left and right, respectively).

to the corresponding E_{miss} distribution. In this fit the shape of semi-inclusive background is fixed by the Monte Carlo sample produced with the LEPTO generator.

To estimate the systematic uncertainty related to the background subtraction it is assumed that the semi-inclusive background contribution in the data is known with the uncertainty of 10%. This assumption is supported by the similar estimation performed in the ρ^0 analysis, where the value 10% has been found from a comparison between MC samples produced with LEPTO and PYTHIA generators, see Sec. 6.4.3. In the case of the ω analysis, the production of a second MC sample for the purpose of this test would take more than one month and it would use a lot of computing resources. Therefore, such effort has been avoided and an estimate of the systematic uncertainty related to the semi-inclusive background contribution is evaluated using the aforementioned assumption.

To assign the systematic uncertainty related to the semi-inclusive background subtraction, the background contribution in each of four subsamples that are used by the estimator is modified artificially by -10% and $+10\%$. The values of asymmetries extracted in such a way are compared with those obtained in the standard extraction, *i.e.* with the unmodified background contributions. The outcome of this test is shown in Fig. 7.14.

Let $A^{\text{mod}} \pm \sigma^{\text{mod}}$, where $\text{mod} = \sin(\phi - \phi_S), \sin(\phi + \phi_S), \dots$, be the result of the nominal extraction. The extraction performed with the modified background contributions are denoted by $A^{\text{mod},\pm} \pm \sigma^{\text{mod},\pm}$, where the plus sign in the superscript denotes the $+10\%$ increase, while the minus sign denotes the -10% decrease. For a given asymmetry the systematic uncertainty accounts for

two components

$$\sigma_{sys}^{mod} = \max(A^{mod,+} - A^{mod}, A^{mod,-} - A^{mod}) + \max\left(\sqrt{|(\sigma^{mod,+})^2 - (\sigma^{mod})^2|}, \sqrt{|(\sigma^{mod,-})^2 - (\sigma^{mod})^2|}\right). \quad (7.14)$$

The first component accounts for the maximal differences between the values of asymmetries obtained in the nominal and modified extractions. It gives the estimation of the systematic uncertainty that is sensitive to the true values of the signal and background asymmetries. If both of those values are small, the value of the estimation approximately vanishes, regardless of the modification of the background contribution introduced in this test. The second component in Eq. (7.14) accounts for the change of the statistical precision, which is caused by the modified background contributions. The found values of systematic uncertainties are summarised in Table 7.5.

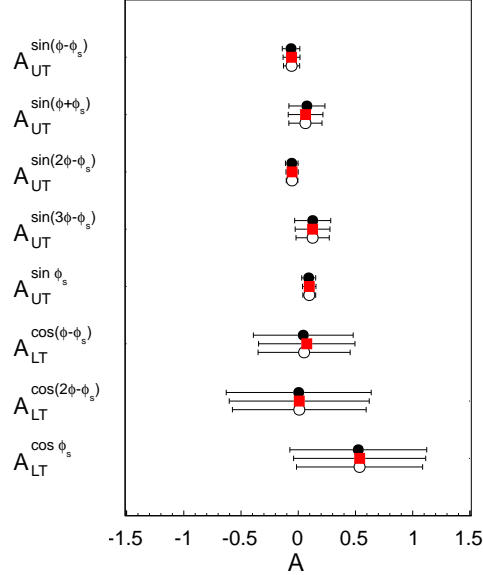


Figure 7.14: Comparison of the physics asymmetries extracted with the modified contribution of the semi-inclusive background. The filled circles are for -10% modification, while the open ones are for $+10\%$ modification. The nominal extraction with the unmodified background contribution is denoted by the red squares.

7.2.3 Estimator of the asymmetries

The systematic uncertainty related to the choice of the unbinned maximum likelihood estimator, see Sec. 6.2.5, is estimated in a Monte Carlo study. In this study an asymmetry of known value is introduced to the MC data. It is checked if the estimator extracts this value correctly. In addition, the so-called cross-talking between the asymmetries is investigated, *i.e.* it is checked if an asymmetry with non-zero value does not contribute to any other asymmetry.

For this test MC data were generated with the HEPGEN generator [40] for the exclusive ω channel, full simulation of the COMPASS spectrometer response and with the reconstruction as for the real data. The MC events pass the same selections as are used for the real data, see Sec. 7.1.

The spin-dependent azimuthal asymmetries are not simulated by the MC generator. In order to introduce these asymmetries each event is weighted by the weight that corresponds to the polarisation-dependent part of the cross section, cf. Eq. (6.20). A single weight reads

$$\begin{aligned}
w(\phi, \phi_S, P_T, P_\mu, y, f, \vec{A}) = & 1 + \\
& + P_T f D^{\sin(\phi-\phi_S)}(y) \times A^{\sin(\phi-\phi_S)} \times \sin(\phi - \phi_S) \\
& + P_T f D^{\sin(\phi+\phi_S)}(y) \times A^{\sin(\phi+\phi_S)} \times \sin(\phi + \phi_S) \\
& + P_T f D^{\sin(2\phi-\phi_S)}(y) \times A^{\sin(2\phi-\phi_S)} \times \sin(2\phi - \phi_S) \\
& + P_T f D^{\sin(3\phi-\phi_S)}(y) \times A^{\sin(3\phi-\phi_S)} \times \sin(3\phi - \phi_S) \\
& + P_T f D^{\sin \phi_S}(y) \times A^{\sin \phi_S} \times \sin \phi_S \\
& + P_\mu P_T f D^{\cos(2\phi-\phi_S)}(y) \times A^{\cos(2\phi-\phi_S)} \times \cos(2\phi - \phi_S) \\
& + P_\mu P_T f D^{\cos(3\phi-\phi_S)}(y) \times A^{\cos(3\phi-\phi_S)} \times \cos(3\phi - \phi_S) \\
& + P_\mu P_T f D^{\cos \phi_S}(y) \times A^{\cos \phi_S} \times \cos \phi_S .
\end{aligned} \tag{7.15}$$

In this approach the values of the target polarisation, P_T , and the dilution factor, f , are set to unity, $|P_T| = f = 1$, which increases the statistical sensitivity of this test. The value of the beam polarisation is chosen to be realistic, $P_\mu = -0.8$, as it can influence the cross talking between the single and double spin asymmetries. The sign of target spin is assigned randomly that simulates the target polarisation reversal and allows us to divide the MC sample into four subsamples used by the estimator of asymmetries, see Sec. 6.2.1.

For each MC event the values of azimuthal angles ϕ and ϕ_S and the value of y are assigned separately according to the MC generator information. The depolarisation factors, $D^{\text{mod}}(y)$, where $\text{mod} = \sin(\phi - \phi_S), \sin(\phi + \phi_S), \dots$, are given in Eq. (6.22). Finally, the only parameters in Eq. (7.15) that are left free are the values of asymmetries, $\vec{A} = A^{\sin(\phi-\phi_S)}, A^{\sin(\phi+\phi_S)}, \dots$.

In this test the value of a given asymmetry is scanned in the range between -1 and 1 , while the values of all other asymmetries are always set to be zero. As an example, the results are shown in Fig. 7.15 for the scan of $A^{\sin(\phi-\phi_S)}$ values. Here, the introduced values of asymmetries are compared with those extracted with the 1D, 2D and unbinned maximum likelihood estimators. The complete set of analogous scans can be found in Appendix B as Figs. B.1 - B.8.

As one can conclude from Figs. B.1 - B.8, each estimator introduces a bias on the extraction of some introduced asymmetries, see for instance Fig. B.3. The bias is related to the experimental smearing of the azimuthal angles. For the sample used for this analysis the smearing has been estimated in MC studies to be 0.4 rad and 0.04 rad for the ϕ and ϕ_S angles, respectively. Such large smearing on the ϕ angle is related to the granularisation of the electromagnetic calorimeters that are used for ω analysis. Note, that the bias scales linearly with the values of introduced asymmetries. This feature will be used to assign the values of systematic uncertainty.

The second conclusion as one can draw from Figs. B.1 - B.8 is that the 2D and unbinned maximum likelihood estimators are much less sensitive to the cross-talking between the asymmetries than the 1D estimator. It can be noticed in particular in Fig. B.1, where the introduced values of $A^{\sin(\phi-\phi_S)}$ asymmetry result in false values of $A^{\sin(\phi+\phi_S)}$. Such effect of the cross-talking is related to a non-flat acceptance as a function of the azimuthal angles.

To assign a value of systematic uncertainty each distribution shown in Figs. B.1 - B.8 for the unbinned estimator is fitted with

$$A_{\text{rec}}^{\text{mod}2} = a_{\text{mod}2}^{\text{mod}1} \cdot A_{\text{gen}}^{\text{mod}1} . \tag{7.16}$$

Here, $A_{\text{rec}}^{\text{mod}2}$ are the extracted values of the asymmetry related to the modulation $\text{mod}2 = \sin(\phi - \phi_S)$, $\sin(\phi + \phi_S)$, \dots . These values are shown in Figs. B.1 - B.8 on the vertical axes. The values introduced to the MC data are denoted by $A_{\text{gen}}^{\text{mod}1}$ and they are shown in Figs. B.1 - B.8 on the horizontal axes. The expected values on the $a_{\text{mod}2}^{\text{mod}1}$ parameter are equal to zero if $\text{mod}1 \neq \text{mod}2$ and equal to one if $\text{mod}1 = \text{mod}2$.

The found values of the $a_{\text{mod}2}^{\text{mod}1}$ parameter are listed in Table 7.4. The study demonstrates that the unbinned estimator is not sensitive to the cross-talking between the asymmetries, *i.e.* all values of the $a_{\text{mod}2}^{\text{mod}1}$ parameter are compatible with zero within the statistical fluctuations whenever $\text{mod}1 \neq \text{mod}2$. The bias is visible only in a case of the direct extraction of asymmetries, *i.e.* when $\text{mod}1 = \text{mod}2$.

For a given asymmetry the corresponding systematic uncertainty is estimated as

$$\sigma_{sys}^{\text{mod}} = \left| A^{\text{mod}} - \frac{A^{\text{mod}}}{a_{\text{mod}}^{\text{mod}}} \right|. \quad (7.17)$$

Here, the measured value, A^{mod} , is compared with that corrected one, $A^{\text{mod}}/a_{\text{mod}}^{\text{mod}}$, according to the Monte Carlo study presented in this section. The found values of the systematic uncertainties are listed in Table 7.5.

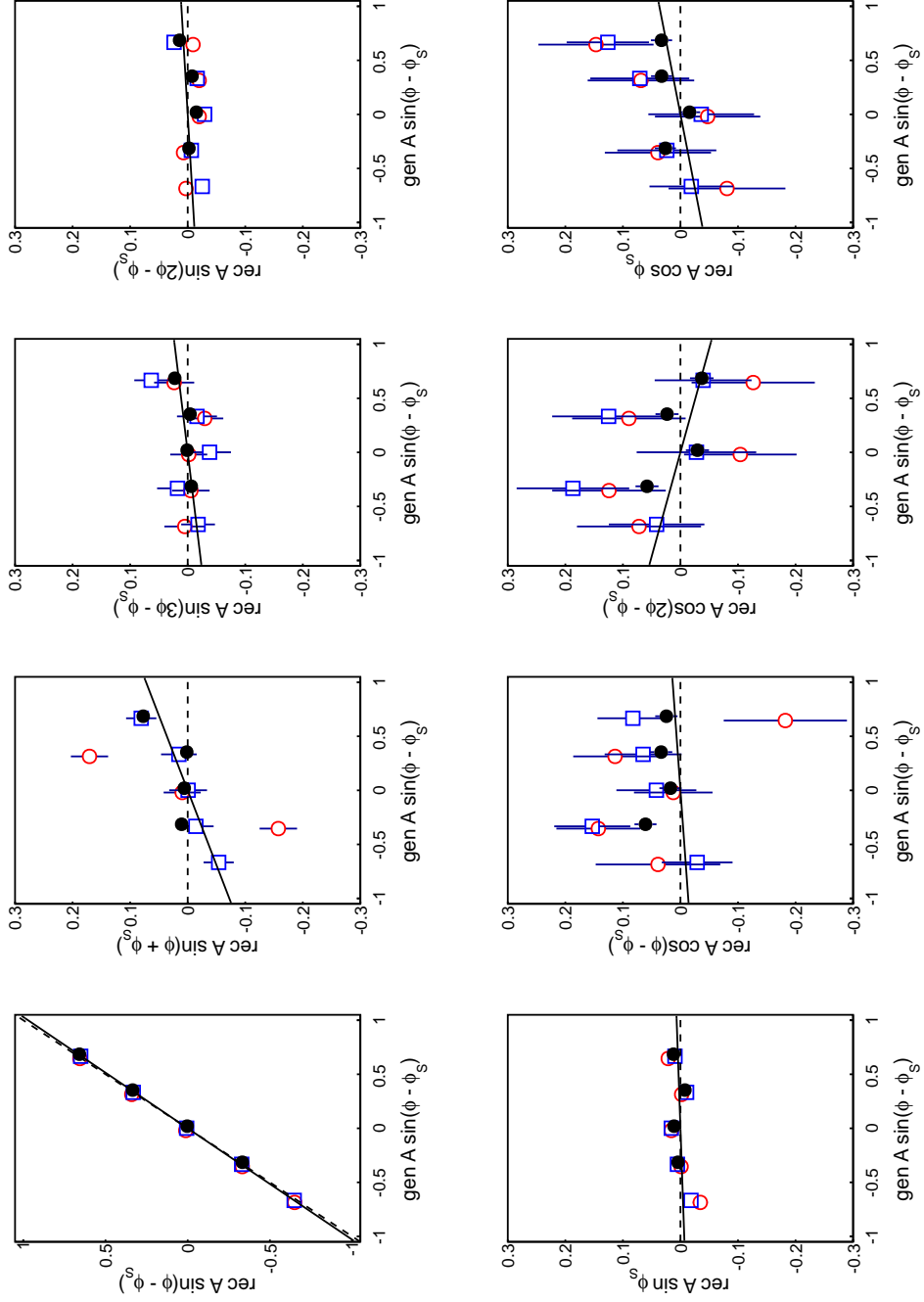


Figure 7.15: Extracted values of asymmetries, recA , as a function of those introduced to the full Monte Carlo simulation, genA , for $A_{UT}^{\sin(\phi - \phi_S)}$ asymmetry. The extraction was performed with the 1D (red open circles) and 2D (blue open squares) and unbinned (black filled circles) maximum likelihood estimators. The dashed line denotes the expected extracted values. The solid line denotes the fit defined in Eq. (7.16) to the values extracted with the unbinned estimator.

7.2.4 Compatibility with alternative estimator

An additional test on the systematic effects is performed by comparing the final results with those extracted with an alternative estimator. In this test the 2D binned maximum likelihood estimator, see Sec. 6.2.4, is used as the alternative estimator. Since the 2D estimator is not compatible with the procedure of background subtraction that is used in the unbinned analysis, in this test the data are corrected for the background by measuring the angular distributions in the large E_{miss} region, see Sec. 6.3.3. It gives an additional possibility to test the agreement between two procedures of the background subtraction.

The result of the comparison between two extractions is shown in Fig. 7.16. Note, that the 2D estimator does not allow to extract simultaneously the azimuthal asymmetries for the signal and background events, therefore the statistical precision given by this estimator is worse than that obtained with the unbinned estimator. Since the differences between values obtained with both estimators are compatible within statistical fluctuations (even by assuming the full correlation between samples), one can conclude a good agreement between both estimators. In addition, since the systematic uncertainties related to the background subtraction and the unbinned estimator are assigned in Secs. 7.2.2 and 7.2.3, respectively, an additional uncertainty is not assigned here.

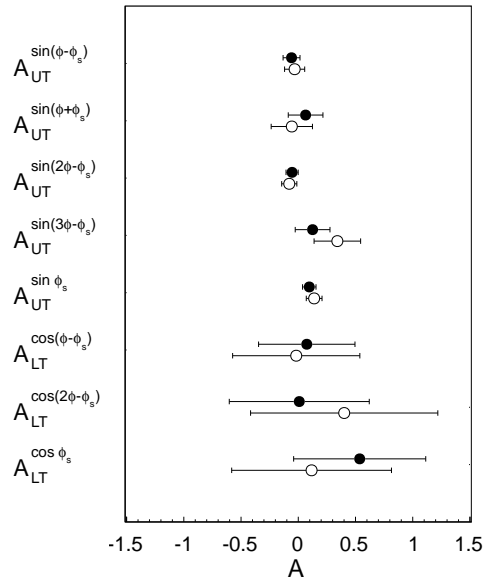


Figure 7.16: Comparison of the physics asymmetries extracted with the 2D and unbinned maximum likelihood estimators (filled and open circles, respectively).

7.2.5 Compatibility between subsamples of the data

In order to test the stability over the data taking period the asymmetries are extracted from two independent subsamples of the data denoted by s_1 and s_2 . Here, s_1 combines 10W23, 10W24, 10W26, 10W27, 10W29, 10W31, 10W33 and 10W35 periods, while s_2 combines 10W37, 10W39, 10W42 and 10W44 periods. Due to the limited statistics it is not possible to perform this test with the asymmetries extracted separately from each COMPASS period of data taking.

As in the case of false asymmetries, see Sec. 7.2.1, this test is performed in the nominal and extended ranges of E_{miss} . Since only the stability of data taking is examined in this test the subtraction of the semi-inclusive background is not done here. Moreover, since the dilution factor is not well defined for a mixture of signal and background events this test is performed for the raw asymmetries, see Eq. (6.21).

The raw asymmetries extracted from the s_1 and s_2 subsamples of the data are shown in Fig. 7.17, separately for the nominal and extended ranges of E_{miss} . Since all values extracted from the s_1 and s_2 subsamples of the data are compatible within the statistical fluctuation, one can conclude that this consistency check is passed successfully and the systematic uncertainty is not assigned here.

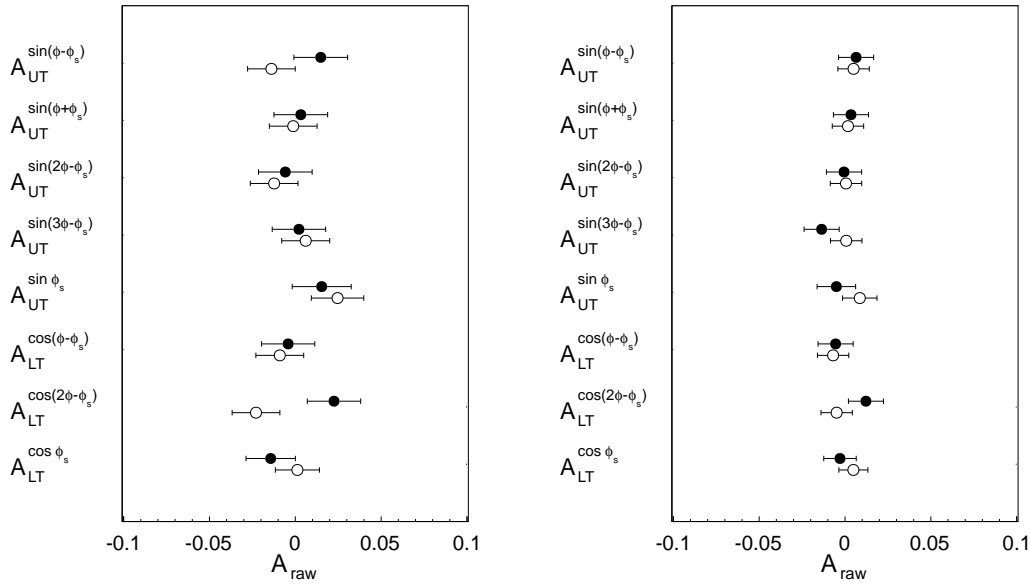


Figure 7.17: Comparison of the background-uncorrected raw asymmetries extracted from the s_1 and s_2 subsamples of the data (filled and open circles, respectively). The extraction is performed in the nominal and extended ranges of E_{miss} (left and right, respectively).

7.2.6 Compatibility of mean asymmetries for Q^2 , x_{Bj} and p_T^2 bins

In this test the values of asymmetries extracted from the integrated sample of data are compared to those extracted in the kinematic bins. Since the fraction of semi-inclusive events varies between the kinematic bins, this test is sensitive to the procedure of background subtraction. In addition, in this test one examines the sensitivity of the estimator to the number of input events.

Let A^{mod} , where $\text{mod} = \sin(\phi - \phi_S), \sin(\phi + \phi_S), \dots$, be an asymmetry extracted from the integrated sample of data. The mean values of asymmetries obtained from Q^2 , x_{Bj} and p_T^2 bins are denoted by $A_{Q^2}^{\text{mod}}$, $A_{x_{Bj}}^{\text{mod}}$ and $A_{p_T^2}^{\text{mod}}$, respectively. For a given asymmetry the systematic uncertainty is estimated to be

$$\sigma_{sys}^{\text{mod}} = \max(|A^{\text{mod}} - A_{Q^2}^{\text{mod}}|, |A^{\text{mod}} - A_{x_{Bj}}^{\text{mod}}|, |A^{\text{mod}} - A_{p_T^2}^{\text{mod}}|). \quad (7.18)$$

The uncertainty is assigned to the asymmetries obtained from the integrated sample of data and to those obtained in the kinematic bins. The values of σ_{sys}^{mod} are summarised in Table 7.5.

7.2.7 Dilution factor, beam and target polarisations

The relative uncertainty for the polarisation value for 160 GeV μ^+ beam is 5%. The relative uncertainty of the target polarisation for the transversely polarised proton target is 3%. The estimate takes into account uncertainties of the measurements with the NMR coils done before and after the transverse polarisation mode but also the uncertainty of the extrapolation between the direct measurements.

The inclusion of nuclear shadowing effect on the calculation of the dilution factor is crucial for the ammonia target. However, this effect has been never measured for exclusive ω meson production in the kinematic region comparable to that covered by the COMPASS experiment. It is assumed that the nuclear shadowing effect for ω is the same as that for ρ^0 . This assumption is supported by the similar quark compositions, quantum numbers (J^P) and masses of both mesons. It leads to the same dilution factor as for incoherent exclusive ρ^0 meson production [23].

The relative uncertainty of the dilution factor is 2%. The estimate takes into account the uncertainties related to the determination of the contribution of different elements to the target material, but also those related to the parametrisation of the nuclear shadowing effect [23].

The single spin asymmetries are proportional to the target polarisation and the dilution factor, see Eq. (6.21). The double spin asymmetries are also proportional to the beam polarisation. Therefore, the scale normalisation systematic uncertainty for the proton target is $0.036 \cdot A_{UT}^{mod}$ for the single spin asymmetries and $0.062 \cdot A_{LT}^{mod}$ for the double spin asymmetries, where $mod = \sin(\phi - \phi_S), \sin(\phi + \phi_S), \dots$

7.2.8 Summary of systematic studies

The systematic uncertainties for all asymmetries are summarised in Table 7.5.

Table 7.5: Summary of systematic uncertainties for the measurement of azimuthal asymmetries in the ω analysis.

	$A_{UT}^{\sin(\phi-\phi_S)}$	$A_{UT}^{\sin(\phi+\phi_S)}$	$A_{UT}^{\sin(2\phi-\phi_S)}$	$A_{UT}^{\sin(3\phi-\phi_S)}$	$A_{UT}^{\sin\phi_S}$	$A_{LT}^{\cos(\phi-\phi_S)}$	$A_{LT}^{\cos(2\phi-\phi_S)}$	$A_{LT}^{\cos\phi_S}$
false asymmetries Sec. 7.2.1	0.015	0.029	0.011	0.029	0.010	0.077	0.114	0.115
background subtraction Sec. 7.2.2	0.025	0.048	0.027	0.051	0.019	0.126	0.181	0.179
Monte Carlo test of estimator Sec. 7.2.3	0.002	0.001	0.010	0.049	0.015	0.001	0.002	0.076
compatibility between extractions from integrated sample and kinematic bins Sec. 7.2.6	0.012	0.021	0.006	0.003	0.010	0.109	0.108	0.123
$f, P_{\text{target}}, P_{\text{beam}}$ (together) Sec. 7.2.7	0.002	0.002	0.002	0.005	0.004	0.005	0.001	0.033
TOTAL σ_{sys} ($\sigma_{\text{sys}}/\sigma_{\text{stat}}$)	0.031 0.42	0.060 0.40	0.031 0.58	0.077 0.51	0.028 0.48	0.184 0.44	0.240 0.40	0.259 0.45

7.3 Results

The values of the azimuthal asymmetries obtained for the whole sample of accepted events together with the corresponding uncertainties are shown in Fig. 7.18. The values of asymmetries and their statistical and systematic uncertainties are given in Table 7.6.

In addition to the extraction from the integrated sample of data, the values of asymmetries have been measured also in bins of Q^2 , x_{Bj} and p_T^2 . The measured values together with the uncertainties are shown in Fig. 7.19 and 7.20 for the single and double spin asymmetries, respectively. The numerical results of this measurement are given in Appendix A in Table A.3.

In Figs. 7.19 and 7.20 the predictions of GPD-based model given by Goloskokov and Kroll [38, 107] are compared with the experimental points. The predictions are calculated for the average W , Q^2 and p_T^2 of the COMPASS data: $W = 7.1 \text{ GeV}/c^2$ and $p_T^2 = 0.17 \text{ (GeV}/c)^2$ for the x_{Bj} and Q^2 dependences and at $W = 7.1 \text{ GeV}/c^2$ and $Q^2 = 2.2 \text{ (GeV}/c)^2$ for the p_T^2 dependence. The predictions are given for the case without the pion pole contribution and for the positive and negative $\pi\omega$ form factor.

The interpretation of ω results in the context of the GPD formalism is more challenging than that for ρ^0 , as exclusive ω meson production is significantly influenced by the pion pole exchange contribution and at present the sign of $\pi\omega$ form factor is unknown. By comparing the results with the predictions of the GK model [107], one may find that two asymmetries, $A_{UT}^{\sin(\phi-\phi_S)}$ and $A_{UT}^{\sin(2\phi-\phi_S)}$, prefer the negative $\pi\omega$ form factor, one asymmetry, $A_{UT}^{\sin\phi_S}$, prefer the positive one and other measured asymmetries are not sensitive to the $\pi\omega$ form factor sign. The explanation of the discrepancy between the model and the experimental data is at present unknown.

There exist preliminary results on the single spin azimuthal asymmetries for protons measured by the HERMES collaboration [108], however without a comparison to the predictions of the most up-to-date version of Goloskokov-Kroll model. Because of a different contribution of the pion pole, one can conclude only a qualitative agreement of these results with those presented in this thesis. Note however, that the latter are more precise by a factor of about two and cover a wider kinematic range.

Table 7.6: The azimuthal asymmetries for exclusive ω meson production on transversely polarised protons without division of data into bins. For the mean values of selected kinematic variables see Table 7.7.

	A	σ_{stat}	σ_{sys}
$A_{UT}^{\sin(\phi-\phi_S)}$	-0.059	0.074	0.031
$A_{UT}^{\sin(\phi+\phi_S)}$	0.06	0.15	0.06
$A_{UT}^{\sin(2\phi-\phi_S)}$	-0.054	0.053	0.031
$A_{UT}^{\sin(3\phi-\phi_S)}$	0.13	0.15	0.08
$A_{UT}^{\sin\phi_S}$	0.096	0.059	0.028
$A_{LT}^{\cos(\phi-\phi_S)}$	0.07	0.42	0.18
$A_{LT}^{\cos\phi_S}$	0.01	0.61	0.24
$A_{LT}^{\cos(2\phi-\phi_S)}$	0.54	0.58	0.26

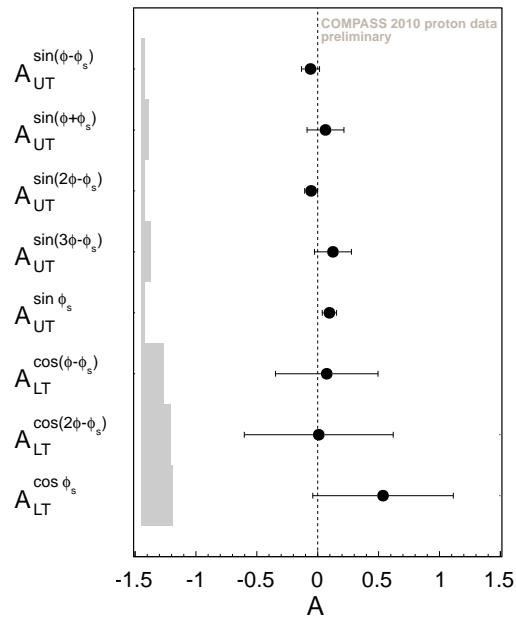


Figure 7.18: The azimuthal asymmetries for exclusive ω meson production on transversely polarised protons without division of data into bins. The error bars (left bands) represent the statistical (systematic) uncertainties. For the mean values of selected kinematic variables see Table 7.7.

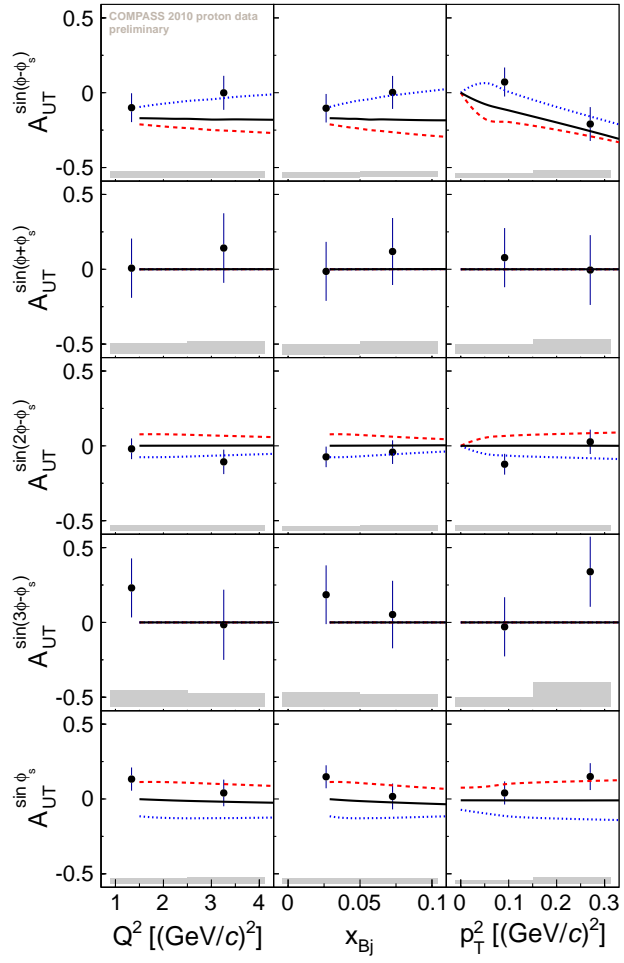


Figure 7.19: Single spin azimuthal asymmetries for exclusive ω meson production on transversely polarised protons. The curves show the predictions of the GPD-based model [38, 107] (see the text for more details). The dashed red and dotted blue curves represent the predictions with the positive and negative $\pi\omega$ form factors, respectively, while the solid black curve represents the predictions without the pion pole.

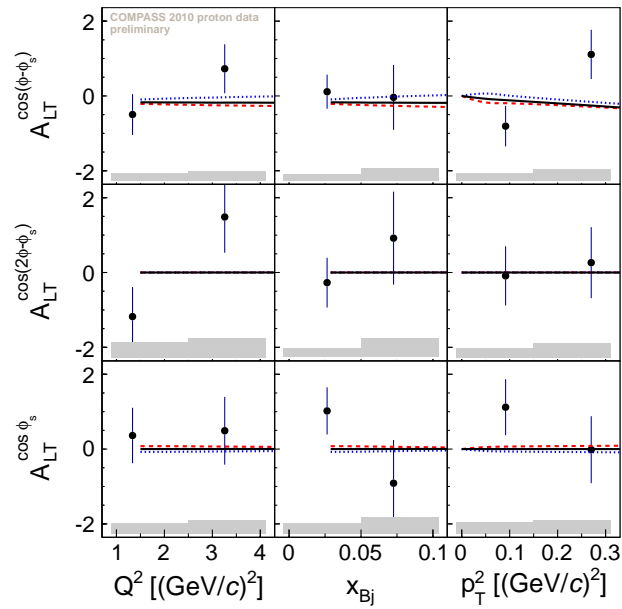


Figure 7.20: Double spin azimuthal asymmetries for exclusive ω meson production on transversely polarised protons. The curves show the predictions of the GPD-based model [38, 107] (see the text for more details). The dashed red and dotted blue curves represent the predictions with the positive and negative $\pi\omega$ form factors, respectively, while the solid black curve represents the predictions without the pion pole.

7.3.1 Mean values of kinematic variables

The calculation of mean values of kinematic variables, $\langle y \rangle$, $\langle Q^2 \rangle$, \dots , has been improved with respect to the analysis of exclusive ρ^0 meson production presented in Chapter 6. In that analysis, the mean values of kinematic variables were calculated as the arithmetic mean of values returned by events reconstructed in the signal window, $-2.5 \text{ GeV} < E_{\text{miss}} < 2.5 \text{ GeV}$. Such method of calculation may introduce a bias, as this range of E_{miss} is populated by both signal and background events. Note, that the semi-inclusive background has different mean values of kinematic variables than the exclusive signal due to the different kinematic dependences, *e.g.* the cross section for exclusive reactions decreases much faster with Q^2 than that for semi-inclusive ones.

The procedure used to calculate the mean values of kinematic variables in the analysis of exclusive ω production is as follows. For a given kinematic variable, $x = y, Q^2, \dots$, the E_{miss} dependence of its arithmetic mean, $\langle x \rangle (E_{\text{miss}})$, is examined in order to find a corresponding value for the exclusive signal, $\langle x_{\text{sig}} \rangle$. The dependence extracted from the data is fitted by

$$\langle x \rangle (E_{\text{miss}}) = f_{\text{sig}} (E_{\text{miss}}) \cdot \langle x_{\text{sig}} \rangle (E_{\text{miss}}) + f_{\text{semi-incl}} (E_{\text{miss}}) \cdot \langle x_{\text{semi-incl}} \rangle (E_{\text{miss}}), \quad (7.19)$$

where $f_{\text{sig}} (E_{\text{miss}})$ and $f_{\text{semi-incl}} (E_{\text{miss}}) = 1 - f_{\text{sig}} (E_{\text{miss}})$ are the fractions of exclusive signal and semi-inclusive background as a function of E_{miss} , respectively. These fractions are calculated from the fit to the E_{miss} distribution obtained for the final sample of data, following the procedure described in Sec. 6.3. For the exclusive events it is assumed that the mean value does not depend on E_{miss} ,

$$\langle x_{\text{sig}} \rangle (E_{\text{miss}}) \equiv \langle x_{\text{sig}} \rangle. \quad (7.20)$$

For the semi-inclusive events it is assumed that the mean value depends on E_{miss} linearly,

$$\langle x_{\text{semi-incl}} \rangle (E_{\text{miss}}) = p_0 + p_1 \cdot E_{\text{miss}}. \quad (7.21)$$

Therefore, the only parameters fitted to the data are $\langle x_{\text{sig}} \rangle$, p_0 and p_1 .

The E_{miss} dependence of the arithmetic mean values of y , Q^2 , W , x_{Bj} and p_T^2 obtained from the data together with the fits given by Eq. (7.19) are shown in Fig. 7.21. The found mean values of kinematic variables for exclusive events are given in Table 7.7. The results of direct calculation in $-3 \text{ GeV} < E_{\text{miss}} < 3 \text{ GeV}$ region, which are influenced by the presence of semi-inclusive background, are also given in Table 7.7 for comparison. Note, that the difference between both estimations is small that justifies the negation of the background effect in the ρ^0 analysis.

Table 7.7: Mean values of selected kinematic variables for events reconstructed in $-3 \text{ GeV} < E_{\text{miss}} < 3 \text{ GeV}$ region after and before the correction for the semi-inclusive background.

	$\langle Q^2 \rangle$ [(GeV/c) ²]	$\langle x_{Bj} \rangle$	$\langle y \rangle$	$\langle W \rangle$ [GeV/c ²]	$\langle p_T^2 \rangle$ [(GeV/c) ²]
signal only	2.2	0.049	0.18	7.1	0.17
signal + background	2.4	0.055	0.17	6.9	0.19

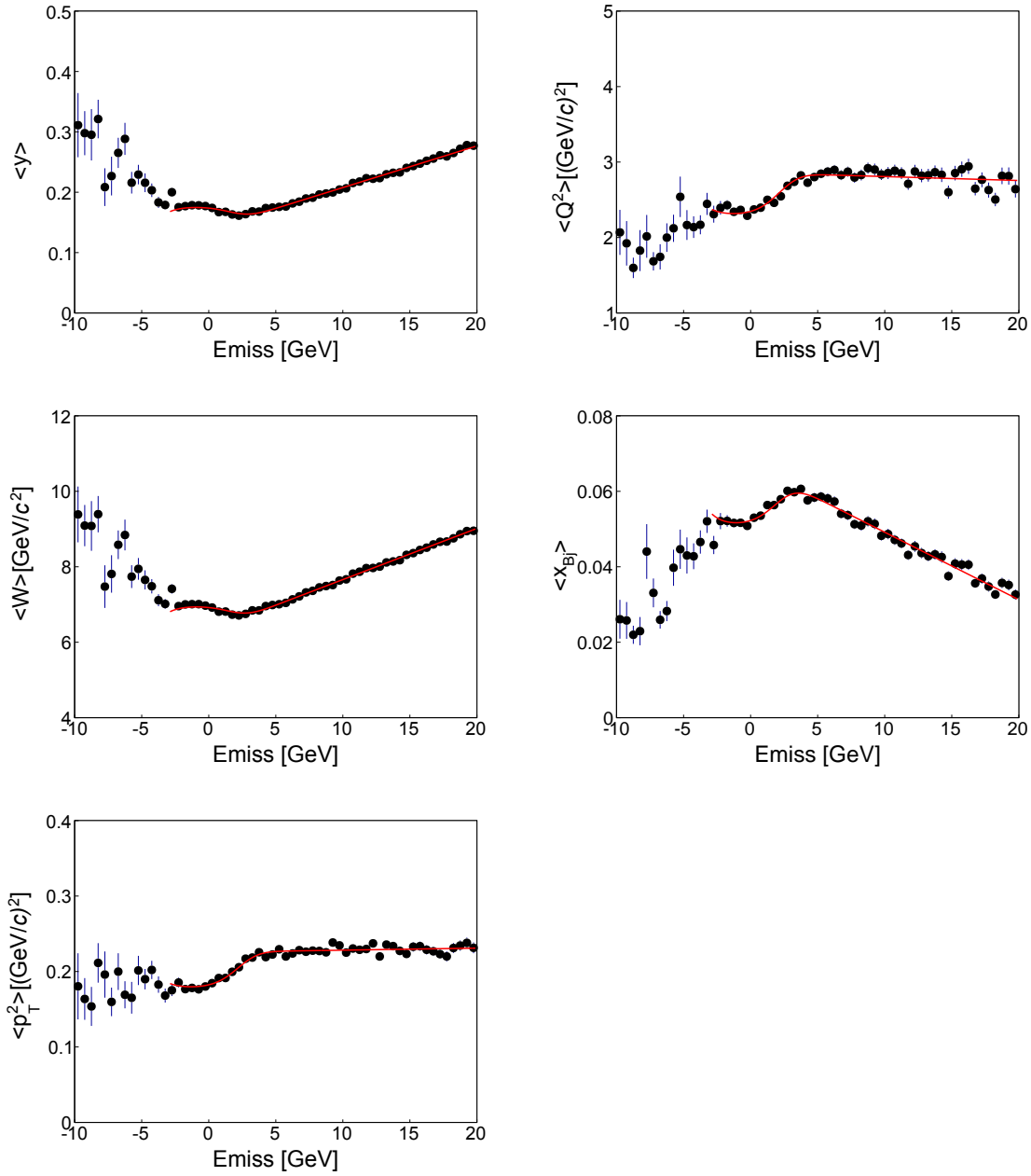


Figure 7.21: Arithmetic mean values of selected kinematic variables as a function of E_{miss} together with the fits given by Eq. (7.19).

Analysis of measured asymmetries in the framework of the Goloskokov-Kroll model

In this analysis the COMPASS results on the $A_{UT}^{\sin(\phi-\phi_S)}$ asymmetry measured on protons will be used to constrain the GPDs $E^{u_{\text{val}}}$ and $E^{d_{\text{val}}}$ for the valence up and down quarks. Since exclusive ρ^0 and ω meson productions probe these GPDs in orthogonal combinations, see Eq. (2.3), results for both mesons could *in principle* allow to disentangle their contributions. With the help of the Ji's sum rule, see Eq. (2.10), the found constraints on the GPDs will be further used to constrain the total angular momentum of the valence quarks.

The analysis rely on a theoretical framework that consists of two ingredients. The first one is a tunable model of the GPDs H and E , while the second one is a GPD-based model of hard exclusive meson production. Since the helicity states of the virtual photon and the produced meson are not distinguished in the present extraction of the $A_{UT}^{\sin(\phi-\phi_S)}$ asymmetry, the model must be able to provide predictions for both longitudinally and transversely polarised virtual photons. The framework that matches these requirements has been proposed by Goloskokov and Kroll [33, 34, 35, 36, 37, 38] and it will be used in these studies. The brief introduction to this formalism, referred in the following to as the GK model, is given in Sec. 8.1.

An unofficial implementation of the GK model written by the author of the thesis is used in these studies. This implementation corresponds to Refs. [33, 34, 35, 36]. A recent addition of the parton helicity-flip GPDs to the GK model [37] has been omitted in this implementation, as an impact of these GPDs on the $A_{UT}^{\sin(\phi-\phi_S)}$ asymmetry is negligible (as a proof one may compare the predictions published in Refs. [36] and [37]). The pion pole exchange contribution to the production mechanism introduced recently to the GK model [38] has been omitted in this implementation as well, as the sign of $\pi\omega$ form factor is at present unknown. One should mention that the contribution of the pion pole exchange to ρ^0 production was estimated to be small in contrast to ω production [38]. As a consequence, the results for exclusive ω meson production, which are significantly influenced by the pion pole, are used in these studies only to investigate their potential for constraining the GPDs E .

8.1 Introduction to the Goloskokov-Kroll model

Let $\mathcal{M}_{\mu'\nu',\mu\nu}^V$ be a helicity-dependent amplitude for the $\gamma^*p \rightarrow Vp$ process, where μ' , ν' , μ and ν denote helicities of produced meson, recoiled proton, virtual photon and initial proton, respectively. In the leading twist approximation, the $A_{UT}^{\sin(\phi-\phi_S)}$ asymmetry involves the following amplitudes, cf. Eqs. (2.20) and (2.21),

$$A_{UT}^{\sin(\phi-\phi_S)} = -2 \frac{\text{Im}(\mathcal{M}_{+-,++}^{V*} \mathcal{M}_{++,+}^V + \epsilon \mathcal{M}_{0-,0+}^{V*} \mathcal{M}_{0+,0+}^V)}{|\mathcal{M}_{++,+}^V|^2 + |\mathcal{M}_{+-,++}^V|^2 + \epsilon \left(|\mathcal{M}_{0+,0+}^V|^2 + |\mathcal{M}_{0-,0+}^V|^2 \right)}. \quad (8.1)$$

A given amplitude can be decomposed as

$$\mathcal{M}_{\mu'\nu',\mu\nu}^V = \mathcal{M}_{\mu'\nu',\mu\nu}^{V,q} + \mathcal{M}_{\mu'\nu',\mu\nu}^{V,g}, \quad (8.2)$$

where $\mathcal{M}_{\mu'\nu',\mu\nu}^{V,q}$ and $\mathcal{M}_{\mu'\nu',\mu\nu}^{V,g}$ correspond to the $\gamma^*q \rightarrow Vq$ and $\gamma^*g \rightarrow Vg$ partonic subprocesses, respectively. Both of them are important at the COMPASS kinematics, as gluons and quarks contribute to hard exclusive meson production at the same order of α_s .

The proton helicity conserving amplitudes read

$$\begin{aligned} \mathcal{M}_{\mu+, \mu+}^{V,q} &= \frac{e}{2} \sum_a e_a C_V^a \int_{\bar{x}}^1 dx \sum_{\lambda} \mathcal{H}_{\mu\lambda, \mu\lambda}^{V,q}(x, \xi, Q^2, t=0) H^a(x, \xi, t), \\ \mathcal{M}_{\mu+, \mu+}^{V,g} &= \frac{e}{2} \sum_a e_a C_V^a \int_{\bar{x}}^1 dx \sum_{\lambda} \mathcal{H}_{\mu\lambda, \mu\lambda}^{V,g}(x, \xi, Q^2, t=0) H^g(x, \xi, t). \end{aligned} \quad (8.3)$$

Here, the first sums run over flavours of quarks forming the meson, while the second sums run over parton helicity states denoted by λ . The charge of a given quark flavour in the positron charge units, e , is denoted by e_a . The weight factors, C_V^a , correspond to the partonic structure of the meson,

$$C_{\rho^0}^u = -C_{\rho^0}^d = C_{\omega}^u = C_{\omega}^d = \frac{1}{\sqrt{2}}. \quad (8.4)$$

The integration over x starts at $\bar{x} = -1$ for quarks and at $\bar{x} = 0$ for gluons. The amplitudes for the subprocesses $\gamma^*q \rightarrow Vq$ and $\gamma^*g \rightarrow Vg$, $\mathcal{H}_{\mu\lambda, \mu\lambda}^{V,i}(x, \xi, Q^2, t=0)$, are introduced in Sec. 8.1.1, while the GPD parameterisations are introduced in Sec. 8.1.2.

The proton helicity flip amplitudes are defined similarly to those when the proton helicity is conserved,

$$\begin{aligned} \mathcal{M}_{\mu-, \mu+}^{V,q} &= -\frac{\sqrt{-t}}{2m} \frac{e}{2} \sum_a e_a C_V^a \int_{\bar{x}}^1 dx \sum_{\lambda} \mathcal{H}_{\mu\lambda, \mu\lambda}^{V,q}(x, \xi, Q^2, t=0) E^a(x, \xi, t), \\ \mathcal{M}_{\mu-, \mu+}^{V,g} &= -\frac{\sqrt{-t}}{2m} \frac{e}{2} \sum_a e_a C_V^a \int_{\bar{x}}^1 dx \sum_{\lambda} \mathcal{H}_{\mu\lambda, \mu\lambda}^{V,g}(x, \xi, Q^2, t=0) E^g(x, \xi, t). \end{aligned} \quad (8.5)$$

The factor $\sqrt{-t}/2m$, where m is the proton mass, is due to the conservation of the angular momentum and it suppresses the proton helicity flip amplitudes as $t \rightarrow 0$.

In the GK model the so-called light-cone helicities are used [45], which appear naturally in the handbag applications. A difference between these helicities and those known from the usual applications contains corrections proportional to $m\sqrt{-t}/W^2$, which may be neglected whenever $-t$ is small and W is large.

The skewness is related to the Bjorken variable by

$$\xi \simeq \frac{x_{Bj}}{2 - x_{Bj}} \left(1 + \frac{m_V^2}{Q^2} \right), \quad (8.6)$$

where m_V denotes the meson mass. In Eq. (8.6) corrections containing the terms x_{Bj}/Q^2 and x_{Bj}^2/Q^2 have been neglected, which is justified for large Q^2 .

The t dependence appears only in the GPDs, see Sec. 8.1.2. In the partonic amplitudes the t dependence introduces corrections proportional to $-t/Q^2$, which may be neglected when $-t$ is small and Q^2 is large.

The application of the model is limited to the following kinematic range: $x_{Bj} \lesssim 0.2$, $-t \lesssim 0.5 (\text{GeV}/c)^2$, $Q^2 \gtrsim 2 (\text{GeV}/c)^2$ and $W \gtrsim 5 \text{ GeV}/c^2$. The restriction on x_{Bj} is due to neglecting of contributions proportional to x_{Bj}^2 and ξ^2 in order to simplify the analysis of hard exclusive meson production. The restrictions on t and Q^2 are also important to justify some of simplifications, however they should also satisfy the requirement $-t/Q^2 \ll 1$, which is crucial for an application of the handbag factorisation. The restriction on W avoids a kinematic region that is not reproducible by the GK model [34, 38].

All values of parameters introduced in Secs. 8.1.1 and 8.1.2 that are used in these studies are summarised in Table 8.1 given at the end of this chapter.

8.1.1 Amplitudes for partonic subprocess

The partonic amplitudes are calculated within a modified perturbative approach [109]. In this approach, transverse momenta of quarks forming the meson and a gluon radiation between these quarks are retained. It allows in particular to avoid large transverse separation between the quarks, which regularises infrared singularities appearing in the collinear approximation for the transversely polarised photons [48, 49]. The approach requires a meson wave function sensitive to the quark transverse momenta.

The partonic amplitude reads

$$\begin{aligned} \mathcal{H}_{\mu\lambda,\mu\lambda}^{V,i}(x, \xi, Q^2, t=0) = \\ = \iiint d\tau d^2\mathbf{b} \hat{\Psi}_V(\tau, -\mathbf{b}) \times \hat{F}_{\mu\lambda,\mu\lambda}(x, \xi, \tau, Q^2, \mathbf{b}) \times \alpha_S(\mu_R) \times \exp[-S(\tau, \mathbf{b}, Q^2)]. \end{aligned} \quad (8.7)$$

Here, τ is the fraction of light-cone plus component of the meson momentum carried by the quark, while the anti-quark carries the fraction $\bar{\tau} = 1 - \tau$. The impact space parameter is denoted by \mathbf{b} . The Sudakov term, $S(\tau, \mathbf{b}, Q^2)$, takes into account a soft gluon radiation between quarks forming the meson. This term is defined in the \mathbf{b} space, thus the meson wave function, $\hat{\Psi}_V(\tau, -\mathbf{b})$, and the hard scattering kernel, $\hat{F}_{\mu\lambda,\mu\lambda}(x, \xi, \tau, Q^2, \mathbf{b})$, entering Eq. (8.7) have to be also given in the \mathbf{b} space. The both terms depend originally on the quark transverse momentum, \mathbf{k}_\perp , however as \mathbf{b} and \mathbf{k}_\perp are canonically conjugated, the transition from one space to another can be obtained with the two-dimensional Fourier transformation,

$$\hat{f}(\mathbf{b}) = \frac{1}{(2\pi)^2} \int d^2\mathbf{k}_\perp \exp(-i\mathbf{k}_\perp \cdot \mathbf{b}) f(\mathbf{k}_\perp). \quad (8.8)$$

The renormalisation scale, μ_R , is taken as the largest mass scale appearing in the hard scattering kernel, $\mu_R = \max(\tau Q, \bar{\tau} Q, 1/b)$. The choice avoids large higher order corrections in the hard scattering kernel. The running coupling constant, $\alpha_S(\mu_R)$, is calculated from the one-loop expression for three active quark flavours and $\Lambda_{\text{QCD}} = 220 \text{ MeV}$.

The hard scattering kernel term is calculated from the lowest order Feynman graphs that are needed to describe the $\gamma^*g \rightarrow Vg$ and $\gamma^*q \rightarrow Vq$ partonic subprocesses. Lengthy formulae of the propagators and the helicity-dependent factors are omitted here. These expressions are given in Ref. [33] for the gluon subprocess and in Refs. [34, 35] for the quark one.

The meson wave function has a Gaussian form as used also in other handbag applications, see for instance Refs. [110, 111],

$$\Psi_V(\tau, \mathbf{k}_\perp) = 8\pi^2 \sqrt{6} f_V(\mu_F) a_V^2 \left[1 + B_2^V C_2^{3/2} (2\tau - 1) \right] \exp \left[-a_V^2 \mathbf{k}_\perp^2 / (\tau\bar{\tau}) \right]. \quad (8.9)$$

The integration of Eq. (8.9) over \mathbf{k}_\perp leads to the so-called asymptotic form of the meson distribution amplitude, $\Psi_{AS}(\tau) = 6\tau\bar{\tau}$, modified by the second Gegenbauer moment [112], where $C_2^{3/2}$ is the second Gegenbauer polynomial. The Gegenbauer coefficient,

$$B_2^V(\mu_F) = B_2^V(\mu_0) \left(\frac{\alpha_S(\mu_F)}{\alpha_S(\mu_0)} \right)^{\gamma_2}, \quad (8.10)$$

depends on the factorisation scale, which in the modified perturbative approach is inversely proportional to the transverse separation between the quarks, $\mu_F = 1/b$. Values of $B_2^V(\mu_0)$ are specific for a given meson and each polarisation state. They were found by analysing σ_L , σ_T and $R = \sigma_L/\sigma_T$ data for hard exclusive meson production [35]. The scale evolution of $B_2^V(\mu_0)$ given by the γ_2 parameter is known from Ref. [113].

Values of the decay constant, f_V , are specific for a given meson and each polarisation state. For longitudinally polarised mesons the values are known from electronic decays [35], while for transversely polarised ones the values scale as a function of the factorisation scale

$$f_{V_T}(\mu_F) = f_{V_T}(\mu_0) \left(\frac{\alpha_S(\mu_F)}{\alpha_S(\mu_0)} \right)^{4/27}, \quad (8.11)$$

where values of $f_{V_T}(\mu_0)$ are known from QCD sum rules [114].

Also values of the transverse size parameter, a_V , are specific for a given meson and each polarisation state. They are used as normalisation parameters in the model and they are fitted to the cross section data for hard exclusive meson production.

The Sudakov term reads

$$S(\tau, b, Q^2) = s(\tau, b, Q^2) + s(\bar{\tau}, b, Q^2) - \frac{4}{\beta_0} \ln \frac{\ln(\mu_R/\Lambda_{\text{QCD}})}{\hat{b}}. \quad (8.12)$$

Here, the Sudakov function, $s(\tau, b, Q^2)$, accounts separately for quark (momentum τ) and antiquark (momentum $\bar{\tau}$) that enter the meson. The function reads

$$s(\tau, b, Q^2) = \frac{8}{3\beta_0} \left(\hat{q} \ln \left(\frac{\hat{q}}{\hat{b}} \right) - \hat{q} + \hat{b} \right) + \text{NLL}, \quad (8.13)$$

where

$$\hat{b} = -\ln(b\Lambda_{\text{QCD}}) \quad (8.14)$$

and

$$\hat{q} = \ln \left(\frac{\tau Q}{\sqrt{2}\Lambda_{\text{QCD}}} \right). \quad (8.15)$$

The next-to-leading-log corrections, denoted by NLL in Eq. (8.13), are given in Ref. [111]. The Sudakov term obeys the following additional rules: $\exp(-S)$ is set artificially to one if $\exp(-S) > 1$, $\exp(-S)$ is set to zero if $b \geq 1/\Lambda_{\text{QCD}}$ and $s(\tau, b, Q^2)$ is set to zero if $b \leq \sqrt{2}/(\beta Q)$.

Note, that the Sudakov term decreases when the transverse separation between the quarks increases, reaching zero at $b = 1/\Lambda_{\text{QCD}}$. This relation regularises the infrared singularities that occur when the transverse separation between the quarks is large.

8.1.2 Model of GPDs

The GPD parameterisations used in the GK model are based on double distributions [43, 58],

$$F^a(x, \xi, t) = \int_{-1}^1 d\beta \int_{-1+|\beta|}^{1-|\beta|} d\alpha \delta(\beta + \xi\alpha - x) f^a(\beta, \alpha, t) . \quad (8.16)$$

Here, $F^a = H^a, E^a$ and $a = q, g$. The internal variables, α and β , are used for the integration. The delta function defines the integration line at the (α, β) plane. The functions $f^a = h^a, e^a$ are associated to the GPDs H and E , respectively, and they will be introduced in the following. Note, that in Eq. (8.16) the so-called D-term [115] corresponding to the highest powers of ξ in the Mellin moments of the GPDs is neglected. This term ensures the polynomiality property for the double distribution representation, see Eq. (2.7), and it is neglected in the GK model, as it contributes only to less important real parts of the helicity-dependent amplitudes [34].

The function associated to the GPDs H reads

$$h^a(\beta, \alpha, t) = |\beta|^{-\alpha'_a t} e^{b_a t} h_a(\beta) \frac{\Gamma(2n_a + 2)}{2^{2n_a+1} \Gamma^2(n_a + 1)} \frac{[(1 - |\beta|)^2 - \alpha^2]^{n_a}}{(1 - |\beta|)^{2n_a+1}} . \quad (8.17)$$

Here, $n_{q_{\text{val}}} = 1$ for valence quarks and $n_{q_{\text{sea}}} = n_g = 2$ for sea quarks and gluons. The $|\beta|^{-\alpha'_a t}$ term has been introduced in order to reproduce the Regge-like behaviour known from the HERA measurements at low x_{Bj} . This term is followed by another one, $\exp(b_a t)$, which describes the t dependence of the Regge residua. The unpolarised PDFs, $h_a(\beta)$, ensure the appropriate $\xi = t = 0$ limit, see Eq. (2.4). The definition of the GPDs is completed with the following relations extending the range of x to the negative values,

$$\begin{aligned} h_g(\beta) &= |\beta| g(|\beta|) , \\ h_q^{\text{val}}(\beta) &= q^{\text{val}}(|\beta|) \Theta(\beta) , \\ h_q^{\text{sea}}(\beta) &= q^{\text{sea}}(|\beta|) \text{sign}(\beta) . \end{aligned} \quad (8.18)$$

The following parameterisation of the PDFs is used in order to integrate Eq. (8.16) analytically

$$h_a(\beta) = \beta^{\delta_a} (1 - \beta)^{2n_a+1} \sum_{j=0}^3 c_{aj} \beta^{j/2} . \quad (8.19)$$

Here, δ_a is the intercept parameter of the corresponding Regge trajectory, while the c_{aj} coefficients have been fitted to the CTEQ6m PDF set [116]. In the model the symmetric quark sea is assumed, *i.e.* $h_{u,\bar{u}}^{\text{sea}}(\beta) = h_{d,\bar{d}}^{\text{sea}}(\beta) = h_{s,\bar{s}}^{\text{sea}}(\beta)$.

The function associated to the GPDs E reads

$$e^a(\beta, \alpha, t) = |\beta|^{-\alpha'_a t} e^{b_a t} e_a(\beta) \frac{3}{4} \frac{[(1 - \beta)^2 - \alpha^2]}{(1 - \beta)^3} . \quad (8.20)$$

Here, the t dependence is similar to that used in the model of the GPDs H , *i.e.* it is also controlled by the Regge trajectories, $\alpha_a^e(t) = \alpha_a^e + \alpha_a^{e'} t$ and the slope b_a^e . For the valence quarks the forward limit reads

$$e_q^{\text{val}}(\beta) = \frac{\Gamma(2 - \delta_q^e + \beta_q^{\text{val}})}{\Gamma(1 - \delta_q^e) \Gamma(1 + \beta_q^{\text{val}})} \kappa_q \beta^{\delta_q^e} (1 - \beta)^{\beta_q^{\text{val}}} . \quad (8.21)$$

Here, κ_q denotes a contribution of the flavour q to the anomalous magnetic moment of proton, δ_q^e is the intercept parameter and β_q^{val} is the shape coefficient fitted to the Pauli form factors data [19].

For sea quarks and gluons the forward limits read

$$\begin{aligned} e_q^{\text{sea}}(\beta) &= N_q^{\text{sea}} \beta^{\delta_q^{\text{sea}}} (1-\beta)^{\beta_q^{\text{sea}}} \\ e_g(\beta) &= N_g \beta^{\delta_g^e} (1-\beta)^{\beta_g} . \end{aligned} \quad (8.22)$$

To constrain the normalisation, N_q^{sea} , N_g , and shape parameters, β_q^{sea} , β_g , the sum rule resulting from the energy-momentum tensor conservation [117] is used

$$\begin{aligned} 0 &= \int_0^1 dx E^g(x, 0, 0) + \sum_q \int_{-1}^1 dx x E^q(x, 0, 0) \\ &= \int_0^1 dx x e^g(x) + \sum_q \int_0^1 dx x (e_q^{\text{val}}(x) + 2e_q^{\text{sea}}(x)) . \end{aligned} \quad (8.23)$$

The second constraint comes from the positivity bound given in Ref. [19],

$$\frac{(e_a(x))^2}{(a(x))^2 - (\Delta a(x))^2} \leq 21.75 m^2 \left[\frac{g_a(x)}{f_a(x)} \right]^3 (f_a(x) - g_a(x)) . \quad (8.24)$$

Here, $e_a(x)$ is given by Eq. (8.22), $a(x)$ and $\Delta a(x)$ are the unpolarised and polarised PDFs, respectively, while $f_a(x)$ and $g_a(x)$ are the profile functions. The latter correspond to the t dependences assumed for the GPDs H^a and E^a ,

$$\begin{aligned} f_a(x) &= \alpha'_a \ln(1/x) + b_a, \\ g_a(x) &= \alpha_a^e \ln(1/x) + b_a^e . \end{aligned} \quad (8.25)$$

Note, that in Eq. (8.24) the helicity PDFs may be neglected, as present experimental results indicate small sea and gluon polarisations. In addition, by analysing Eq. (8.24) the limit on β_a for sea quarks and gluons was found in the GK model [36],

$$\beta_q^{\text{sea}}, \beta_g \geq 6 . \quad (8.26)$$

8.2 Analysis and results

Following the formalism of Ref. [36], in the present studies the β_u^{val} and β_d^{val} parameters are assumed to be unknown, while all other parameters are kept fixed. It allows in particular to check, if constraints on the GPDs $E^{q\text{val}}$ obtained by analysing $A_{UT}^{\sin(\phi-\phi_S)}$ or Pauli form factors data are consistent. By following Ref. [36], five possible scenarios for the GPDs $E^{q\text{val}}$, $E^{q\text{sea}}$ and E^g are considered. To avoid problems related to the pion pole, in these studies only results for exclusive ρ^0 meson production are taken into account. Remarks concerning results for exclusive ω meson production are given at the end of this chapter.

First scenario In this scenario the GPDs E for sea quarks and for gluons are assumed to be negligible, $E^{q\text{sea}} = E^g = 0$. Values of β_u^{val} and β_d^{val} are coupled, $\beta_u^{\text{val}} = f(\beta_d^{\text{val}})$, as a consequence of the sum rule shown in Eq. (8.23). This is the default scenario in the GK model, in which the values $\beta_u^{\text{val}} = 4$ and $\beta_d^{\text{val}} = 5.6$ have been adopted by analysing data on Pauli form factors [19].

Because the signs of $E^{u\text{val}}$ and $E^{d\text{val}}$ are driven by the opposite values of κ_u and κ_d parameters, see Eq. (8.21), the total contribution of the GPDs E to the exclusive ρ^0 meson production,

$$2/3 E^{u\text{val}} + 1/3 E^{d\text{val}} , \quad (8.27)$$

approximately vanishes for any values of coupled β_u^{val} and β_d^{val} . Therefore, the sensitivity to constrain the GPDs $E^{u\text{val}}$ and $E^{d\text{val}}$ by using only ρ^0 data is limited in this scenario. With the present precision of $A_{UT}^{\sin(\phi-\phi_S)}$ data the $E^{q\text{sea}} = E^g = 0$ case is not further considered.

Second scenario In this scenario the GPD E for sea quarks is allowed to be different from zero, $E^{q_{\text{sea}}} \neq 0$, while the GPD E for gluons is neglected, $E^g = 0$. The shape parameter for the forward limit of the GPDs $E^{q_{\text{sea}}}$ is set to be $\beta_q^{\text{sea}} = 6$, while the corresponding normalisation parameter is fixed for a given set of β_u^{val} and β_d^{val} values by Eq. (8.23), $N_q^{\text{sea}} = f(\beta_u^{\text{val}}, \beta_d^{\text{val}})$.

The result for this scenario is shown in Fig. 8.1. The procedure to obtain this results was as follows. For a given combination of β_u^{val} and β_d^{val} values the normalisation parameter for sea quarks, N_q^{sea} , was calculated from Eq. (8.23). With the GPDs fixed, the GK model was used to calculate predictions for the $A_{UT}^{\sin(\phi-\phi_S)}$ asymmetry. The predictions were calculated separately for each p_T^2 bin used for the measurement, see Table A.2, assuming the mean values of Q^2 , W and p_T^2 as determined from the data. A χ^2 comparison between the predictions and the data was used to obtain the exclusion lines, which correspond to a change of the reduced χ^2 value by one, two or three units. In Fig. 8.1 additional exclusion lines come from the positivity bound for sea quarks, see Eq. (8.24). Note, that the sea quarks saturate this bound very quickly.

In Fig. 8.1 the blue line indicates the values of β_u^{val} and β_d^{val} for which $E^{q_{\text{sea}}} = 0$ (and $E^g = 0$), *i.e.* the values of these parameters satisfy Eq. (8.23). The line denotes the situation equivalent to the first scenario. As one can see from Fig. 8.1, the line proceeds approximately along the χ^2 region preferred by the experiment (between $\Delta\chi^2 < 1$ exclusive lines). This observation confirms the small sensitivity of ρ^0 data to constrain separately the GPDs $E^{u_{\text{val}}}$ and $E^{d_{\text{val}}}$ when $E^{q_{\text{sea}}} = E^g = 0$.

By knowing the spin contribution to the nucleon spin, $S^{q_{\text{val}}}$, and by using the Ji's sum rule (2.10) to calculate the total angular momentum, $J^{q_{\text{val}}}$, the values of β_u^{val} and β_d^{val} may be used to calculate the orbital angular momenta of valence quarks, $L^{q_{\text{val}}} = J^{q_{\text{val}}} - S^{q_{\text{val}}}$. These values are shown in Fig. 8.1 in the upper and right axes. Note, that the values of $S^{q_{\text{val}}}$ were calculated from the LSS10 parameterisations of the helicity distributions [118].

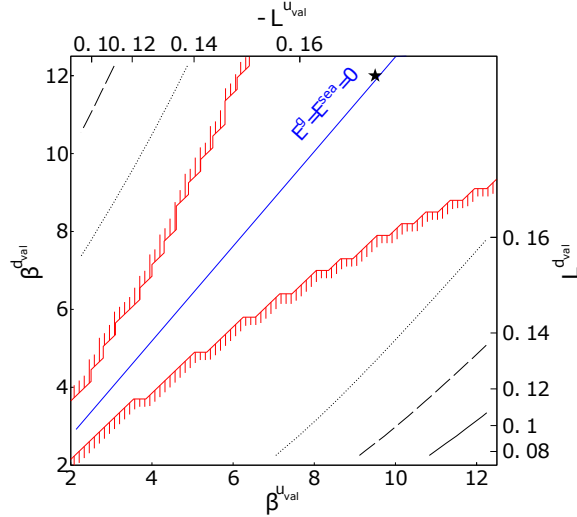


Figure 8.1: Constraints from the second scenario ($E^{q_{\text{sea}}} \neq 0$, $E^g = 0$) for exclusive ρ^0 meson production. The black dotted, dashed and solid lines indicate $\Delta\chi^2 = 1$, $\Delta\chi^2 = 2$ and $\Delta\chi^2 = 3$ values, respectively. The regions between these lines indicate the domain of β_u^{val} and β_d^{val} preferred by the experimental data on the level of $\Delta\chi^2 < 1$, $\Delta\chi^2 < 2$ and $\Delta\chi^2 < 3$, respectively. The minimum value of χ^2 corresponds to the star. The region between the red lines indicates the domain allowed by the positivity bound defined in Eq. (8.24). The blue line indicates the values of β_u^{val} and β_d^{val} for which $E^{q_{\text{sea}}} = E^g = 0$.

Third scenario In this scenario the GPD E for sea quarks are assumed to be $E^{q_{\text{sea}}} = 0$, while the GPD E for gluons may be different from zero, $E^g \neq 0$. This scenario is similar to the previous one. Also here, the shape parameter for the forward limit of the GPDs E^g is set to be $\beta_g = 6$, while the corresponding normalisation parameter is fixed for a given set of β_u^{val} and β_d^{val} values by Eq. (8.23), $N_g = f(\beta_u^{\text{val}}, \beta_d^{\text{val}})$.

The result for this scenario is shown in Fig. 8.2. Note, that in the considered range of β_u^{val} and β_d^{val} values the positivity bound shown in Eq. (8.24) was checked for gluons as well. However, the gluons do not saturate this bound, as their density inside the nucleon is much larger than that for sea quarks.

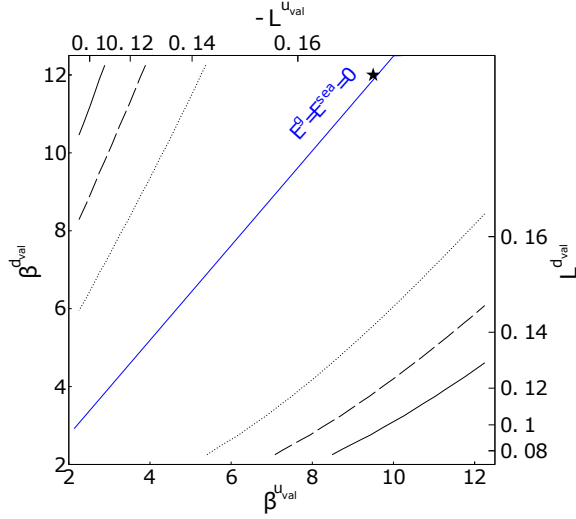


Figure 8.2: Constraints from the third scenario ($E^{q_{\text{sea}}} = 0$, $E^g \neq 0$) for exclusive ρ^0 meson production. For the description of this figure see Fig. 8.1.

Fourth and fifth scenarios In these scenarios both the GPDs E for sea quarks and gluons may be different from zero, $E^{q_{\text{sea}}}, E^g \neq 0$. The shape parameters for the forward limits of both GPDs are set to $\beta_q^{\text{sea}} = \beta_g = 6$. The normalisation parameter for sea quarks, N_q^{sea} , is set to saturate the positivity bound. The value of N_q^{sea} may be either negative (fourth scenario) or positive (fifth scenario). The normalisation parameter for gluons is fixed for a given set of β_u^{val} and β_d^{val} values by Eq. (8.23), $N_g = f(\beta_u^{\text{val}}, \beta_d^{\text{val}})$. The results for the fourth and fifth scenarios are shown in Figs. 8.3 and 8.4, respectively.

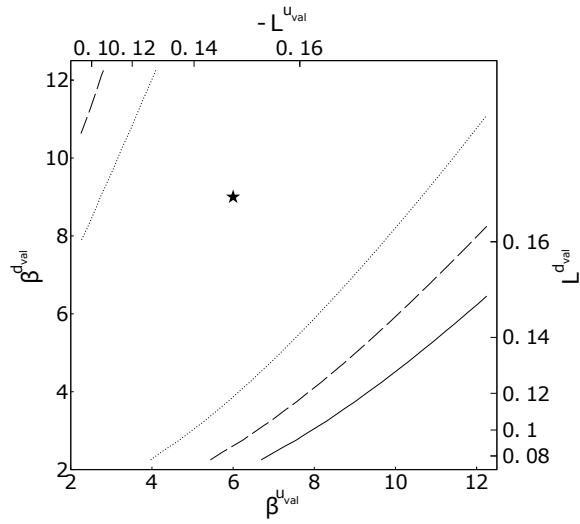


Figure 8.3: Constraints from the fourth scenario ($E^{q_{sea}} < 0, E^g \neq 0$) for exclusive ρ^0 meson production. For the description of this figure see Fig. 8.1.

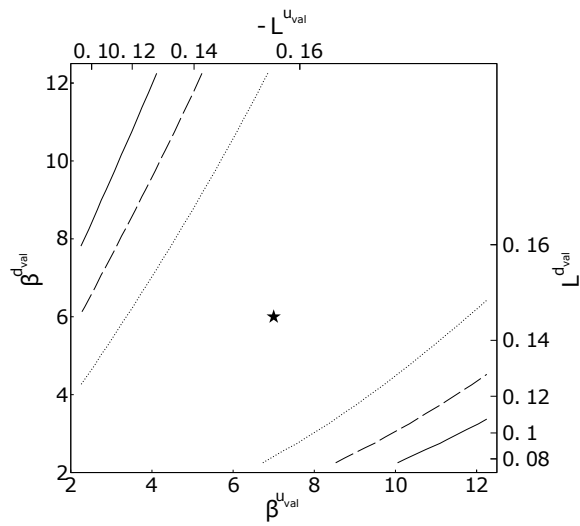


Figure 8.4: Constraints from the fifth scenario ($E^{q_{sea}} > 0, E^g \neq 0$) for exclusive ρ^0 meson production. For the description of this figure see Fig. 8.1.

Exclusive ω meson production The results of the analysis of $A_{UT}^{\sin(\phi-\phi_S)}$ asymmetries measured for exclusive ω meson production are used provisionally in these studies, because of the model uncertainty related to the pion pole exchange. However, one can still demonstrate a potential of these results to constrain the GPDs $E^{u_{\text{val}}}$ and $E^{d_{\text{val}}}$. For this purpose, the analysis for the second scenario ($E^{q_{\text{sea}}} \neq 0$ and $E^g = 0$) was performed for exclusive ω meson production. The predictions of the GK model obtained for a given combination of β_u^{val} and β_d^{val} values were compared with the single data-like point, $A_{UT}^{\sin(\phi-\phi_S)} = -0.1 \pm 0.08$. Here, the central value of this point corresponds to the value of $A_{UT}^{\sin(\phi-\phi_S)}$ asymmetry predicted by a version of the model that neglect the pion pole exchange contribution [36], while the uncertainty corresponds to the overall uncertainty of the ω measurement, see Table 7.6. The result of this investigation is shown in Fig. 8.5.

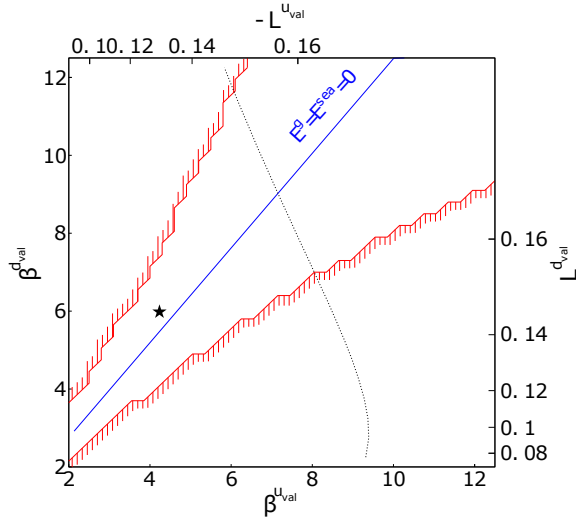


Figure 8.5: Constraints from the second scenario ($E^{q_{\text{sea}}} \neq 0$, $E^g = 0$) for exclusive ω meson production. For the description of this figure see Fig. 8.1. The $\Delta\chi^2 < 1$ region contains the star.

8.3 Conclusions

The model-dependent studies presented in this chapter demonstrate the importance of hard exclusive meson production in the exploration of the GPDs. In these studies, the COMPASS data on the $A_{UT}^{\sin(\phi-\phi_S)}$ asymmetry were used to constrain specific parameters of GPD parameterisations used in the GK model. As one can conclude, the data for exclusive ρ^0 production prefer approximately symmetric values of β_u^{val} and β_d^{val} parameters and exclude very asymmetric combinations. This observation is in agreement with the analysis of Pauli form factors data referred in Ref. [19]. The impact of the GPDs $E^{q_{\text{sea}}}$ and E^g on the $A_{UT}^{\sin(\phi-\phi_S)}$ asymmetry measured in exclusive production of ρ^0 meson is limited, as indicated by the similar results for the different studied scenarios.

After resolving the problem with the pion pole exchange contribution in exclusive ω meson production, it will become mandatory to perform a combined analysis of results for the ρ^0 and ω mesons. The study presented in this chapter demonstrates the complementary role of both processes, which can be noticed by comparing directions of exclusion lines in Figs. 8.1 and 8.5.

8.4 Parameters of the model

Table 8.1: The values of GK model parameters used in this analysis. The values marked by the asterisk have been varied in the performed analysis.

Meson wave function						
Parameter	Symbol [units]		Value			
			ρ_L^0/ω_L	ρ_T^0/ω_T		
decay constant (values given at $\mu_0 = 1$ GeV, see Eq. (8.11))	f_V [GeV]		0.209/0.187	0.167/0.150		
Gegenbauer coefficient (values given at $\mu_0 = 1$ GeV, see Eq. (8.10))	B_2^V		0	0.1		
Scale evolution parameter	γ_2		0.62	0.49		
Transverse size parameter	a_V [GeV $^{-1}$]		1	0.75		
GPD parameterisations						
Parameter	GPD	Symbol [units]	Value			
			$u_{\text{val}}/d_{\text{val}}$	q_{sea}	g	
Regge residuum parameter	H	b_a [GeV $^{-2}$]	0	b_g	$2.58 + 0.25 \ln(m^2/(m^2+Q^2))$	
	E	b_a^e [GeV $^{-2}$]	0	$0.9b_q^{\text{sea}}$	$0.9b_g$	
Regge slope	H	α'_a [GeV $^{-2}$]	0.9	0.15	0.15	
	E	$\alpha_a^{e'}$ [GeV $^{-2}$]	$\alpha_q^{\text{val}'}$	$\alpha_q^{\text{sea}'}$	α'_g	
Regge intercept	H	δ'_a	0.48	$1 + \delta_g$	$0.1 + 0.06 \ln(Q^2/4)$	
	H	$\delta_a^{e'}$	δ_q^{val}	δ_g	δ_g	
forward limit normalisation coefficient	H	c_{aj}	see Ref. [35]			
	E	κ_a	1.67/ - 2.03			
	E	N_a	0 (*)		0 (*)	
forward limit shape coefficient	H	n_a	1	2	2	
	E	β_a	4/5.6 (*)	6	6	

Summary and outlook

The main objective of this thesis is a study of the nucleon structure, which could be described in terms of the recently developed framework of the generalised parton distributions (GPD). The GPDs provide a novel and comprehensive description of partonic structure of the nucleon. In particular, the evaluation of the GPDs may provide an insight into such a fundamental property of the nucleon as the orbital angular momentum of quarks. This may help to resolve the long standing "nucleon spin crisis". The mapping of nucleon GPDs requires a comprehensive programme of measuring various observables in hard exclusive processes, like DVCS and HEMP, in a broad kinematic range.

In this thesis new results on the azimuthal transverse target spin asymmetries were presented for hard exclusive ρ^0 and ω meson productions. The data used for the extraction of these asymmetries were collected by the COMPASS experiment that is situated at the M2 beam line of the CERN Super Proton Synchrotron. The experiment was carried out by scattering a 160 GeV polarised positive muon beam on a transversely polarised target filled either with lithium deuteride (${}^6\text{LiD}$) or ammonia (NH_3) to provide polarised deuterons or protons, respectively. The COMPASS detector is a versatile forward two-stage spectrometer. At the time of data taking the spectrometer was not optimised for measurements of exclusive processes. The absence of recoil detector and in the consequence a significant contribution of non-exclusive background in the selected sample posed a challenge and required an involved procedure to minimise effects due to this background.

Azimuthal asymmetries for exclusive ρ^0 meson production were measured for transversely polarised protons and deuterons. The values of these asymmetries were extracted over the COMPASS kinematic domain as a function of Q^2 , x_{Bj} and p_T^2 . The $A_{UT}^{\sin(\phi-\phi_S)}$ asymmetry was measured for both protons and deuterons. The asymmetries are found to be small and consistent with zero. The results of a similar measurement for ρ^0 production on the proton target by HERMES experiment [22] are compatible with the COMPASS measurement, while the latter is more precise by a factor of about three and cover a wider kinematic range. The results for the deuteron target are obtained for the first time. The results for both targets are compatible with predictions of the GPD-based model proposed by Goloskokov and Kroll [33, 34, 35, 36, 37, 38]. The small values of the $A_{UT}^{\sin(\phi-\phi_S)}$ asymmetry for the ρ^0 meson are interpreted as an approximate cancellation of contributions from the GPDs $E^{u_{\text{val}}}$ and $E^{d_{\text{val}}}$ for valence quarks due to their different sign but similar magnitude. This observation agrees with lattice QCD calculations [10], which predict similar magnitude but opposite sign of the orbital angular momentum for valence up and down quarks. The gluon and sea quarks GPDs, E^g and $E^{q_{\text{sea}}}$, have a very small effect on the predicted values of the $A_{UT}^{\sin(\phi-\phi_S)}$ asymmetry.

The large statistics of the proton data makes also possible the extraction of seven remaining transverse target spin asymmetries for exclusive ρ^0 meson production. The measured values are in a good agreement with predictions of the Goloskokov-Kroll model. The comparison of measured values of $A_{UT}^{\sin\phi_S}$ (negative) and $A_{UT}^{\sin(2\phi-\phi_S)}$ (vanishing) asymmetries implies a non-negligible contribution of the GPDs H_T that are related to the transversity distributions. It is the first experimental evidence from hard exclusive ρ^0 meson production for the observation of these parton helicity flip GPDs.

All eight transverse target spin asymmetries were also measured for exclusive ω meson production on protons. The interpretation of these results in the context of the GPD formalism is more challenging than that for ρ^0 , as the ω production is significantly influenced by the pion pole exchange contribution. This contribution was described recently in the GK model [38], however with an uncertainty on the $\pi\omega$ form factor sign appearing in the production amplitudes, which could not be resolved with previously available experimental data. It was shown in Ref. [38], that the sensitive observables to determine the $\pi\omega$ form factor sign are the transverse target spin asymmetries. By comparing the results for exclusive ω meson production with the most up-to-date predictions of the GK model [107], one may find that two asymmetries, $A_{UT}^{\sin(\phi-\phi_S)}$ and $A_{UT}^{\sin(2\phi-\phi_S)}$, prefer the negative $\pi\omega$ form factor, one asymmetry, $A_{UT}^{\sin\phi_S}$, prefer the positive one and other measured asymmetries are not sensitive to the $\pi\omega$ form factor sign. The explanation of the discrepancy between the model and the experimental data is at present unknown.

Hard exclusive meson production is sensitive to various combinations of the GPDs depending on the wave function of produced meson. In particular, exclusive ρ^0 and ω meson productions on protons are sensitive to the orthogonal combinations of the GPDs for up and down quarks, $2/3F^u + 1/3F^d$ and $2/3F^u - 1/3F^d$, respectively, where F denotes any GPD. In addition, there exists a sensitivity of the production mechanism depending on the target particle. For instance, the ρ^0 production on protons probe aforementioned combination of the GPDs for up and down quarks. By assuming the isospin invariance and by neglecting nuclear effects, for the incoherent production on nucleons in the deuteron the same GPDs are effectively probed as $E^u + E^d$. These properties may be used to disentangle contributions coming from the GPDs for up and down quarks and they motivate measurements performed for various mesons and for various targets.

The measured values of $A_{UT}^{\sin(\phi-\phi_S)}$ asymmetry for exclusive ρ^0 and ω meson productions on protons were analysed in order to set constraints on the GPDs E for the valence up and down quarks. This was done within the GPD-based model of the HEMP reaction proposed by Goloskokov and Kroll [33, 34, 35, 36, 37, 38]. The analysis is in agreement with that presented in Ref. [19] for Pauli form factors. In addition, the analysis has demonstrated the potential of $A_{UT}^{\sin(\phi-\phi_S)}$ results for constraining the GPDs E and the complementary roles of exclusive ρ^0 and ω meson productions.

The precision of the physics results discussed in this thesis depends on two algorithms developed by the author in order to improve the quality of the reconstructed data. The new algorithm for the reconstruction of tracks in the beam momentum station (BMS) is characterised by an improved efficiency and purity. In addition, a precision of the momentum reconstruction has been increased by including two additional detection planes in the reconstruction and by an improved bend-to-momentum parameterisation. The new BMS algorithm became a part of the official COMPASS software used for all recently performed reconstructions of the muon data. Also, for the first time the vertical alignment of the BMS detection planes has been checked and corrected.

The next algorithm was designed and implemented in order to improve the electromagnetic calorimeter calibration that is important for the reconstruction of π^0 and ω mesons. The algorithm analyses properties of the π^0 peak obtained from the data. The genetic algorithm is used to find a minimum of the calibration-dependent χ^2 function for a large number of unknowns of the order of few thousand. It allowed to constrain the calibration of all calorimeter cells in a wide energy range and for separate subsamples of the data.

In summary, the two measurements presented in this thesis extend significantly a pool of data sensitive to the "elusive" GPDs E , which are related to the orbital angular momenta of quarks. Those data are limited, as only few observables are sensitive to the GPDs E , such as Pauli form factors, azimuthal asymmetries for exclusive processes on transversely polarised targets and the DVCS cross section on unpolarised neutrons. Note, that the presented results are characterised by a good precision and they cover a wide kinematic range. *In principle*, they may be used in global fits in order to constrain the GPDs E . In addition, the results are sensitive to the poorly known GPDs H_T , which are related to the transversity distributions, and to the pion pole exchange contribution to the production mechanism.

The GPDs have been widely recognised as key objects in a study the nucleon structure and their exploration became a subject of interest for physics programmes of several experiments. In particular, the GPDs will be explored at COMPASS-II in two phases. The first phase, carried out with an unpolarised liquid hydrogen target and a recoil detector, is devoted mainly to the study of GPDs H that are key objects for the nucleon tomography. The second phase (still to be approved) will be carried out with polarised targets and a recoil detector in order to constrain the GPDs E . In addition, in the near future the 12 GeV upgrade at JLAB will allow to explore the GPDs at the valence region with an unprecedented precision. A further constrain of the GPDs, mostly for gluon and sea quarks, is expected after data from a future polarised electron-proton collider become available.

Acknowledgement

I would like to sincerely thank my advisor, Andrzej Sandacz, for his continuous guidance and support. I acknowledge also present and former members of Warsaw COMPASS group for being a friendly community and for sharing willingly their knowledge with me. In addition, I would like to express my gratitude to the management of National Centre for Nuclear Research and to my institute colleagues, in particular Katarzyna Deja, Stanisław Mrówczyński, Lech Szymanowski, Teresa Świerczyńska and Jakub Wagner.

I thank my colleagues from the COMPASS collaboration for their professional and merit cooperation. I express my special gratitude to Nicole d'Hose and Horst Fisher for their personal support and genuine kindness.

Finally, I would like to thank my family for their wholehearted support. I consider their encouragement as one of the most important motivations for me.

Numerical results

Table A.1: The azimuthal asymmetry $A_{UT}^{\sin(\phi-\phi_S)}$ measured on the deuteron target in bins of Q^2 , x_{Bj} or p_T^2 for exclusive ρ^0 meson production.

		$\langle Q^2 \rangle$ [[GeV/c] ²]	$\langle x_{Bj} \rangle$	$\langle p_T^2 \rangle$ [[GeV/c] ²]	$A_{UT}^{\sin(\phi-\phi_S)} \pm \sigma_{stat} \pm \sigma_{sys}$
Q^2 bin [[GeV/c] ²]	1.0 – 1.2	1.1	0.018	0.23	$0.09 \pm 0.05 \pm 0.03$
	1.2 – 1.6	1.4	0.023	0.23	$0.00 \pm 0.05 \pm 0.02$
	1.6 – 2.4	1.9	0.031	0.23	$-0.03 \pm 0.06 \pm 0.03$
	2.4 – 10.0	3.9	0.059	0.24	$0.00 \pm 0.07 \pm 0.03$
x_{Bj} bin	0.003 – 0.02	1.4	0.013	0.23	$0.03 \pm 0.04 \pm 0.02$
	0.02 – 0.03	1.6	0.025	0.23	$0.01 \pm 0.06 \pm 0.03$
	0.03 – 0.05	2.0	0.038	0.23	$-0.02 \pm 0.06 \pm 0.03$
	0.05 – 0.30	3.9	0.078	0.24	$0.04 \pm 0.09 \pm 0.05$
p_T^2 bin [[GeV/c] ²]	0.10 – 0.15	1.9	0.031	0.12	$0.02 \pm 0.05 \pm 0.02$
	0.15 – 0.25	2.0	0.031	0.19	$0.04 \pm 0.05 \pm 0.02$
	0.25 – 0.35	2.0	0.032	0.30	$-0.01 \pm 0.07 \pm 0.03$
	0.35 – 0.50	2.1	0.033	0.42	$-0.03 \pm 0.08 \pm 0.04$

Table A.2: The azimuthal asymmetries measured on the proton target in bins of Q^2 , x_{Bj} or p_T^2 for exclusive ρ^0 meson production.

		$\langle Q^2 \rangle$ [[GeV/c] ²]	$\langle x_{Bj} \rangle$	$\langle p_T^2 \rangle$ [[GeV/c] ²]	$A_{UT}^{\sin(\phi-\phi_S)} \pm \sigma_{stat} \pm \sigma_{sys}$
Q^2 bin [[GeV/c] ²]	1.0 – 1.2	1.1	0.019	0.18	$-0.019 \pm 0.020 \pm 0.005$
	1.2 – 1.6	1.4	0.025	0.18	$-0.015 \pm 0.019 \pm 0.005$
	1.6 – 2.4	1.9	0.035	0.18	$-0.002 \pm 0.021 \pm 0.005$
	2.4 – 10.0	4.0	0.076	0.19	$0.015 \pm 0.030 \pm 0.008$

Continued on the next page

Table A.2 – continued from the previous page

	0.003 – 0.02	1.4	0.013	0.17	$-0.017 \pm 0.016 \pm 0.004$
x_{Bj} bin	0.02 – 0.03	1.6	0.025	0.18	$0.013 \pm 0.022 \pm 0.006$
	0.03 – 0.05	1.9	0.038	0.18	$-0.021 \pm 0.022 \pm 0.006$
	0.05 – 0.30	3.8	0.088	0.19	$0.023 \pm 0.038 \pm 0.010$
	0.05 – 0.10	2.1	0.037	0.07	$-0.008 \pm 0.017 \pm 0.004$
p_T^2 bin [[GeV/c] ²]	0.10 – 0.15	2.1	0.039	0.12	$0.007 \pm 0.024 \pm 0.006$
	0.15 – 0.25	2.2	0.040	0.20	$0.002 \pm 0.023 \pm 0.006$
	0.25 – 0.35	2.2	0.042	0.30	$-0.058 \pm 0.035 \pm 0.009$
	0.35 – 0.50	2.3	0.043	0.42	$0.003 \pm 0.041 \pm 0.010$
		$\langle Q^2 \rangle$ [[GeV/c] ²]	$\langle x_{Bj} \rangle$	$\langle p_T^2 \rangle$ [[GeV/c] ²]	$A_{UT}^{\sin(\phi+\phi_S)} \pm \sigma_{stat} \pm \sigma_{sys}$
Q^2 bin [[GeV/c] ²]	1.0 – 1.2	1.1	0.019	0.18	$-0.055 \pm 0.042 \pm 0.013$
	1.2 – 1.6	1.4	0.025	0.18	$-0.029 \pm 0.039 \pm 0.012$
	1.6 – 2.4	1.9	0.035	0.18	$0.016 \pm 0.044 \pm 0.013$
	2.4 – 10.0	4.0	0.076	0.19	$-0.034 \pm 0.060 \pm 0.018$
x_{Bj} bin	0.003 – 0.02	1.4	0.013	0.17	$-0.018 \pm 0.036 \pm 0.011$
	0.02 – 0.03	1.6	0.025	0.18	$-0.031 \pm 0.044 \pm 0.013$
	0.03 – 0.05	1.9	0.038	0.18	$-0.082 \pm 0.044 \pm 0.013$
	0.05 – 0.30	3.8	0.088	0.19	$0.038 \pm 0.072 \pm 0.021$
p_T^2 bin [[GeV/c] ²]	0.05 – 0.10	2.1	0.037	0.07	$0.004 \pm 0.036 \pm 0.011$
	0.10 – 0.15	2.1	0.039	0.12	$-0.045 \pm 0.050 \pm 0.015$
	0.15 – 0.25	2.2	0.040	0.20	$-0.033 \pm 0.049 \pm 0.015$
	0.25 – 0.35	2.2	0.042	0.30	$-0.096 \pm 0.071 \pm 0.021$
0.35 – 0.50	2.3	0.043	0.42	$-0.005 \pm 0.083 \pm 0.024$	
		$\langle Q^2 \rangle$ [[GeV/c] ²]	$\langle x_{Bj} \rangle$	$\langle p_T^2 \rangle$ [[GeV/c] ²]	$A_{UT}^{\sin(2\phi-\phi_S)} \pm \sigma_{stat} \pm \sigma_{sys}$
Q^2 bin [[GeV/c] ²]	1.0 – 1.2	1.1	0.019	0.18	$0.008 \pm 0.015 \pm 0.006$
	1.2 – 1.6	1.4	0.025	0.18	$0.007 \pm 0.014 \pm 0.005$
	1.6 – 2.4	1.9	0.035	0.18	$0.002 \pm 0.016 \pm 0.006$
	2.4 – 10.0	4.0	0.076	0.19	$-0.010 \pm 0.023 \pm 0.008$
x_{Bj} bin	0.003 – 0.02	1.4	0.013	0.17	$0.011 \pm 0.013 \pm 0.005$
	0.02 – 0.03	1.6	0.025	0.18	$-0.015 \pm 0.016 \pm 0.006$
	0.03 – 0.05	1.9	0.038	0.18	$0.008 \pm 0.017 \pm 0.006$
	0.05 – 0.30	3.8	0.088	0.19	$-0.005 \pm 0.028 \pm 0.010$
p_T^2 bin [[GeV/c] ²]	0.05 – 0.10	2.1	0.037	0.07	$0.017 \pm 0.013 \pm 0.005$
	0.10 – 0.15	2.1	0.039	0.12	$0.004 \pm 0.019 \pm 0.007$
	0.15 – 0.25	2.2	0.040	0.20	$-0.012 \pm 0.018 \pm 0.006$
	0.25 – 0.35	2.2	0.042	0.30	$0.034 \pm 0.026 \pm 0.009$
0.35 – 0.50	2.3	0.043	0.42	$-0.045 \pm 0.031 \pm 0.011$	

Continued on the next page

Table A.2 – continued from the previous page

		$\langle Q^2 \rangle$ [[GeV/c] ²]	$\langle x_{Bj} \rangle$	$\langle p_T^2 \rangle$ [[GeV/c] ²]	$A_{UT}^{\sin(3\phi-\phi_S)} \pm \sigma_{stat} \pm \sigma_{sys}$
Q^2 bin [[GeV/c] ²]	1.0 – 1.2	1.1	0.019	0.18	$-0.028 \pm 0.046 \pm 0.015$
	1.2 – 1.6	1.4	0.025	0.18	$0.096 \pm 0.043 \pm 0.014$
	1.6 – 2.4	1.9	0.035	0.18	$0.000 \pm 0.049 \pm 0.015$
	2.4 – 10.0	4.0	0.076	0.19	$0.059 \pm 0.065 \pm 0.021$
x_{Bj} bin	0.003 – 0.02	1.4	0.013	0.17	$0.021 \pm 0.040 \pm 0.013$
	0.02 – 0.03	1.6	0.025	0.18	$0.012 \pm 0.048 \pm 0.015$
	0.03 – 0.05	1.9	0.038	0.18	$0.084 \pm 0.048 \pm 0.015$
	0.05 – 0.30	3.8	0.088	0.19	$-0.004 \pm 0.077 \pm 0.024$
p_T^2 bin [[GeV/c] ²]	0.05 – 0.10	2.1	0.037	0.07	$-0.003 \pm 0.039 \pm 0.012$
	0.10 – 0.15	2.1	0.039	0.12	$0.001 \pm 0.055 \pm 0.017$
	0.15 – 0.25	2.2	0.040	0.20	$0.033 \pm 0.053 \pm 0.017$
	0.25 – 0.35	2.2	0.042	0.30	$0.106 \pm 0.077 \pm 0.024$
	0.35 – 0.50	2.3	0.043	0.42	$0.137 \pm 0.090 \pm 0.029$
		$\langle Q^2 \rangle$ [[GeV/c] ²]	$\langle x_{Bj} \rangle$	$\langle p_T^2 \rangle$ [[GeV/c] ²]	$A_{UT}^{\sin \phi_S} \pm \sigma_{stat} \pm \sigma_{sys}$
Q^2 bin [[GeV/c] ²]	1.0 – 1.2	1.1	0.019	0.18	$-0.006 \pm 0.016 \pm 0.006$
	1.2 – 1.6	1.4	0.025	0.18	$-0.035 \pm 0.015 \pm 0.006$
	1.6 – 2.4	1.9	0.035	0.18	$-0.008 \pm 0.017 \pm 0.007$
	2.4 – 10.0	4.0	0.076	0.19	$-0.028 \pm 0.023 \pm 0.009$
x_{Bj} bin	0.003 – 0.02	1.4	0.013	0.17	$-0.031 \pm 0.013 \pm 0.005$
	0.02 – 0.03	1.6	0.025	0.18	$-0.011 \pm 0.016 \pm 0.007$
	0.03 – 0.05	1.9	0.038	0.18	$-0.012 \pm 0.017 \pm 0.007$
	0.05 – 0.30	3.8	0.088	0.19	$-0.016 \pm 0.030 \pm 0.012$
p_T^2 bin [[GeV/c] ²]	0.05 – 0.10	2.1	0.037	0.07	$-0.019 \pm 0.013 \pm 0.005$
	0.10 – 0.15	2.1	0.039	0.12	$-0.002 \pm 0.019 \pm 0.007$
	0.15 – 0.25	2.2	0.040	0.20	$-0.014 \pm 0.018 \pm 0.007$
	0.25 – 0.35	2.2	0.042	0.30	$-0.044 \pm 0.026 \pm 0.010$
	0.35 – 0.50	2.3	0.043	0.42	$-0.038 \pm 0.032 \pm 0.012$
		$\langle Q^2 \rangle$ [[GeV/c] ²]	$\langle x_{Bj} \rangle$	$\langle p_T^2 \rangle$ [[GeV/c] ²]	$A_{LT}^{\cos(\phi-\phi_S)} \pm \sigma_{stat} \pm \sigma_{sys}$
Q^2 bin [[GeV/c] ²]	1.0 – 1.2	1.1	0.019	0.18	$0.13 \pm 0.09 \pm 0.05$
	1.2 – 1.6	1.4	0.025	0.18	$0.12 \pm 0.08 \pm 0.06$
	1.6 – 2.4	1.9	0.035	0.18	$-0.06 \pm 0.10 \pm 0.06$
	2.4 – 10.0	4.0	0.076	0.19	$0.13 \pm 0.14 \pm 0.08$
x_{Bj} bin	0.003 – 0.02	1.4	0.013	0.17	$0.03 \pm 0.05 \pm 0.03$
	0.02 – 0.03	1.6	0.025	0.18	$0.02 \pm 0.11 \pm 0.06$
	0.03 – 0.05	1.9	0.038	0.18	$0.10 \pm 0.16 \pm 0.09$
	0.05 – 0.30	3.8	0.088	0.19	$0.36 \pm 0.29 \pm 0.16$

Continued on the next page

Table A.2 – continued from the previous page

	0.05 – 0.10	2.1	0.037	0.07	$0.09 \pm 0.08 \pm 0.04$
p_T^2 bin	0.10 – 0.15	2.1	0.039	0.12	$0.03 \pm 0.11 \pm 0.06$
$[(\text{GeV}/c)^2]$	0.15 – 0.25	2.2	0.040	0.20	$0.02 \pm 0.11 \pm 0.06$
	0.25 – 0.35	2.2	0.042	0.30	$0.04 \pm 0.16 \pm 0.09$
	0.35 – 0.50	2.3	0.043	0.42	$0.37 \pm 0.20 \pm 0.11$
		$\langle Q^2 \rangle$ $[(\text{GeV}/c)^2]$	$\langle x_{Bj} \rangle$	$\langle p_T^2 \rangle$ $[(\text{GeV}/c)^2]$	$A_{LT}^{\cos(2\phi - \phi_S)} \pm \sigma_{stat} \pm \sigma_{sys}$
	1.0 – 1.2	1.1	0.019	0.18	$0.01 \pm 0.13 \pm 0.06$
Q^2 bin	1.2 – 1.6	1.4	0.025	0.18	$0.09 \pm 0.13 \pm 0.06$
$[(\text{GeV}/c)^2]$	1.6 – 2.4	1.9	0.035	0.18	$0.09 \pm 0.15 \pm 0.06$
	2.4 – 10.0	4.0	0.076	0.19	$0.20 \pm 0.21 \pm 0.09$
	0.003 – 0.02	1.4	0.013	0.17	$0.02 \pm 0.07 \pm 0.03$
x_{Bj} bin	0.02 – 0.03	1.6	0.025	0.18	$0.10 \pm 0.17 \pm 0.07$
	0.03 – 0.05	1.9	0.038	0.18	$0.24 \pm 0.22 \pm 0.10$
	0.05 – 0.30	3.8	0.088	0.19	$0.18 \pm 0.40 \pm 0.17$
	0.05 – 0.10	2.1	0.037	0.07	$0.06 \pm 0.12 \pm 0.05$
p_T^2 bin	0.10 – 0.15	2.1	0.039	0.12	$-0.01 \pm 0.16 \pm 0.07$
$[(\text{GeV}/c)^2]$	0.15 – 0.25	2.2	0.040	0.20	$0.14 \pm 0.16 \pm 0.07$
	0.25 – 0.35	2.2	0.042	0.30	$0.08 \pm 0.23 \pm 0.10$
	0.35 – 0.50	2.3	0.043	0.42	$0.28 \pm 0.28 \pm 0.12$
		$\langle Q^2 \rangle$ $[(\text{GeV}/c)^2]$	$\langle x_{Bj} \rangle$	$\langle p_T^2 \rangle$ $[(\text{GeV}/c)^2]$	$A_{LT}^{\cos \phi_S} \pm \sigma_{stat} \pm \sigma_{sys}$
	1.0 – 1.2	1.1	0.019	0.18	$0.01 \pm 0.12 \pm 0.07$
Q^2 bin	1.2 – 1.6	1.4	0.025	0.18	$-0.34 \pm 0.12 \pm 0.07$
$[(\text{GeV}/c)^2]$	1.6 – 2.4	1.9	0.035	0.18	$0.04 \pm 0.13 \pm 0.08$
	2.4 – 10.0	4.0	0.076	0.19	$-0.08 \pm 0.19 \pm 0.11$
	0.003 – 0.02	1.4	0.013	0.17	$-0.05 \pm 0.06 \pm 0.04$
x_{Bj} bin	0.02 – 0.03	1.6	0.025	0.18	$-0.08 \pm 0.15 \pm 0.09$
	0.03 – 0.05	1.9	0.038	0.18	$-0.31 \pm 0.20 \pm 0.12$
	0.05 – 0.30	3.8	0.088	0.19	$0.02 \pm 0.36 \pm 0.21$
	0.05 – 0.10	2.1	0.037	0.07	$-0.03 \pm 0.11 \pm 0.06$
p_T^2 bin	0.10 – 0.15	2.1	0.039	0.12	$-0.22 \pm 0.15 \pm 0.09$
$[(\text{GeV}/c)^2]$	0.15 – 0.25	2.2	0.040	0.20	$-0.08 \pm 0.15 \pm 0.09$
	0.25 – 0.35	2.2	0.042	0.30	$-0.15 \pm 0.22 \pm 0.13$
	0.35 – 0.50	2.3	0.043	0.42	$-0.21 \pm 0.26 \pm 0.15$

Table A.3: The azimuthal asymmetries measured on the proton target in bins of Q^2 , x_{Bj} or p_T^2 for exclusive ω meson production.

		$\langle Q^2 \rangle$ [[GeV/c] ²]	$\langle x_{Bj} \rangle$	$\langle p_T^2 \rangle$ [[GeV/c] ²]	$A_{UT}^{\sin(\phi-\phi_S)} \pm \sigma_{stat} \pm \sigma_{sys}$
Q^2 bin	1.0 – 1.8	1.3	0.030	0.17	$-0.10 \pm 0.10 \pm 0.04$
	1.8 – 10.0	3.3	0.071	0.17	$0.00 \pm 0.11 \pm 0.04$
x_{Bj} bin	0.003 – 0.04	1.5	0.026	0.17	$-0.10 \pm 0.10 \pm 0.04$
	0.04 – 0.30	3.1	0.073	0.17	$0.00 \pm 0.11 \pm 0.04$
p_T^2 bin	0.05 – 0.15	2.2	0.049	0.09	$0.07 \pm 0.10 \pm 0.03$
	0.15 – 0.50	2.3	0.050	0.27	$-0.21 \pm 0.11 \pm 0.05$
		$\langle Q^2 \rangle$ [[GeV/c] ²]	$\langle x_{Bj} \rangle$	$\langle p_T^2 \rangle$ [[GeV/c] ²]	$A_{UT}^{\sin(\phi+\phi_S)} \pm \sigma_{stat} \pm \sigma_{sys}$
Q^2 bin	1.0 – 1.8	1.3	0.030	0.17	$0.01 \pm 0.20 \pm 0.07$
	1.8 – 10.0	3.3	0.071	0.17	$0.14 \pm 0.23 \pm 0.09$
x_{Bj} bin	0.003 – 0.04	1.5	0.026	0.17	$-0.01 \pm 0.20 \pm 0.07$
	0.04 – 0.30	3.1	0.073	0.17	$0.12 \pm 0.22 \pm 0.08$
p_T^2 bin	0.05 – 0.15	2.2	0.049	0.09	$0.08 \pm 0.20 \pm 0.06$
	0.15 – 0.50	2.3	0.050	0.27	$-0.01 \pm 0.23 \pm 0.09$
		$\langle Q^2 \rangle$ [[GeV/c] ²]	$\langle x_{Bj} \rangle$	$\langle p_T^2 \rangle$ [[GeV/c] ²]	$A_{UT}^{\sin(2\phi-\phi_S)} \pm \sigma_{stat} \pm \sigma_{sys}$
Q^2 bin	1.0 – 1.8	1.3	0.030	0.17	$-0.020 \pm 0.069 \pm 0.039$
	1.8 – 10.0	3.3	0.071	0.17	$-0.107 \pm 0.082 \pm 0.035$
x_{Bj} bin	0.003 – 0.04	1.5	0.026	0.17	$-0.074 \pm 0.069 \pm 0.033$
	0.04 – 0.30	3.1	0.073	0.17	$-0.042 \pm 0.079 \pm 0.040$
p_T^2 bin	0.05 – 0.15	2.2	0.049	0.09	$-0.123 \pm 0.070 \pm 0.036$
	0.15 – 0.50	2.3	0.050	0.27	$0.027 \pm 0.081 \pm 0.035$
		$\langle Q^2 \rangle$ [[GeV/c] ²]	$\langle x_{Bj} \rangle$	$\langle p_T^2 \rangle$ [[GeV/c] ²]	$A_{UT}^{\sin(3\phi-\phi_S)} \pm \sigma_{stat} \pm \sigma_{sys}$
Q^2 bin	1.0 – 1.8	1.3	0.030	0.17	$0.23 \pm 0.20 \pm 0.11$
	1.8 – 10.0	3.3	0.071	0.17	$-0.02 \pm 0.23 \pm 0.09$
x_{Bj} bin	0.003 – 0.04	1.5	0.026	0.17	$0.19 \pm 0.20 \pm 0.10$
	0.04 – 0.30	3.1	0.073	0.17	$0.05 \pm 0.23 \pm 0.09$
p_T^2 bin	0.05 – 0.15	2.2	0.049	0.09	$-0.03 \pm 0.20 \pm 0.06$
	0.15 – 0.50	2.3	0.050	0.27	$0.34 \pm 0.23 \pm 0.16$

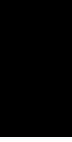
Continued on the next page

Table A.3 – continued from the previous page

		$\langle Q^2 \rangle$ [[GeV/c] ²]	$\langle x_{Bj} \rangle$	$\langle p_T^2 \rangle$ [[GeV/c] ²]	$A_{UT}^{\sin \phi_S} \pm \sigma_{stat} \pm \sigma_{sys}$
Q^2 bin	1.0 – 1.8	1.3	0.030	0.17	$0.133 \pm 0.078 \pm 0.034$
[[GeV/c] ²]	1.8 – 10.0	3.3	0.071	0.17	$0.040 \pm 0.089 \pm 0.040$
x_{Bj} bin	0.003 – 0.04	1.5	0.026	0.17	$0.148 \pm 0.077 \pm 0.035$
	0.04 – 0.30	3.1	0.073	0.17	$0.017 \pm 0.086 \pm 0.037$
p_T^2 bin	0.05 – 0.15	2.2	0.049	0.09	$0.040 \pm 0.077 \pm 0.025$
[[GeV/c] ²]	0.15 – 0.50	2.3	0.050	0.27	$0.150 \pm 0.090 \pm 0.043$
		$\langle Q^2 \rangle$ [[GeV/c] ²]	$\langle x_{Bj} \rangle$	$\langle p_T^2 \rangle$ [[GeV/c] ²]	$A_{LT}^{\cos(\phi - \phi_S)} \pm \sigma_{stat} \pm \sigma_{sys}$
Q^2 bin	1.0 – 1.8	1.3	0.030	0.17	$-0.50 \pm 0.54 \pm 0.21$
[[GeV/c] ²]	1.8 – 10.0	3.3	0.071	0.17	$0.73 \pm 0.65 \pm 0.26$
x_{Bj} bin	0.003 – 0.04	1.5	0.026	0.17	$0.11 \pm 0.46 \pm 0.17$
	0.04 – 0.30	3.1	0.073	0.17	$-0.03 \pm 0.87 \pm 0.32$
p_T^2 bin	0.05 – 0.15	2.2	0.049	0.09	$-0.81 \pm 0.54 \pm 0.21$
[[GeV/c] ²]	0.15 – 0.50	2.3	0.050	0.27	$1.11 \pm 0.66 \pm 0.30$
		$\langle Q^2 \rangle$ [[GeV/c] ²]	$\langle x_{Bj} \rangle$	$\langle p_T^2 \rangle$ [[GeV/c] ²]	$A_{LT}^{\cos(2\phi - \phi_S)} \pm \sigma_{stat} \pm \sigma_{sys}$
Q^2 bin	1.0 – 1.8	1.3	0.030	0.17	$-1.18 \pm 0.79 \pm 0.41$
[[GeV/c] ²]	1.8 – 10.0	3.3	0.071	0.17	$1.48 \pm 0.95 \pm 0.52$
x_{Bj} bin	0.003 – 0.04	1.5	0.026	0.17	$-0.27 \pm 0.66 \pm 0.24$
	0.04 – 0.30	3.1	0.073	0.17	$0.92 \pm 1.24 \pm 0.51$
p_T^2 bin	0.05 – 0.15	2.2	0.049	0.09	$-0.07 \pm 0.79 \pm 0.24$
[[GeV/c] ²]	0.15 – 0.50	2.3	0.050	0.27	$0.26 \pm 0.95 \pm 0.38$
		$\langle Q^2 \rangle$ [[GeV/c] ²]	$\langle x_{Bj} \rangle$	$\langle p_T^2 \rangle$ [[GeV/c] ²]	$A_{LT}^{\cos \phi_S} \pm \sigma_{stat} \pm \sigma_{sys}$
Q^2 bin	1.0 – 1.8	1.3	0.030	0.17	$0.36 \pm 0.74 \pm 0.27$
[[GeV/c] ²]	1.8 – 10.0	3.3	0.071	0.17	$0.49 \pm 0.91 \pm 0.35$
x_{Bj} bin	0.003 – 0.04	1.5	0.026	0.17	$1.02 \pm 0.63 \pm 0.28$
	0.04 – 0.30	3.1	0.073	0.17	$-0.91 \pm 1.16 \pm 0.45$
p_T^2 bin	0.05 – 0.15	2.2	0.049	0.09	$1.10 \pm 0.75 \pm 0.30$
[[GeV/c] ²]	0.15 – 0.50	2.3	0.050	0.27	$-0.02 \pm 0.90 \pm 0.37$

APPENDIX

B



Systematic studies plots

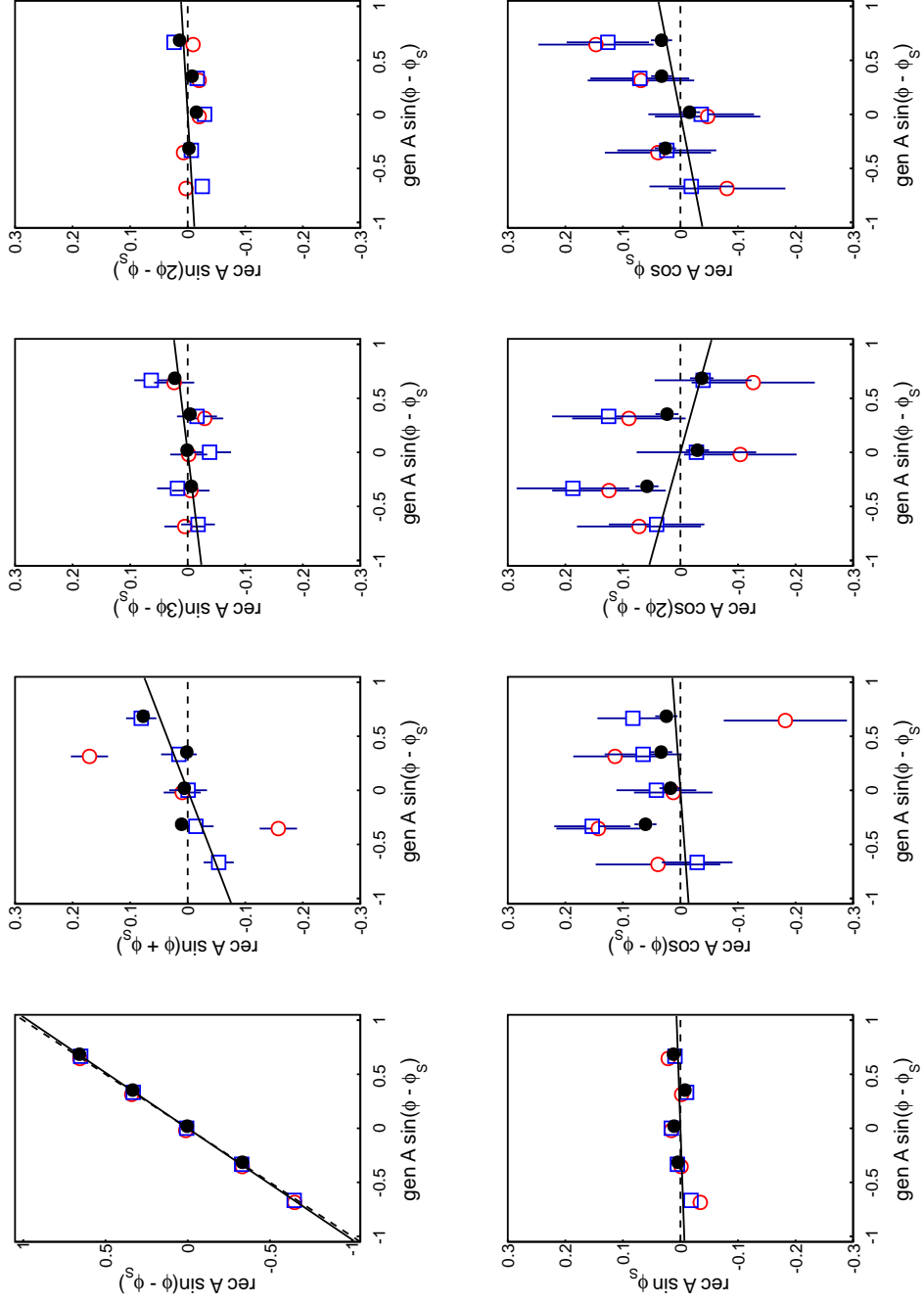


Figure B.1: Extracted values of asymmetries, $\text{rec}A$, as a function of those introduced to the full Monte Carlo simulation, $\text{gen}A$, for $A_{UT}^{\sin(\phi - \phi_S)}$ asymmetry. The extraction was performed with the 1D (red open circles) and 2D (blue open squares) and unbinned (black filled circles) maximum likelihood estimators. The dashed line denotes the expected extracted values. The solid line denotes the fit defined in Eq. (7.16) to the values extracted with the unbinned estimator. The scan is done for the exclusive ω meson production.

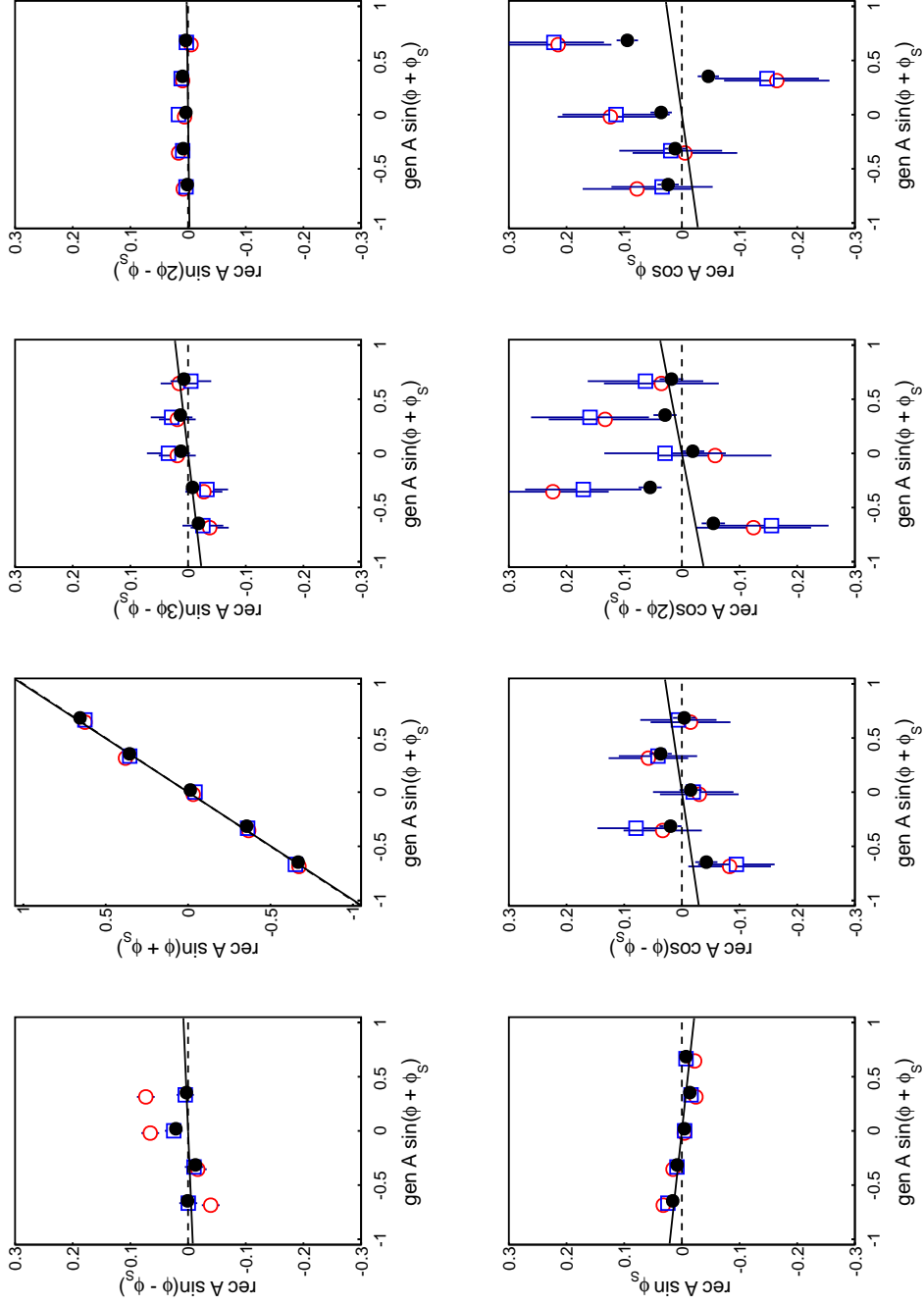


Figure B.2: Extracted values of asymmetries, $\text{rec}A$, as a function of those introduced to the full Monte Carlo simulation, $\text{gen}A$, for $\mathcal{A}_{UT}^{\sin(\phi+\phi_S)}$ asymmetry. The extraction was performed with the 1D (red open circles), 2D (blue open squares) and unbinned (black filled circles) maximum likelihood estimators. The dashed line denotes the expected extracted values. The solid line denotes the fit defined in Eq. (7.16) to the values extracted with the unbinned estimator. The scan is done for the exclusive ω meson production.

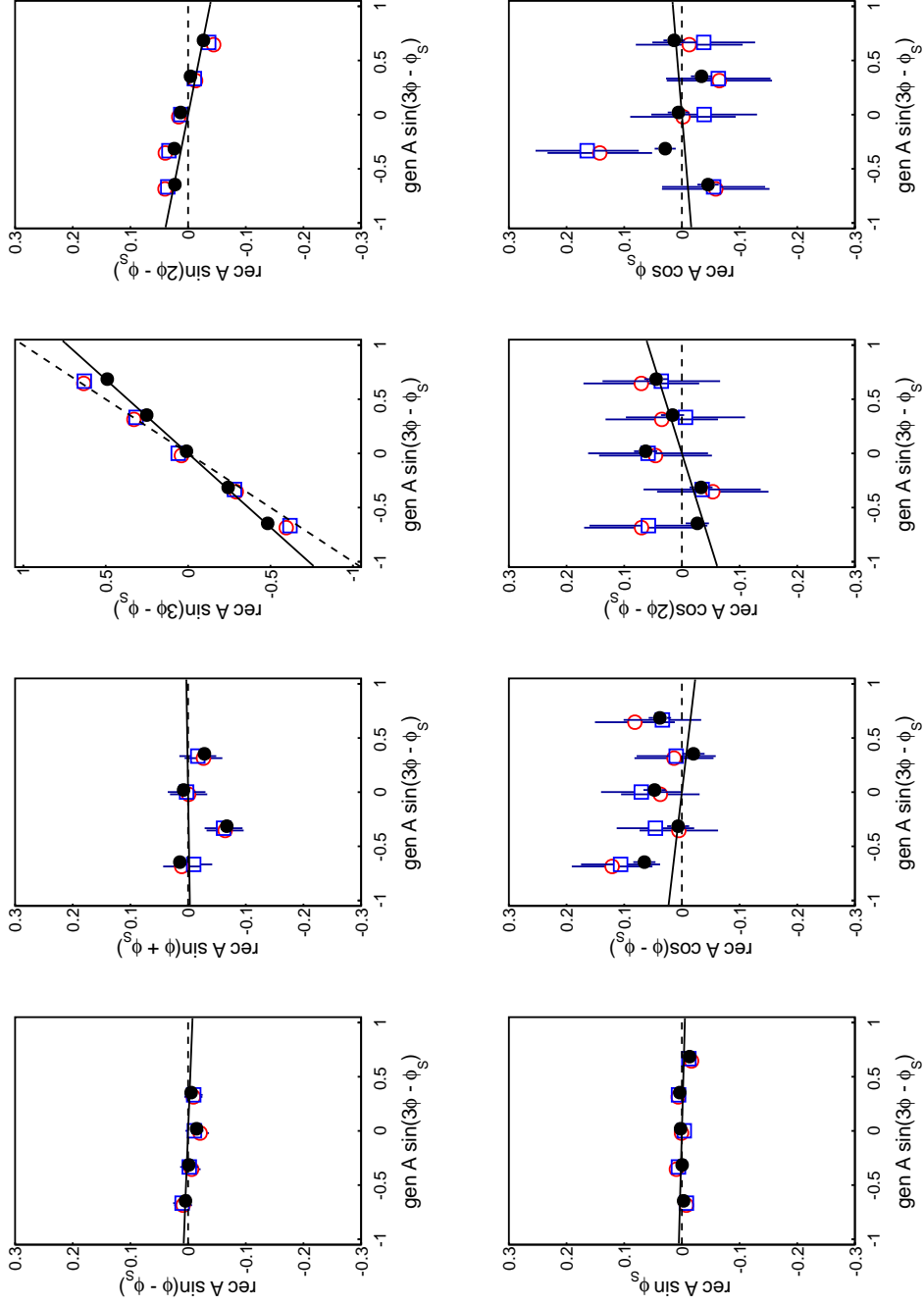


Figure B.3: Extracted values of asymmetries, $\text{rec}A$, as a function of those introduced to the full Monte Carlo simulation, $\text{gen}A$, for $A_{UT}^{\sin(3\phi - \phi_S)}$ asymmetry. The extraction was performed with the 1D (red open circles), 2D (blue open squares) and unbinned (black filled circles) maximum likelihood estimators. The dashed line denotes the expected extracted values. The solid line denotes the fit defined in Eq. (7.16) to the values extracted with the unbinned estimator. The scan is done for the exclusive ω meson production.

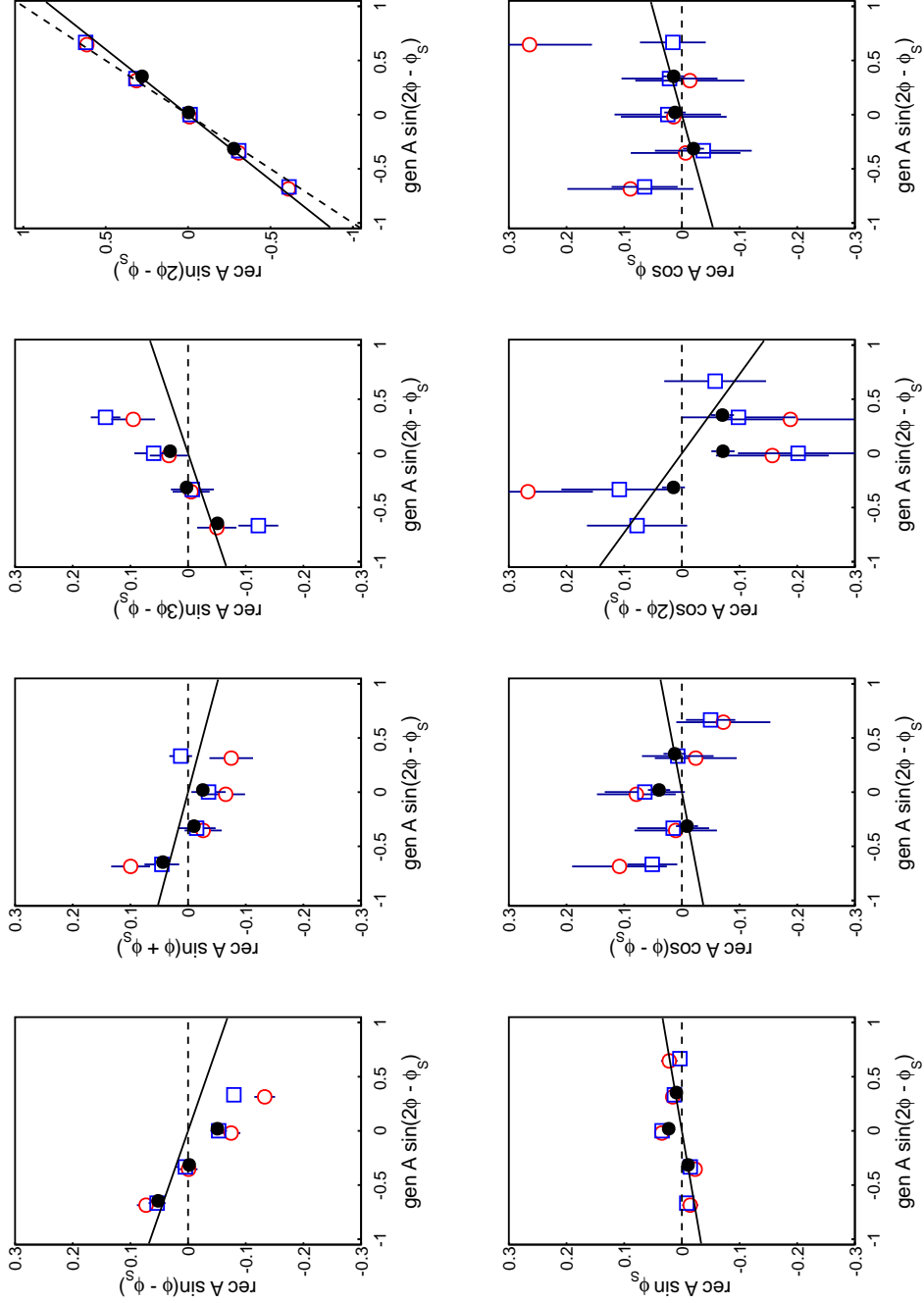


Figure B.4: Extracted values of asymmetries, $\text{rec}A$, as a function of those introduced to the full Monte Carlo simulation, $\text{gen}A$, for $A_{UT}^{\sin(2\phi - \phi_S)}$ asymmetry. The extraction was performed with the 1D (red open circles), 2D (blue open squares) and unbinned (black filled circles) maximum likelihood estimators. The dashed line denotes the expected extracted values. The solid line denotes the fit defined in Eq. (7.16) to the values extracted with the unbinned estimator. The scan is done for the exclusive ω meson production.

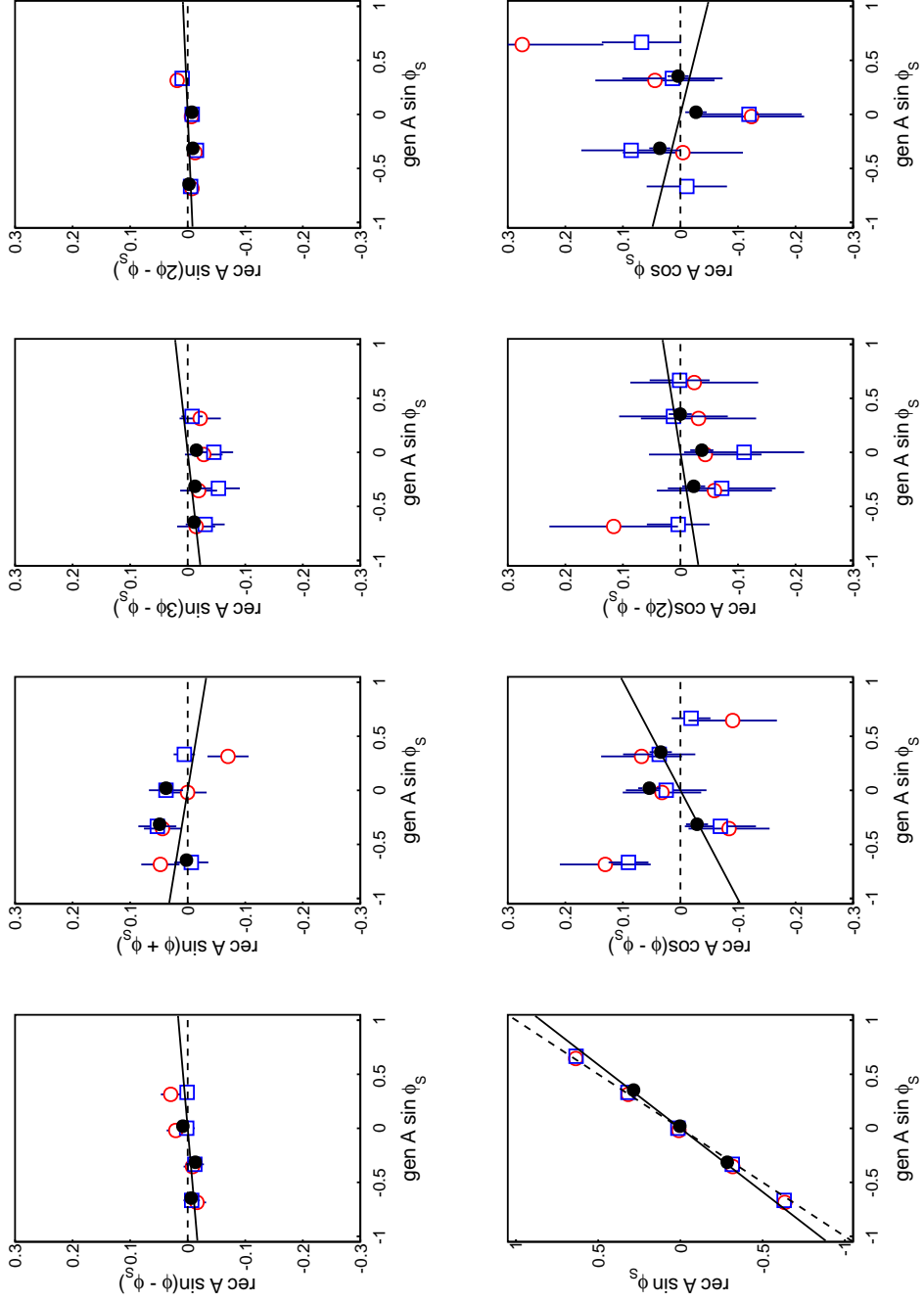


Figure B.5: Extracted values of asymmetries, $\text{rec } A$, as a function of those introduced to the full Monte Carlo simulation, $\text{gen } A$, for $A_{UT}^{\sin(\phi_S)}$ asymmetry. The extraction was performed with the 1D (red open circles) and 2D (blue open squares) and unbinned (black filled circles) maximum likelihood estimators. The dashed line denotes the expected extracted values. The solid line denotes the fit defined in Eq. (7.16) to the values extracted with the unbinned estimator. The scan is done for the exclusive ω meson production.

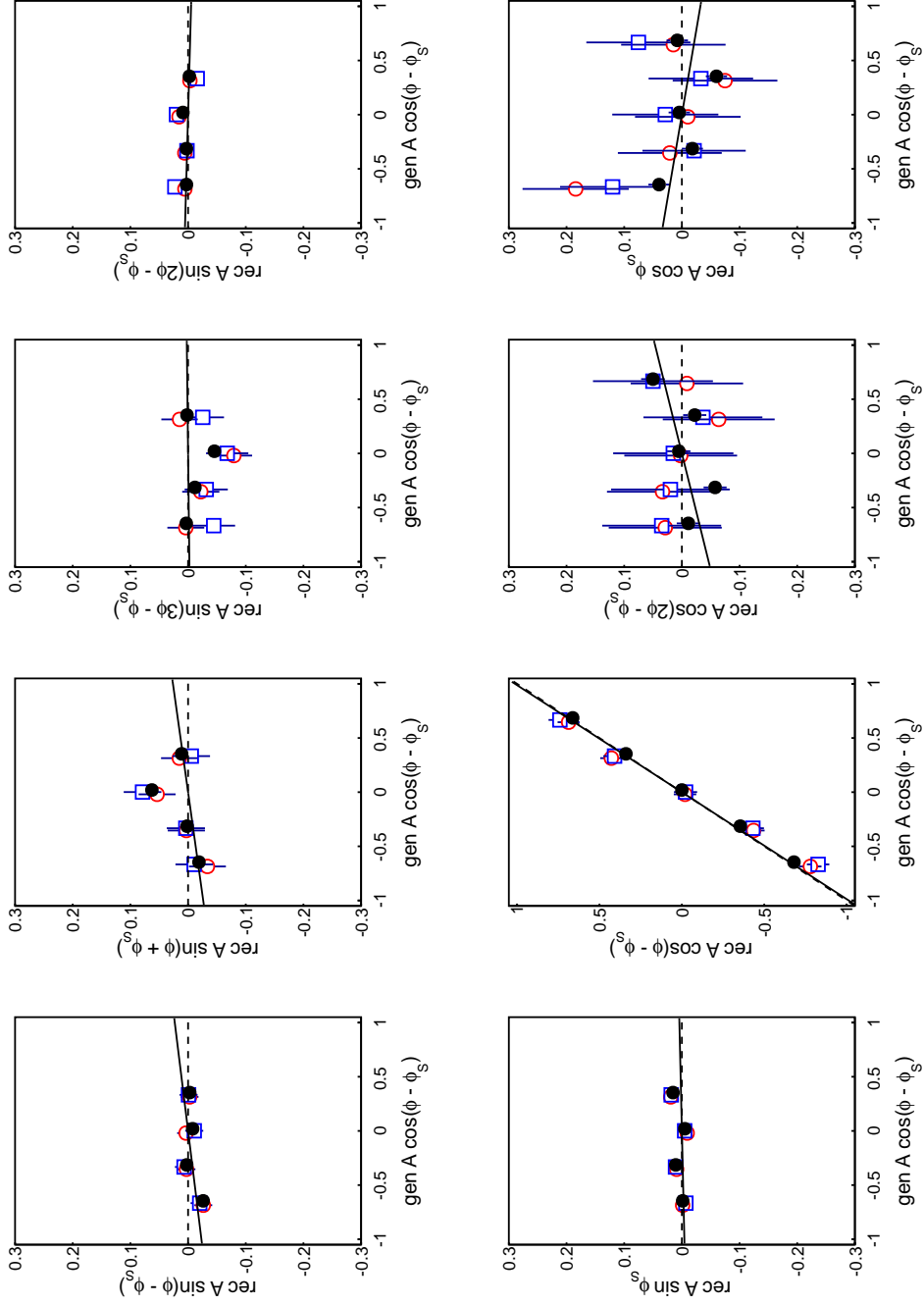


Figure B.6: Extracted values of asymmetries, $\text{rec } A$, as a function of those introduced to the full Monte Carlo simulation, $\text{gen } A$, for $A_{LT}^{\cos(\phi - \phi_S)}$ asymmetry. The extraction was performed with the 1D (red open circles), 2D (blue open squares) and unbinned (black filled circles) maximum likelihood estimators. The dashed line denotes the expected extracted values. The solid line denotes the fit defined in Eq. (7.16) to the values extracted with the unbinned estimator. The scan is done for the exclusive ω meson production.

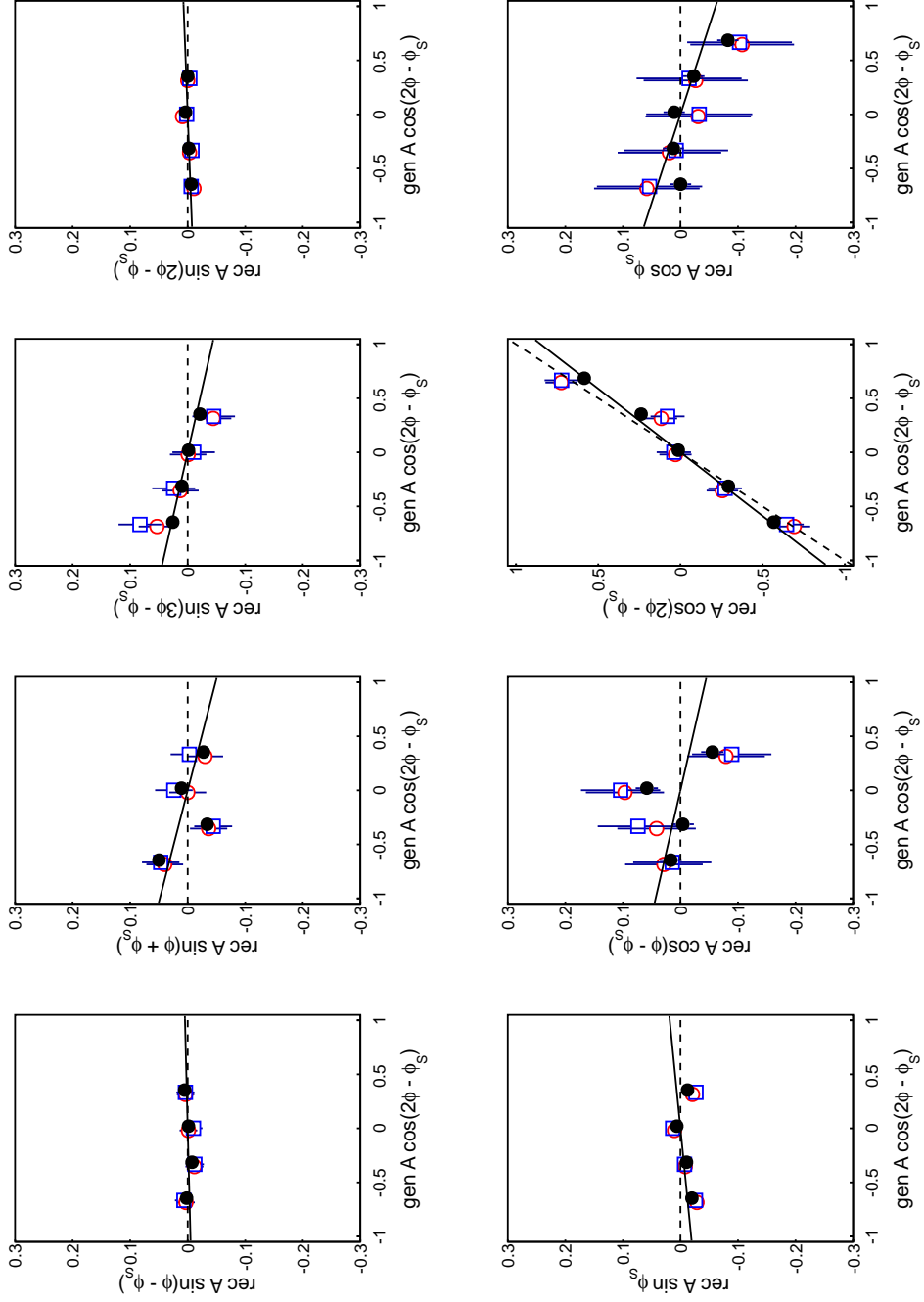


Figure B.7: Extracted values of asymmetries, $\text{rec}A$, as a function of those introduced to the full Monte Carlo simulation, $\text{gen}A$, for $A_{LT}^{\cos(2\phi - \phi_S)}$ asymmetry. The extraction was performed with the 1D (red open circles), 2D (blue open squares) and unbinned (black filled circles) maximum likelihood estimators. The dashed line denotes the expected extracted values. The solid line denotes the fit defined in Eq. (7.16) to the values extracted with the unbinned estimator. The scan is done for the exclusive ω meson production.

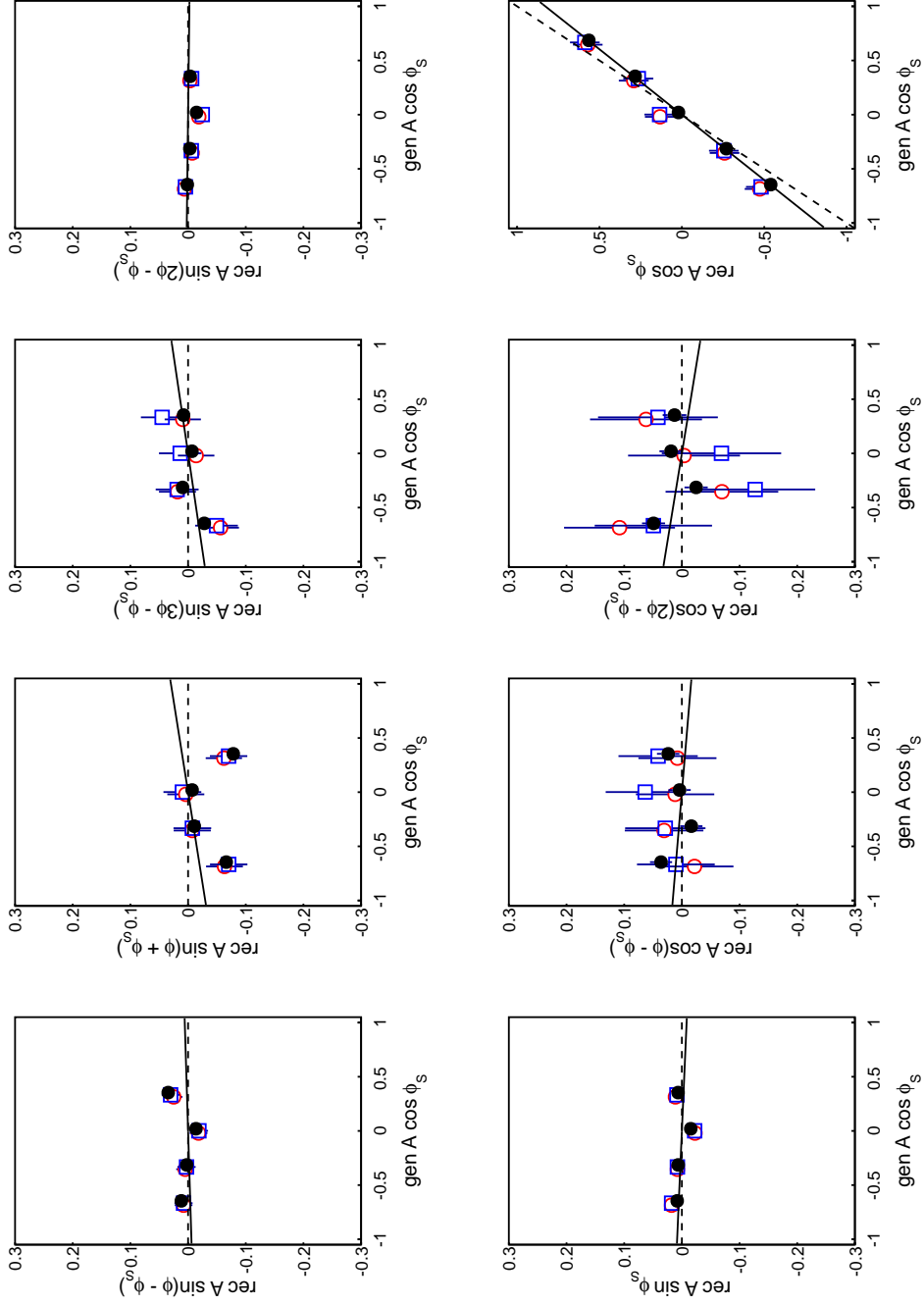


Figure B.8: Extracted values of asymmetries, $\text{rec}A$, as a function of those introduced to the full Monte Carlo simulation, $\text{gen}A$, for $A_{LT}^{\cos(\phi_S)}$ asymmetry. The extraction was performed with the 1D (red open circles) and 2D (blue open squares) and unbinned (black filled circles) maximum likelihood estimators. The dashed line denotes the expected extracted values. The solid line denotes the fit defined in Eq. (7.16) to the values extracted with the unbinned estimator. The scan is done for the exclusive ω meson production.

Bibliography

- [1] J. Ashman *et al.*, Phys. Lett. B **206**, 364 (1988).
- [2] J. Ashman *et al.*, Nucl. Phys. B **328**, 1 (1989).
- [3] D. de Florian, R. Sassot, M. Stratmann, and W. Vogelsang, Phys. Rev. Lett. **101**, 072001 (2008).
- [4] M. Gluck, E. Reya, M. Stratmann, and W. Vogelsang, Phys. Rev. D **63**, 094005 (2001).
- [5] B. Adeva *et al.*, Phys. Rev. D **70**, 012002 (2004).
- [6] A. Airapetian *et al.*, JHEP **1008**, 130 (2010).
- [7] E. Ageev *et al.*, Phys. Lett. B **633**, 25 (2006).
- [8] C. Adolph *et al.*, Phys. Rev. D **87**, 052018 (2013).
- [9] C. Adolph *et al.*, Phys. Lett. B **718**, 922 (2013).
- [10] P. Hagler, Phys. Rept. **490**, 49 (2010).
- [11] M. Burkardt, Phys. Rev. D **62**, 071503 (2000), Erratum in Ref. [119].
- [12] M. Burkardt, Int. J. Mod. Phys. A **18**, 173 (2003).
- [13] M. Burkardt, Phys. Lett. B **595**, 245 (2004).
- [14] X.-D. Ji, Phys. Rev. Lett. **78**, 610 (1997).
- [15] M. Guidal, M. Polyakov, A. Radyushkin, and M. Vanderhaeghen, Phys. Rev. D **72**, 054013 (2005).
- [16] K. Kumerički and D. Mueller, Nucl. Phys. B **841**, 1 (2010).
- [17] G. R. Goldstein, J. O. Hernandez, and S. Liuti, Phys. Rev. D **84**, 034007 (2011).
- [18] M. Guidal, H. Moutarde, and M. Vanderhaeghen, Rept. Prog. Phys. **76**, 066202 (2013).
- [19] M. Diehl, T. Feldmann, R. Jakob, and P. Kroll, Eur. Phys. J. C **39**, 1 (2005).
- [20] M. Mazouz *et al.*, Phys. Rev. Lett. **99**, 242501 (2007).
- [21] A. Airapetian *et al.*, JHEP **0806**, 066 (2008).
- [22] A. Airapetian *et al.*, Phys. Lett. B **679**, 100 (2009).

- [23] C. Adolph *et al.*, Nucl. Phys. B **865**, 1 (2012).
- [24] C. Adolph *et al.*, Phys. Lett. B **731**, 19 (2014).
- [25] A. Airapetian *et al.*, Phys. Rev. Lett. **94**, 012002 (2005).
- [26] A. Airapetian *et al.*, Phys. Rev. Lett. **103**, 152002 (2009).
- [27] M. Alekseev *et al.*, Phys. Lett. B **692**, 240 (2010).
- [28] C. Adolph *et al.*, Phys. Lett. B **717**, 383 (2012).
- [29] V. Y. Alexakhin *et al.*, Phys. Rev. Lett. **94**, 202002 (2005).
- [30] E. Ageev *et al.*, Nucl. Phys. B **765**, 31 (2007).
- [31] M. Alekseev *et al.*, Phys. Lett. B **673**, 127 (2009).
- [32] M. Anselmino *et al.*, *Comparing extractions of Sivers functions*, in *Proceedings of the Transversity-2005 conference*, 2005, hep-ex/0511017.
- [33] S. V. Goloskokov and P. Kroll, Eur. Phys. J. C **42**, 281 (2005).
- [34] S. V. Goloskokov and P. Kroll, Eur. Phys. J. C **50**, 829 (2007).
- [35] S. V. Goloskokov and P. Kroll, Eur. Phys. J. C **53**, 367 (2008).
- [36] S. V. Goloskokov and P. Kroll, Eur. Phys. J. C **59**, 809 (2009).
- [37] S. V. Goloskokov and P. Kroll, Eur. Phys. J. C **74**, 2725 (2014).
- [38] S. V. Goloskokov and P. Kroll, Eur. Phys. J. A **50**, 146 (2014).
- [39] COMPASS Collaboration, *Transverse target spin asymmetries in exclusive ω muoproduction*, to be published in Nucl. Phys. B, 2015.
- [40] A. Sandacz and P. Sznajder, *HEPGEN - generator for hard exclusive leptoproduction*, 2012, arXiv:hep-ph/1207.0333.
- [41] X.-D. Ji, Phys. Rev. D **55**, 7114 (1997).
- [42] A. Radyushkin, Phys. Lett. B **385**, 333 (1996).
- [43] D. Mueller, D. Robaschik, B. Geyer, F. Dittes, and J. Horejsi, Fortsch. Phys. **42**, 101 (1994).
- [44] K. Goeke, M. V. Polyakov, and M. Vanderhaeghen, Prog. Part. Nucl. Phys. **47**, 401 (2001).
- [45] M. Diehl, Phys. Rept. **388**, 41 (2003).
- [46] X. Ji, Ann. Rev. Nucl. Part. Sci. **54**, 413 (2004).
- [47] S. Boffi and B. Pasquini, Riv. Nuovo Cim. **30**, 387 (2007).
- [48] L. Mankiewicz and G. Piller, Phys. Rev. D **61**, 074013 (2000).
- [49] I. Anikin and O. Teryaev, Phys. Lett. B **554**, 51 (2003).
- [50] V. Gribov and L. Lipatov, Sov. J. Nucl. Phys. **15**, 438 (1972).
- [51] L. Lipatov, Sov. J. Nucl. Phys. **20**, 94 (1975).

- [52] G. Altarelli and G. Parisi, Nucl. Phys. B **126**, 298 (1977).
- [53] Y. L. Dokshitzer, Sov. Phys. JETP **46**, 641 (1977).
- [54] A. Efremov and A. Radyushkin, Phys. Lett. B **94**, 245 (1980).
- [55] G. P. Lepage and S. J. Brodsky, Phys. Lett. B **87**, 359 (1979).
- [56] M. Vanderhaeghen, P. A. Guichon, and M. Guidal, Phys. Rev. Lett. **80**, 5064 (1998).
- [57] M. Vanderhaeghen, P. A. Guichon, and M. Guidal, Phys. Rev. D **60**, 094017 (1999).
- [58] A. Radyushkin, Phys. Lett. B **449**, 81 (1999).
- [59] D. Mueller and A. Schafer, Nucl. Phys. B **739**, 1 (2006).
- [60] B. Pire, J. Soffer, and O. Teryaev, Eur. Phys. J. C **8**, 103 (1999).
- [61] M. Diehl, T. Feldmann, R. Jakob, and P. Kroll, Nucl. Phys. B **596**, 33 (2001), Erratum in Ref. [120].
- [62] P. Pobylitsa, Phys. Rev. D **65**, 077504 (2002).
- [63] P. Pobylitsa, Phys. Rev. D **65**, 114015 (2002).
- [64] P. Pobylitsa, Phys. Rev. D **66**, 094002 (2002).
- [65] P. Pobylitsa, Phys. Rev. D **67**, 034009 (2003).
- [66] P. Pobylitsa, Phys. Rev. D **67**, 094012 (2003).
- [67] P. Pobylitsa, Phys. Rev. D **70**, 034004 (2004).
- [68] E. Leader and C. Lorce, Phys. Rept. **541**, 163 (2013).
- [69] M. Wakamatsu, Int. J. Mod. Phys. A **29**, 1430012 (2014).
- [70] M. Diehl and S. Sapeta, Eur. Phys. J. C **41**, 515 (2005).
- [71] M. Alekseev *et al.*, Phys. Lett. B **693**, 227 (2010).
- [72] N. Makke for the COMPASS Collaboration, PoS **DIS2013**, 202 (2013).
- [73] C. Adolph *et al.*, Phys. Lett. B **717**, 376 (2012).
- [74] C. Adolph *et al.*, Eur. Phys. J. A **50**, 79 (2014).
- [75] C. Adolph *et al.*, *Observation of a new narrow axial-vector meson $a_1(1420)$* , Submitted to Phys. Rev. Lett., 2015.
- [76] C. Adolph *et al.*, Phys. Rev. Lett. **114**, 062002 (2015).
- [77] G. Baum *et al.*, *Common Muon and Proton Apparatus for Structure and Spectroscopy*, CERN/SPSLC 96-14, 1996.
- [78] F. Gautheron *et al.*, *COMPASS-II Proposal*, CERN/SPSC-P-340, 2010.
- [79] P. Abbon *et al.*, Nucl. Instrum. Meth. A **577**, 455 (2007).
- [80] P. Abbon *et al.*, Nucl. Instrum. Meth. A **779**, 69 (2015).

- [81] A. Abragam, *The Principles of Nuclear Magnetism* (Clarendon Press, 1961).
- [82] J. Koivuniemi *et al.*, J. Phys. Conf. Series **150**, 012023 (2009).
- [83] C. Bernet *et al.*, Nucl. Instrum. Meth. A **550**, 217 (2005).
- [84] F. Nerling for the COMPASS Collaboration, *COMPASS calorimetry in view of future plans*, in *Proceedings of the SPIN-Praha-2008 conference*, 2010, hep-ex/1007.2948.
- [85] V. Polyakov, *Radiation hard shashlik calorimeter*, CERN IRC and SAC review meeting, 2010.
- [86] Y. Bedfer, *COMPASS track reconstruction algorithm*, COMPASS Note 2004-1.
- [87] L. Gatignon, private communication, 2004.
- [88] L. Gatignon, private communication, 2010.
- [89] I. Jolliffe, *Principal Component Analysis* (Springer, 2002).
- [90] R. Joosten, private communication, 2012.
- [91] M. von Hodenberg, *First measurement of the gluon polarisation in the nucleon using D mesons at COMPASS*, PhD thesis, Albert-Ludwigs-Universität Freiburg, 2005.
- [92] R. Brun and F. Rademakers, Nucl. Instrum. Meth. A **389**, 81 (1997).
- [93] M. Mitchell, *An Introduction to Genetic Algorithms* (MIT Press, 1996).
- [94] Lyon computing farm, <http://cc.in2p3.fr> .
- [95] CERN computing farm, <http://information-technology.web.cern.ch/services/batch> .
- [96] H. Wollny, *Measuring azimuthal asymmetries in semi-inclusive deep-inelastic scattering off transversely polarized protons*, PhD thesis, Albert-Ludwigs-Universität Freiburg, 2010.
- [97] COMPASS analysis software, <http://cern.ch/ges/phast> .
- [98] M. H. Ross and L. Stodolsky, Phys. Rev. **149**, 1172 (1966).
- [99] P. Soding, Phys. Lett. **19**, 702 (1966).
- [100] J. Breitweg *et al.*, Eur. Phys. J. C **12**, 393 (2000).
- [101] S. Chekanov *et al.*, PMC Phys. A **1**, 6 (2007).
- [102] F. Aaron *et al.*, JHEP **1005**, 032 (2010).
- [103] G. Ingelman, A. Edin, and J. Rathsman, Comput. Phys. Commun. **101**, 108 (1997).
- [104] N. Doble, L. Gatignon, G. von Holtey, and F. Novoskoltsev, Nucl. Instrum. Meth. A **343**, 351 (1994).
- [105] B. Adeva *et al.*, Nucl. Instrum. Meth. A **343**, 363 (1994).
- [106] S. V. Goloskokov and P. Kroll, private communication, 2013.
- [107] S. V. Goloskokov and P. Kroll, private communication, 2014.
- [108] W. Augustyniak for the HERMES Collaboration, AIP Conference Proceedings **1441**, 126 (2012).

- [109] J. Botts and G. F. Sterman, Nucl. Phys. B **325**, 62 (1989).
- [110] R. Jakob and P. Kroll, Phys. Lett. B **315**, 463 (1993), Erratum in Ref. [121].
- [111] M. Dahm, R. Jakob, and P. Kroll, Z. Phys. C **68**, 595 (1995).
- [112] V. Chernyak and A. Zhitnitsky, Phys. Rept. **112**, 173 (1984).
- [113] M. A. Shifman and M. I. Vysotsky, Nucl. Phys. **B186**, 475 (1981).
- [114] P. Ball and V. M. Braun, Phys. Rev. **D54**, 2182 (1996).
- [115] M. V. Polyakov and C. Weiss, Phys. Rev. D **60**, 114017 (1999).
- [116] J. Pumplin *et al.*, JHEP **0207**, 012 (2002).
- [117] M. Diehl and W. Kugler, Eur. Phys. J. C **52**, 933 (2007).
- [118] E. Leader, A. V. Sidorov, and D. B. Stamenov, Phys. Rev. D **82**, 114018 (2010).
- [119] M. Burkardt, Phys. Rev. D **66**, 119903 (2002).
- [120] M. Diehl, T. Feldmann, R. Jakob, and P. Kroll, Nucl. Phys. B **605**, 647 (2001).
- [121] R. Jakob and P. Kroll, Phys. Lett. B **319**, 463 (1993).